UNSTEADY LOADING OF
HIGH SOLIDITY VERTICAL AXIS WIND TURBINES

A NUMERICAL AND EXPERIMENTAL STUDY OF UNSTEADY LOADING OF HIGH SOLIDITY VERTICAL AXIS WIND TURBINES

BY

KEVIN W. MCLAREN, B.ENG.

A Thesis
Submitted to the School of Graduate Studies
In Partial Fulfilment of the Requirements
for the Degree
Doctor of Philosophy

McMaster University

DOCTOR OF PHILOSOPHY (2011) McMaster University
(Mechanical Engineering) Hamilton, Ontario

TITLE: A Numerical and Experimental Study of Unsteady Loading of High Solidity Vertical Axis Wind Turbines

AUTHOR: Kevin W. McLaren, B.Eng. (Mechanical, McMaster University)

SUPERVISORS: Dr. S. Tullis
Dr. S. Ziada

NUMBER OF PAGES: xix, 251

ABSTRACT

This thesis reports on a numerical and experimental investigation of the unsteady loading of high solidity vertical axis wind turbines (VAWTs). Two-dimensional, unsteady Reynolds averaged Navier-Stokes simulations of a small scale, high solidity, H-type Darrieus vertical axis wind turbine revealed the dominant effect of dynamic stall on the power production and vibration excitation of the turbine. Operation of the turbine at low blade speed ratios resulted in complex flow-blade interaction mechanisms. These include; dynamic stall resulting in large scale vortex production, vortex impingement on the source blade, and significant flow momentum extraction.

To validate the numerical model, a series of full-scale experimental wind tunnel tests were performed to determine the aerodynamic loading on the turbine airfoils, vibration response behaviour, and wake velocity. In order to accomplish this, a complex force measurement and wireless telemetry system was developed. During the course of this investigation, high vibration response of the turbine was observed. This resulted in conditions that made it difficult or impossible to measure the underlying aerodynamic loading. A vibration mitigation methodology was developed to remove the effect of vibration from the measured aerodynamic forces. In doing so, an accurate and complete measurement of the aerodynamic loading on the turbine blades was obtained.

Comparison of the two-dimensional numerical model results to the experimental measurements revealed a considerable over-prediction of the turbine aerodynamic force and power coefficients, and wake velocity. From this research, it was determined that the three-dimensional flow effects due to the finite aspect ratio of the turbine and blades, as well as parasitic losses, could be accounted for through the application of inlet velocity and turbine height correction factors. In doing so, the two-dimensional numerical model results could be properly scaled to represent the three-dimensional flow behaviour of the turbine prototype. Ultimately, a validated VAWT design tool was developed.

ACKNOWLEDGEMENTS

First and foremost I would like to thank my supervisors Dr. Stephen Tullis and Dr. Samir Ziada for their invaluable expertise, guidance, and encouragement throughout my graduate studies. Thanks also to my supervisory committee members Dr. Marilyn Lightstone and Dr. Michael Tait for their guidance and advice.

Many thanks also go to the faculty and staff of McMaster University's Mechanical Engineering Department for their help in guiding, preparing for, and performing this research. I am particularly grateful to the members of the Mechanical Engineering Machine Shop for their assistance in the manufacturing of the equipment and instrumentation necessary to perform the experimental wind tunnel tests. The patience with which Joe Verhaeghe was able to assist in the wiring of the strain gauges, turbine control system, and telemetry system components is much appreciated. I would also like to recognise the assistance of Gord Hitchman at the University of Waterloo Fire Research Facility for his guidance and direction during the course of the wind tunnel tests.

McMaster University's Vertical Axis Wind Turbine Research Group members, Rafael Bravo, Kareem Aly, Stephen Kooiman, Andrzej Fiedler, and Shawn Armstrong, played a large and important role in performing this research. My thanks go to them for their countless efforts to assist in the realization of this thesis.

I am thankful for the financial support from the Natural Sciences and Engineering Research Council of Canada, the Ontario Graduate Scholarship program, the Ontario Centres of Excellence, and Cleanfield Energy, without whom this research would not have been possible.

Finally, I would like to thank my colleagues, friends, and family for their unwavering support, love, and encouragement throughout my entire university career. In particular, I would like to thank my wife for her patience, understanding, and support; and for whom my accomplishments were made all the more worthwhile.

TABLE OF CONTENTS

LIST OF FIGURES

LIST OF TABLES

NOMENCLATURE

A_p – Planform Area = (cH) [m^2]
AR – Blade Aspect Ratio = H/c [-]
C_F – Force Coefficient = $F/(½\rho U_\infty{}^2 A_p)$ [-]
C_M – Moment Coefficient = $(M/c)/(½\rho U_\infty{}^2 A_p)$ [-]
Cp – Power Coefficient = P_T/P_W [-]
D – Turbine Diameter [m]
F_D – Drag Force [N]
F_L – Lift Force [N]
F_R – Radial Force [N]
F_T – Thrust Force [N]
H – Turbine Height [m]
H_{Eff} – Effective Turbine Height = τH [m/s]
L – Distance from Turbine [m]
M – Pitching Moment [N/m]
M_a – Mach Number = U_∞/a [-]
N – Number of Turbine Blades [-]
P – Mean Pressure [Pa]
P_T – Turbine Power = $\omega RN\ 1/360 \int_0^{360} F_T\, d\theta$ [W]
P_W – Power Available in the Wind = $1/2\ \rho U_\infty^3 2RH$ [W]
R – Turbine Radius [m]
Re – Reynolds Number = $U_\infty c/\nu$ [-]
T – Temperature [°C]
$\boldsymbol{U}$ – Mean Eulerian Velocity [m/s]
U_{Eff} – Effective Flow Velocity = κU_∞ [m/s]
$U_{Downstream}$ – Wind Velocity Downstream of the Turbine [m/s]
$U_{incident}$ – Incident Wind Velocity [m/s]
$U_{rotation}$ – Wind Velocity due to Rotation [m/s]
$U_{Upstream}$ – Wind Velocity Directly Upstream of the Turbine [m/s]
U_∞ – Free Stream Wind Velocity [m/s]
a – Speed of Sound [m/s]
a – Offset in Mounting Location from Leading Edge [m]
c – Airfoil Chord Length [m]
f – Pitching Frequency [Hz]
k – Reduced Frequency = $\pi f c/U_\infty$ [-]

k_e – Effective Reduced Frequency $= \pi f c/U_{\text{incident}}$ [-]
k – Turbulent Kinetic Energy [m^2/s^2]
n – Positive Integer, 1, 2, 3, ... [-]
p – Pressure [Pa]
p' – Fluctuating Pressure [Pa]
t – Maximum Airfoil Thickness [m]
$\boldsymbol{u}$ – Eulerian Velocity [m/s]
$\boldsymbol{u}'$ – Fluctuating Eulerian Velocity [m/s]
w – Downwash Velocity [m/s]
x – Downstream Location [m]
y – Cross-stream Location [m]
y^+ – Dimensionless Wall Distance [-]
z – Vertical Location [m]
α – Relative Angle of Attack [Deg]
α_o – Mean Angle of Attack [Deg]
α_{DS} – Dynamic Stall Angle [Deg]
α_i – Induced Angle of Attack [Deg]
α_{max} – Maximum Angle of Attack [Deg]
α_{min} – Minimum Angle of Attack [Deg]
α_{ss} – Steady State Stall Angle [Deg]
$\Delta\alpha$ – Oscillation Amplitude [Deg]
β – Preset Pitch Angle [Deg]
δ – Offset in Mounting Location from Mid-chord [m]
ε – Rate of Dissipation of Turbulent Kinetic Energy [m^2/s^3]
θ – Angle of Rotation [Deg]
κ – Inlet Velocity Correction Factor [-]
λ – Blade Speed Ratio = $(\omega R/U_\infty)$ [-]
μ – Dynamic Viscosity [kg/m s]
ν – Kinematic Viscosity = μ/ρ [m^2/s]
ν_T – Turbulent Viscosity [m^2/s]
ρ – Fluid Density [kg/m^3]
σ – Solidity Ratio = $NcH/2RH$ [-]
τ – Turbine Height Correction Factor [-]
ω – Rotational Velocity [rad/s]
ω – Turbulence Frequency [Hz]

CHAPTER 1

INTRODUCTION

A recent increase in prevalence of vertical axis wind turbines (VAWT) has renewed interest in studying numerous aspects of their long-term operation; including vibration excitation, and response behaviour. Because the fatigue life of a VAWT is often considered as equally important as power output, it will have a substantial impact on the cost effectiveness of a wind turbine system (Carne, Lauffer, Gomez, & Ashwill, 1989; Veers, 1983). As such, the fatigue life of a VAWT is an important consideration during the turbine design process. Because the fatigue life of a VAWT is directly proportional to periodic loading, the proposed research endeavours to build upon previous numerical and experimental studies to further the fundamental understanding of VAWT aerodynamics, and thus vibration excitation and response. Through a better definition of the loading behaviour, the structural requirements of the turbine will be realized. In doing so, this will allow for optimal strength, lightweight blades and support structures to be designed. Thus, by developing better predictive tools, more efficient and lower-cost wind turbines can then be produced in the future (Leishman, 2002).

Prior research performed on Darrieus-type vertical axis wind turbines by research groups at Sandia National Laboratories (Klimas & Sheldahl, 1978; Sheldahl, Klimas, & Feltz, 1980) and the National Research Council of Canada (South & Rnagi, 1975), amongst many others, has focused on *low solidity* turbines operating at high rotational velocities; where the solidity ratio is defined by the ratio of the total blade area to the turbine swept area. The main reason for a low solidity design is to maximize efficiency and reduce material costs for large scale turbines. As such, prior research is primarily concerned with maximizing the power output of the turbine per unit cost. Conversely, this study focuses on analysing the aerodynamic loading of *high solidity* VAWT designs. The motivation behind this design approach is to keep the optimum turbine rotational velocity relatively low in order to minimize vibration response due to turbine imbalance, as well as reduce aerodynamic losses. Thus, the principal goal of this design is to maximize turbine longevity while producing substantial power output.

As a result of the unique operating conditions that exist at low rotational velocity however, complex periodic aerodynamic loading is expected to occur. This is namely in the form of dynamic stall, which refers to the periodic flow separation on the suction side of the blade, and the resulting unsteady lift fluctuations. In direct contrast to the design objective, in the event that dynamic stall is significant, it has been shown to produce dynamic loads that may quickly exceed structural fatigue limits. By considering the effects of dynamic stall in the turbine design, a more accurate definition of the operational and performance boundaries can be made (Leishman, 2002). The greatest challenge of this work however is the prediction of the combination of conditions that will produce dynamic stall, as well as the subsequent effects on blade loads and performance. Ultimately, due to the complicated non-linear physics of dynamic stall, it has been suggested that this behaviour can only be completely modelled by means of numerical solution of the Navier–Stokes equations (Leishman, 2002). As such, the present study will employ a coupled experimental and numerical modelling approach to provide a greater understanding of dynamic stall and its effect on blade loading and vibration excitation potential for high solidity VAWT.

The wind turbine prototype under investigation is a 3 bladed H-type vertical axis wind turbine (Figure 1.1) produced by Cleanfield Energy located in Ancaster, Ontario, Canada. The target market for this particular turbine design is commercial, municipal, and residential developments located within the urban environment. The concept of the design is to produce electrical energy at the location at which it is consumed in order to reduce expenses and losses associated with transportation.

Figure 1.1: Cleanfield Energy V3.5 production model vertical axis wind turbine (Courtesy of Cleanfield Energy, © 2010)

Because of the built-up nature of the urban environment, the large capital investment associated with the construction of tower structures in order to place the turbine higher in the atmospheric boundary layer where wind speeds are greater can be avoided. Furthermore, noise measurement studies (Appendix A.6) have indicated that the sound output level of a vertical axis wind turbine is very low as compared to other local sources of noise (traffic, AC units, etc.), and is thus ideal for urban applications. Because of the intended operating location however, the structural dynamics of this design are crucial. Excessive vibration of the turbine, mounting structure, or the building itself, as well as fatigue failure of the turbine could prove to be catastrophic. The health and safety of the local population is of utmost importance, making it imperative that the turbine has a long operational lifetime with minimal impact beyond power production.

A plan view of the vertical axis wind turbine investigated in this study is sketched in Figure 1.2. The primary turbine design parameters identified in Figure 1.2 are; the number of airfoils, N, the blade chord length, c, the turbine radius, R, and the preset pitch, β. Note that the preset pitch of the turbine blades has been exaggerated in order to clearly demonstrate its location and orientation.

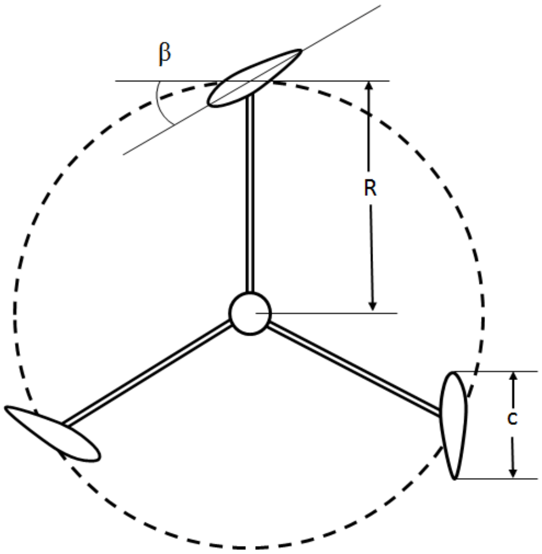

Figure 1.2: Plan view of the vertical axis wind turbine prototype

The impact of a change in two primary design parameters on the wind turbine aerodynamics will be independently investigated in this study. The first of which is the effect of a change in the preset pitch of the airfoils. As shown in Figure 1.2, the preset pitch, β, is the angle between the chord line of the airfoil and the tangent of the circular path traversed throughout a rotation. It is anticipated that a change in the preset pitch of the airfoils will have a relatively large influence on the onset and duration of dynamic stall. The second parameter which will be investigated is the effect of a change in the airfoil thickness ratio. In this study, three symmetric airfoils of varying chord length and thickness will be tested in order to determine how airfoil thickness ratio influences dynamic stall behaviour, and the resulting aerodynamic loading on the airfoils. It is expected that a change in airfoil thickness will have a large impact on the nature of the dynamic stall onset, and thus the power production and vibration excitation loads.

1.1. General Approach

1.1.1. URANS Model

The first stage of the research strategy was the development of a computational fluid dynamics (CFD) model capable of accurately representing the aerodynamics of a high-solidity VAWT cross-section. This was accomplished through the use of a rigorous series of independence and validation tests. The simulations determined the aerodynamic loading on the airfoils and wake properties for a range of blade speed ratios from 0.40 to 2.30; where the blade speed ratio is the ratio of blade velocity to the ambient wind velocity. Numerical modelling was carried out through the use of the commercial code ANSYS CFX due to its superior ability to incorporate rotating machinery. A high-resolution spatial numerical discretization scheme was applied through the use of a hybrid finite-volume/finite-element method.

1.1.2. Experimental Investigation

The second stage of this research focused on performing a series of experimental tests in order to determine the aerodynamic loading on the wind turbine airfoils (blades), the vibration response of the wind turbine, and the behaviour of the turbine wake. Three different blade profiles were tested over a range of flow velocities from 6 to 11 m/s both with and without a custom guy wire support system in place. Measurements of rotational velocity, net power output, wind velocity, aerodynamic loading, angular position and acceleration of the turbine support shaft were simultaneously recorded. Wake velocity measurements of the flow entering, exiting, and flowing around the turbine were acquired in separate flow mapping tests. The open air wind tunnel employed to perform the current study is located at the University of Waterloo Fire Research Facility in Ontario, Canada.

1.1.3. Turbine Design

The final stage of this research consisted of applying the information obtained from the experimental test program to validate, refine, and improve the numerical model prediction. The numerical model was then employed to gain a greater understanding of the aerodynamics and loading patterns of a high-solidity VAWT. This included an analysis of three-dimensional flow effects due to the finite aspect ratio of the turbine and airfoils, as well as the effect of blade design on dynamic stall and thus vibration excitation loading. Through the knowledge gained from the numerical model a set of high potential design parameters were then developed.

1.2. Contributions to the State of Knowledge

1.2.1. Develop Methods to Study Aerodynamic Loading on VAWT

Design and implementation of an accurate dynamic load measurement system was accomplished. This system consists of many components, including a series of custom load measurement devices, as well as a wireless telemetry system to remotely capture the data obtained from the rotating VAWT. Due to the high vibration response of the turbine, a custom guy wire support system was also designed to minimize the effects of turbine vibrations on aerodynamic load measurements. In order to ensure that the aerodynamic load measurements were free from any remaining effects of turbine vibration, an extensive vibration mitigation methodology was also developed. This included the amalgamation of data from different wind speeds, as well as the use of custom filtering techniques.

1.2.2. Expand the Experimental Measurement Database

Testing performed on a full scale, high solidity VAWT at high Reynolds numbers, expands the current experimental measurement database for aerodynamic loading, vibration response and wake behaviour; specifically at very low blade speed ratios where dynamic stall effects are predominant. The effect of a change in blade thickness and preset pitch on the prevalence of dynamic stall was also investigated by testing several different blade designs.

1.2.3. Improve the Fundamental Understanding of VAWT Aerodynamics

The results obtained from both the experimental and numerical stages of the current research provide a better understanding of the fundamental aerodynamic loading on high solidity VAWTs. In particular, the effects of the following aspects on turbine performance were investigated:

- Dynamic stall and its effect on vortex production and propagation, and the resultant aerodynamic loading behaviour
- Flow momentum loss through and downwind of the turbine
- Flow divergence and local acceleration due to effective turbine blockage
- The effect of turbine and airfoil aspect ratio on overall performance

1.2.4. Vertical Axis Wind Turbine Design Tool

The numerical model developed through this research study can be used to simulate countless VAWT configurations, designs, sizes, and potential environmental conditions. Design for optimization of vibration behaviour (minimize) and power output (maximize) can then be accomplished through the use of the numerical model, reducing the need for expensive and time consuming wind turbine prototypes.

1.3. Thesis Outline

This thesis consists of seven chapters. Chapter 2 outlines the previous research performed within the field of study, namely on dynamic stall, and experimental studies and numerical modelling of VAWT, through an extensive literature review. Chapter 3 describes the stages involved in the development of the vertical axis wind turbine cross-section numerical model. Chapter 4 consists of an outline of the test facility and instrumentation employed in the experimental investigation. Chapter 5 explores the results of the experimental study, including aerodynamic loading, vibration response of the turbine, and turbine power output. Refinement and application of the numerical model is the subject matter of Chapter 6. Finally, the conclusions drawn from the research as well as recommendations for future research are provided in Chapter 7.

CHAPTER 2

LITERATURE REVIEW

Because the current research is focused on the unsteady airfoil loading conditions of high solidity ($\sigma = Nc/2R > 0.4$), low blade speed ratio ($\lambda = \omega R/U_{\infty} < 2.0$), vertical axis wind turbines, understanding the fundamentals of dynamic stall and the ability to numerically model this phenomenon is imperative. Due to the nature of the turbine design, the airfoils' relative angle of attack is expected to vary by upwards of ± 50°, while being subjected to incoming flow velocity variations in excess of ± 50% of the mean wind speed. Additionally, because of the passing of the airfoils on the upstream pass, the turbulent properties of the flow vary dramatically throughout a single rotation. All of these conditions are large contributing factors to the development of dynamic stall.

Dynamic stall is a non-linear unsteady aerodynamic effect that occurs when the pitch angle of an airfoil is rapidly changed. This results in highly dynamic flows over the surface of the airfoil which exhibit far different behaviour then steady state flow. This motion often causes strong vortices to be shed from the leading edge, and travel backwards over the upper surface. These vortices briefly increase the lift produced by the airfoil, however, as soon they pass behind the trailing edge, the lift reduces dramatically and the airfoil is in normal stall. The resultant unsteady variation in the lift, drag and moment acting on the airfoil is directly related to the pitching rate, the maximum pitch angle and the conditions of the oncoming flow, amongst several other things.

As such, the following chapter will primarily serve to investigate the effect of dynamic stall properties on the nature and severity of dynamic stall and the resultant unsteady aerodynamic loading on the airfoil. The experimental studies and numerical models which have been developed to study this phenomenon in relation to VAWTs will also be thoroughly explored. Ultimately, through the lessons learned from the literature and the current study, alteration of the turbine design and operation will be employed to take advantage of the positive aspects, and negate or avoid the negative effects, of high solidity VAWT dynamics, including stall.

2.1. Normal Stall

Prior to investigating the phenomenon of dynamic stall, definition of normal stall and the variables used to characterize stall behaviour will be examined. Normal or 'classical' stall is the result of flow separation occurring over the upper surface of an airfoil. As the angle of attack of the airfoil is increased, the stagnation point moves back along the lower surface of the airfoil. As a result, the flow must then accelerate around the nose of the airfoil, causing the minimum pressure on the upper surface to drop and move toward the leading edge. In turn, a large adverse pressure gradient forms downstream of the minimum pressure location. At a critical angle of attack, the flow momentum within the boundary layer can no longer overcome the growing adverse pressure gradient, at which point the flow stops and reverses its direction (Anderson, 1989). This causes the flow to separate and places the airfoil into the stall regime. This condition is most apparent in the behaviour of the steady state lift, drag and moment coefficients (Equations 2.1, 2.2, and 2.3),

$$C_L \equiv \frac{F_L}{\frac{1}{2}\rho U_\infty^2 A_p} \qquad 2.1$$

$$C_D \equiv \frac{F_D}{\frac{1}{2}\rho U_\infty^2 A_p} \qquad 2.2$$

$$C_M \equiv \frac{M/c}{\frac{1}{2}\rho U_\infty^2 A_p} \qquad 2.3$$

where ρ is the fluid density, U_∞ is the flow velocity, A_P is the plan form area, c is the chord length, M is the pitching moment and F_L and F_D are the lift and drag forces respectively. Separation of the flow from the upper surface of the airfoil raises the mean pressure on the upper surface (pressure distribution on the lower surface is relatively unaffected), resulting in a drastic drop in the lift coefficient, accompanied by a sharp rise in the drag coefficient (Figure 2.1, $\alpha_{ss} \approx 12°$). In order to avoid this dramatic drop in the lift to drag ratio, most airfoil applications are designed to operate with a maximum angle of attack which is well below the onset of normal stall.

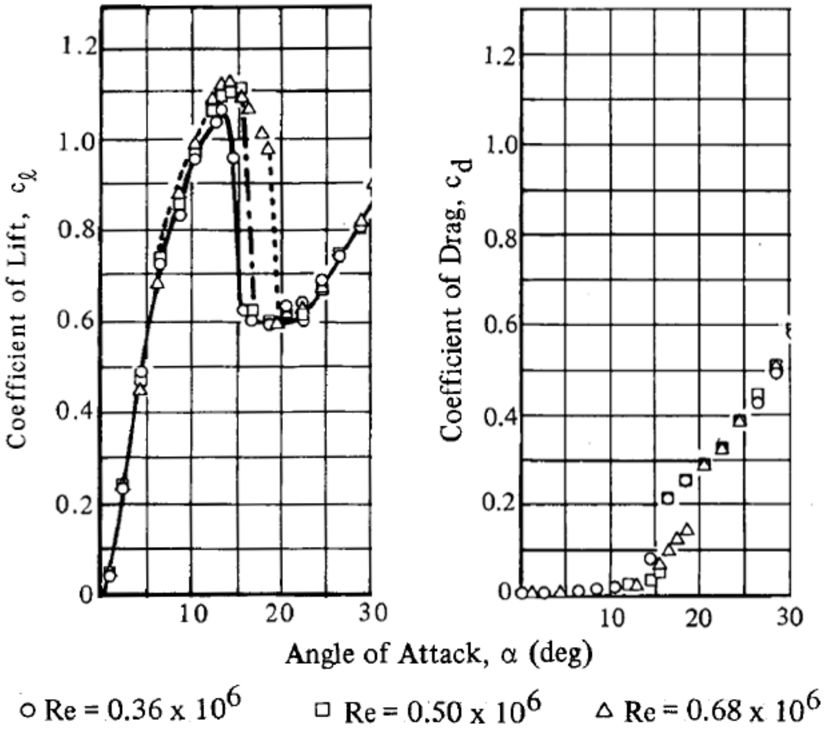

Figure 2.1: NACA 0015 lift and drag coefficients, adapted from (Sheldahl & Klimas, 1981)

From Figure 2.1, a change in airfoil performance with Reynolds number can also be identified. At high Reynolds numbers, stall is delayed to greater angles of attack and higher lift force coefficients are obtained. One of the primary reasons for this behaviour is the transition from laminar to turbulent flow. This transition in flow regimes will have a direct impact on the onset of stall, as a laminar boundary layer has less flow momentum near the airfoil surface, and thus is more prone to separation.

Numerous studies have been performed by the National Advisory Committee for Aeronautics (NACA), as well as other international organizations and researchers, to quantify this behaviour for all manner of airfoil shapes and Reynolds numbers (Jacobs & Sherman, 1973; Jacobs, Ward & Pinkerton, 1933; Loftin & Smith, 1949; Sheldahl & Klimas, 1981). In addition to these experimental studies, a great deal of effort has also been devoted to numerically modelling this phenomenon with markedly improving results. From classical aerodynamic theory, which states that at low angles of attack an airfoil can be modelled as a flat plate ($C_L = 2\pi\alpha$, α in radians), to models employing the circulation methods of the Kutta-Joukowski theorem (Batchelor, 1967), and vortex panel methods (Kuethe & Chow, 1986). More recently, advanced computational fluid dynamics models which solve the Reynolds averaged Navier-Stokes (RANS) equations to obtain pressure distributions over the surface of the airfoil have also been used (Kroll, Rossow, Schwamborn, Becker, & Heller, 2002).

2.2. Dynamic Stall

The most important conditions for obtaining reliable and repeatable steady-state force and moment coefficient data for an airfoil are; that the desired angle of attack is reached by *slowly changing the pitch of the airfoil*, ensuring that the *airfoil remains at a fixed angle* for the duration of the test, and waiting a sufficient period between tests to *allow for transient flow conditions to subside*. It is these three conditions which distinguish steady-state loading data from its dynamic counterpart. In contrast to these conditions, dynamic loading data obtained by *rapidly pitching an airfoil* shows large differences with the static loading results.

A thorough review of dynamic stall characteristics and behaviour was performed by McCroskey (1981, 1982), and will form the basis of the present literature review. Based upon experimentally obtained results, it has been identified that when an airfoil undergoes a rapid increase in the angle of attack, large overshoots in lift, drag, and pitch moment take place, and stall is delayed to higher angles of attack as compared to normal stall values. This behaviour is known as ‘dynamic stall’, sketches of which are shown below in Figure 2.2. The light dynamic stall regime is characterized by a small region of flow separation, and is typically generated at relatively small angles of attack and airfoil pitch rates. Conversely, large vortex structures and considerable hysteresis in airfoil loading dominate the deep dynamic stall flow regime, and are generally formed when the airfoil is rapidly pitched at high angles of attack. “This time-dependent vortical wake is an important distinguishing feature of unsteady airfoils” (McCroskey, 1982).

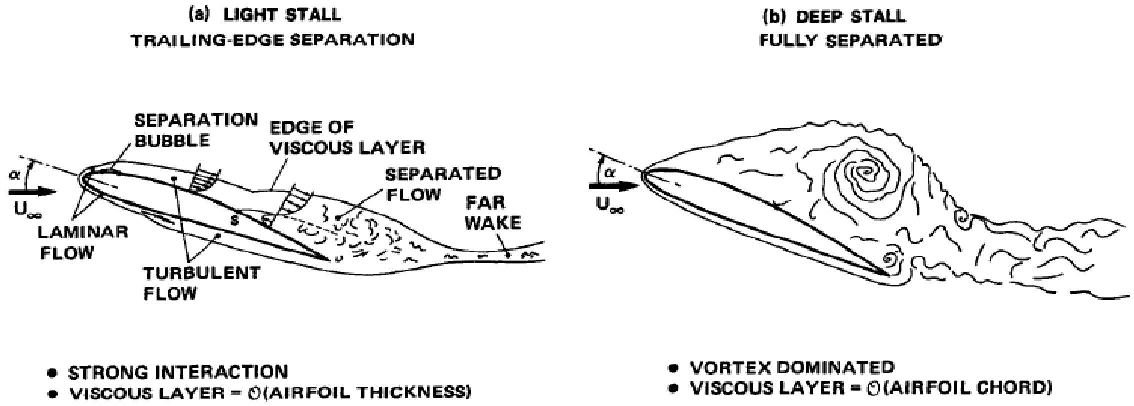
(a) LIGHT STALL
TRAILING-EDGE SEPARATION

(b) DEEP STALL
FULLY SEPARATED

Figure 2.2: Sketches of flow fields during a) light dynamic stall; and b) deep dynamic stall, adapted from (McCroskey, 1982)

It has also been shown that during deep dynamic stall, the “loss of lift is far more abrupt and more persistent then that of static stall” (Tsang, So, Leung & Wang, 2008). It is the convection of the large vortices from the leading edge of the upper surface beyond the trailing edge of the airfoil that produces this effect. Reattachment of the flow is only accomplished by lowering the pitch of the airfoil to well below its steady state stall angle, α_{ss} (Figure 2.3).

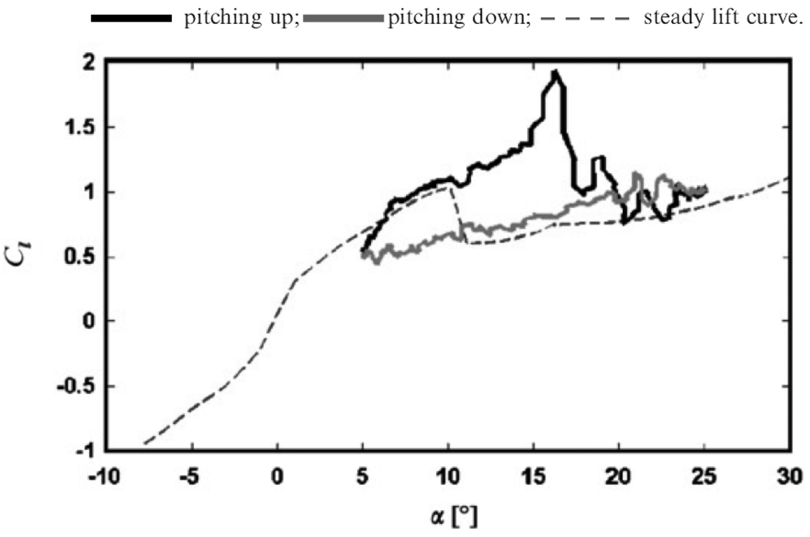

Figure 2.3: Phase-averaged lift coefficient (α = 15° ± 10°), adapted from (Tsang et al., 2008)

This hysteresis in the local flow field produces large phase variations in the unsteady aerodynamic load on the airfoil, which is strongly dependent on whether the flow is separating, fully separated, or reattached (Leishman, 2000). The periodic variation in loading on the airfoil as a result of the flow hysteresis can be a strong source of flow induced vibration. During some phases of dynamic stall, the net aerodynamic work per cycle of oscillation, or the ‘aerodynamic damping’ can become negative, at which time “the airfoil extracts energy from the flow, and the pitch oscillations will tend to increase in amplitude, unless restrained” (McCroskey, 1982).

This ‘stall flutter’ as it is known has a tendency to occur when the airfoil is pitching in and out of stall. As can be seen in Figure 2.4 below, for oscillations within the region where no stall occurs (α_0 = 7.3°), as well as the region where the airfoil remains stalled for the duration of the oscillation (α_0 = 24.6°), only positive damping exists. However, when the airfoil oscillates with a mean angle of attack of α_0 = 14.8°, it is only stalled for a portion of the time, resulting in the negative damping loop which occurs over the range of α = 10° to 17°, establishing stall flutter (McCroskey, 1981).

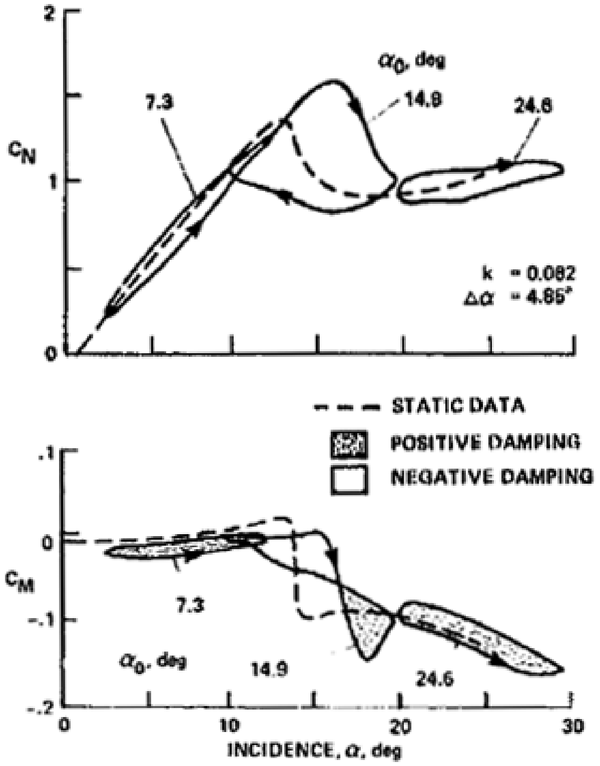

Figure 2.4: Effect of mean angle on lift and moment coefficients and aerodynamic damping ($\alpha = \alpha_0 \pm \Delta\alpha$), adapted from (McCroskey, 1981)

2.2.1. Dynamic Stall Parameters

Beyond the mean angle of attack, dynamic loading data is further characterized by a number of parameters, namely the amplitude of oscillation, airfoil shape, reduced frequency, $k = \pi f c / U_\infty$, Reynolds number, $Re = U_\infty c / \nu$, and Mach number, $M_a = U_\infty / a$, where f is the pitching frequency in Hz, ν is the kinematic viscosity, a is the speed of sound, and U_∞ is the free stream velocity (Tsang et al., 2008). The focus of the present research is directed toward obtaining an understanding of the dynamic stall behaviour associated with low rotational velocity VAWT, and as such, the compressibility effects associated with high Mach numbers (M_a > 0.3) will not be investigated. The three parameters which will be explored in some detail are the pitch angle, reduced frequency, and airfoil shape, while the effect of Reynolds number will only be observed in an indirect manner.

2.2.1.a Pitch Angle

The pitch angle range of an airfoil for a given dynamic test is a function of both the mean angle of attack α_0 and the amplitude of oscillation $\Delta\alpha$, such that the maximum and minimum angle of attack are $\alpha_{max} = \alpha_0 + \Delta\alpha$ and $\alpha_{min} = \alpha_0 - \Delta\alpha$, respectively. Previous research has shown that it is the value of α_{max} which has the greatest influence on the behaviour of the force and moment coefficients. This is because it is the determining factor for the degree of flow separation and thus defines what dynamic stall regime the airfoil is operating within (McCroskey, 1982). Four distinct dynamic stall regimes have be identified, examples of which are depicted below in Figure 2.5, where $\alpha_{ss} \approx 14°$. Again, the regions of negative damping have been identified, indicating the zones over which stall flutter can be excited.

The first flow regime on the far left of Figure 2.5 is the 'no stall' regime where the airfoil is oscillating with $\alpha_{max} = 13°$, just slightly below the normal stall angle of attack. Within this flow regime "there is almost no separation throughout the cycle, although unsteady boundary-layer displacement thickness effects are not completely negligible" (McCroskey, 1981). Following the 'no stall' flow regime is the 'stall onset' regime, where $\alpha_{max} = \alpha_{ss}$, and a slight distortion of the hysteresis loops can be observed. This has the potential to be a very important flow regime with respect to VAWT optimization as it represents the maximum lift force that can be obtained from an unsteady airfoil without any significant concessions in pitching moment or drag force (McCroskey, 1981). The 'light stall' regime is the next level of viscous-inviscid interaction (Figure 2.2a), and as can be seen from Figure 2.5, can be produced when the maximum angle of attack exceeds the static stall angle of attack by a very small margin of just 1°. This flow regime exhibits many of the features of normal stall, including dramatic loss of lift and increase in drag loading beyond a critical angle of attack. However, it is at this stage that the hysteresis in the airfoil loading grows to a dominant level and the propensity to develop negative aerodynamic damping, and thus stall flutter, is strongest (McCroskey, 1982). The final flow regime depicted on the far right of Figure 2.5 is the 'deep stall' regime, where

α_{max} = 20° far exceeds the incidence of static stall. The deep stall regime is distinct in that it is characterized by strong vortex disturbances being generated on the airfoil, shed from the boundary layer, and convected downstream. This produces lift, drag and moment values which greatly exceed their corresponding static values, large hysteresis loops in the loading curves, and a large viscous interaction zone on the upper surface of the airfoil (Figure 2.2b).

Due to the relatively low rotational velocity of a high solidity VAWT, the airfoils will be subjected to excessively high relative angles of attack. As such, it is expected that the airfoils will operate within the deep dynamic stall regime for large portions of the turbine rotation.

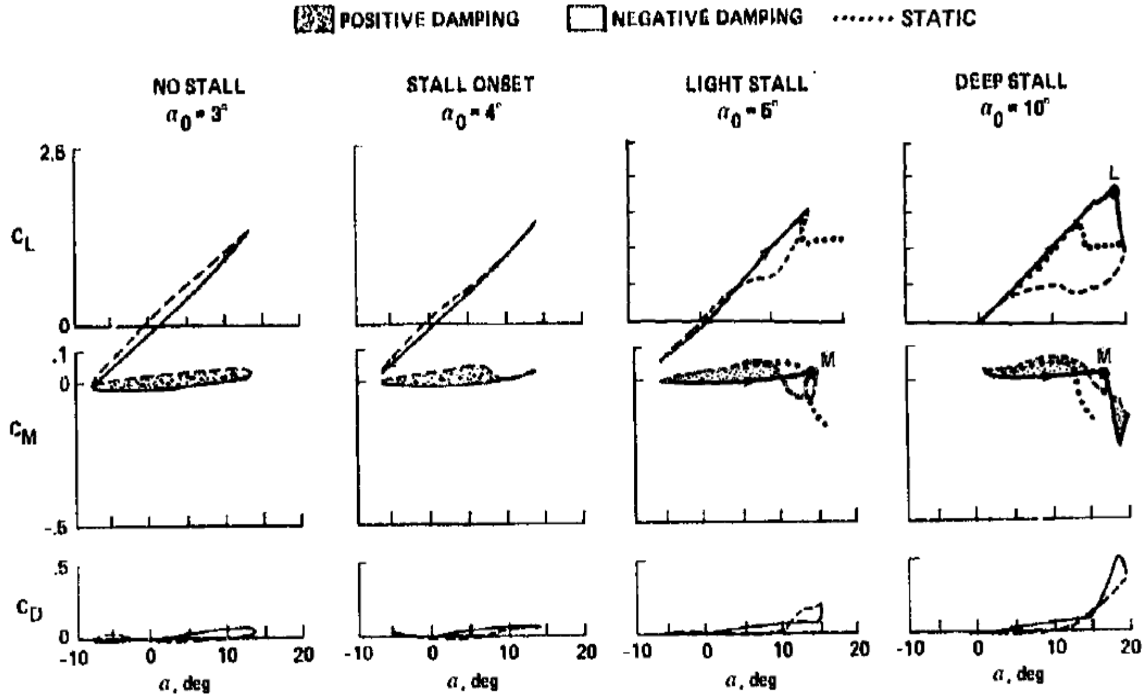

Figure 2.5: Dynamic stall regimes ($\alpha = \alpha_0 \pm 10°$, $k = 0.10$), adapted from (McCroskey, 1981)

2.2.1.b Reduced Frequency

The reduced frequency of the airfoil oscillation is defined as $k = \pi f c / U_\infty$, and is used as a time scale for periodic phenomena of frequency f imposed on the flow. In essence, it is a ratio of the airfoil pitching rate (πf) to the rate at which flow passes over the airfoil (U_∞ / c). For simplicity sake, we will begin our analysis of the effect of reduced frequency by first exploring the behaviour at very small values. For very small values of k, $\mathcal{O}(10^{-3})$, the airfoil pitching rate is relatively small in comparison to the ambient flow velocity, and as expected the dynamic test results closely resemble the now familiar quasi-steady state data. The effect of the reduced frequency above very small values however, is highly dependent on the stalling regime that the airfoil is operating within.

In 1994, Piziali performed a comprehensive experimental investigation of the pressure distribution over a symmetric NACA 0015 airfoil undergoing pitching motions representative of a helicopter rotor blade. This is a fundamental study on oscillating airfoil aerodynamics for a range of angles of attack including stall, and will form the basis of the analysis on the effect of reduced frequency. From a representative cross-section of the vast array of experimental data obtained by Piziali (Re = 2.0 x 10^6, $\alpha_{ss} \approx 13°$), several qualitative observations can be made on the effects of increasing k.

For the 'no stall' regime (α = 9° ± 4°), an increase in reduced frequency has little effect on the loading characteristics of the airfoil beyond a slight increase in the hysteresis of the drag and moment coefficients. Within the 'light stall' regime (α = 11° ± 4°), an increase in reduced frequency lowers the negative damping of the system and reduces the hysteresis in the lift profile of the airfoil, effectively adding stability to the system while increasing performance. In contrast to this behaviour, an increase in k within the 'deep stall' (α = 15° ± 4°) and 'fully stalled' (α = 17° ± 4°) regimes, where high solidity VAWT airfoils are expected to operate, results in a significant increase in both lift hysteresis and negative damping of the system.

From a quantitative perspective, analysis of the dynamic stall angle and maximum lift coefficient behaviour will be used to further investigate the effect of reduced frequency. From Figure 2.6a it can be seen that an increase in reduced frequency causes an increase in the dynamic stall angle for all but the 'no stall' regime (linear interpolation is performed for visualization purposes only). The lower and upper limits to the dynamic stall angle appear to be the static stall angle, where the dashed lines indicate projection of the data to this limit, and α_{max}, respectively. This behaviour indicates that beyond a threshold reduced frequency the airfoil will not stall until the pitch direction is reversed.

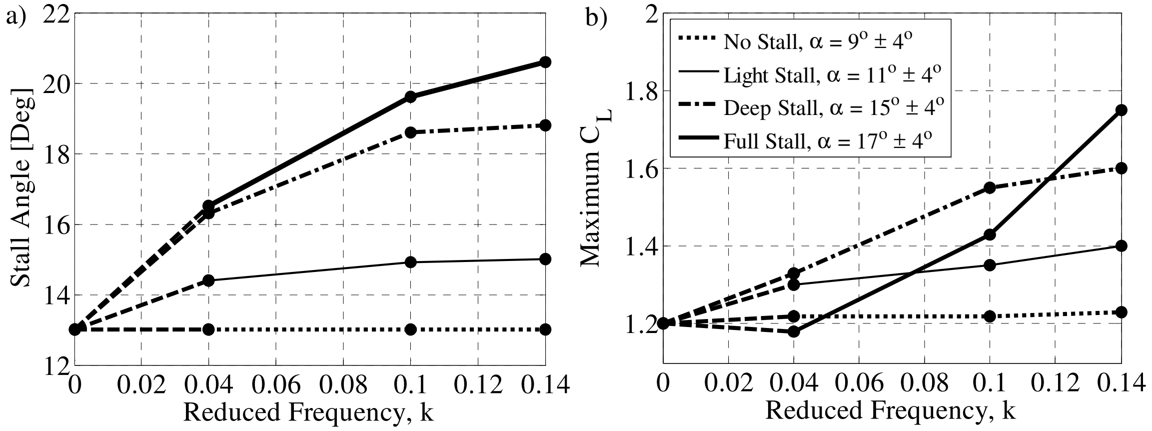

Figure 2.6: Effect of reduced frequency on a) Dynamic stall angle; and b) Maximum lift coefficient

Figure 2.6b depicts the effect of reduced frequency on the maximum lift coefficient, where again the dotted lines project the data to the perceived lower limit defined by the maximum steady state lift coefficient. However, for the case of the maximum lift coefficient there appears to be no well defined upper limit with respect to increases in reduced frequency for the available data. One interesting phenomenon which may play an important role in high solidity VAWT operation, where the maximum relative angle of attack is expected to be very large, is the initial reduction, followed by a rapid increase, in maximum lift coefficient within the 'fully stalled' regime.

2.2.1.c Airfoil Shape

The effect of airfoil shape on unsteady airfoil performance is most profoundly observed in the nature and location of separation within the light stall regime, where it has been identified that it is the leading-edge geometry of the airfoil that is the major contributing factor. Airfoil designs that have a relatively sharp leading edge "tend to develop severe adverse pressure gradients in the first few percent of chord, leading to abrupt boundary-layer separation ... that spreads rapidly downstream" (McCroskey, 1981). This 'leading-edge stall' as it is known, is characterized by highly concentrated vortex production which in turn results in sudden variations in the loading coefficients during dynamic stall. Conversely, blunt nosed airfoils tend to produce 'trailing-edge stall', where separation is initiated at the trailing edge of the airfoil before propagating upstream over the upper surface. Trailing-edge stall typically progresses in a more gradual manner then leading-edge stall, where separation is suppressed by unsteady effects, and negative damping is less likely to develop (McCroskey, 1981).

A study performed by McCroskey, McAlister, Carr, Pucci, and Lambert, in 1980 on a series of airfoils designed for pitch controlled helicopters clearly demonstrates this behaviour, where L.E. and T.E. denote leading-edge and trailing-edge stall respectively (Figure 2.7). The Sikorsky SC-1095 and NLR-1 are good examples of airfoils with sharp leading edges, developing dramatic leading-edge stall, while the AMES-01 and NLR-7301 have blunt leading edges and gradual trailing-edge stall.

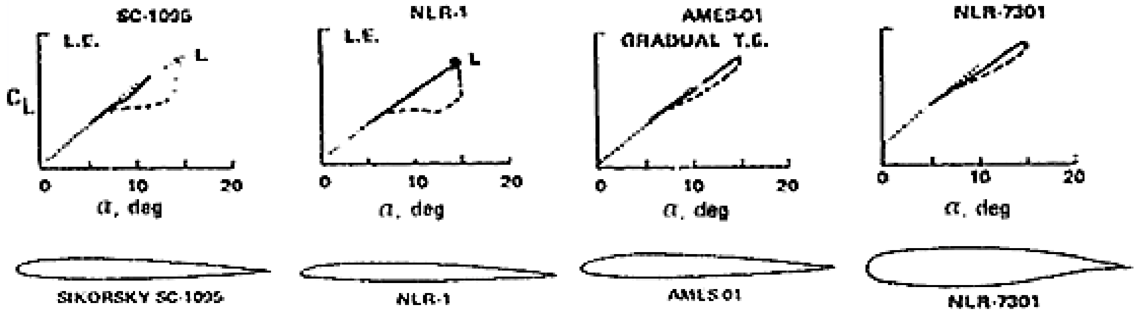

Figure 2.7: Light stall airloads for various airfoil designs ($\alpha = 10° \pm 5°$, $k = 0.10$), adapted from (McCroskey et al., 1980)

2.2.2. Numerical Models

Numerical modelling of dynamic stall is very difficult due in part to the large number of variables which affect transition from laminar to turbulent flow, flow separation, and the formation, convection and dissipation of large scale vortical structures. For this reason, most of the methods of calculation solve for the loading coefficients over a narrow range of parameters or a specific dynamic stall regime, and typically employ considerable assumptions and approximations. This review will focus on exploring a number of the more successful and widely used dynamic stall numerical models which exhibit potential for VAWT modeling.

2.2.2.a Discrete Potential Vortex Approach

The vortex model is an excellent example of a modelling approach designed for a specific flow regime. As was previously stated, the deep stall regime is characterized by a large viscous layer which contains well defined vortex structures. As such, the discrete potential vortex approach models the vortex-shedding phenomenon as a series of emitted vortices analogous to the simple model originally proposed by Ham in 1968 for a thin flat plate. Extensions of the flat plate model for use with airfoils of finite thickness in the deep stall regime include; calculation of the flow field resulting from the combination of the body and free vortices by an adaption of the numerical potential-flow technique (Giesing, 1968), adaption of a boundary-layer analysis to determine the flow separation and vortex emission point (Baudu, Sagner, & Souquet, 1973), and satisfying the no-slip condition by modelling the boundary layer as a thin layer of discrete vortices of appropriate size and strength (Ono, Kuwahara, & Oshima, 1980).

In essence, the vortex model determines the velocity field through a superposition of the induced vortex velocity and the undisturbed potential flow velocity around the airfoil, where the strength assigned to each vortex emitted from the airfoil is determined by the boundary-layer separation characteristics of the airfoil itself. In turn, based upon the induced velocity distribution determined from this calculation, airfoil section data is then used to determine the lift and drag forces on the airfoil segments. Despite the large number of approximations employed, the results for low Reynolds number flows appear to be quite accurate. However, limitation of the model to the deep dynamic stall regime has prevented it from being widely applied.

2.2.2.b Zonal Methods

Zonal methods are named as such due to the fact that the various regions, or 'zones', within the flow field are solved separately and then coupled in some manner. Unlike the discrete potential vortex approach, zonal methods are more appropriately designed for modelling light dynamic stall due to the relatively thin viscous region that exists within this regime (Figure 2.2a). These methods are derived from classical Prandtl boundary-layer equations, where an order of magnitude analysis on the Navier-Stokes equations for a viscous fluid separates the flow into a viscous boundary layer region close to the airfoil surface and an inviscid free stream region. One such model, from Crimi and Reeves (1972), models both the airfoil and the separated flow region as distributed source and vortex singularities, known as the 'vortex panel method'. This method models the surface of the airfoil as a concentrated sheet of vorticity, where the strength of the vorticity field is such that there is no flow through the surface of the airfoil. In order to obtain closure of this model, the Kutta-Joukowski condition must be employed. This condition assumes that flow cannot go around the trailing edge of the airfoil, but must leave from there. While this method has had a measure of success in modelling static airfoil behaviour, its applicability to oscillating airfoils is questionable.

This model then employs a simple turbulent viscosity model (explained below) to solve for the turbulent flow parameters within the unsteady boundary-layer equations, while inviscid flow theory is employed to solve for the free-stream flow. Despite being able to predict the advent of leading-edge stall with some measure of success (based upon the existence or bursting of the leading-edge separation bubble) the extension of this model to various airfoil designs, Reynolds numbers, and trailing-edge stall airfoils was generally unsuccessful.

2.2.2.c Empirical Correlation Techniques

Developed mostly by and for the helicopter industry, numerous empirical correlation techniques based on vast arrays of wind-tunnel data have been formulated to estimate the loading parameters of unsteady airfoils. However, in order to satisfy the objective of this particular review, only models which are typically employed in VAWT modelling will be explored to any great depth.

The Boeing-Vertol dynamic stall model (Gormont, 1973) was originally developed for thin (t/c < 0.12, t is the maximum airfoil thickness) airfoils operating below the deep stall regime ($\alpha_{max} < \alpha_{ss} + 5°$). Later modified by Strickland, Webster, and Nguyen (1979), this model "assumes that the lift-curve slope and zero-lift angle remain unchanged, and that dynamic effects only modify the angle of attack at which stall occurs" (Paraschivoiu & Allet, 1988),

$$\alpha_M = \alpha_B - \gamma K_1 \left(\left|\frac{c\dot{\alpha}_B}{2U_\infty}\right|\right)^{\frac{1}{2}} S_{\dot{\alpha}} \qquad 2.4$$

where U_∞ is the flow velocity, α_B is the effective airfoil angle of attack, $S_{\dot{\alpha}}$ is the sign of $\dot{\alpha}_B$, and γ and K_1 are empirical constants which are a function of airfoil thickness, Mach number and pitch direction. This particular formulation allows for dynamic overshoot of the lift coefficient beyond its steady state value, but makes no effort to account for changes in drag or moment coefficients. Equation 2.5 is the lift coefficient expression given by the Boeing-Vertol method, where α_{B0} is the effective airfoil angle of attack at zero lift (Paraschivoiu & Allet, 1988).

$$C_L = \left(\frac{\alpha_B}{\alpha_M - \alpha_{B0}}\right) C_L(\alpha_M) \qquad 2.5$$

An alternative method, the MIT model, differs greatly from the Boeing-Vertol model in that the dynamic stall angle is specified implicitly as $\alpha_{DS} = \alpha_{SS} + 3°$ for all airfoil shapes, pitch rates, etc. For $\alpha \leq \alpha_{SS}$, the static stall data is used exactly, while from

$\alpha_{SS} < \alpha < \alpha_{DS}$ the data is extrapolated from the behaviour below static stall. "Starting at $\alpha = \alpha_{DS}$, C_L and C_M are assumed to increase linearly with time over a specified time interval, from inviscid values to peak values that depend on $\dot{\alpha}c/U_\infty$ at the instant of dynamic stall" (McCroskey, 1981). If the angle of attack is still increasing after this peak point, then C_L and C_M remain constant until the angle of attack starts to decrease and the separation state begins (Paraschivoiu & Allet, 1988). At this point, the lift and moment coefficients decay exponentially until static stall values are obtained. Beyond this, the dynamic loading coefficients assume the unstalled static section values. Again, no effort is made to dynamically model the drag coefficient behaviour. Obvious limitations of this dynamic stall model are its non-physical specification of a dynamic stall angle, and its nearly arbitrary extrapolation and interpolation techniques.

A number of other empirical models have been used in the past, showing marginal success under varying conditions (McCroskey, 1981). Amongst these is the table lookup correlation method, which determines C_L and C_M from three independent airfoil parameters, namely the instantaneous incidence, $\alpha(t)$, an angular velocity parameter, $A = \dot{\alpha}c/2U_\infty$, and an angular acceleration parameter, $B = \ddot{\alpha}c^2/4{U_\infty}^2$ (Carta, Commerford, Carlson, & Blackwell, 1972). A number of phase-lag and time-delay methods also exist, which introduce a universal dimensionless time constant, $\tau = U_\infty \Delta t/c$, that is used to delay the onset of dynamic stall and raise the maximum lift coefficient beyond its steady state stall value. Finally, there exists a unique method which decomposes each of the load coefficients into a linear and non-linear ordinary differential equation, and then alters the non-linear coefficient values within the stall region as a function of the angle of attack to produce the desired effect.

2.2.2.d Unsteady Reynolds Averaged Navier-Stokes Equations

Solution of the conservation equations about the airfoil can be obtained through the use of finite-element discretization of the flow domain. In doing so, the pressure and velocity distributions about the airfoil, and thus the aerodynamic forces and pitching moment applied to the airfoil, can then be determined. For an isothermal, incompressible, Newtonian fluid, these equations consist of the conservation of mass and conservation of momentum (Navier-Stokes equation),

$$\frac{\partial \boldsymbol{u}_i}{\partial x_i} = 0 \tag{2.6}$$

$$\frac{\partial \boldsymbol{u}_i}{\partial t} + \boldsymbol{u}_j \frac{\partial \boldsymbol{u}_i}{\partial x_j} = -\frac{1}{\rho}\frac{\partial p}{\partial x_i} + \nu \frac{\partial^2 \boldsymbol{u}_i}{\partial x_j^2} \tag{2.7}$$

In order to solve the conservation equations for most practical turbulent flow problems, the equations are averaged over time. In order to do so, the instantaneous velocity and pressure parameters are decomposed into average, $\boldsymbol{U}_i$ and P, and fluctuating, $\boldsymbol{u}_i'$ and $\boldsymbol{p}'$, components.

$$\boldsymbol{u}_i = \boldsymbol{U}_i + \boldsymbol{u}_i' \tag{2.8}$$

$$p = P + p' \tag{2.9}$$

Substitution of these parameters into the conservation equations reduces them to the Unsteady Reynolds Averaged Navier-Stokes (URANS) equations for turbulent flows.

$$\frac{\partial \boldsymbol{U}_i}{\partial x_i} = 0 \tag{2.10}$$

$$\frac{\partial \boldsymbol{U}_i}{\partial t} + \boldsymbol{U}_j \frac{\partial \boldsymbol{U}_i}{\partial x_j} = -\frac{1}{\rho}\frac{\partial P}{\partial \mathrm{x}_\mathrm{i}} + \nu \frac{\partial^2 \boldsymbol{U}_i}{\partial x_j^2} - \frac{\partial \overline{\boldsymbol{u}_i'\boldsymbol{u}_j'}}{\partial x_j} \tag{2.11}$$

From these expressions it is clear that the Reynolds averaged form of the Navier-Stokes equations differs only by the presence of the Reynolds stresses term $\partial\overline{\boldsymbol{u}_i'\boldsymbol{u}_j'}/\partial x_j$. Because the Reynolds stresses introduce an additional set of variables that must be solved for without the addition of any further equations, this crucial difference leads to a closure problem. Classically, the approach taken to overcome the closure problem is through the turbulent-viscosity hypothesis. This hypothesis assumes that the Reynolds-stress tensor is directly related to the mean rate-of-strain tensor in a manner directly analogous to that of viscous stresses in a Newtonian fluid. This results in the following relationship for the Reynolds stresses, and subsequently, the mean-momentum equation incorporating the turbulent-viscosity hypothesis,

$$\overline{\boldsymbol{u}_i'\boldsymbol{u}_j'} = \frac{2}{3}\mathrm{k}\delta_{ij} - \nu_T\left(\frac{\partial \boldsymbol{U}_i}{\partial x_j} + \frac{\partial \boldsymbol{U}_j}{\partial x_i}\right) \quad 2.12$$

$$\frac{\partial \boldsymbol{U}_i}{\partial t} + \boldsymbol{U}_j\frac{\partial \boldsymbol{U}_i}{\partial x_j} = \frac{\partial}{\partial x_j}\left[\big(\nu + \nu_T(x,t)\big)\left(\frac{\partial \boldsymbol{U}_i}{\partial x_j} + \frac{\partial \boldsymbol{U}_j}{\partial x_i}\right)\right] - \frac{1}{\rho}\frac{\partial}{\partial x_i}\left(P + \frac{2}{3}\rho\mathrm{k}\right) \quad 2.13$$

where ν_T is the unknown turbulent viscosity, k is the turbulent kinetic energy, and $(P + 2/3\,\rho\mathrm{k})$ is the modified mean pressure. While the Reynolds stresses have been eliminated from the mean momentum expression, a turbulence model is now required to determine the turbulent viscosity and kinetic energy, and provide closure to the model. Due to the importance of accomplishing this, the focus of the following analysis will be on evaluating turbulence models for use with the URANS solution of dynamic stall.

Many different strategies of solving for the turbulent viscosity term have been developed over time. Typically, each new model introduces an extra level of complexity in order to reduce the number of assumptions and approximations made within the previous model. A select few studies on the application of the more popular turbulence models to the solution of dynamic stall have been performed by Srinivasan, Ekaterinaris, and McCroskey (1995), Martinat, Braza, Hoarau, and Harran (2008), and Ahmadi, Sharif, and Jamshidi (2009). In this review, after a brief description of each turbulence model, the details of which can be found within the literature, a short comparison of their ability to determine loading coefficients under dynamic stall conditions will be given.

The Baldwin-Lomax model is known as a zero-equation model because it does not require the solution of any additional transport equations in order to determine the turbulent viscosity. Instead, the turbulent viscosity is defined as a function of a mixing length, l_m^2 , and a mean rate of rotation, $\bar{\Omega}_{ij}$ (Baldwin & Lomax, 1978). In addition, this particular zero-equation model has a series of conditions which force the turbulent viscosity to assume a value of zero at the wall surface as well as within the outer flow far from the wall (Srinivasan et al., 1995). Despite the difficulty associated with specifying an accurate mixing length, and its poor performance in flows which exhibit large separation, the Baldwin-Lomax model is often used as a first approximation due to its simplicity and low computational time.

A major limitation of a zero-equation model is the implicit condition that the turbulent production is identically equal to dissipation. The half-equation turbulence model of Johnson and King (1985) overcomes this shortcoming by taking into account the convection and diffusion effects on the Reynolds shear stress $-u_i'u_j'$ in the streamwise direction through the solution of an additional ordinary differential equation (Srinivasan et al., 1995). In turn, this allows for the calculation of a non-equilibrium turbulent boundary layer. As such, the Johnson-King model is an improvement upon the zero-equation models because it takes into account the evolution of the maximum shear stress, and thus the upstream history of the flow (Srinivasan et al., 1995).

Both the zero-equation and half-equation models are hampered by the need to solve for a flow-dependent length scale, such as the boundary layer thickness. Conversely, the one-equation models of Baldwin and Barth (1991) and Spalart and Allmaras (1992) avoid this constraint by solving a partial differential equation for a pertinent flow characteristic. While the Baldwin-Barth model solves for a 'turbulent Reynolds number', $\tilde{R}_T$, from which the turbulent viscosity can be determined, the Spalart-Allmaras model solves a partial differential equation for turbulent viscosity directly. As such, the models have many similarities, each requiring the specification of a series of model constants which can be adjusted and tuned to the given flow conditions.

The solution of a second partial differential equation is required to define both a length and a time quantity, and satisfy the conditions for completeness. The two most widely used and well known two-equation models are the k-ε model of Jones and Launder (1972) and the k-ω model developed by Wilcox (1993a). Both of these models define the turbulent viscosity as $\nu_T = C_\mu k^2/\varepsilon$, where C_μ is a constant, k is the turbulent kinetic energy, and ε is the rate of dissipation of turbulent kinetic energy. Thus, from the solution of a transport equation for k, and another for either ε or ω (ε ≡ kω, where ω is the turbulence frequency), the turbulent viscosity can be determined. While both of the models define the transport equation for k in an identical manner, each solves for ε in a slightly different way. This results in an additional term ($(2\nu_T/\sigma_\omega \mathrm{k})\nabla\omega \cdot \nabla \mathrm{k}$, where σ_ω is the turbulent Prandtl number) appearing in the k-ε formulation of the implied transport equation for ω. This small variation in the model formulations results in rather different performance. While the k-ε model performs well in the outer part of the boundary layer due to its freestream independence, the k-ω model has a more robust and accurate formulation in the near wall region (Menter, 1994).

Recognising the strengths and deficiencies of each model, Menter introduced the SST model in 1994, which applies a blending function to the additional term in the k-ε formulation. At the wall, the value of the blending function is zero and the model takes on the form of the k-ω model, while away from the surface the blending function increases to a value of unity and the model takes on the form of the k-ε model. In addition, Menter applied a modification to account for the transport of the principal turbulent shear stress, thus optimizing the model for aerodynamic flows with large adverse pressure gradient boundary layers (Menter, 1994).

Having outlined the basic principles of a number of the most widely used turbulence models, the ability of each to model dynamic stall will now be explored. The performance of the zero-, half- and one-equation models described above will be assessed against the experimental data of Piziali (1994) as documented in a study by Srinivasan et al. (1995). This study modelled a symmetric NACA 0015 airfoil at $Re = 1.95 \times 10^6$, for four mean angles of attack of, α_0 = 4, 11, 15 and 17°, with a pitch amplitude of $\Delta\alpha$ = 4.2° and a reduced frequency of k = 0.1.

From this study it was concluded that within the ‘no stall’ regime “the unsteady attached flow calculated with the Johnson-King and Spalart-Allmaras models has good agreement with experiments for lift, drag, and pitching moment hysteresis," (Srinivasan et al., 1995) while the Baldwin-Lomax and Baldwin-Barth models perform poorly.

The results for the light and deep stall regimes on the other hand were far more varied and inconsistent. Within the light-stall regime, the Johnson-King and Spalart-Allmaras models produced good predictions for the upstroke but over-predicted the extent of separation, resulting in poor pitching moment predictions on the down stroke (Srinivasan et al., 1995). The Baldwin-Barth model exhibited far lower lift predictions on the down stroke because of slow flow recovery, but predicted drag and pitching moment with far greater accuracy. The Baldwin-Lomax model performed poorly in all aspects within the light-stall regime.

For the deep stall and fully stalled regimes, the Spalart-Allmaras model had superior performance once again, predicting qualitatively correct loading hysteresis, along with the Baldwin-Barth model. The Johnson-King model was observed to produce some oscillatory behaviour during the down stroke for the fully-stalled flow scenario. Furthermore, the Johnson-King model is unable to even predict qualitatively correct results within this dynamic stall regime, leading to extremely poor drag and pitching moment hysteresis.

From the study of Srinivasan et al. (1995), it was concluded that overall, the one equation models provided significant improvement over the algebraic and half equation models. It should be noted that due to the solution of an additional transport equation, the one equation models required slightly greater computational resources, and thus had longer simulation times.

A more recent study by Martinat et al. (2008), tests Chien's low Reynolds number adaptation of the k-ε model (1982), and the k-ω SST model of Menter (1994), against the relatively successful Spalart-Allmaras model and a series of experimental results (Berton, Allain, Favier, & Maresca, 2002; McAlister, Carr, & McCroskey, 1978).

In comparison to the experimental results of Berton et al. (2002), it was observed that both the k-ε model of Chien and the Spalart-Allmaras one-equation model overestimate the maximum lift and drag coefficients, as well as the area under the hysteresis loop. However, the k-ε Chien model does this to a lesser degree than the Spalart–Allmaras model. This behaviour is most likely due to an excessive dissipative character within the Spalart-Allmaras model, which results in an "underestimation of the adverse pressure gradient at high incidence leading to a delay on the prediction of dynamic stall" (Martinat et al., 2008). In addition, it is probable that discrepancy between the models and the experimental results can be partially attributed to the transitional character of the boundary layer in the experiment which is not accounted for by the fully turbulent boundary layer assumption of the models.

Further tests were performed by Martinat et al. to compare the experimental results of McAlister et al. (1978) to the k-ε Chien and k-ω SST models. The k-ε Chien model produced results close to the experiment with a good prediction of lift and a small over-prediction of drag, but a large delay in the predicted stall angle (Martinat et al., 2008). This indicates that the model has an excessive dissipative character, resulting in the model behaviour being forced by the movement of the structure. Conversely, the SST model produced the most accurate results, predicting the dynamic stall angle and upstroke behaviour well, but overall gives a far less smooth character (Martinat et al., 2008).

A study performed by Ahmadi, Sharif, and Jamshidi (2009) on a NACA 0012 airfoil pitching over a range of -41.81° to 41.81° confirmed the superior performance of the SST turbulence model for $Re = 9.71 \times 10^5$ to 22.65×10^5. This study compared the performance of the Spalart-Allmaras, SST, SST with γ-θ transition model, and k-ω turbulence models with the specific intention of applying the results to VAWT modelling (hence the very large pitch angle range). As before, the major conclusion of this research was that the SST turbulence model was the best choice that leads to the least numerical error. In addition, it was determined that the dynamic stall phenomenon is more likely to occur at lower wind speeds where the lift force is low (Ahmadi et al., 2009).

2.3. Dynamic Stall of Vertical Axis Wind Turbines

Due to the anticipated impact of dynamic stall on high solidity VAWTs, application of the above research to the study of vertical axis wind turbine aerodynamic performance will be the focus of the remainder of this review. The basic principle of operation of a VAWT is as follows. As the vertically aligned blades of the turbine turn about the central shaft they encounter an incident wind, $U_{incident}$, that is composed of the ambient local wind velocity, U_{∞}, and the blade rotational velocity, $U_{rotation} = \omega R$. The incident wind approaches the airfoil at a local angle of attack, α, which is a function of the rotational angle of the turbine, θ, where θ = 0° is when the blade is travelling directly upstream. Flow over the airfoil generates lift and drag forces which can be decomposed into a thrust force (primarily power production) and a radial force (strictly vibration excitation) on the turbine struts (Figure 2.8).

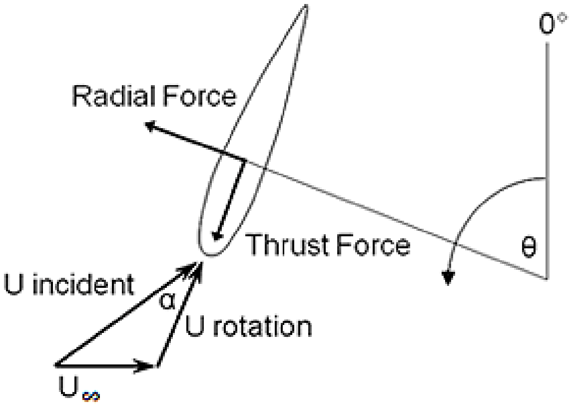

Figure 2.8: Thrust and radial force components on an airfoil generated by the incident wind approaching at a local angle of attack α (McLaren et al., 2011)

Due to the unique flow conditions which are imposed upon the airfoils of a high solidity, low rotational velocity VAWT as it rotates about the central shaft of the turbine, complex dynamic stall behaviour is expected to occur. As such, a number of the system parameters that determine the relationship between the angle of rotation, dynamic stall and aerodynamic loading, are explored below. A number of experimental techniques and numerical models which have been developed to study the behaviour of VAWTs will also be critically reviewed.

2.3.1. VAWT Dynamic Stall Parameters

2.3.1.a Maximum Pitch Angle

As is the case for a stationary pitching airfoil, a rotating airfoil is subjected to a maximum pitch angle, α_{max}. Assuming that there is no loss in flow momentum through the turbine, the local angle of attack of the airfoil can be defined as,

$$\alpha = tan^{-1}[-sin\,(\theta)/(\lambda + cos\,(\theta))] \qquad 2.14$$

where $\lambda = U_{rotation}/U_{\infty}$, and is known as the 'blade speed ratio'. While this assumption introduces considerable error on the downstream portion of the rotation (180° $\leq \theta \leq$ 360°), the above expression provides some understanding of the severity of the relative angle of attack and location of dynamic stall onset on the upstream portion of the rotation (0° $\leq \theta \leq$ 180°). From Figure 2.9 it is evident that as the blade speed ratio is reduced the maximum local angle of attack is dramatically increased. For the high solidity, $\sigma = Nc/2R \approx 0.44$, low rotational velocity turbine under investigation, which optimally operates at blade speed ratios of 1.4 to 1.8 (Bravo, Tullis, & Ziada, 2007), the maximum angle of attack is very large, upwards of ± 55°. As such, it is expected that the airfoil will be exposed to the deep dynamic stall flow regime characterized by the production of large scale vortices and considerable loading hysteresis (McCroskey, 1982).

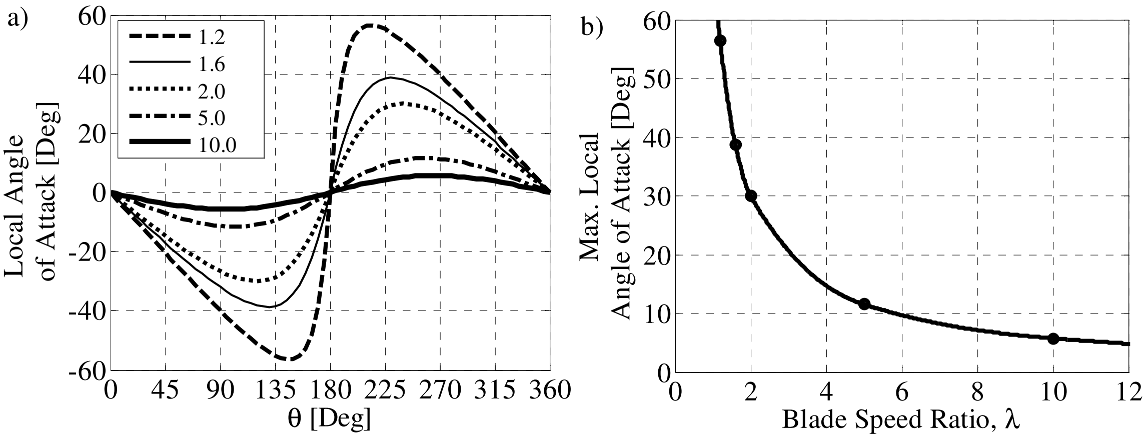

Figure 2.9: Local angle of attack as a function of blade speed ratio

Conversely, traditionally designed low solidity turbines ($\sigma \leq 0.2$) operate at high RPM, resulting in high blade speed ratios of 5.0 – 10.0, and much smaller maximum angles of attack on the order of ± 15°. This means that the airfoil is limited to the 'no stall' and 'light stall' regimes where dynamic flow effects are minimal and large vortex production typically does not occur (see above).

2.3.1.b Effective Reduced Frequency

Due to the rotation of the turbine, the airfoil is subjected to an effective reduced frequency $k_e = \pi f c / U_{incident}$, where f is the rotational frequency of the turbine. For low solidity VAWTs, it is assumed that $U_{incident}$ is the airfoil's rotational velocity, $2\pi f R$, where R is the turbine radius. This assumption inherently implies the condition that the ambient wind velocity is negligible, and thus that the turbine must be operating at a high blade speed ratio. For the purpose of this analysis we will assume that this is true and the effective reduced frequency simplifies to $k_e = \mathrm{c}/2R$. Thus, for a low solidity turbine, $c \ll R$, the airfoil is subjected to a very small effective reduced frequency. Under these conditions, dynamic stall is minimal and the loading behaviour has been studied extensively (see above). However, for the high solidity turbine prototype which is the motivation for the present research, $c = 0.42m, R = 1.40m$, and $k_e = 0.15$. For pitching airfoils subjected to reduced frequencies of this magnitude, it was observed that dynamic stall is greatly delayed and high maximum lift coefficients are obtained (Piziali, 1994). From a VAWT power production prospective, it appears that this is a positive effect as turbine thrust force is highly dependent on airfoil lift. However, a large effective reduced frequency also results in large hysteresis loops with considerable phase variations in the unsteady loading curves, making the airfoil susceptible to flutter and vibration excitation.

2.3.1.c Changes in Flow Velocity

As the turbine rotates, the local flow velocity over the airfoil will vary considerably due to the change in relative ambient flow direction. Figure 2.10 below shows the relative airfoil velocity normalized by the rotational flow velocity for a number of blade speed ratios, once again based upon the assumption that there is no loss in flow momentum through the turbine. For a low solidity turbine operating at high blade speed ratios ($\lambda \geq 5.0$), the change in flow velocity is limited to approximately ± 20%. Conversely, a high solidity ratio turbine like the one under investigation operating at low blade speed ratios ($\lambda \leq 2.0$) will be subjected to changes in flow velocity as high as ± 80%. Because the aerodynamic forces are proportional to the square of the incident flow velocity, this severe fluctuation will have a large impact on both the nature and magnitude of the loading on the airfoils, and thus the overall performance and output of the turbine.

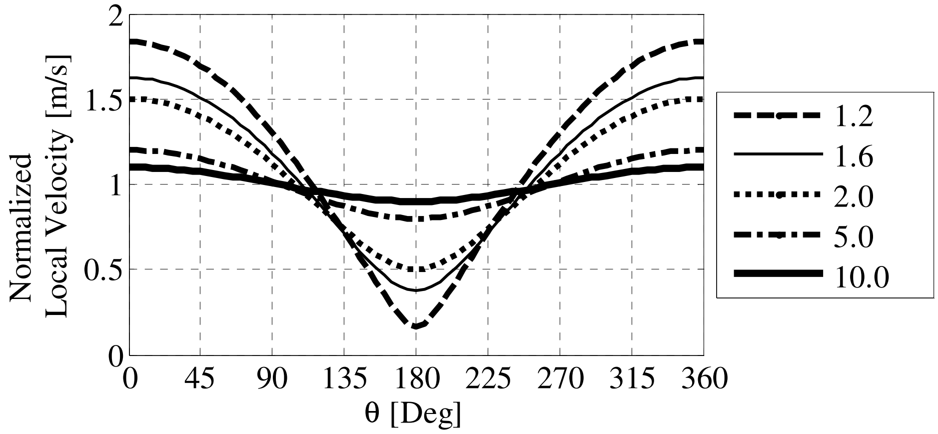

Figure 2.10: Normalized local flow velocity as a function of blade speed ratio

2.3.1.d Downstream Flow Structures

The particular turbine examined has a peak power coefficient at a blade speed ratio of $\lambda \approx 1.6$ (Bravo et al., 2007). Because the time for the airfoil to make one half of a rotation is nearly the same as the time for the flow to convect across the width of the turbine ($\pi R/1.6U_\infty \approx 2R/U_\infty$) it is expected that each airfoil will interact on its downstream pass with its own wake generated on its upstream pass. Indeed, studies by Fujisawa and Shibuya (2001) indicate that for blade speed ratios of $\lambda = 1$ and $\lambda = 2$ there is significant airfoil/vortex interaction for a large portion of the rotation (Figure 2.11).

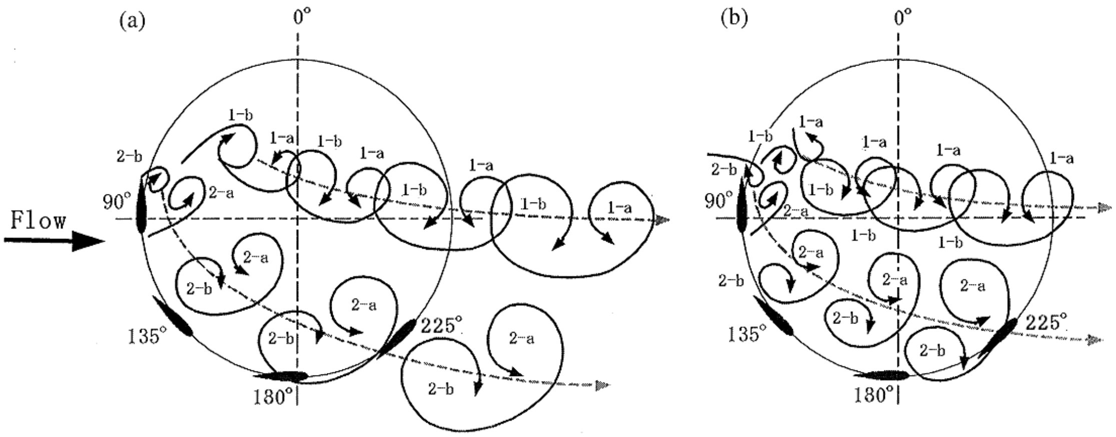

Figure 2.11: Schematic illustration of dynamic stall (a) $\lambda = 1$, (b) $\lambda = 2$, adapted from (Fujisawa & Shibuya, 2001)

The vortices in Figure 2.11 are labelled based upon their order of appearance (1, 2) and whether they are generated from leading edge (1-a, 2-a) or trailing edge (1-b, 2-b) dynamic stall. From this figure it is clear that there are extended durations where the flow over the surface of the airfoil is highly complex, with large periods of flow reversal and vortex impingement. While the study of Fujisawa and Shibuya (2001) demonstrates the significant contribution of dynamic stall to the formation and convection of large scale vortex structures at low blade speed ratios, the experimental tests were performed at a chord Reynolds number of just $Re_c = 500$. The laminar boundary layer which exists at this low of a Reynolds number will likely have far different separation characteristics than the turbulent boundary layer which forms on the surface of the blades of a full-scale turbine at typical operational wind velocities.

For turbine operation at high blade speed ratios, the flow behaviour is far less complex over the surface of the downstream airfoils due to the high rate of rotation, small reduced frequency, and low maximum pitch angle, all of which reduce the likelihood of large vortex structure production (Paraschivoiu, 2002). A study performed by Strickland et al. (1979) tracked the streaklines of particles emitted from the trailing edge of a turbine blade at high blade speed ratios ($\lambda = 2.5$, 5.0, and 7.5). Due to the high rate of rotation of the turbine, and minimal dynamic stall of the airfoils, little vortex production or interaction with any of the turbine blades on the downstream pass was observed.

2.3.1.e Three-Dimensional Effects

A number of three-dimensional effects also come into play when extending dynamic stall theory, experimental test results and numerical models to vertical axis wind turbine dynamic stall behaviour. These include, the effect of support structure (struts and shaft), finite airfoil length (tip effects, flow divergence), and local flow disturbances (trees, buildings, other turbines, etc.). The resultant change in dynamic stall, downstream flow behaviour, and turbine performance due to these factors has the potential to be significant.

The support structure for this turbine design is small relative to the swept area and is expected to have minimal impact on the dynamic stall behaviour of the airfoils, and thus the net flow dynamics. However, parasitic losses introduced by the support structure may have a significant impact on the net power production of the turbine. In addition to the parasitic losses generated by the support structure, it is anticipated that induced drag will be generated due to tip vortices forming at the blade tips. While the presence of end effects have been incorporated into some VAWT numerical models, these effects are estimated based upon Prandtl's finite-wing theory for airfoils in steady flow, and do not take into account the effect of dynamic stall (Paraschivoiu, 2002). However, because the existing numerical models are typically designed for low solidity turbines operating at high blade speed ratios, dynamic stall effects are often not an important consideration. In essence, while end effects have been accounted for, the nature of the flow structures at the blade tips, and their effect on dynamic stall, is not fully understood.

Additionally, because of the finite aspect ratio of the turbine as a whole, the approaching flow is capable of diverging both above and below the turbine swept area. This will result in a reduction in the effective flow velocity that the turbine is subjected to, as compared to an equivalent infinite aspect ratio turbine. Because this effect will be dependent on the turbine aspect ratio rather than the blade aspect ratio, this is an additional three-dimensional flow effect which must be taken into account.

Finally, for this study, the mean flow velocities for the numerical model and wind tunnel are unobstructed, such that upwind flow structures due to large scale atmospheric turbulence and flow disturbances do not exist. Under normal operating conditions however, large variations in atmospheric wind velocity are expected to play an important role in both power output and vibration excitation.

2.3.2. VAWT Experimental Measurements

2.3.2.a Aerodynamic Force

In an effort to determine their aerodynamic performance characteristics, experimental measurement of the power output of VAWTs has been undertaken to considerable lengths (Bravo et al., 2007; Burg, Klimas, & Stephenson, 1990; Dodd, 1990; Ferreira, van Kuik, & van Bussel, 2006; Fiedler & Tullis, 2009; Howell, Qin, Edwards, & Durrani, 2010; Sheldahl, Klimas, & Feltz, 1980; Worstell, 1978; Worstell, 1982). While these measurements provide valuable information on the net and gross power output of the turbine, the details of the instantaneous aerodynamic loading are lost in the integration of the thrust loading over time. Having identified this shortcoming, a number of researchers turned their attention to taking measurements of the instantaneous loading on the airfoils themselves (Akins, Klimas, & Croll, 1983; Oler, Strickland, Im, & Graham, 1983; Vittecoq & Laneville, 1983; Webster, 1978; Zervos, Morfiadakis, & Stefanatos, 1989; Zervos & Morfiadakis, 1990). However, these early studies are primarily limited to conventional, low solidity ratio designs operating at high blade speed ratios ($\lambda > 2.0$), such that dynamic stall is not a major contributing factor to aerodynamic loading.

Obtaining reliable, repeatable measurements of aerodynamic loading on vertical axis wind turbine blades is a considerable challenge (Oler et al., 1983; Vittecoq & Laneville, 1983). Typically, aerodynamic loading is measured either through the use of pressure-taps mounted within the surface of the airfoil (Oler et al., 1983, Zervos & Morfiadakis, 1990), or by a strain gauge system mounted to the blade support structure (McLaren, Tullis, & Ziada, 2010; Vittecoq & Laneville, 1983) (Figure 2.12). While both of these methods have their advantages, one of the greatest difficulties encountered is the relative magnitude of the two primary loading components; radial (normal) force F_R, and thrust (tangential) force F_T (McLaren et al., 2010). In general, radial force can be as much as an order of magnitude greater than thrust force at a given angle of rotation, θ. As such, some steps must be taken in order to sufficiently increase the sensitivity of the measurements to the smaller thrust force component. In a study performed by Strickland, Smith, and Sun (1981), a similar arrangement to that of Oler et al. (1983) was employed with the exception that an increase in sensitivity was accomplished by changing the cross-sectional area upon which the thrust force measuring strain gauge was mounted. Unfortunately, due to the nature of their design, a similar change in sensitivity cannot be accomplished for surface pressure measurements.

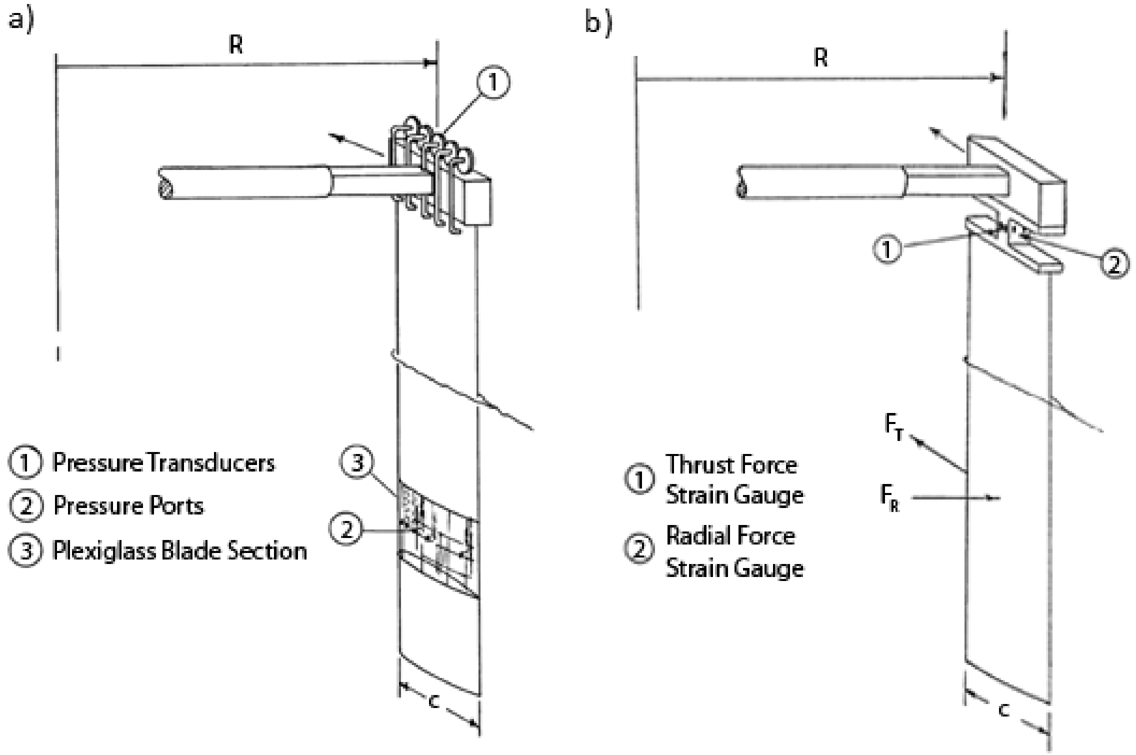

Figure 2.12: Aerodynamic force measurement. (a) Pressure-tap arrangement, (b) strain gauge instrumentation, adapted from (Oler et al., 1983)

The second major challenge encountered when measuring aerodynamic loading on a VAWT blade, is the presence of flow-induced vibrations. For a small scale, high solidity VAWT, both the rotational frequency and natural frequencies of the turbine are quite low. As such, the turbine is very susceptible to resonant vibrations excited by the aerodynamic loading at integer multiples of the rotational frequency. As a result, some method of either avoiding resonant excitation of the turbine natural frequencies, or filtering the resonant response of the turbine from the load measurements, needs to be applied (McLaren et al., 2010; Vittecoq & Laneville, 1983). In the study performed by Vittecoq and Laneville (1983) turbine stiffening was applied in order to raise the primary natural frequencies of the turbine beyond the expected excitation frequencies. A low-pass filter was then applied to eliminate any remaining high frequency noise.

Difficulties associated with obtaining measurements from rotating machinery, pressure measurement integration, system calibration, centrifugal loading, and geometric tolerances of the turbine components, all introduce further complication to the measurement of aerodynamic forces on VAWT blades. In fact, considerable differences in the force coefficients obtained from pressure measurements and those calculated from strain gauge sensors during the same test run have been observed (Oler et al., 1983).

A characteristic sample of the available thrust force measurement data from the study of Oler et al. (1983), for a low solidity ratio turbine (σ = 0.12) operating at high blade speed ratios (λ = 2.5, 5.1, and 7.6) is shown below (Figure 2.13). Here, the large variation in thrust loading that a VAWT airfoil is subjected to throughout a single rotation can clearly be observed. This large cyclic loading on the turbine applied at a frequency of N^*f and $2N^*f$ [Hz], where N is the number of turbine airfoils, is the primary source of vibration loading for VAWTs. Note that measurements were obtained for just 6 full rotations of the turbine, over which time there are large variations in the measured loading behaviour.

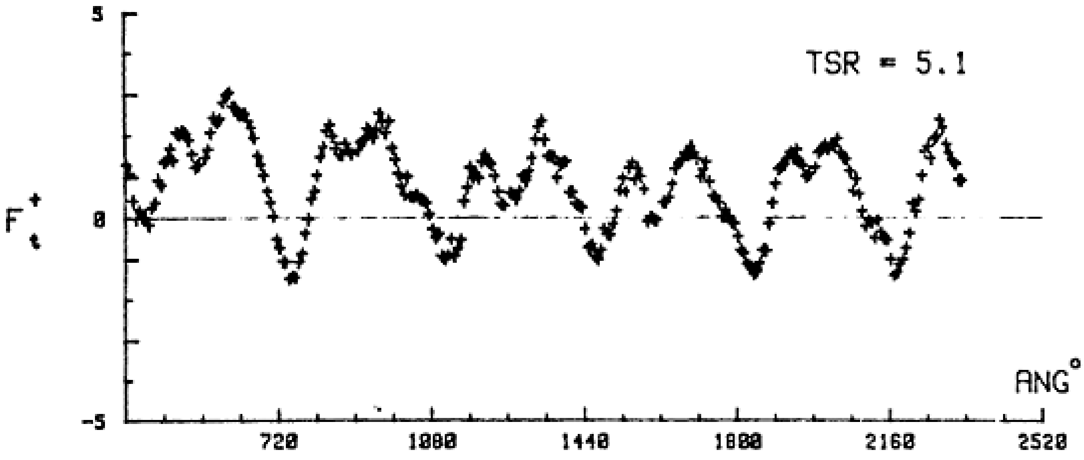

Figure 2.13: Tangential pressure force data for a single bladed NACA 0015 rotor (σ = 0.12, λ = 5.1, Re_c = 67,000), adapted from (Oler et al., 1983)

Aerodynamic force measurements for a slightly higher solidity VAWT (σ = 0.20) have been obtained by Vittecoq and Laneville (1983), at somewhat lower blade speed ratios ($1.5 \leq \lambda \leq 5.0$). From these tests results, it was observed that due to pronounced dynamic stall, the airfoils were subjected to considerably higher frequency loading components. Dynamic stall was identified at blade speed ratios of $\lambda \leq 3.5$ based upon the reduction in thrust force (increase in drag) prior to the reduction in radial force (decrease in lift), as is the case in deep dynamic stall (McCroskey & Pucci, 1982). This deep dynamic stall behaviour at blade speed ratios of less than 3.5 has a dramatic impact on the aerodynamic loading of the airfoil. As an example, Figure 2.14 plots the thrust and radial force measurements at a blade speed ratio of λ = 2.0, the lowest at which experimental thrust force data is available. Here, dynamic stall occurs abruptly at $\theta \approx 65°$, resulting in a rapid decrease in thrust force, and a large negative thrust force peak shortly thereafter. A loading component applied at a rate of approximately 8 cycles per revolution can then be observed in both of the aerodynamic loading components. Note that due to the low solidity of this turbine design, a blade speed ratio of λ = 2.0 is at the lower operating capability of the turbine, where net power production is negligible.

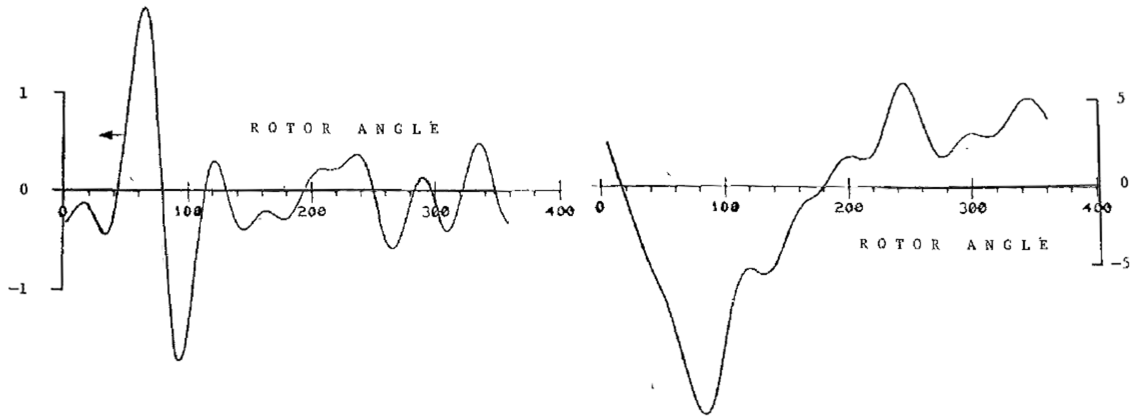

Figure 2.14: Thrust and radial force coefficients on a NACA 0018 airfoil ($\sigma = 0.20$, $\lambda = 2.0$, $Re_c = 38{,}000$), adapted from (Vittecoq & Laneville, 1983)

It is expected that at the very low blade speed ratios that high solidity turbine designs operate ($0.4 \leq \lambda \leq 2.0$), that dynamic stall will occur earlier on in the rotation. This will lead to even more abrupt changes in thrust and radial loading, which will be applied at much higher frequencies per rotation. It is this intense dynamic stall behaviour which overdrives the aerodynamic lift when the relative angle of attack is rapidly increasing and decreasing (Paraschivoiu & Allet, 1988). These abrupt changes in aerodynamic lift significantly increase the unsteady airfoil loads that can be very damaging to both the wind turbine and the structure on which it is mounted (Akins et al., 1983). As a result, the effects of dynamic stall have a direct impact on the robustness and factors of safety required in drive-train calculations, generator sizing, and overall system design (Paraschivoiu & Allet, 1988). Additionally, as stated above, because the peak net power output of the turbine occurs near a blade speed ratio of $\lambda = 1.6$, it is expected that any flow structures generated by dynamic stall will convect alongside the airfoil and have a prolonged influence on the aerodynamic loading behaviour.

2.3.2.b Velocity Field

VAWT flow visualization and wake measurement studies by Blackwell, Sheldahl, and Feltz (1976), Ferreira et al. (2006), Ferreira et al. (2007), Fiedler (2009), Fujisawa and Shibuya (2001), and Hofemann et al. (2008) have also been carried out, providing invaluable information on the formation, shedding and convection of vortex structures within the turbine wake. Typically these measurements are obtained in conjunction with power measurements and as such are generally performed at high blade speed ratios. These studies have consisted of particle image velocimetry (PIV), laser-doppler velocimetry (LDV), and hot-wire measurements, as well as CCD camera images using tufts, dye emission, and hydrogen bubbles.

An example of the results obtained from a PIV measurement of the flow field over a single bladed VAWT operating at a blade speed ratio of $\lambda = 2$ is given below (Figure 2.15). From this figure, the formation and shedding of a large vortex structure from the leading edge of the inner surface of the airfoil can clearly be seen. Ultimately, this study concluded that despite the relatively low Reynolds number at which the experiments were performed (Re_c = 70,000 based upon the airfoil rotational velocity), the PIV measurements of the leading edge laminar separation are useful for the validation of numerical models

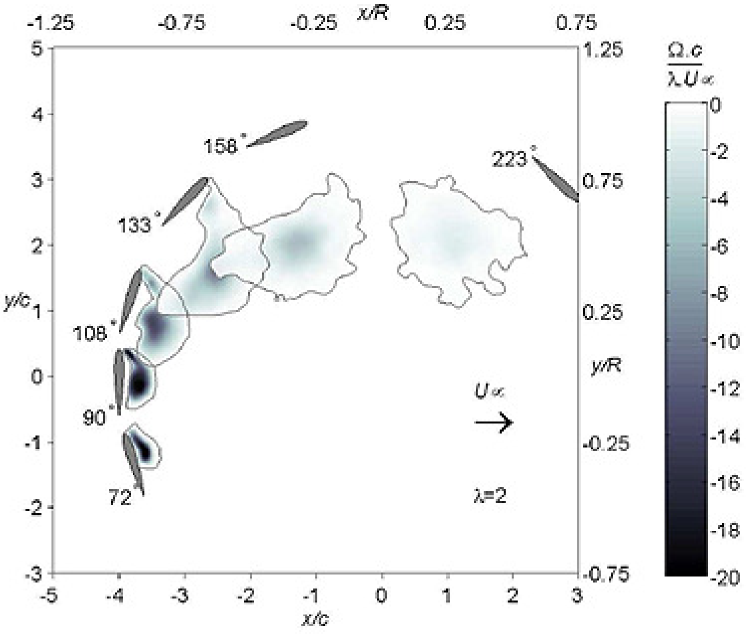

Figure 2.15: PIV experimental data of the evolution of the circulation of leading edge separated vortex for λ = 2, σ = 0.125, Ω - vorticity [s^{-1}] (Ferreira et al., 2007)

A recent study performed by Fiedler (2009) on a high solidity VAWT ($\sigma = 0.41$), recorded CCD camera images of an array of bi-coloured Mylar tufts attached to the inner surface of the NACA 0015 airfoils. In doing so, the location and severity of dynamic stall on the surface of the airfoils could be characterized for a full-scale turbine at typical operational Reynolds numbers ($Re_c = 250{,}000$). A summary of the separation behaviour of the airfoils at low blade speed ratios ($1.1 \leq \lambda \leq 1.6$) is given in Figure 2.16. From this figure it can be seen that flow separation, and thus the onset of dynamic stall, occurs at an angle of rotation of just 55° at a blade speed ratio of $\lambda = 1.1$, and persists for a total of 180° degrees. For a blade speed ratio of $\lambda = 1.3$, dynamic stall is delayed to an angle of rotation of approximately 70°, and lasts for a considerably shorter duration (160°). Because the region of fully reversed flow over the airfoil is also considerably reduced at a blade speed ratio of $\lambda = 1.3$, this indicates that not only is dynamic stall being delayed, but it is also occurring in a more abrupt manner. Finally, for the peak net power output blade speed ratio of $\lambda = 1.6$, the onset of dynamic stall is delayed further to an angle of rotation of 85°. At the same time, the duration of dynamic stall is increased slightly to 170°, signifying that dynamic stall is now occurring more gradually at high blade speed ratios.

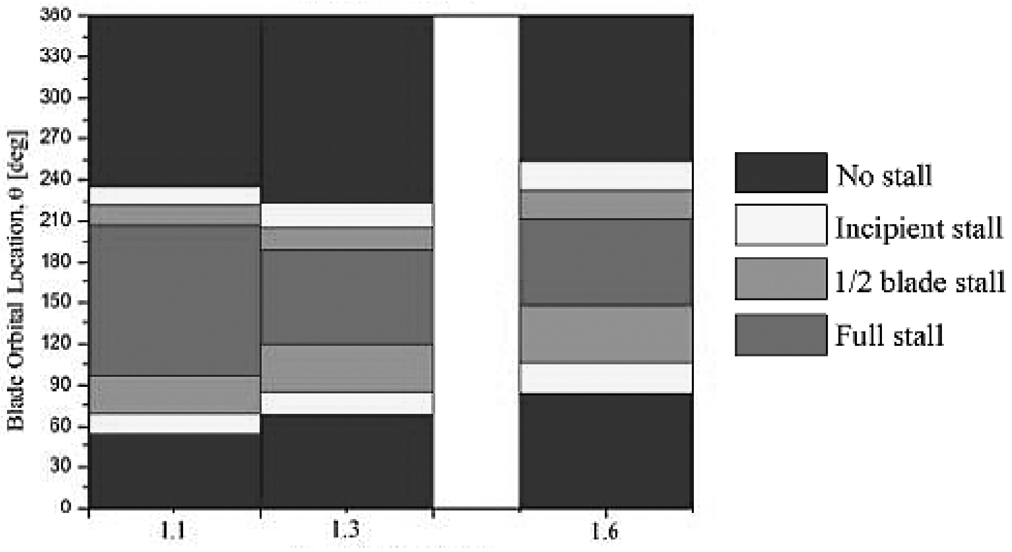

Figure 2.16: Stall plots for one of three NACA 0015 airfoils ($U_\infty = 10$ m/s, $\beta = 0°$, $\sigma = 0.41$), adapted from (Fiedler, 2009)

Measurement of the turbine wake profile is another important tool in determining the aerodynamic performance of a VAWT. By measuring the downstream wind velocity, the effect of dynamic stall and the amount of momentum extracted from the flow by the turbine can be approximated. The results of an LDV study by Brochier, Fraunié, Béguier and Paraschivoiu (1986) demonstrates the substantial decrease in flow velocity through the turbine (upwards of 60% at 2.5 radii downstream), as well as local acceleration of flow around the turbine (Figure 2.17). This information has important implications for the placement of arrays of VAWTs, as the unsteady wake generated by one turbine may strongly influence the vibration excitation of another turbine placed downstream. Data of this nature would also be a valuable tool in evaluating the accuracy of any numerical model predictions. Note that the very high blockage ratio of the water tunnel used in this study (3/5) made have greatly exaggerated the flow acceleration around the turbine.

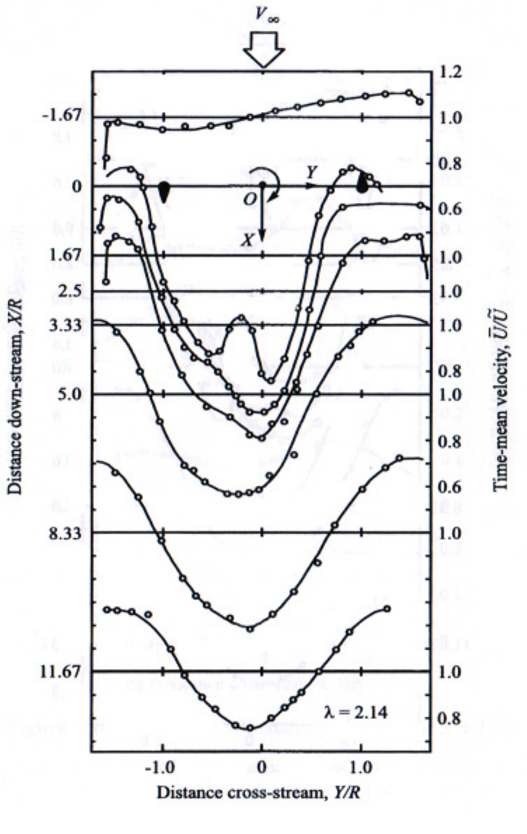

Figure 2.17: Streamwise mean velocity profiles for $\lambda = 2.14$, $N = 2$, $\sigma = 0.33$ (Brochier et al., 1986)

2.3.2.c Turbine Vibrations

A number of studies have been performed to determine the vibration response of VAWTs as a function of the rotational velocity, the turbine structural modes that are being excited, and the resultant stresses and fatigue loading on the turbine blades and structural components (Ashwill, 1989; Ashwill, Sutherland & Veers, 1990; Ashwill & Veers, 1990; Dohrmann & Veers, 1989). However, the results of these studies have been limited to field measurements of traditional low solidity turbine designs, are specific to the particular turbine design under consideration, and do not take into account the blade speed ratio at which the turbine is operating.

At present, while considerable effort has been focused on determining the power producing aerodynamic loads, little attention has been paid to quantifying the aerodynamic vibration excitation sources. This is despite the fact that turbine vibrations in general have been identified as a major contributing factor to the longevity of VAWTs. In particular, the effect of dynamic stall on vibration excitation has mainly been overlooked due to the high blade speed ratios at which most conventional VAWTs operate.

2.3.3. VAWT Numerical Models

The following numerical models are the most commonly employed methods used to determine aerodynamic loading on VAWTs. A number of the more well-established models however, are either engineered for traditionally designed low solidity VAWTs which operate at high blade speed ratios, or incorporate steady state empirical lift and drag data. As such, these models are not optimized to account for high pitch rates, large variations in angle of attack and flow velocity, or large downstream flow structures, all of which are expected to play a large role in high solidity, low blade speed ratio, VAWT aerodynamics. Nevertheless, they have shown great success in modelling the conditions for which they were designed, and will form the basis of this review.

2.3.3.a Vortex Model

Starting in 1975 (Larsen), it was recognised that the discrete potential vortex approach used to model deep dynamic stall for oscillating airfoils (described above) could easily be adapted to model VAWTs. Previous dynamic stall studies which indicated that this method was only appropriate for highly separated, low Reynolds number flows, support the identification that this method is suitable for modelling low rotational velocity VAWTs. Since then, modelling of VAWT aerodynamics with the vortex approach has been extensively performed (Fanucci & Walters, 1976; Holmes, 1976; Scheurich, Fletcher, & Brown, 2011; Strickland et al., 1979; Wilson, 1978; Zervos, 1988). A sample comparison of numerical results of the highly developed vortex model of Strickland et al. (1979) to experimental data obtained by Webster (1978) indicates that the model is very good at obtaining radial (normal) coefficients for all angles of rotation (Figure 2.18). However, considerable under-prediction occurs for the model determination of the thrust coefficient on the downstream portion of the rotation. Ultimately, this model is limited by the assumption that potential flow exists in the wake, and that the effect of viscosity on the airfoil aerodynamics can be included through the use of empirical force coefficients (Islam, Ting, & Fartaj, 2008).

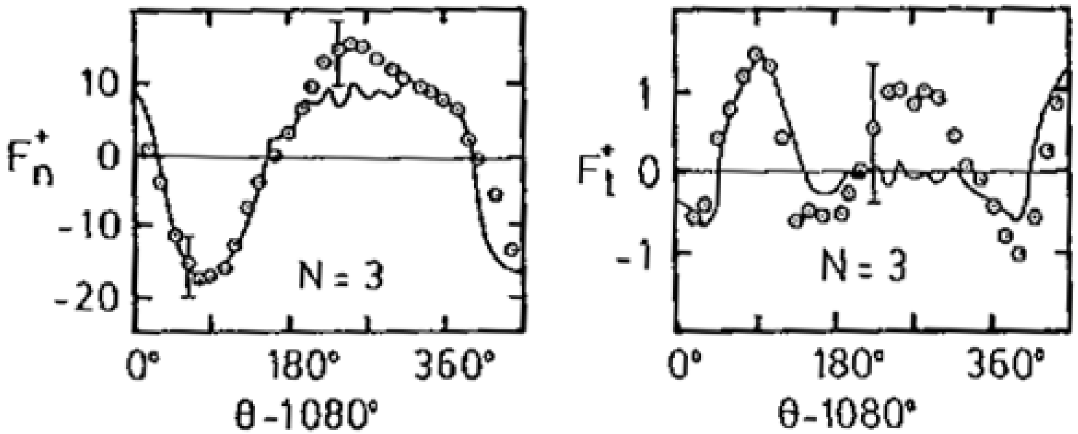

Figure 2.18: Vortex model normal and thrust coefficient loads, λ = 5.0, σ = 0.225, *Re* = 40,000 (Strickland et al., 1979)

2.3.3.b Double-Multiple Streamtube Model

The double-multiple streamtube (DMST) model is part of a class of models referred to as momentum or Blade Element/Momentum (BEM) models. These models are based upon calculation of the flow velocity through the turbine by equating the streamwise aerodynamic force on the blades with the rate of change of flow momentum, which is equal to the overall change in the product of flow velocity and mass flow rate (Paraschivoiu, 2002). The double multiple streamtube model is a direct descendent of the single (Templin, 1974) and multiple (Wilson & Lissaman, 1974) streamtube models. These early momentum models solved for the velocity field through application of the actuator disc theory for horizontal axis wind turbines, which assumes that the flow velocity through the turbine is constant. The major drawback of the single streamtube model is its inability to predict wind velocity variations across the rotor which are considerable for high solidity and tip speed ratios. The multiple streamtube model accounts for velocity variations in the cross-stream direction, but is still unable to accurately describe the flow field.

In 1981, Paraschivoiu introduced the double multiple streamtube theory which solves for the flow field by modelling the upstream and downstream half-cycles of the turbine as two actuator discs in tandem, as per the concept of Lapin (1975). Considerable improvement over the single and multiple streamtube models was realized due primarily to the fact that the upstream and downstream induced velocities are calculated separately. For the upstream half-cycle, the induced velocity is represented by,

$$V = uV_{\infty i} \qquad 2.15$$

where $u < 1$ is the interference factor for the upstream half cycle, and $V_{\infty i}$ is the local ambient wind velocity of streamtube *I*. Note that because the DMST model solves for the flow momentum at each level of the turbine, variations in ambient wind velocity (V_{∞}) and turbine geometry (R, c, blade type) with respect to height can be incorporated into the numerical model. The equilibrium velocity at the turbine mid-plane is then given by,

$$V_e = V_{\infty i}\left(2\frac{V}{V_{\infty i}} - 1\right) = V_{\infty i}(2u - 1) \qquad 2.16$$

For the downstream half-cycle, the equilibrium velocity V_e is now the input velocity, and the downstream induced velocity is given by,

$$V' = u'V_e = u'V_{\infty i}(2u - 1) \qquad 2.17$$

where u' is the downstream interference factor (Paraschivoiu. 2002). Through the use of airfoil sectional data, the induced velocities can then be calculated by a double iteration process applied over thin streamwise slices of the turbine cross-section, or ‘streamtubes’ as shown in Figure 2.19.

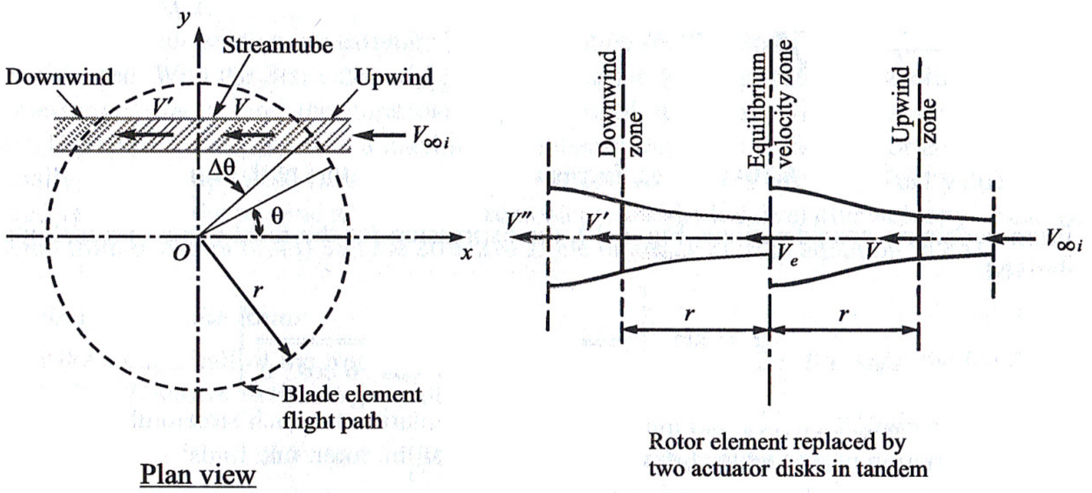

Figure 2.19: Schematic of double-multiple streamtube model (Paraschivoiu, 2002)

Once the local relative velocity field and effective angle of attack are determined, the loading coefficients for a given angle of rotation can then be calculated. Considerable effort has been applied in modifying and adjusting this model to determine the optimal expression for the interference factors as well as incorporate the secondary effects of the blade geometry, support structure and aerodynamic spoilers. (Paraschivoiu, 1988; Paraschivoiu, Desy, & Masson, 1988; Paraschivoiu & Delclaux, 1983; Shankar, 1976; Sheldahl & Klimas, 1978; Strickland, 1975).

This work also includes using data obtained from dynamic stall models in place of the airfoil sectional data from which the aerodynamic loading is determined (Paraschivoiu, 1983). Below is a comparison of the Gormont (Boeing-Vertol) and the Massachusetts Institute of Technology (MIT) models' ability to predict the normal force coefficient for a 17m Darrieus wind turbine (Figure 2.20). While both models provide reasonable predictions, they both over-predict the normal force coefficient on the upstream portion of the rotation where dynamic stall exists and a large hysteresis loop is formed. While the Gormont model does this in a less severe manner, it incorrectly predicts dynamic stall on the downstream portion of the rotation where the experimental data indicates there is none.

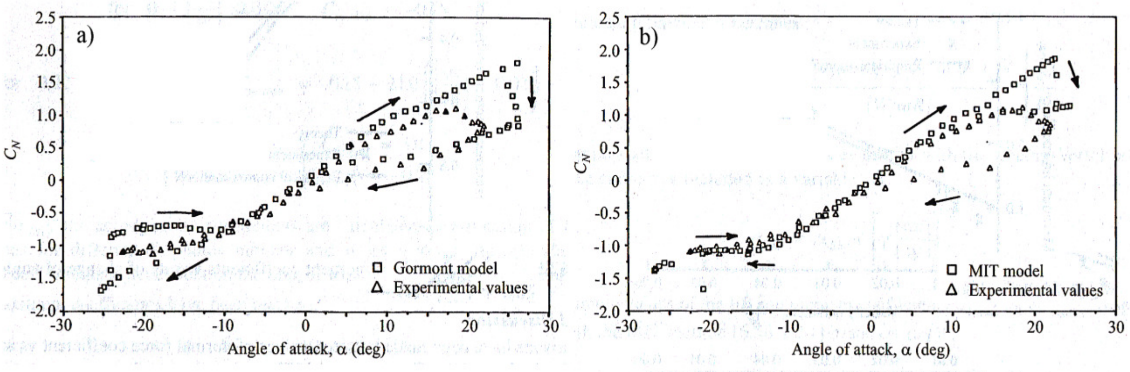

Figure 2.20: Normal force coefficient prediction for a) Boeing-Vertol and b) MIT dynamic stall models (λ = 2.6), adapted from (Paraschivoiu, 2002)

The effect on the aerodynamic force components of incorporating a dynamic stall model within the DMST theory is shown below. The DMST model 'without dynamic stall' obtains the lift and drag coefficients from tables of static airfoil data directly, while 'with dynamic stall' the model applies the Boeing-Vertol dynamic-stall model (Gormont, 1973) to generate the lift and drag coefficients (Paraschivoiu, 1983). For simplicity sake, the DMST model shown here employs constant upstream and downstream interference factors. As expected, for the high blade speed ratio of λ = 3, the outcome of including dynamic stall effects is to delay the upstream drop in thrust and radial (normal) force, while increasing the magnitude of the loading components and bringing the numerical prediction closer to the experimental data. Similar improvement can also be observed on the downstream portion of the rotation (Figure 2.21).

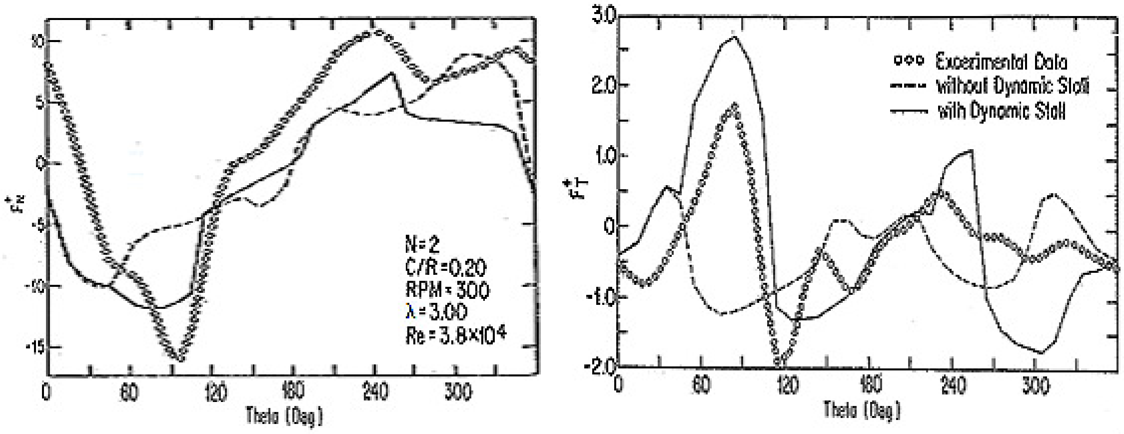

Figure 2.21: DMST normal (F_N) and thrust (F_T) force coefficients with and without dynamic stall model (σ = 0.20, λ=3.00), adapted from (Paraschivoiu, 1983)

However, even when variable interference factors were applied, far less accurate predictions were obtained from the DMST model with the dynamic stall model incorporated at a blade speed ratio of λ = 1.50 (Figure 2.22). At lower blade speed ratios, the model is unable to resolve high frequency fluctuations in the thrust loading component (Paraschivoiu, 1983).

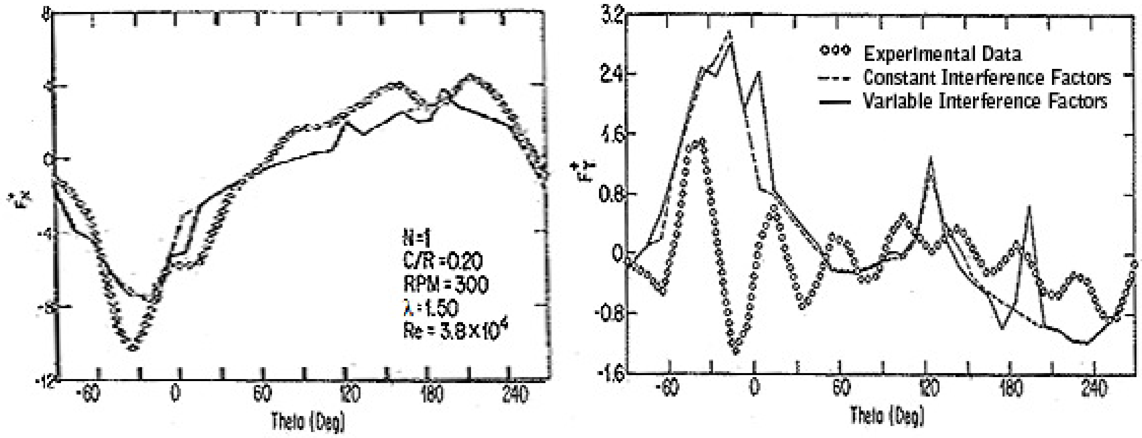

Figure 2.22: DMST with dynamic stall model normal (F_N) and thrust (F_T) force coefficients with constant and variable interference factors (σ = 0.10, λ=1.50), adapted from (Paraschivoiu, 1983)

Ultimately, the major fallback of even the most advanced streamtube model is that they are quasi-steady state and based upon empirical airfoil lift and drag data. As such, these models do not properly address the important dynamic effects which are expected to dominate the aerodynamics of high solidity, low rotational velocity turbines. In fact, it has been identified that streamtube models become invalid for high rotor solidities and large tip speed ratios, where dynamic stall and secondary effects have a large impact on aerodynamic loading, because the momentum equations in these instances are inadequate (Paraschivoiu, 2002). Furthermore, while momentum based models are capable of determining the mean flow field downstream of the turbine, they are unable to predict the formation of large scale flow structures in the near wake, which are expected to be a large source of vibration excitation loading.

2.3.3.c URANS for VAWT

Application of the two-dimensional URANS equations to solve for the aerodynamics of VAWTs is a logical progression from the studies on stationary pitching airfoils undergoing dynamic stall (2.2.2.d). As described above, a turbulence model is required to provide closure to the URANS equations, and a sample of the more successful models is given below. Unfortunately, little experimental thrust and radial loading coefficient data exists at present, particularly for low blade speed ratios, and the thrust data which is available is often criticized due to difficulties in obtaining reliable results (Allet, Halle, & Paraschivou, 1999). Hence, a number of the numerical models are simulated at conditions where there is no experimental data for validation.

The first two turbulence models which will be discussed are the zero-equation model of Cebeci and Smith (1974) and the half-equation model of Johnson and King (1985). The Cebeci-Smith model is very much like the Baldwin-Lomax model described above but for that it requires the solution of a boundary layer thickness. From Figure 2.23 it can be seen that as compared to the experimental results of Oler et al. (1983), very good agreement is obtained for the normal force coefficient, while the thrust (tangential) coefficient is largely over-predicted by both models on the upstream pass. Some of the major limitations of these early models include, low grid refinement, and simulation of too few turbine rotations, due in part to computational limitations. Note the appreciable difference in the tangential force coefficients when calculated using strain gauge and pressure data, due to experimental difficulties (2.3.2.a).

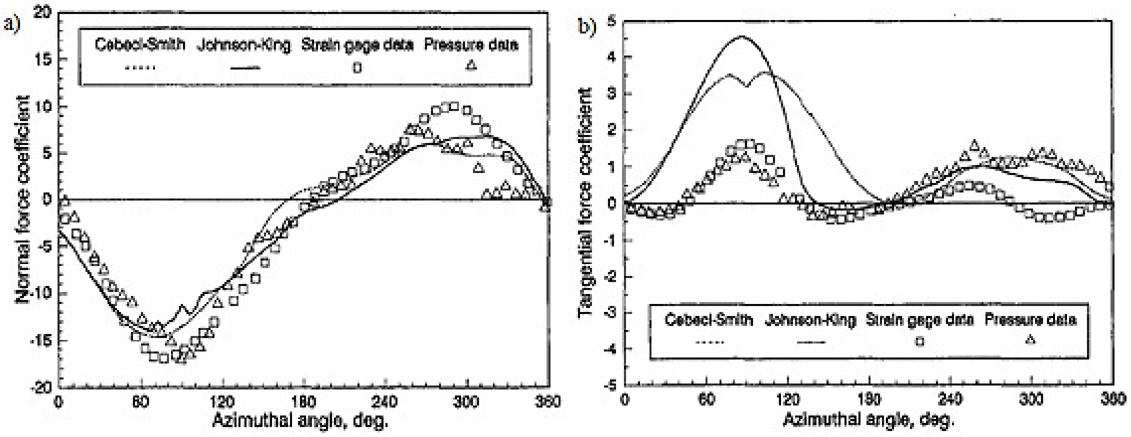

Figure 2.23: Aerodynamic force coefficients for Cebeci-Smith and Johnson-King turbulence models for VAWT, λ = 2.5, σ = 0.125, *Re* = 67,000 (Allet et al., 1999)

From Figure 2.24 below the results of test cases with the more complex Spalart-Allmaras and k-ε models can be seen, however, due to the lack of comparable experimental data, the validity of these results is unknown (Ferreira, Bijl, Van Brussel, & Van Kuik, 2007). Additional test results for the k-ε model can be found in Hamada, Smith, Durrani, Qin, and Howell (2008) and Howell et al. (2010). The model of Howell et al. (2010) has even been expanded to incorporate three-dimensional flow effects and showed improved agreement with experimental power curves. However, even as noted by the authors, the mesh was particularly coarse due to computational limitations (Hamada et al., 2008).

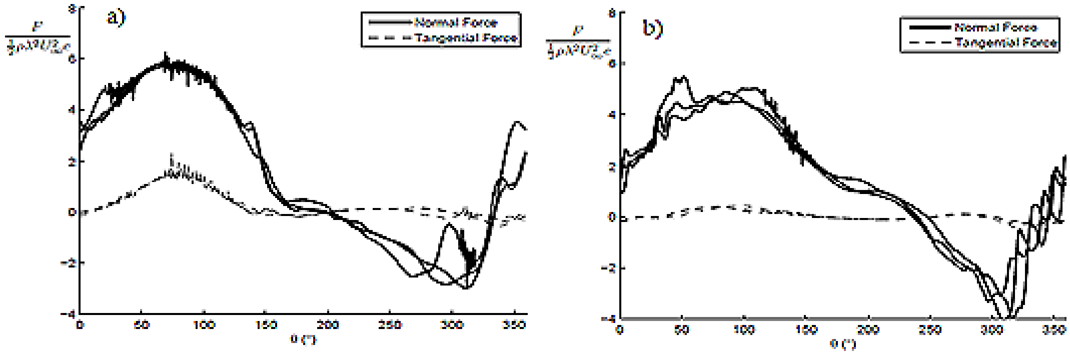

Figure 2.24: Load coefficients for a) Spalart-Allmaras and b) k-ε turbulence models for VAWT for three full rotations of the turbine, $\lambda = 2$, $\sigma = 0.125$, $Re = 50{,}000$ (Ferreira et al., 2007)

A study by Guerri, Sakout, and Bouhadef (2007) explores the use of Menter's Shear Stress Transport (SST) turbulence model. This model is particularly well suited to highly separated flows due to its ability to model strong adverse pressure gradients, and has shown considerable success in modelling dynamic stall behaviour (see above) as well as performing horizontal axis wind turbine aerodynamic analysis (Sorensen, Michelson, & Schreck, 2002). Again, the flow conditions simulated ($\sigma = 0.16$, $\lambda = 1.05$ and 1.88, $Re_c = 7.2 \times 10^4$) do not correspond to those for which experimental force coefficients have been obtained and validation is not yet possible.

2.3.3.d Large-Eddy and Detached-Eddy Simulation

In contrast to URANS, in Large-Eddy Simulation (LES) the conservation equations are not averaged in time, but rather are averaged in space. In doing so, the computational requirements are increased in order to solve directly for the larger scales of turbulence. Turbulence modeling is then reduced to only the sub-grid scale (SGS). However, even with the application of a wall-treatment (SGS model), the computational expense associated with the required grid refinement at the blade surface is considerable. As such, a hybrid method combining URANS within the boundary layer region and LES within the free-stream region has been developed (Spalart, Jou, Strelets, & Allmaras, 1997). This method is known as the Detached-Eddy Simulation (DES), and has shown to provide improved predictions of the generation, shedding and convection of vorticity for VAWT modelling as compared to the LES model (Ferreira et al., 2007). Figure 2.25 below plots the numerical prediction of normal and tangential force coefficients for both the DES and LES models. As can be seen from this image, both models produce similar aerodynamic loading data to the URANS models above, however repeatability from one rotation to the next is low. Additionally, high frequency fluctuations, likely due to numerical convergence effects, dominate the loading behaviour (Ferreira et al., 2007).

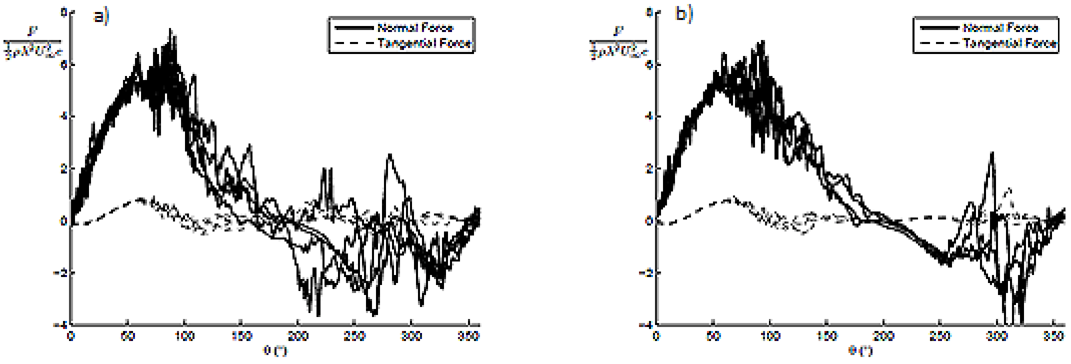

Figure 2.25: Load coefficients for a) DES and b) LES models for VAWT for four rotations of the turbine, $\lambda = 2$, $\sigma = 0.125$, $Re = 50,000$ (Ferreira et al., 2007)

2.4. Summary

Based upon the literature reviewed, it has been determined that due to the high relative angles of attack and pitch rates that the airfoils of a high solidity VAWT are subjected to, considerable periods of flow separation and dynamic stall will exists. This will result in the formation of large scale flow structures, which will have a direct impact on the unsteady aerodynamic loads, and thus vibration excitation of the wind turbine. Most importantly, due to the range of blade speed ratios over which the high solidity turbine prototype typically operates ($0.4 \leq \lambda \leq 2.0$), any vortices which are shed from the airfoil are expected to be convected downstream at nearly the same rate as the turbine blades. As such, extensive airfoil/vortex interaction is expected to occur throughout an entire rotation of the turbine.

Existing empirical, quasi-steady state, numerical models do not adequately resolve these highly dynamic flows. As such, they will not be pursued as a potential method with which to investigate the aerodynamics of VAWTs operating at very low blade speed ratios. Large-eddy and detached-eddy simulations of the flow field were also evaluated for this purpose. But, due in large part to the computational expense associated with the fine mesh spacing required, they too are not employed in the present study. URANS simulation of the flow around the wind turbine however, was demonstrated to be capable of solving for the dominant flow separation and history effects, and requires realizable computational resources. However, existing URANS models of VAWTs are primarily limited to low solidity designs operating at high blade speed ratios and low Reynolds numbers. As such, the development of a two-dimensional URANS model of a full-scale, high solidity VAWT is proposed. The primary objective of this study will be to better understand the effects of dynamic stall on the vibration excitation and power producing loads at very low blade speed ratios.

From the available literature, it was also determined that there is a lack of existing experimental aerodynamic load measurements for high solidity, VAWTs operating at low blade speed ratios, with which to validate the proposed numerical model. As such, full-scale, wind tunnel tests will be performed to acquire the necessary data. Unlike prior experimental investigations, measurements will be obtained over a range of flow velocities in order to ensure Reynolds number independence of the results. These tests will include much needed measurements of the wind turbine vibration response, in order to determine the influence of dynamic stall on the vibration excitation loading behaviour. Wind turbine wake velocity measurements were also shown to be a valuable tool for validating numerical model results, and as such will also be obtained.

CHAPTER 3

NUMERICAL MODEL DEVELOPMENT

This chapter outlines the numerical modelling approach employed in the present study on high solidity VAWTs. Based upon the literature reviewed, it was determined that a two-dimensional URANS simulation was the most favourable method to determine the influence of dynamic stall on VAWT vibration excitation at low blade speed ratios. By limiting the numerical modelling domain to a single cross-section of the wind turbine, the computational expense could be minimized. Previous URANS simulations of VAWTs have generally employed a similar approach. However, they have typically been limited to low solidity, low Reynolds number investigations, with lower order turbulence models.

Initial development of the model consisted of steady state simulations of a single, non-rotating airfoil, in order to perform a preliminary validation of the mesh density and turbulence model (refer to Appendix A.1). This model was then expanded to incorporate the effects of all three blades rotating about the central support shaft subjected to cross flow. The complexity of this model was considerably greater than the original due to the need for an appropriate domain size, the presence of rotating meshes, and transient time step calculations and analysis. Once the necessary independence and steady state validation tests were performed, simulation of each of the blade profiles over a range of blade speed ratios was carried out. From this model, important aerodynamic loading characteristics, vivid flow behaviour images, vibration excitation loading, and turbine power output were obtained.

3.1. Numerical Modelling Technique

Numerical simulation of the flow field was performed using the hybrid finite-volume/finite-element method of ANSYS CFX. The code solves the incompressible unsteady Reynolds averaged Navier-Stokes equations throughout the entire flow domain. Turbulent quantities were solved through the use of a turbulent-viscosity model. Solution of the energy equation was not required as the flow was considered to be isothermal.

Numerical discretization of the governing equations was carried out through the use of a finite-volume scheme. The governing equations were integrated over each control volume, and the discrete values of the relevant quantities were stored at the centre of the control volume. Finite-element shape functions were used to evaluate surface flow terms at integration points within the control volume, while advection terms required at the control volume faces were interpolated from discrete control volume values. The High Resolution Scheme was used to perform the interpolation (Barth & Jesperson, 1989). A second order Backward Euler scheme was employed to model transient terms.

A coupled solver was employed to solve the hydrodynamic equations as a single system. This approach employs a fully implicit discretization of the equations at each timestep. For each timestep the non-linear equations were linearized and assembled into a solution matrix. The linear equations were then solved in an iterative manner using an Algebraic Multigrid method (Raw, 1996).

3.2. Dynamic Model of Rotating Turbine

In order to numerically obtain the necessary aerodynamic force coefficients, a model capable of producing a solution independent of the boundary conditions, timestep size, convergence limits, and other pertinent modelling conditions was developed. The final conditions that were settled upon were based on the initial steady state model validation (Appendix A.1), single rotating blade simulations (McLaren, Tullis, & Ziada, 2007a, McLaren, Tullis, & Ziada, 2007b), and the additional independence tests outlined below. For clarity reasons, the results of these tests are presented in a simple progressing manner. However, in reality each of the independence tests was dependent on one another, such that a much more involved process was required to settle upon these conditions.

The two-dimensional computational domain was designed to simulate the flow in a cross-section through the turbine (Figure 3.1). A small rotating domain 7.5 m in diameter was contained within a large stationary rectangular domain 22 m in crosswind width by 36 m in stream-wise length. The numerical model incorporates three blades within the rotating domain at a radius of R = 1.4 m from the axis of rotation as well as a 0.1 m diameter central shaft.

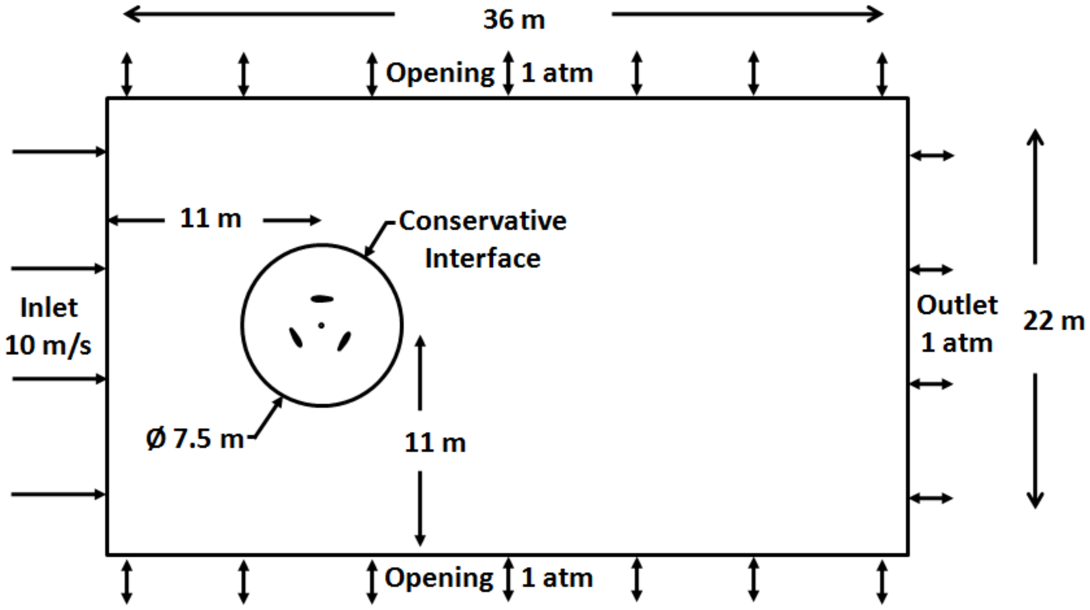

Figure 3.1: Open air numerical model domain (airfoils not to scale)

The inlet flow condition was fixed at U_∞ = 10.00 m/s normal to the boundary, with turbulent intensity of 10%. The resulting Reynolds number based on free-stream velocity and turbine blade chord is 270,000. Reynolds number dependence tests showed little change in loading coefficients for $Re_c \geq 210{,}000$, which agrees well with experimentally observed behaviour (Fiedler & Tullis, 2009). The outlet and side surfaces of the stationary domain were set to allow both inflow (where the total pressure is set to 1 atm) and outflow (in which case the average static pressure is set as 1 atm), and were located at a great enough distance from the turbine blades that the solution was independent of the domain size, and thus the boundary conditions. The turbulent properties were set to have zero gradients at these three surfaces. The surface of the blades and shaft were modelled as smooth, no-slip surfaces. The initial condition in the entire domain was the same uniform velocity as the inlet condition.

A sliding mesh interface with a conservative mass and momentum flux condition was set at the boundary of the rotating and stationary domains (Blades & Marcum, 2007; Mathur, 1994). An unstructured mesh was employed in the free-stream region of the domain, resulting in a total of approx. 475,000 nodes. An unstructured triangular mesh was required within the bulk of the flow in order to avoid directionality effects as the circular domain rotates. A highly refined mesh was applied within close proximity of the blades, resulting in a total of 989 elements over the surface of each blade, with the first node occurring at an average y^+ of 1.3 and a maximum y^+ of 5.6. The 7.5 m diameter of the rotating domain was determined such that the refined mesh surrounding the blades remained with the blades as the domain rotated. A fully implicit time advancement scheme was used with a time step size corresponding to a turbine rotation of 1.0 degrees. Convergence criteria were set to satisfy a maximum RMS residual of 2.0×10^{-5} as well as a minimum of 5 solution iterations per timestep. Based upon the findings available in the literature, the turbulence model which was employed was the Shear Stress Transport (SST) model. Steady state validation tests confirm the appropriateness of this turbulence model for highly separated aerodynamic flows (Appendix A.1).

3.2.1. Domain Size Independence

In order to determine the domain size necessary to ensure that the boundary conditions had a minimal effect on the force coefficients obtained from the model, a series of domain size independence tests were performed. Figure 3.2 below demonstrates the effect of a change in the outer dimensions of the flow domain. As can be seen from this figure, for a very small domain of just 8 metres in cross-stream width by 14 metres in streamwise length, a considerable increase in thrust force is observed on both the upstream and downstream portions of the rotation. However, the change in the maximum thrust force coefficient between the 35 x 20 metre domain and the 42 x 24 metre domain is less than 2% while the change in power coefficient is less than 1.5%.

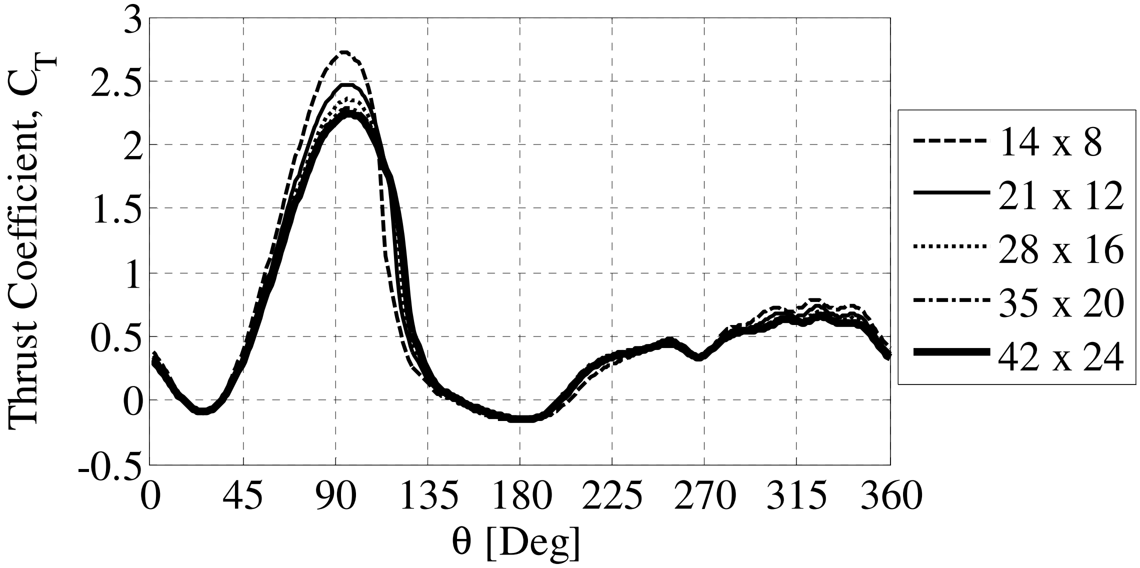

Figure 3.2: Thrust force coefficient as a function of domain size, length [m] x width [m] (U_∞ = 10 m/s, λ = 1.6)

3.2.2. Mesh Size Independence

One of the most important characteristics of the numerical model definition is the mesh density. The number and distribution of nodal points within the flow domain dictates the accuracy of the final solution to a large degree. Based upon the meshing parameters developed from the steady state model validation (refer to Appendix A.1), a very refined boundary layer mesh was placed on the surface of the blades as well as the central rotating shaft. Within the bulk of the flow domain an unstructured triangular mesh was employed. This was particularly important in the rotating domain as any directionality of the mesh structure may have resulted in unfavourable results as the domain moved with respect to the primary flow direction.

Figure 3.3 displays the effect of a change in the mesh density from a very coarse 72,000 nodes to a much more refined 567,000 nodes. While the entire mesh is not fully described by the total number of nodal points alone, similar scaling factors were applied to both the refined boundary layer mesh and the unstructured global mesh. This resulted in just 5 boundary layer cells for the coarsest mesh, while the most refined mesh had a total of 40 cells within the refined boundary layer. From Figure 3.3 it is clear that the coarsest mesh is unable to capture the behaviour of the flow, most likely due to large mesh spacing near the walls and a breakdown of the conditions necessary to satisfy the turbulence model. However, for the four finest meshes the power coefficient varies by just 5%, while the maximum thrust force coefficient varies by less than 2.5% of the most refined mesh results.

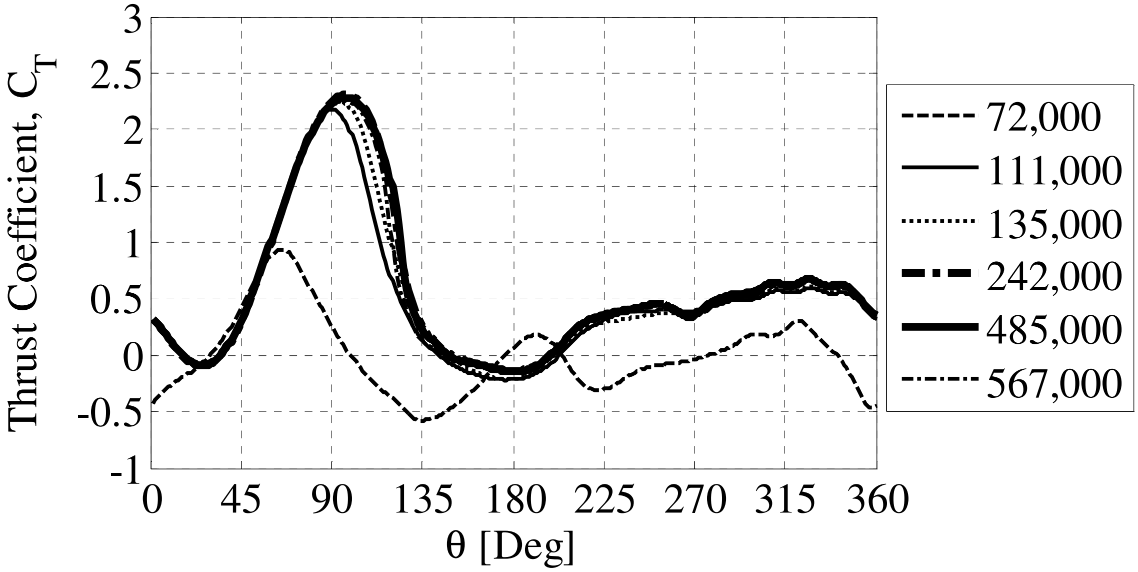

Figure 3.3: Thrust force coefficient as a function of the number of nodal points within the mesh (U_∞ = 10 m/s, λ = 1.6)

3.2.3. Time-step Independence

In order to ensure sufficient resolution of the numerical results an appropriate timestep size is required. For the given geometry, five different timestep sizes were tested corresponding to 10, 5, 2.5, 1.0 and 0.5 degrees of rotation of the inner circular domain. Table 1 illustrates the effect of a change in timestep size on the distance traversed by the blade over a single timestep.

Degrees of Rotation / Timestep	% of Chord length / Timestep
10.0	54.5
5.0	27.3
2.5	13.6
1.0	5.5
0.5	2.7

Table 1: Percent of chord length traversed in a single timestep

For timestep sizes corresponding to 10.0 and 5.0 degrees of rotation the blade moves by a rather substantial portion of its chord length resulting in a considerable change in the local body of fluid surrounding the blade. For smaller time-steps of 2.5, 1.0 and 0.5 degrees, the blade advances only a small percentage of its chord length, allowing the flow variables to adjust in an appropriate manner. Figure 3.4 highlights this effect by the drastic difference in the solution for the thrust coefficient as a function of the timestep size changing from 5.0 to 2.5 degrees. For the three smallest timestep sizes the power coefficient varies by just 1.5%, while the maximum thrust force coefficient varies by less than 2% of the smallest timestep size results.

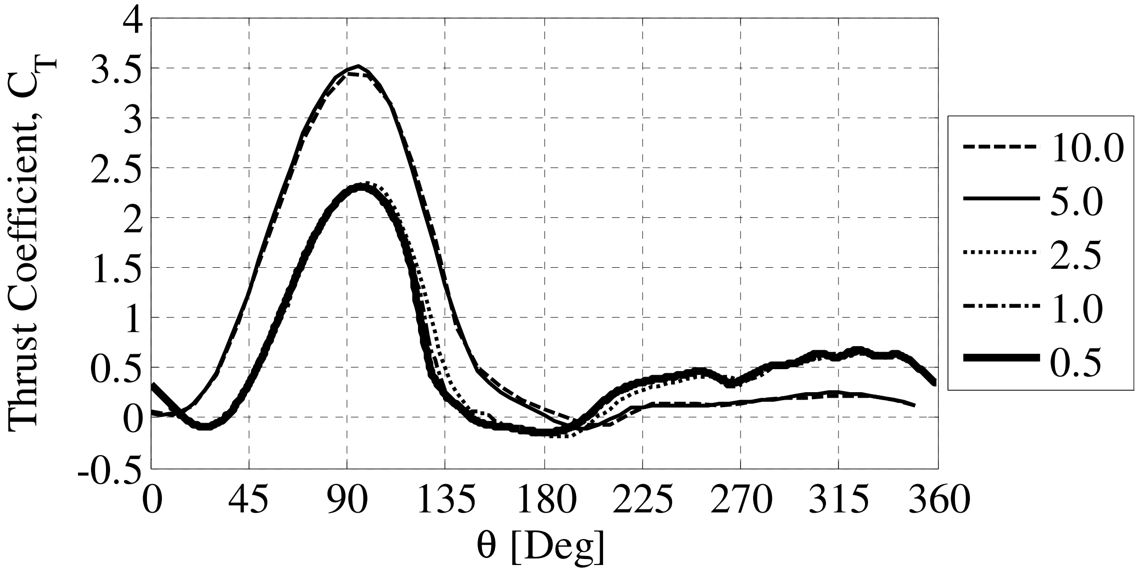

Figure 3.4: Thrust force coefficient as a function of the number of degrees of rotation per timestep (U_∞ = 13.45 m/s, λ = 1.6)

3.2.4. Total Number of Revolutions

The final criteria that needed to be assessed prior to settling on a final numerical model design was the total number of revolutions that needed to be simulated in order to overcome the initial values of the simulation. Figure 3.5 below demonstrates that while the first two rotations display considerable effects of the initial conditions, the third and higher revolutions are rather similar. In fact, the power coefficient and maximum thrust force predicted by the 5th, 6th and 7th revolutions differ by less than 1.5 and 2% respectively. For this reason, all of the data presented herein is obtained from the fifth revolution of the turbine.

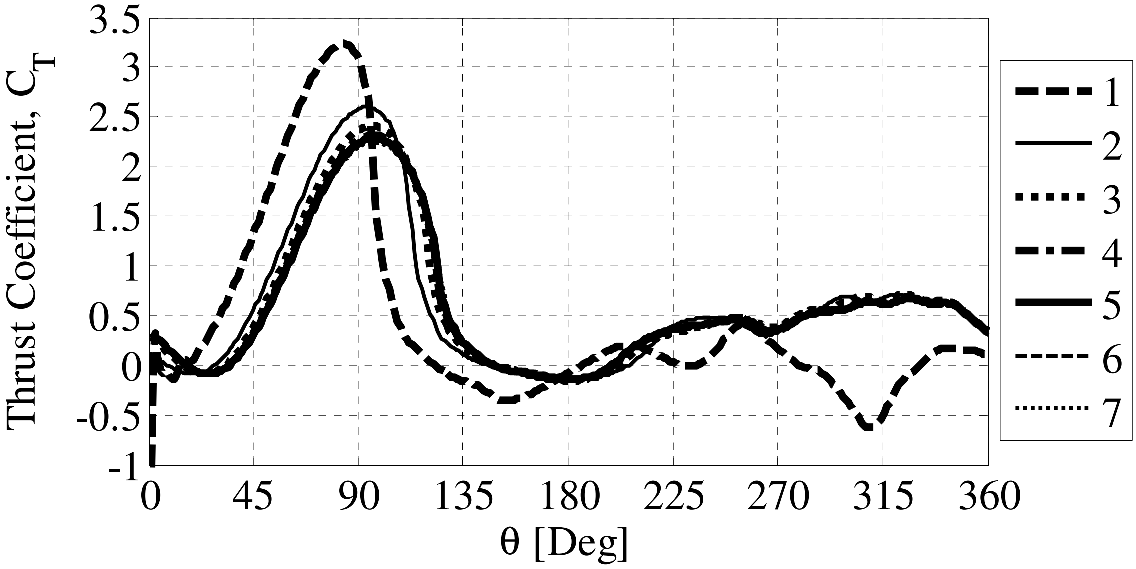

Figure 3.5: Thrust force coefficient as a function of the number of turbine rotations (U_∞ = 13.45 m/s, λ = 1.6)

3.3. Two-Dimensional Numerical Model Results

Once the appropriate domain size, mesh density, time-step size, and total number of required revolutions were determined, a series of preliminary simulations were performed. These tests consisted of simulating the three different blade types, at two different preset pitch angles, over a range of blade speed ratios. A sample of the results from the numerical model simulations is given below. While these simulations are performed for a two-dimensional cross-section of the wind turbine prototype, a series of correction factors will be developed in the Numerical Model Validation and Application chapter (6.2) in order to account for three-dimensional flow effects.

3.3.1. Thrust and Radial Force Coefficients

A small sample of the thrust and radial forces obtained from these simulations is given in Figure 3.6. From these predictions some important loading characteristics can be determined. As anticipated, one of the most important features of the aerodynamic loading is the relative magnitude of the thrust and radial force components. From Figure 3.6 it is predicted that the aerodynamic radial force applied to the airfoil will in general be three to four times greater than the thrust force for all blade speed ratios. In addition to the aerodynamic loading components, a mean radial force component due to centrifugal loading will also be applied. These two factors were given considerable consideration when designing the load measurement system, as the sensitivity to the thrust force component had to be considerably greater than to the radial force component.

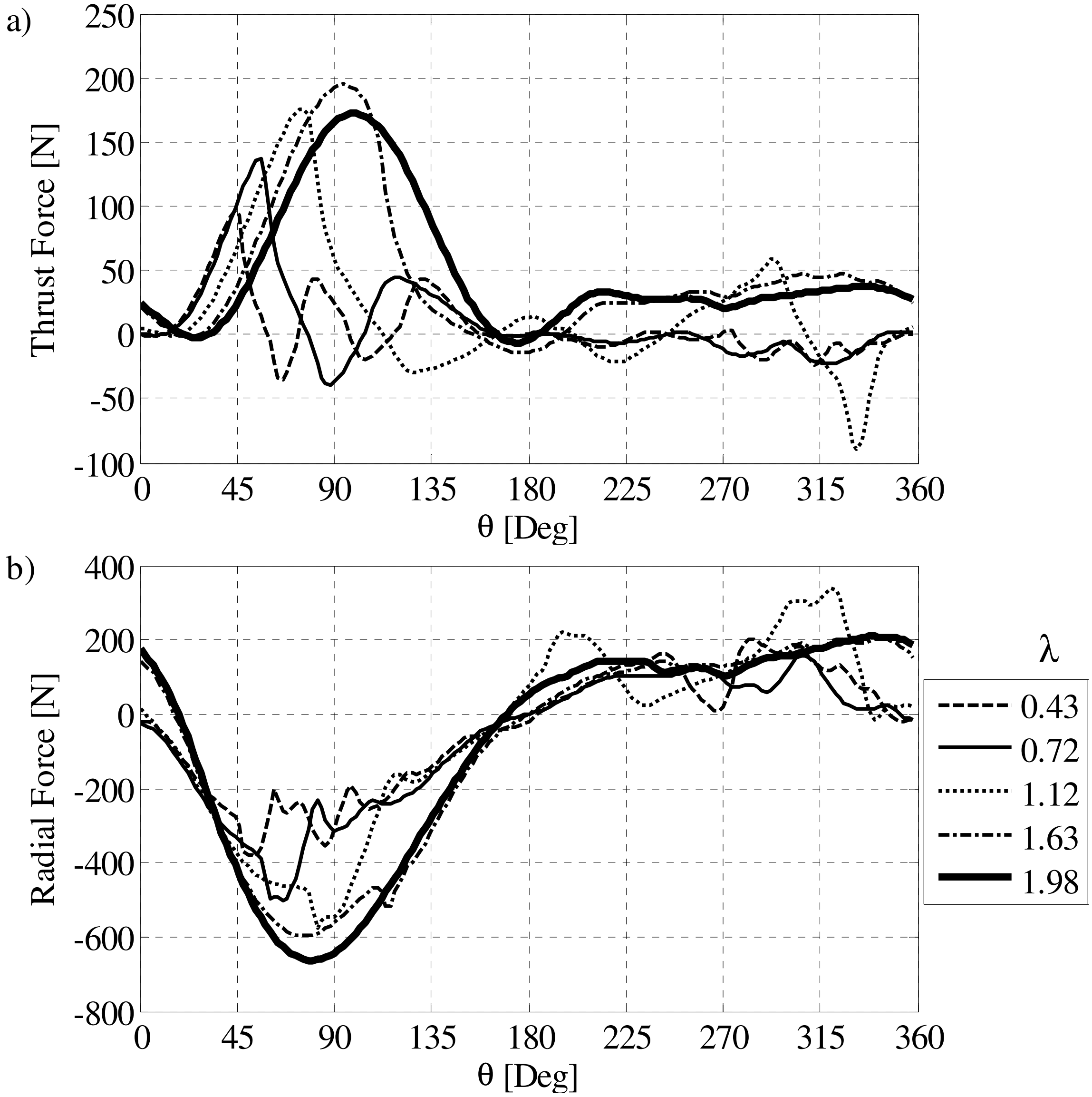

Figure 3.6: Predicted force on a single blade as a function of the angle of turbine rotation for a flow velocity of 10 m/s (NACA 0015, c = 420 mm, β = 0°). (a) thrust force, (b) radial force

Secondly, from the predicted flow velocity field within the turbine, it was determined that, as had been anticipated, the large thrust and radial force peak on the upstream portion of the rotation ($0° \leq \theta \leq 180°$) is generated as the airfoil dynamically stalls. The amplitude of this peak loading feature and the angle of rotation at which it occurs is largely a function of blade speed ratio. To further investigate the effect of blade speed ratio on the dynamic stall behaviour of the airfoil and the resultant fluctuations in thrust and radial loading throughout a full rotation, time series of velocity vectors around one of the three blades will be analysed. Because of the large number of vortex structures formed in the wake of the airfoil, the labelling convention of Fujisawa and Shibuya (2001) has been applied to clearly indicate the order of vortex production (1,2,3) at each location (a – leading edge, b – trailing edge). The angle of rotation at which dynamic stall occurs is defined here as the angle at which the maximum thrust force is obtained.

For the high blade speed ratio of $\lambda = 1.98$, dynamic stall is mainly suppressed and thrust and radial force are applied and removed in a gradual manner. As can be seen in Figure 3.7, the flow remains attached to the surface of the airfoil for the vast majority of the rotation. A small trailing-edge vortex (1-b) is produced as the blade dynamically stalls at $\theta \approx 99°$, but remains confined to a relatively small region within the wake of the blade until it dissipates at $\theta \approx 200°$. Both thrust and radial loading maintain a relatively constant value throughout the remainder of the downstream portion of the rotation, once this vortex has been shed from the surface of the airfoil. The broad power producing peak on the upstream pass and minimal fluctuations in loading on the downstream pass observed in Figure 3.6 can both be attributed to the high rotational velocity of the turbine that suppresses the development of dynamic stall. It is because of the limited extent of dynamic stall that the DMST and other quasi-steady state models have proven to perform well at high blade speed ratios. Despite the appreciable gross power output of the turbine at $\lambda = 1.98$, due to the considerable friction and aerodynamic losses encountered at high rotational velocities, net power output is negligible and this blade speed ratio represents the upper operating capabilities of the turbine prototype.

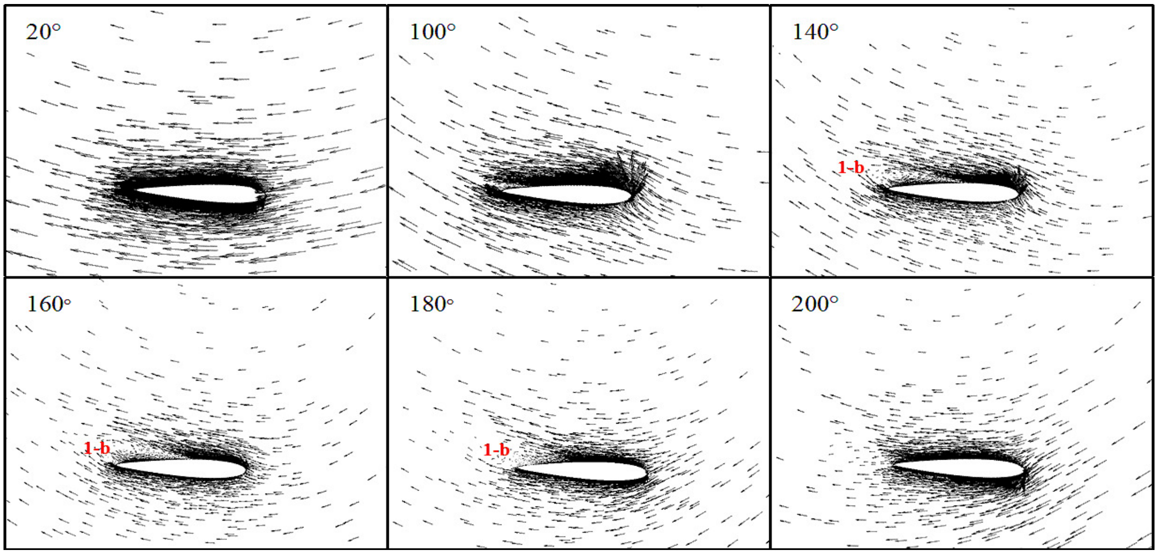

Figure 3.7: Flow over the blade shown with velocity vectors (λ = 1.98, U_∞ = 10 m/s, NACA 0015, c = 420 mm, β = 0°). Dynamic stall is limited to the production of a single relatively small vortex over the range of $\theta \approx$ 99 to 200°

From Figure 3.6a, it can be seen that for the intermediate blade speed ratio of λ = 1.63, dynamic stall occurs at a slightly lower angle of attack. This results in an increase in the maximum thrust force amplitude and a narrowing of the primary dynamic stall peak, while the downstream thrust force output remains relatively unchanged. From the time series of velocity vectors in Figure 3.8, it can be seen that the blade undergoes trailing-edge dynamic stall on its upstream pass (1-b), followed shortly after by leading-edge dynamic stall (1-a). These two positive vorticity structures then merge together to produce a single large vortex that is convected alongside the blade as it travels downstream (θ = 140°). The spike in radial force observed in Figure 3.6b (θ = 115°) signifies the formation of the leading edge vortex (1-a), which also results in a decrease in the rate at which the thrust force is declining. The resultant vortex structure causes extensive flow reversal over the blade, and even negative thrust loading, until the vortex finally departs from the trailing edge at $\theta \approx$ 200°. The flow then reattaches to the surface of the blade for the remainder of the rotation, after which the cycle is repeated. As expected, a blade speed ratio of $\lambda \approx$ 1.6 is unique in that only a single large vortex convects downstream at the same speed as the turbine blade.

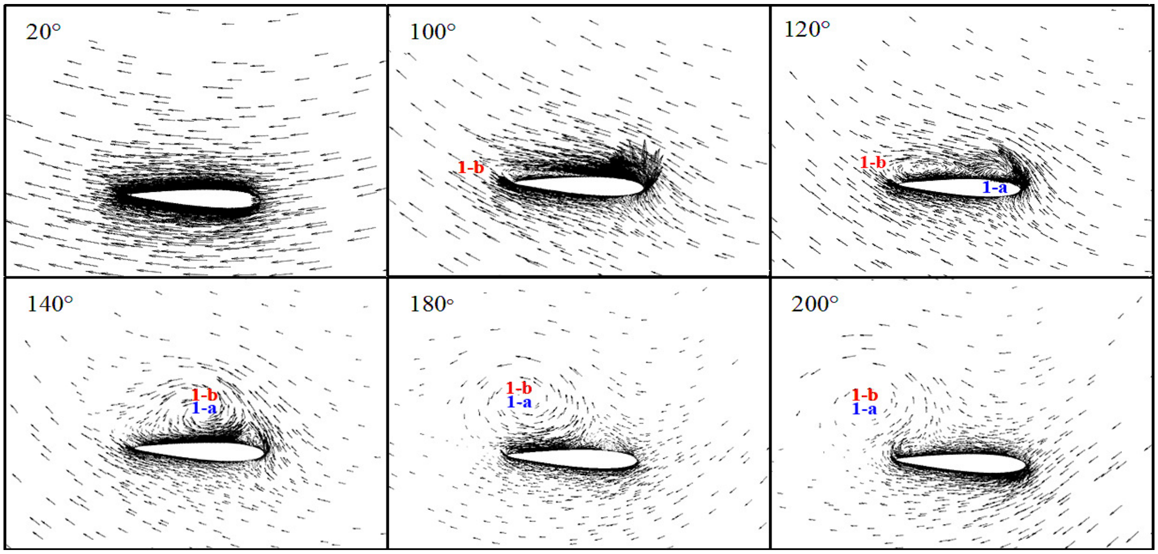

Figure 3.8: Flow over the blade shown with velocity vectors (λ = 1.63, U_∞ = 10 m/s, NACA 0015, c = 420 mm, β = 0°). The large vortex dominating the flow field was formed when the blade dynamically stalled at $\theta \approx 94^o$

Figure 3.9 shows a snapshot image of the pressure field surrounding the turbine as predicted by the two-dimensional numerical model at the optimal power producing blade speed ratio of λ = 1.63. In this figure, the low pressure cores of multiple shed vortices being convected downstream are clearly visible. As was expected, the large vortex structures that are produced on the upstream portion of the blade rotation travel downstream at approximately the same speed as the turbine blades.

In order for large scale flow structures to be generated by dynamic stall and shed into the turbine wake, the turbine must be operating at a low blade speed ratio ($\lambda \leq 1.7$) such that the relative angle of attack, α, is large. However, because the turbine is operating at such a low blade speed ratio, any vortex structures which are produced on the upstream pass will be convected downstream at such a rate that they will generally not interact with any of the other turbine blades. As such, while the presence of the other blades affects the pressure drop and loss in flow momentum through the turbine considerably, vortex structures formed by dynamic stall will have limited interaction with any blade other than the one that they were produced by.

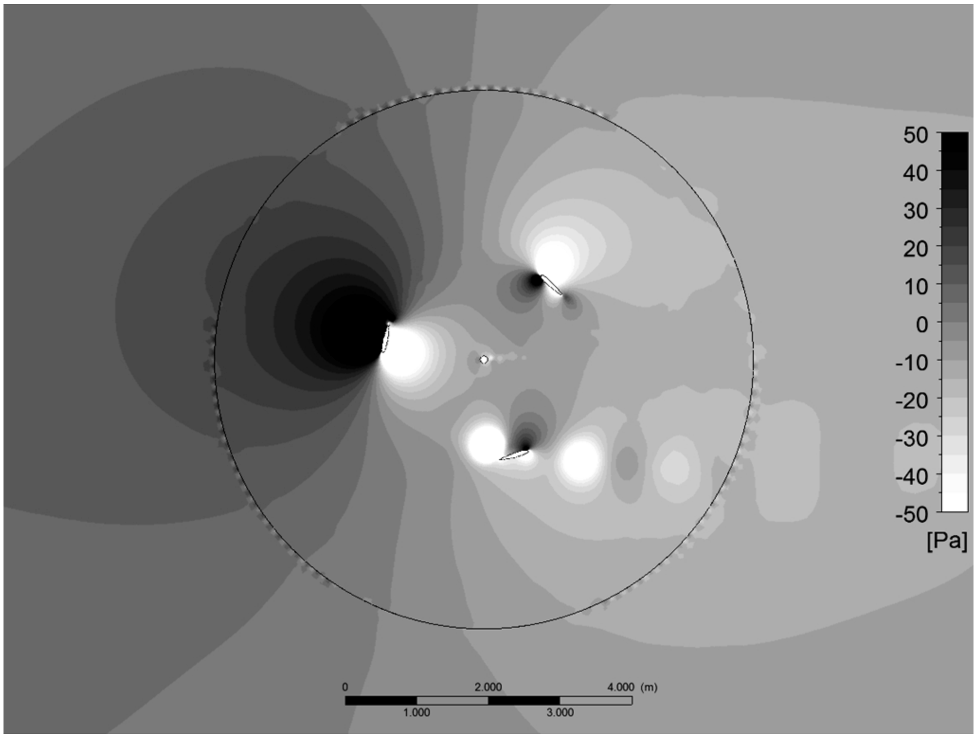

Figure 3.9: Pressure field within the computational domain, blades are located at θ = 80°, 200° and 320° (the large circle denotes the boundary between the rotating and stationary domains) (λ = 1.63, U_∞ = 10 m/s, NACA 0015, c = 420 mm, β = 0°)

Operation at blade speed ratios below the optimum value of λ = 1.6 is expected to occur during starting and stopping or during sudden gusts. Because this small-scale turbine is intended to be installed in the urban environment where the wind flow is particularly unsteady, the loading and flow characteristics at off-peak performance blade speed ratios are an important design consideration. For a blade speed ratio slightly greater than unity (λ = 1.12) the generation and shedding of vortices from the surface of the blade occur at a greater frequency, resulting in high amplitude, sudden, and abrupt changes in both thrust and radial loading (Figure 3.6). The primary dynamic stall peak occurs at an angle of rotation of $\theta \approx 75°$ (1-b). At approximately 90°, leading edge separation occurs, generating a vortex (1-a) which then merges with the initial vortex structure shortly downstream. A second large vortex (2-b) is shed from the trailing edge of the inner surface of the blade at $\theta \approx 120°$. This vortex has much less of an impact on the thrust and radial loading, and convects along with the blade until $\theta = 180°$. At this point, as the blade begins its downstream pass (180º ≤ $\theta \leq$ 360º), the vortex production shifts from the inner (top) to the outer (bottom) surface of the blade (Figure 3.10). Of special note is the large vortex (3-a) that is produced on the downstream pass at $\theta \approx$ 300º, which is then shed from the blade surface at θ = 340º, resulting in the large fluctuation in thrust and radial loading late in the downstream pass (Figure 3.6a).

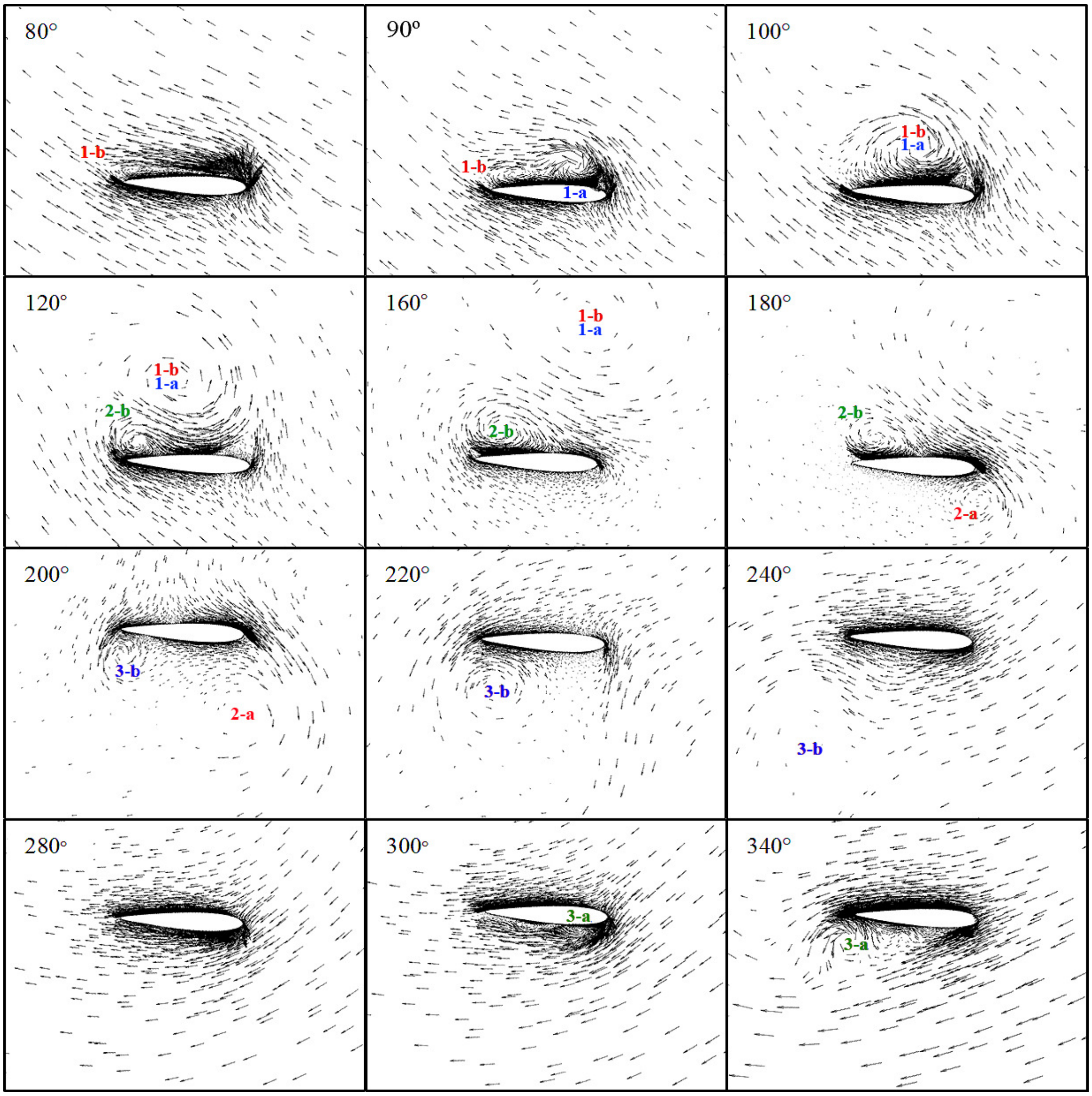

Figure 3.10: Flow over the blade shown with velocity vectors (λ = 1.12, U_∞ = 10 m/s, NACA 0015, c = 420 mm, β = 0°). Dynamic stall is initiated on the inner surface of the blade at θ = 75º on the upstream pass. Flow reattaches to the surface of the blade at $\theta \approx$ 240º, but dynamically stalls again at θ = 300º

For these higher blade speed ratios ($1.12 \leq \lambda \leq 1.98$), the numerical model predictions of the dynamic stall behaviour on the inner surface of the blade show relatively good agreement with the location and duration of flow separation seen in the tuft visualizations performed by Fiedler (2009) on a similar high solidity VAWT.

For $\lambda < 1$, there are numerous low amplitude fluctuations in both thrust and radial loading on the upstream portion of the rotation. The opposite is true on the downstream portion of the rotation, where the thrust load is very low, and relatively constant. This behaviour will result in a large decrease in the gross power production of the turbine. It is expected that this transition in loading behaviour can be directly attributed to the extreme relative angles of attack that the airfoil is subjected to on the upstream portion of the rotation, and the very low relative flow velocity as the blade travels downstream.

At a blade speed ratio of $\lambda = 0.72$ (Figure 3.11), the very slow rotation of the turbine blade relative to the oncoming flow velocity causes the local effective angle of attack on the upstream pass to become very large, very quickly. The blade dynamically stalls on the trailing edge at $\theta \approx 55°$ (1-b), and on the leading edge at $\theta \approx 60°$ (1-a). By an angle of rotation of just 87°, a second large vortex (2-b) has been formed at the trailing edge of the blade and the thrust force obtains a local minimum. Shortly thereafter, the thrust force increases prior to undergoing dynamic stall once more at $\theta \approx 119°$ (2-a). However, in this instance it is leading edge stall that produces the large vortex that convects along with the blade until $\theta = 180°$. As the airfoil begins the downstream pass ($\theta = 180$ to 220º), because of the very low blade speed ratio, the ambient flow velocity is greater than the blade velocity and the flow direction is reversed over the blade. The blade then produces a number of leading-edge and trailing-edge vortices on the outer surface of the blade. Each successive vortex that is shed from the blade surface results in a small undulation in the thrust loading curve. However, because of the very slow relative flow velocity on the downstream portion of the rotation, these vortex structures have very little effect on the aerodynamic loading on the airfoil.

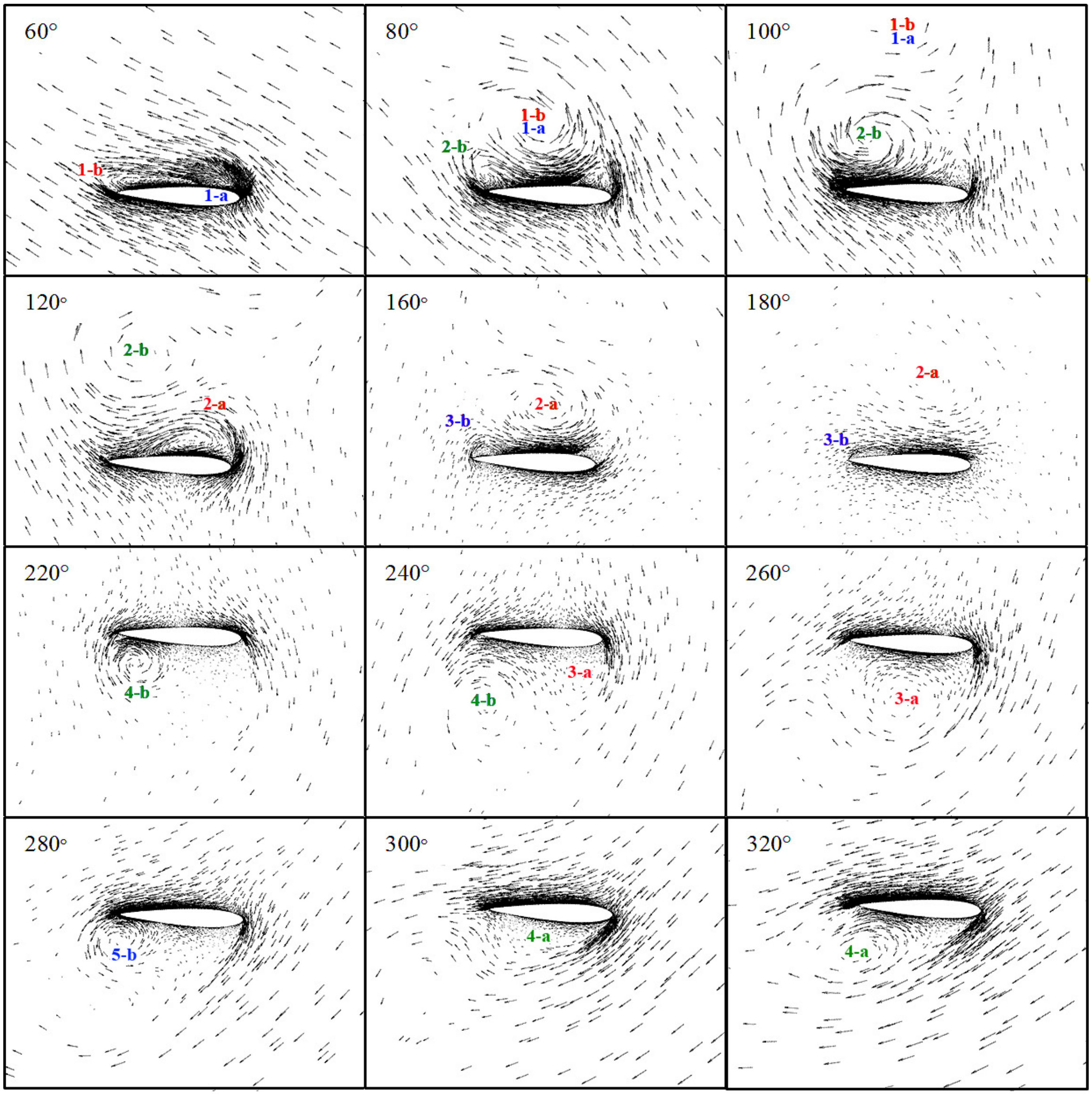

Figure 3.11: Flow over the blade shown with velocity vectors ($\lambda = 0.72$, $U_\infty = 10$ m/s, NACA 0015, $c = 420$ mm, $\beta = 0°$). Dynamic stall is initiated on the inner surface of the blade at $\theta \approx 60^o$ on the upstream pass, and on the outer surface of the blade at $\theta \approx 200^o$ on the downstream pass

For the very small blade speed ratio of $\lambda = 0.43$, because of the extremely slow rotation of the turbine blade relative to the oncoming flow velocity, the blade dynamically stalls only 45° into the rotation (1-b). After another 5°, a leading edge vortex forms (1-a) and merges with the trailing edge vortex, and as before this results in a spike in radial loading. The second vortex formed from the trailing edge of the blade (2-b) increases the thrust force until an angle of rotation of 81°, at which point the vortex formed on the leading edge of the blade (2-a) causes thrust force to drop once again. A third trailing edge vortex (3-b) causes the thrust force to rise until θ = 131°, when a leading edge vortex (3-a) reduces thrust force for a final time. At an angle of rotation of θ = 190° flow over the blade is observed to be entirely reversed due to the extremely low blade speed ratio (Figure 3.12). Much like a blade speed ratio of λ = 0.72, after this point in the rotation a number of smaller vortices are shed from the outer surface of the airfoil and the thrust force maintains a relatively constant value. A blade speed ratio of λ = 0.43 represents the lower bound of the operating capabilities of the turbine, due to the very low mean thrust loading component, and extremely low net power production.

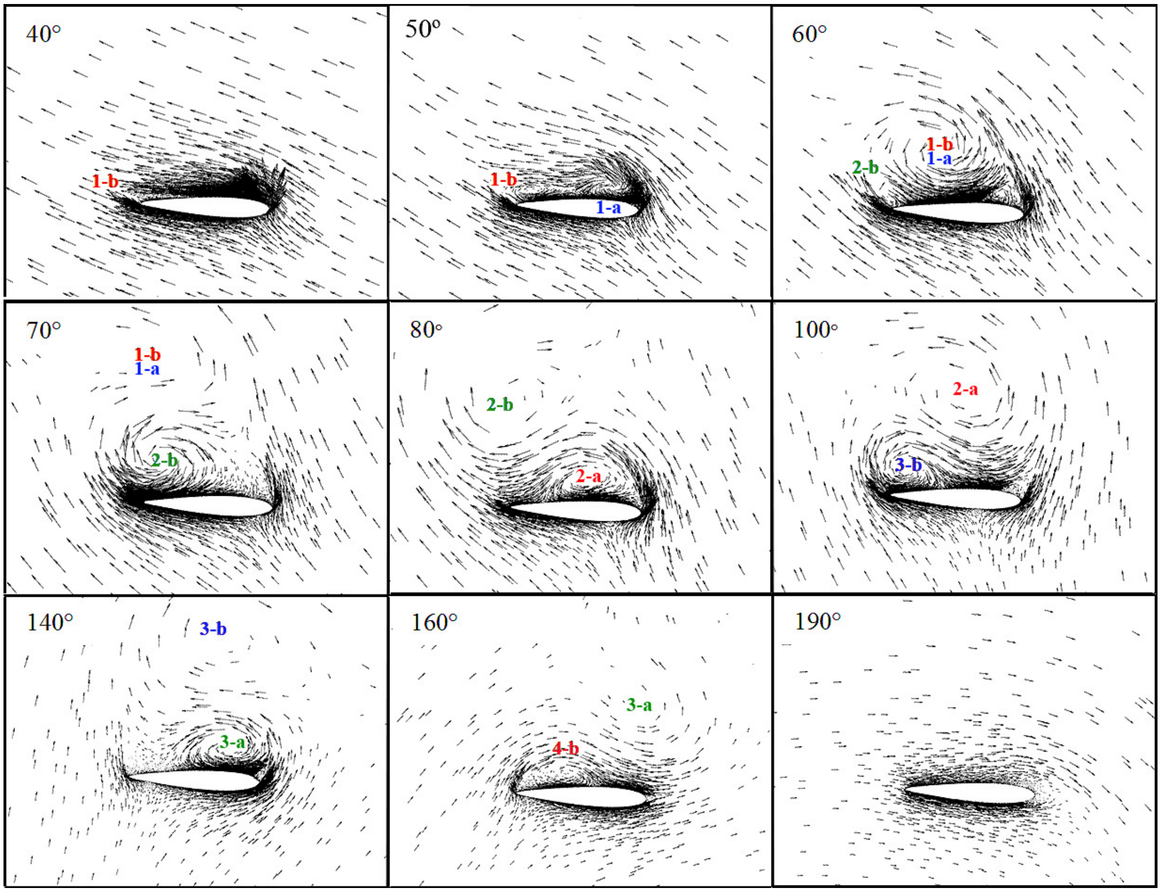

Figure 3.12: Flow over the blade shown with velocity vectors (λ = 0.43, U_∞ = 10 m/s, NACA 0015, c = 420 mm, β = 0°). Dynamic stall is initiated seven times on the upstream portion of the rotation on the inner surface of the blade

For all three low blade speed ratio cases (λ = 1.12, 0.72, and 0.43), the first large vortex structure is formed by the merging of vortices 1-b and 1-a, and rotates counter clockwise, causing significant flow separation. The second is produced at the trailing edge (2-b) and rotates in a clockwise direction, resulting in flow reattachment. The distinguishing feature between these three cases is the duration of the rotation over which these two structures last. For λ = 1.12, these two vortices persist over the full upstream portion of the rotation. For λ = 0.72, the two vortices only last until an angle of rotation of θ = 120°. Finally, for λ = 0.43, these two vortices have already dissipated by just 80° of rotation. In all three cases, these two vortex structures cause first a dramatic decrease, followed by a slight increase, in thrust force. Thus, the mechanism for the first two peaks in thrust loading for these three cases is the same; it simply persists for different durations due to the change in the relative ambient flow velocity. This has a direct impact on the thrust force magnitude of the dynamic stall peaks, and thus the turbine power output. This separation and then reattachment of flow on the inner surface of the airfoil on the upstream pass at low blade speed ratios ($0.7 \leq \lambda \leq 0.9$) was observed by Armstrong, Fiedler, and Tullis (2011) in a series of tuft visualizations performed on a similar high solidity VAWT (σ = 0.41).

3.3.2. Vibration Excitation Loads

The thrust and radial forces on the individual blades are given in terms of a rotating coordinate system. These forces can also be presented in terms of the stationary coordinate system of the turbine itself. By performing a vector summation of the loading from each blade, the total aerodynamic load being applied to the turbine in the streamwise and cross-stream directions as a function of the angle of rotation can then be obtained. Figure 3.13 plots the streamwise and cross-stream force on the entire turbine for the cases shown above. Some important characteristics of the nature of the net turbine loading can be determined from these numerical predictions. First, it is anticipated that, independent of the blade speed ratio, the net load on the turbine will be applied at a rate of three cycles per revolution or the "blade pass frequency". Second, the streamwise and cross-stream loading are typically out of phase by 30 to 40 degrees of rotation, indicating that the turbine will be highly susceptible to excitation of the primary whirl mode. Finally, for low blade speed ratios, the load application and removal is sudden and abrupt, while for high blade speed ratios the load application is nearly sinusoidal, and of greater amplitude.

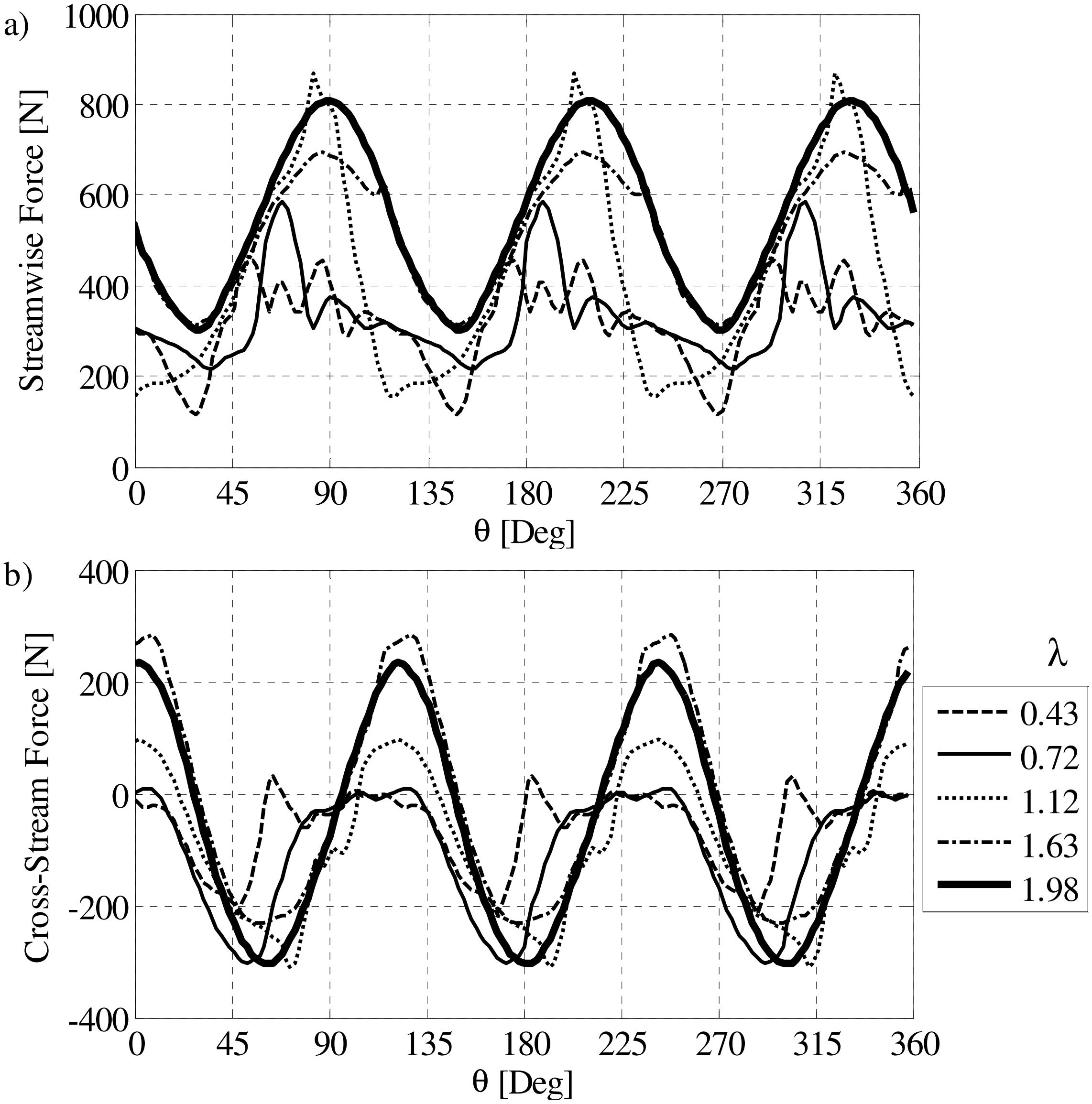

Figure 3.13: Predicted force on the turbine as a function of the angle of turbine rotation for a flow velocity of 10 m/s (NACA 0015, c = 420 mm, β = 0°). (a) streamwise force, (b) cross-stream force

The streamwise and cross-stream loading components can also be plotted against one another to further demonstrate the potential for excitation of the primary whirl mode of the turbine. From Figure 3.14 it can be seen that at high blade speed ratios the net turbine loading is applied in an almost circular pattern at a rate of three cycles per revolution. For lower blade speed ratios this orbital pattern is more erratic, but still applied in a nearly circular pattern. A blade speed ratio of λ = 1.12 is the exception, in that because of the sharp variations in thrust and radial loading due to abrupt dynamic stall on both the upstream and downstream portions of the rotation, the orbital pattern is oblong, with considerably greater excitation loading in the streamwise direction as compared to the cross-stream direction.

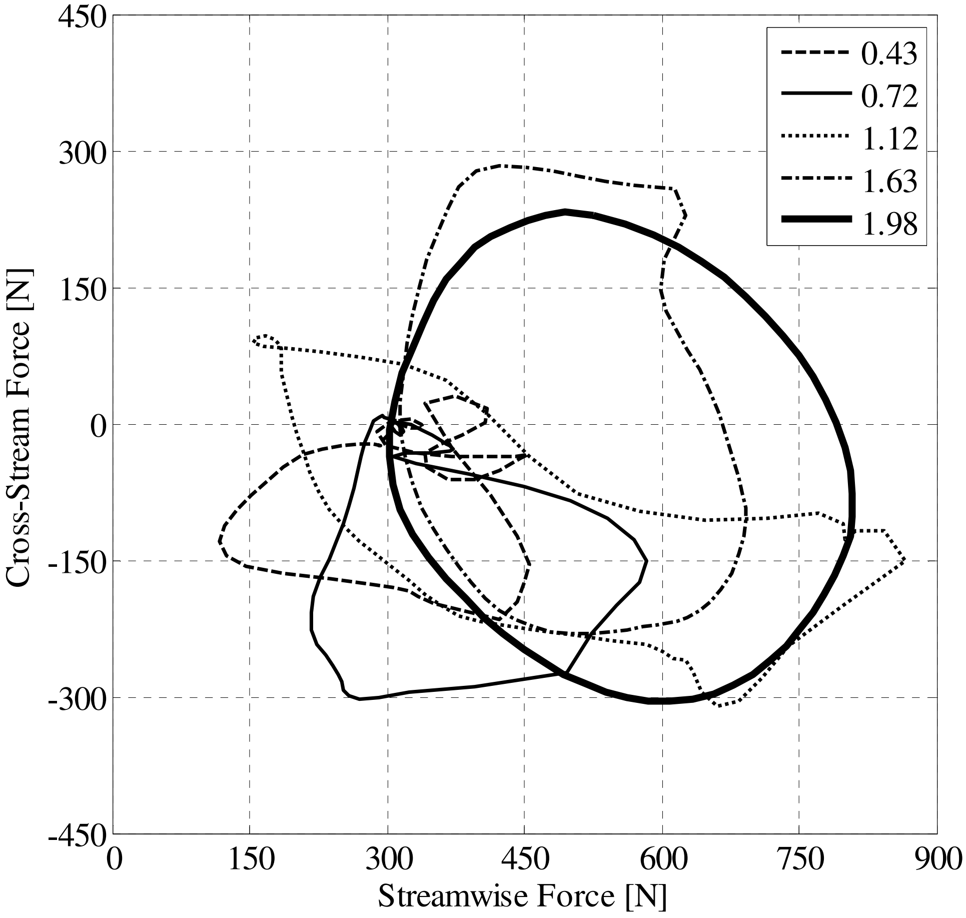

Figure 3.14: Predicted vibration excitation loading on the turbine for a flow velocity of 10 m/s (NACA 0015, c = 420 mm, β = 0°)

3.3.3. Power Coefficient

While the core motivation for this research is to investigate the vibration excitation and response mechanisms of high solidity VAWTs, the power output of the turbine is an equally important consideration. By calculating the product of the rotational velocity, turbine radius, and the average thrust force on the turbine blades over a full rotation, the power output of the turbine, P_T, can be determined. Normalizing the turbine power output by the power available in the oncoming flow, P_W, provides a measure of the efficiency of the turbine, referred to as the turbine's power coefficient, C_P.

$$P_T = \omega RN \frac{1}{360} \int_0^{360} F_T \, d\theta \qquad 3.1$$

$$P_W = \frac{1}{2} \rho U_\infty^3 2RH \qquad 3.2$$

$$C_P = P_T / P_W \qquad 3.3$$

A plot of the power coefficient of the turbine as a function of blade speed ratio is given in Figure 3.15. As suspected, operation of the turbine at $\lambda < 1$ produces very little power output. However, once the blade speed ratio advances beyond this threshold, power production increases rapidly. This can primarily be attributed to the significant increase in the duration of the dynamic stall peak on the upstream portion of the rotation. Additionally, power production on the downstream portion of the rotation has also undergone a noticeable increase due to an overall increase in thrust loading. The maximum power output plateau at a blade speed ratio of $\lambda = 2.1$ is also visible. Beyond this blade speed ratio the amplitude of the primary dynamic stall peak continues to decline, and turbine power output begins to decrease.

As compared to the gross power coefficients calculated from measurements of turbine shaft torque, obtained by means of the method of Fiedler (2009) and Armstrong (2011), it is clear that not only does the numerical model significantly over-predict the maximum turbine power output, but also the blade speed ratio at which it occurs. It is believed that this is due in part to flow diverging above and below the turbine prototype, such that the two-dimensional numerical model is subjected to an effectively higher flow velocity. Additional sources of discrepancy include losses generated by interference drag, and the formation of blade-tip vortices. While the power coefficient predictions are quite high, they still fall well below the theoretical limit for two disks in tandem of Cp = 0.640, as determined by Newman (1983). Note that this theoretical limit is calculated in the same manner as Betz's (1920) classical single-disk limit for horizontal axis wind turbines of Cp = 0.593.

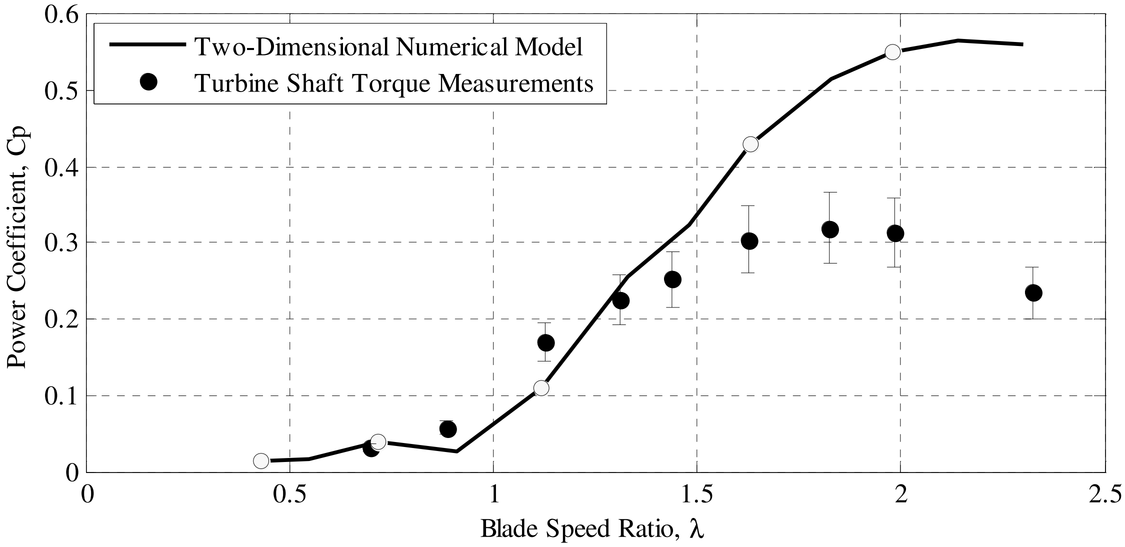

Figure 3.15: Turbine gross power coefficients. Open circles correspond to the conditions at which the above velocity vector predictions were obtained (NACA 0015, c = 420 mm, β = 0°)

This sample data-set represents a small cross-section of the numerous simulation results obtained from the preliminary investigation. As such, the above analysis is intended to provide an overview of the general loading and flow behaviour characteristics. It is important to note that the load measurement system employed in the experimental study was developed based upon the loading trends and amplitudes determined from the preliminary numerical model predictions.

3.4. Summary

Initial development of a two-dimensional URANS model of a high solidity VAWT was carried out through the use of steady-state mesh density and turbulence model validation tests (Appendix A.1). Based upon the literature reviewed and these simulation results it was determined that the SST model of Menter (1994) was the most appropriate turbulence model available. The numerical model was then expanded to incorporate all three turbine blades rotating about a central support shaft. Domain size independence tests had to be performed in order to ensure that the boundary conditions used in this model did not affect the simulation results. Due to the transient nature of these simulations, time-step independence tests had to be performed as well as analysis of the number of rotations required to overcome initial conditions within the flow domain.

From these simulations, the thrust and radial forces on the individual blades were determined. Unfortunately, no experimental force coefficient data currently exists within the literature to validate these results against. The experimental data that is available is for much lower solidity turbine designs, which operate at much higher blade speed ratios. Additionally, the data that does exist is often criticized due to difficulties in obtaining reliable/repeatable measurements (Allet, Halle, & Paraschivoiu, 1999). However, these simulation results did provide valuable insights into the effect of dynamic stall and blade/vortex interaction on turbine wake behaviour, vibration excitation, and power output. Fortunately, considerable power coefficient measurements have been obtained for high solidity VAWTs, such that validation of the turbine power output predictions could be performed. Ultimately, it was concluded that considerable over-prediction of the turbine power output occurred due to the two-dimensional nature of the numerical model.

In order to validate the aerodynamic force predictions, an experimental test program is developed and addressed in the next chapter. The objective of this experimental investigation is to measure the aerodynamic loads applied to the blades, and better understand the effects of dynamic stall and the impact of three-dimensional flow effects on the numerical model predictions.

CHAPTER 4

EXPERIMENTAL TEST FACILITY AND INSTRUMENTATION

This chapter details the experimental set-up employed in the present study. The contents of this chapter consist of a description of the facility used to perform the experimental tests, the VAWT prototype design specifications, and particulars on the instrumentation necessary to acquire the experimental data. This equipment consists of many off-the-shelf instruments, such as the anemometers (wind speed), accelerometers (vibration response), and wireless telemetry system (remote data capture). However, a number of additional components had to be designed in order to perform this particular study. These include; a control system for maintaining the turbine rotational velocity, a guy wire support system for stiffening the turbine and minimizing vibration response, a complex force measurement system, and an angular position detection instrument. Also included in this chapter is a thorough description of the practices and procedures followed for the equipment preparation, calibration, preliminary tests, and data acquisition.

4.1. Wind Tunnel

The open loop wind tunnel employed to perform the current study is located at the University of Waterloo Fire Research Facility in Ontario, Canada. The wind tunnel consists of a 19.5 metre long test enclosure 15.4 metres wide by 7.6 metres high with a gable roof 12.8 metres high at its peak (Figure 4.1).

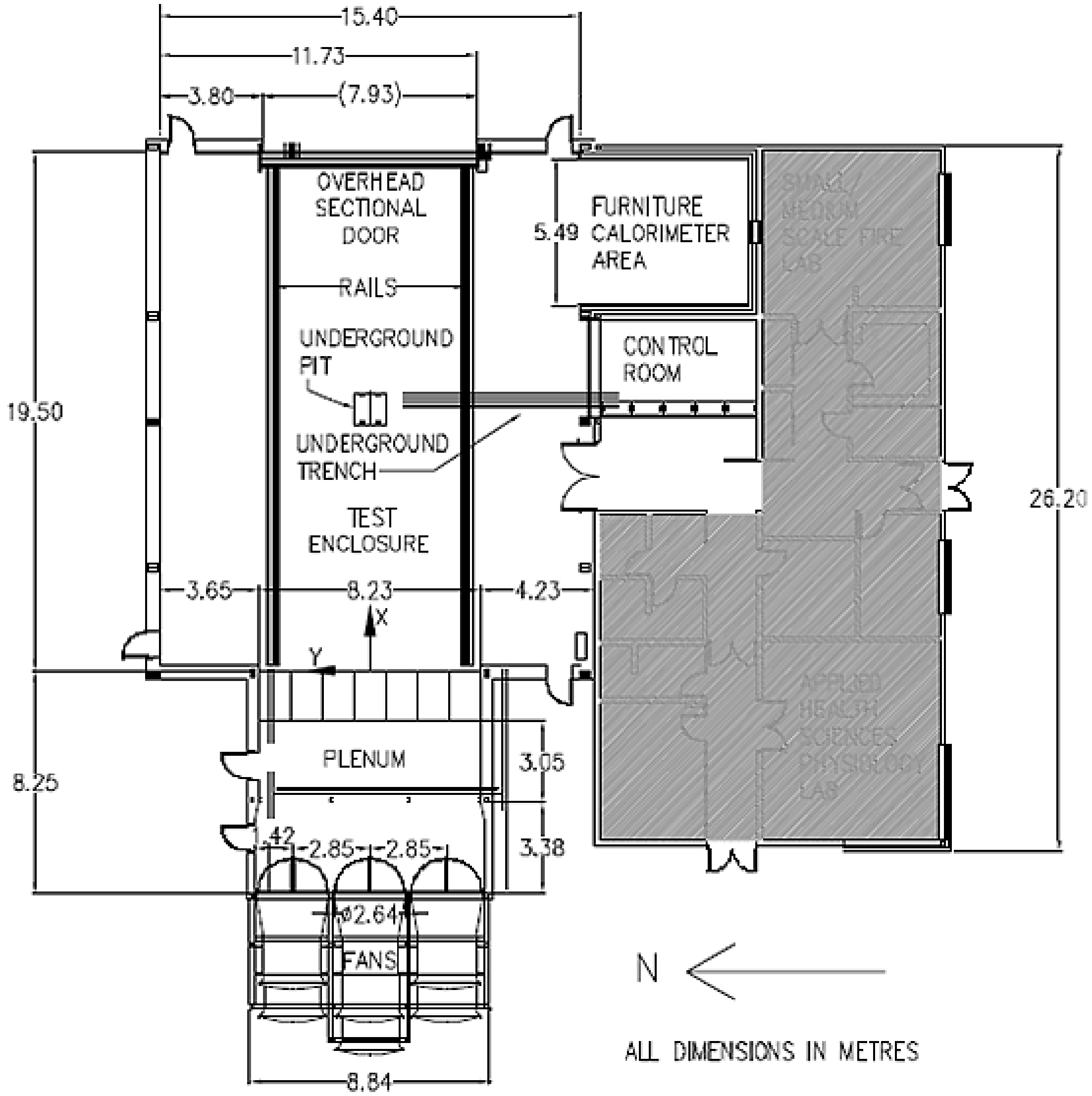

Figure 4.1: University of Waterloo Live Fire Research Facility floor plan, adapted from (Weisinger, 2004)

An array of six 75 kW vane axial fans arranged in 2 rows, 3 wide, drives the flow in the test section at velocities of upwards of 12 m/s. Flow rate through the test section is controlled by adjusting the fan speed with a variable speed controller. Flow from the bank of 6 fans initially charges an 8.2 metre long by 8.5 metre wide by 5.9 meter high plenum. Flow in the plenum is conditioned through a pair of flow settling screens located 3.6 metres from the fan outlets as well as an array of flow straightening ducts at the plenum exit (Figure 4.2).

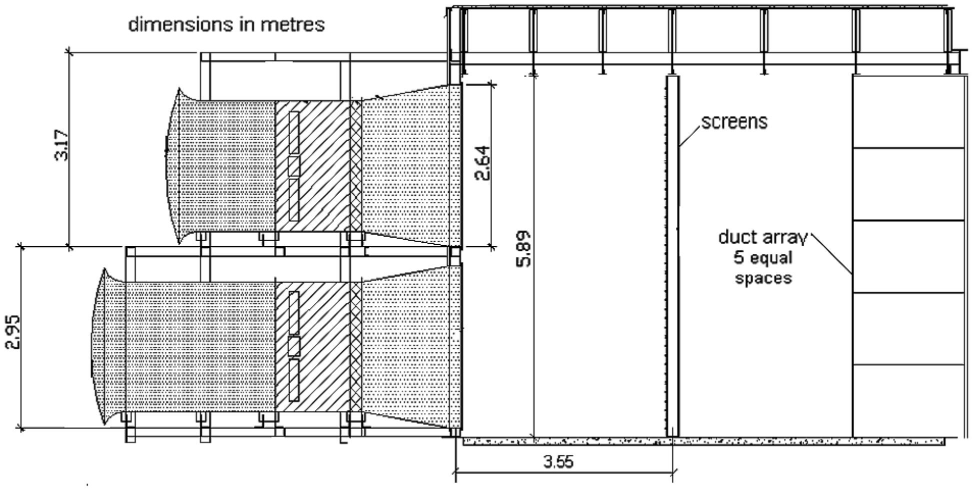

Figure 4.2: Wind generation system cross-sectional view. Flow conditioning screens are 3.55 metres from the fan outlets while flow straightening ducts are located at the plenum exit, adapted from (Weisinger, 2004)

For all test cases the turbine prototype was situated 8 metres downstream from the plenum exit where flow measurement calibration studies indicate a relatively uniform flow field with a core region 6.8 metres wide by 5.0 metres high (Devaud, Weisinger, Johnson, & Weckman, 2009). Because of the large expansion ratio in cross-sectional area of the test section to that of the plenum exit (3:1), considerable flow divergence around the wind turbine was expected. This behaviour is representative of the conditions typically present in unducted atmospheric flows that the turbine will be subjected to during field operation. Finally, flow exits the wind tunnel through a 7.9 metre high by 7.9 metre wide opening in the far wall of the wind tunnel facility. Further details of the wind tunnel and its operating conditions can be found in Weisinger (2004).

4.2. Wind Turbine Prototype

4.2.1. Turbine Design

The wind turbine prototype under investigation is a 3 bladed H-type vertical axis wind turbine (refer to Figure 1.1). The turbine consists of 3 straight blades made from two internally reinforced fibreglass shells. The blades are each 3 metres in length and are capped with small endplates that extend approx 2 cm beyond the airfoil profile. The turbine blades are fixed to the turbine structure at two locations along the span of the blades 0.68 metres from each end. At these mounting points steel inserts are enclosed within the blades to provide a surface to mate to the support struts and distribute the substantial radial loads encountered during operation. Extending out of the surface of the blades at each mounting location are four internally threaded steel sleeves which allow the blades to be mounted normal to the support struts with four corresponding bolts. Three different symmetric blade cross-sectional geometries were investigated in the present study in order to determine the effects of blade thickness, chord length, and trailing edge geometry (Figure 4.3).

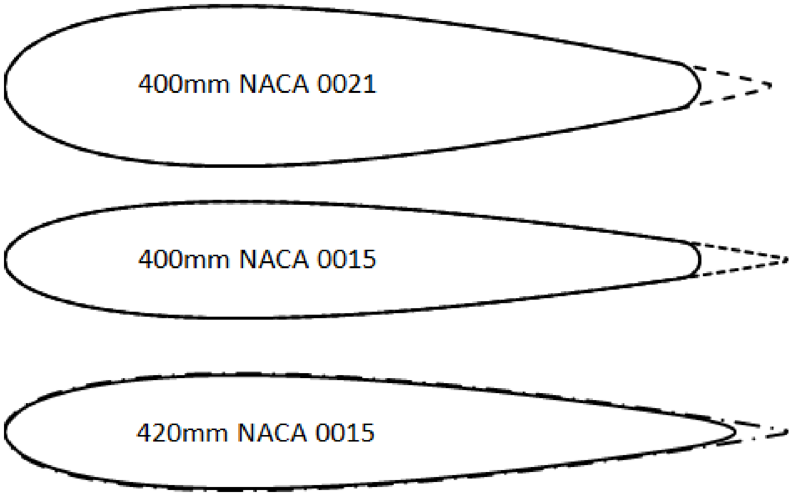

Figure 4.3: Symmetric blade profiles shown to scale

As shown in Figure 4.3, the three blade profiles are; a 440mm NACA 0021 airfoil rounded at the trailing edge to a final chord length of 400mm, a 450mm NACA 0015 airfoil rounded at the trailing edge to a final chord length of 400mm, and a 450mm NACA 0015 airfoil rounded at the trailing edge to a final chord length of 420mm. The rounding of the trailing edge was performed primarily to increase the strength of the bond securing the two halves of the fibreglass shells at this location. The inner surfaces of the blades were reinforced at both the leading and trailing edges for additional strength.

The steel mounting inserts located within the blades are offset from the leading edge by a = 155mm for the 400mm chord length blades, and a = 150mm for the 420mm chord length blades. As investigated by Fiedler and Tullis (2009), the offset in the mounting location from the mid-chord of the blade, δ, results in an effective preset pitch angle of the blade, β_{Eff} (Figure 4.4).

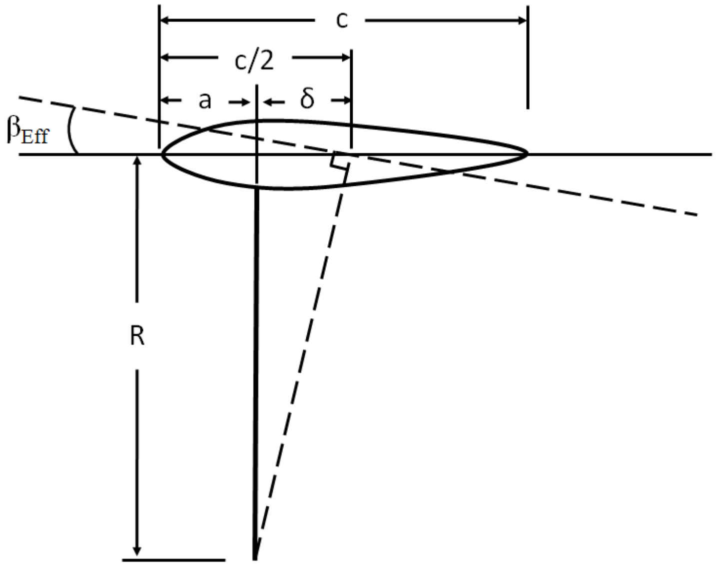

Figure 4.4: Effective preset pitch angle of the blade, β_{Eff}, as a result of an offset in the mounting location from the mid-chord of the blade, δ (offset and chord length have been exaggerated for emphasis).

Because the blades are mounted forward of the mid-chord location, an effective toe-in pitch angle ($+\beta_{Eff}$) exists for all blade designs tested. This is equivalent to mounting the blades at the mid-chord location with a toe-in pitch of $\beta = 2.25°$ for the 400 mm chord length blades, and β = 2.66° for the 420 mm chord length blades. In order to compensate for this effect, small steel shims were inserted between the leading edge mounting locations and the ends of the support struts. In addition to the effective toe-in cases, this modification allowed for tests equivalent to the blades mounted at the mid-chord position normal to the support struts (β = 0°) to be performed. For the remainder of this thesis, the preset pitch angle will be quoted for an equivalent mid-chord mount location.

Each of the blades is attached to two aluminum struts with a NACA 0030 cross-sectional geometry in order to minimize drag while providing ample horizontal bending stiffness. The aluminum struts are internally supported by two vertical cross members in order to provide additional vertical stiffness to support the weight of the blades (Figure 4.5). The importance of the strut cross-sectional geometry will be made apparent in the Strain Gauge Instrumentation section of this chapter (4.5.1).

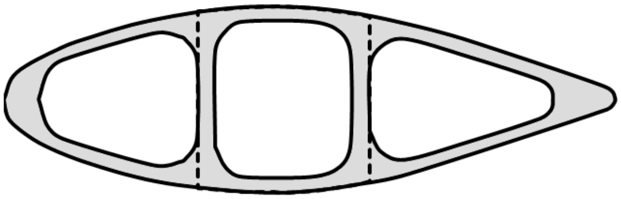

Figure 4.5: Support strut cross-sectional geometry, dotted lines indicate the core region of the strut

The 1.25 metre long support struts are in turn bolted to the turbine support shaft such that the blade mounting surface is a total of 1.35 metres from the axis of rotation. The support shaft consists of an inner stationary shaft and an outer 4” (102mm) diameter rotating shaft. The outer shaft is supported by three roller bearings; one at the top of the shaft, one at the bottom of the shaft, and another at the bottom of the generator, on top of which the turbine is mounted. In turn, the generator is mounted on a steel frame consisting of a short pipe segment directly below the generator base, mounted atop a square-tubing skid. Because the skid was designed to allow access for a pallet jack in order to move the turbine, it is somewhat wider in the cross-stream direction than in the streamwise direction (1 metre by 0.5 metres). This asymmetry in the base support results in complex phenomenon discussed further in the Natural Frequency Characterization section (5.1.1). Overall, the combined height of the generator and base support position the bottom strut mount-point at 1.25 metres from ground level. This means that during operation, the bottom of the turbine blades are approximately 0.6 meters above the floor.

4.2.2. Control System

While the ultimate purpose of the VAWT is to generate electrical energy, for the present study the full capabilities of the generator are not utilized. The generator is wired only to an emergency shutdown switch that, when engaged, short circuits the generator wiring, resulting in an induced magnetic field that serves to slow the turbine. In place of the control system developed for use with the generator, a custom mechanical control system is implemented. This system incorporates a proximity sensor mounted to the base of the turbine to determine its rotational frequency, and a servo-controlled mechanical variable load (Bravo et al., 2007). The mechanical variable load consists of a disc brake calliper driven by an electro-hydraulic servo-actuator installed on a linear bearing abutting a load cell. From the load cell a measure of the torque produced by the turbine and transmitted through the brake can then be acquired (Bravo et al., 2007).

The wind turbine rotational speed was monitored and controlled through the use of an active closed-loop speed control system. This allowed the rotational velocity of the turbine to be maintained within ±2% over the entire operational range. Additionally, a closed-loop controller allows for data to be acquired on the portion of the torque vs. rotational velocity curve where the torque increases with turbine rotational velocity, and the system is not self regulating. In contrast, the constant or slow varying load provided by an open loop controller would result in either runaway of the turbine to high RPM or stoppage of the turbine. The primary reason for using this rather simple control system however, is to ensure that there are no electrical losses that are not accounted for when calculating the gross power output of the turbine.

4.2.3. Guy Wire System

While not required under normal operating conditions, an extension to the stationary inner shaft of the turbine was manufactured in order to allow for the use of a guy wire support system. This guy wire system was implemented in order to raise the turbine natural frequencies and minimize the likelihood of resonant vibration of the turbine at typical operating rotational velocities. Mounted to the top of the 1.3 meter long 51 mm diameter inner shaft extension is a large eyebolt and a collection of high strength shackles to which the support guy wires were attached. The six guy wires were 3/8" (9.5 mm) steel cables, fixed to the wind tunnel support structure at evenly spaced intervals of approximately 60°. Two cables extended upstream and were attached on either side of the plenum exit; two cables were attached at nearly cross-stream locations on the wind tunnel walls; and two cables extended downstream and were attached on either side of the wind tunnel outlet. Each cable could be independently tensioned to a maximum of 14,000 lbs (66.7 kN) through the use of turnbuckles mounted to the wind tunnel walls. In order to ensure that the turbine remained vertically aligned when cable tension was applied (for proper alignment of the inner and outer shafts), two lasers were focused on the apex of the turbine, one facing upstream, the other cross-stream. Careful monitoring of the cable tension and compensation for the laser position while tensioning, ensured that the top of the turbine did not deflect by more than the diameter of the laser dots, equivalent to approximately ¼" (6 mm).

4.3. Velocity Measurement Instruments

For this study, wind speed was measured through the use of both a sonic and a propeller type anemometer. The propeller type wind monitor was mounted at mid height of the turbine and was primarily used to record the mean wind tunnel flow velocity. The propeller type anemometer (Campbell Scientific Model 05305-L) has a flow velocity range of 0 to 50 m/s, an accuracy of ±0.2 m/s or 1% of the reading, and a starting threshold of 0.4 m/s. This anemometer was located upstream of the turbine approximately midway between the plenum exit and the upstream surface of the turbine. Special care was taken to ensure that the anemometer was not positioned in the wake of the flow straightening vanes. Due to its ability to simultaneously record all three flow velocity components (u_x, u_y, u_z), the 3-D sonic anemometer was used to map the turbine wake velocity at multiple heights both upstream and downstream of the turbine. The sonic anemometer (Campbell Scientific Model CSAT3) has a flow velocity range of ±30, ±60, and ± 8 m/s for each of the velocity components respectively. The accuracy of the measurements is dependent on the angle to the horizontal at which the flow enters the device. However, for the majority of the measurements this angle was relatively small ($< 5°$) and the measurements were accurate to within ±2%.

4.4. Vibration Measurement Instruments

In order to measure the vibration response of the turbine in the streamwise and cross-stream directions, two Kistler piezoelectric accelerometers were mounted to flat surfaces machined into the stationary support shaft extending out the top of the turbine. Mounting the accelerometers at approximately ¾ of the turbine height was mainly a function of the limited exposure of the stationary inner shaft. However, it was determined that this location was ideal as it was a position of large deflection and acceleration both with and without the cable system attached. With the cable system attached the primary bending mode of the turbine has a fixed-pinned condition (maximum deflection near mid-height), while without it is a fixed-free condition (maximum deflection at full-height). Hence, the ¾ height location was a compromise that allowed the accelerometers to be mounted to the stationary surface, while still being at a location of appreciable acceleration under both end conditions. The sensitivity of each sensor was certified to within 0.2% for frequencies up to 7 kHz. The magnetic bases used to mount the accelerometers added considerable mass to the accelerometer assemblies and lowered the upper frequency limit to approximately 3 kHz, which is still well above the expected vibration response range. Standard cable tension release techniques were observed in order to prevent any cable motion from affecting the accelerometer outputs.

4.5. Force Measurement System

4.5.1. Strain Gauge Instrumentation

In order to understand the underlying physics of the flow through a high solidity VAWT, a method to measure the aerodynamic loading on the turbine blades had to be developed. Previous studies (Akins et al., 1983; Oler et al., 1983) used either pressure taps mounted within the blade surface, or strain gauges mounted to structural members of the turbine. Based upon the critiques of the previous work, it was determined that due to the errors associated with interpolating and integrating the pressure measurements, as well as the difficulty in obtaining the measurements themselves, that strain gauges were the more appropriate method.

In order to mount the strain gauges to the turbine structure, three ports (Figure 4.6) were machined into each of the two struts supporting a single blade. This exposed the interior square-tube geometry of the struts, which forms an ideal, nearly symmetric, cross-section (refer to Figure 4.5). As can be seen from Figure 4.6, the ports were designed such that while the entire load supported by the strut was transferred through the square-tube cross-section, in the event that excessive bending of the struts occurred, small tabs located at the leading and trailing edges of the strut would support a portion of the load. While this design approach was taken to ensure that catastrophic failure of the turbine did not occur during testing, it also allowed for a thin aluminum tape cover to be placed over the ports. This provided the strain gauge sensors with some protection from airborne debris and maintained the streamlined profile of the support strut.

The strain gauges were cemented to the surface of the inner square-tube on the leading and trailing faces, as indicated by the highlighted region in Figure 4.6. Two strain gauges were mounted atop one another on either side of the square-tube cross-section. One of the gauges in each pair was orientated vertically, while the other was orientated horizontally. The strain gauges used in this study were 350Ω foil gauges with a gauge factor of 2.14 ± 1%. The power supply and measurement leads from the two pairs of strain gauges were then wired together on a small terminal adjacent to the strain gauges to form a four-arm Wheatstone bridge. The signal cables that attach the Wheatstone bridge terminal to the wireless telemetry system located at the turbine shaft were then run through the void formed by the leading edge of the strut. This ensured that the cables would not be subjected to wind buffeting during operation.

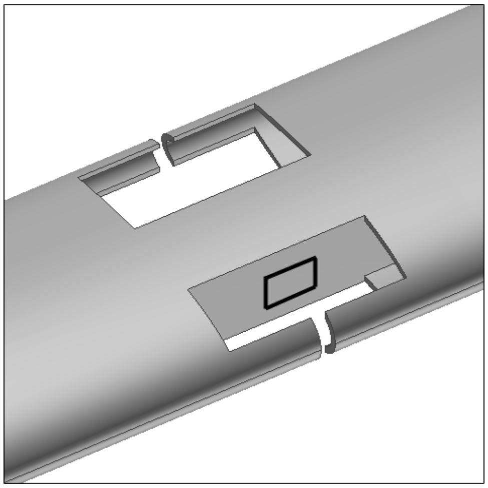

Figure 4.6: Strut port machined to accommodate strain gauge sensors located within the highlighted region

The design of a strain gauge Wheatstone bridge allows for very small material strains, measured as small changes in resistance, to translate into appreciable changes in output voltage. Through proper arrangement of the strain gauges within the Wheatstone bridge, the effect of a change in resistance can be amplified or nullified. In one configuration, a horizontal bending moment applied to the strut results in equal and opposite changes in resistance in the strain gauges on either side of the strut, and a significant change in output voltage. However, any tensile load applied to the strut under this same configuration results in equal changes in resistance, and no change in output voltage. In a similar manner, the strain gauges can be arranged within the Wheatstone bridge such that the voltage output is sensitive to tensile loading, but does not respond to horizontal bending. However, because the cross-sectional geometry is not perfectly symmetric, and the strain gauges are not mounted exactly opposite one another, some cross-talk between loading components exists.

Figure 4.7 shows the layout of the three port locations within the support strut. The strain gauges within the Wheatstone bridge mounted closest to the turbine blade (1) were wired in such a manner so as to make it capable of measuring tensile loading, while being insensitive to horizontal bending. Conversely, the strain gauge Wheatstone bridges mounted in the middle of the strut (2) and closest to the shaft (3) were wired to be sensitive to horizontal bending and insensitive to tension.

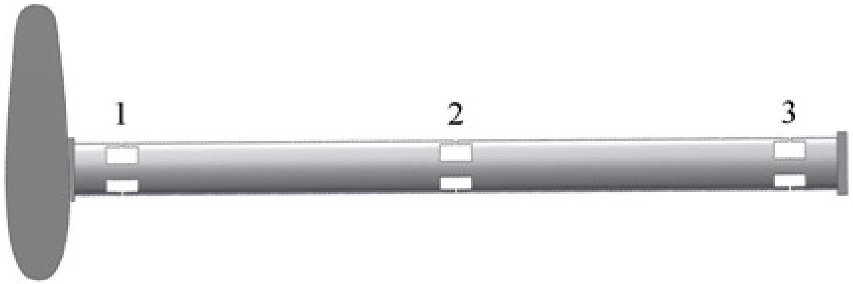

Figure 4.7: Turbine support strut instrumented with strain gauge Wheatstone bridges. (1) Tension, (2) & (3) horizontal bending moment

The tension and bending moment sensors were arranged in this manner in order to minimize the amount of error introduced by crosstalk between loading components. Close to the blade, the radial arm formed between the gauge and the chord line of the blade is relatively small and as such so is the bending moment. Thus, this sensor is capable of obtaining the radial load with relatively little noise from the thrust loading component. Conversely, the two horizontal bending moment sensors are mounted far from the blade, such that the moment arm is large and the bending moment produced by the thrust force is greatly amplified. Two horizontal bending moment sensors are required in order to be able to differentiate between the effect of bending due to the thrust component at the chord line of the blade, and bending due to the radial load that is offset from the centreline of the strut. Together these three sensors are capable of determining the radial and thrust loads as well as the position along the chord of the blade at which the radial load is being applied (it is assumed that thrust is applied at the chord line of the blade).

4.5.2. Calibration

Because of the complexity of the load measurement system, an appreciable amount of cross-talk between channels, and a strong dependence on temperature, an elaborate calibration procedure was required. While the details of both the calibration and data processing procedure can be found in Appendix A.2, a short description will be provided here. To calibrate both of the instrumented struts, a calibration fixture was developed that consisted of two lengths of angle aluminum (1.2 m in length) mounted back-to-back and secured horizontally to the free end of the turbine strut in place of the blade. Along the length of this fixture were a series of holes through which small steel cables were threaded. Combined with a large A-frame stand and a low friction pulley, these cables formed a block and tackle system which was employed to apply fixed loads to the instrumented struts. Both negative and positive thrust loads were applied to either end of the fixture at a radius equivalent to the chord line of the airfoil. Radial loads were applied at multiple locations along the length of the fixture in order to determine the effect of an offset in radial load from the centreline of the struts. In order to apply large radial loads at the centreline of the struts, the fixture was removed and replaced with a 15.24 cm diameter, 6 cm thick, steel disk, the weight of which was equivalent to that of ½ of a turbine blade. The two instrumented struts were then mounted opposite to one another, and the turbine was driven over a range of rotational velocities.

In addition to these tests it was deemed necessary to determine the effects of the strut drag and radial load due to self-weight on the sensor outputs. As such, a series of tests were performed by rotating the turbine with the blades removed in order to quantify the impact of these loads. Finally, due to the large radial loads applied to the blades as a result of centrifugal acceleration, considerable bending of the blades was expected to occur. This results in a bending load on the ends of the struts about the chord line of the airfoil, as well as a vertical load as a result of the blade shortening due to bending. The effect of this loading was quantified by first recording the sensor output during rotation with a standard blade on the turbine, and then comparing that to the output obtained during rotation with a blade that had been cut in half. By placing a lightweight shroud around the seam to prevent end losses, it was possible to make an accurate comparison of the sensor output with and without the effects of blade bending. With the exception of the blade bending tests which were performed at just 12 and 20 °C, these tests were all performed at 0, 8, 13, 18, and 23 °C. This was deemed necessary in order to account for the effects of changes in temperature on the strain gauge factor and material elasticity.

Note that the use of pre-calibrated load-cell instruments to obtain the aerodynamic load components was also considered for this study. This would likely have reduced the amount of cross-talk between loading components and simplified the calibration procedure greatly. However, because of the difficulty involved in implementing the load-cells such that they would be able to measure the aerodynamic loading components without major modifications to the wind turbine, they were not employed.

4.5.3. Angular Position Detection

In order to determine the angular position of the instrumented arms as they acquire strain measurements, a novel proximity sensor/trigger pin system was developed. Atop the turbine a trigger pin was fixed to the stationary inner shaft extension of the turbine at $\theta = 0°$. Directly opposed to the trigger pin is a proximity sensor mounted to the rotating outer shaft. As the turbine rotates, the passing of the proximity sensor by the trigger pin results in a distinct square wave pattern that can be used to determine the location of the $\theta = 0°$ position for each rotation within the strain measurement signals. Because the proximity sensor is rotating with the turbine, its output is transmitted through the telemetry system along with the load measurements. Thus, the position and load measurements were obtained simultaneously, and no post-synchronization was required.

4.6. Telemetry System

Due to the rotating frame of reference that the load and position measurements are being taken, some form of remote data capture was necessary. Traditionally, slip ring systems were used in order to accomplish this (Vittecoq & Laneville, 1983); however these systems typically introduce considerable noise into the load measurements. As such, it was determined that a wireless telemetry system was the most appropriate method to acquire the necessary data remotely.

4.6.1. Housing

Because of the potentially harsh environment that the turbine operates in (rain, extreme cold, and high wind) a robust casing was built to house the wireless transmitter and power supply. The housing consists of two boxes, each approx. 8 cm x 12 cm x 19 cm, mounted opposite one another on either side of the turbine support shaft. The boxes were mounted horizontally such that they presented a minimal frontal area to the oncoming flow. One box contains a bank of six 9V batteries to power the transmitter and proximity sensor, while the other houses the transmitter and its associated wiring. A custom interface was made on the lower surface of both boxes to allow for connections to be made to the Wheatstone bridges, proximity sensor and power supply. Both boxes are thermally insulated in order to prevent the batteries and transmitter from becoming excessively cold. Additionally, several compartments were incorporated into the boxes to hold chemical heat packs to provide heat to the electrical components in the event that temperatures dropped significantly.

4.6.2. Device Specifications

The wireless telemetry system is an Enhanced Series 500e Digital Telemetry System produced by SRI/PMD. The device is capable of reading 8 sensor inputs at a maximum data rate of 152.3 bps. With a 16 bit resolution this translates into a maximum sampling rate of 1058 Hz per channel. However, because the turbine operates over a very broad range of rotational velocities the sampling resolution per revolution varies greatly. That being said, for 97% of the data acquired the rotational velocity was less than 135 RPM, such that the sampling resolution was 0.75° or smaller. The wireless transmitter is capable of maintaining communication over distances of 100 feet or greater at a frequency of 915 MHz. Despite this, some interference was observed when the transmitter fell in the shadow of the both the central shaft and one of the turbine blades, resulting in small interruptions in data transfer. In order to ensure that the operating temperature of the transmitter does not deviate from its calibration range (0°C to 85°C), temperature detection and monitoring systems are included within the transmitter. A complete schematic of the wireless telemetry system signal conditioning (low-pass filter was not utilized), transmission, and processing is given in Figure 4.8. Once the signal is processed by the receiver, the analog output is passed through a data acquisition card and on to a PC with custom data processing software for online display and storage.

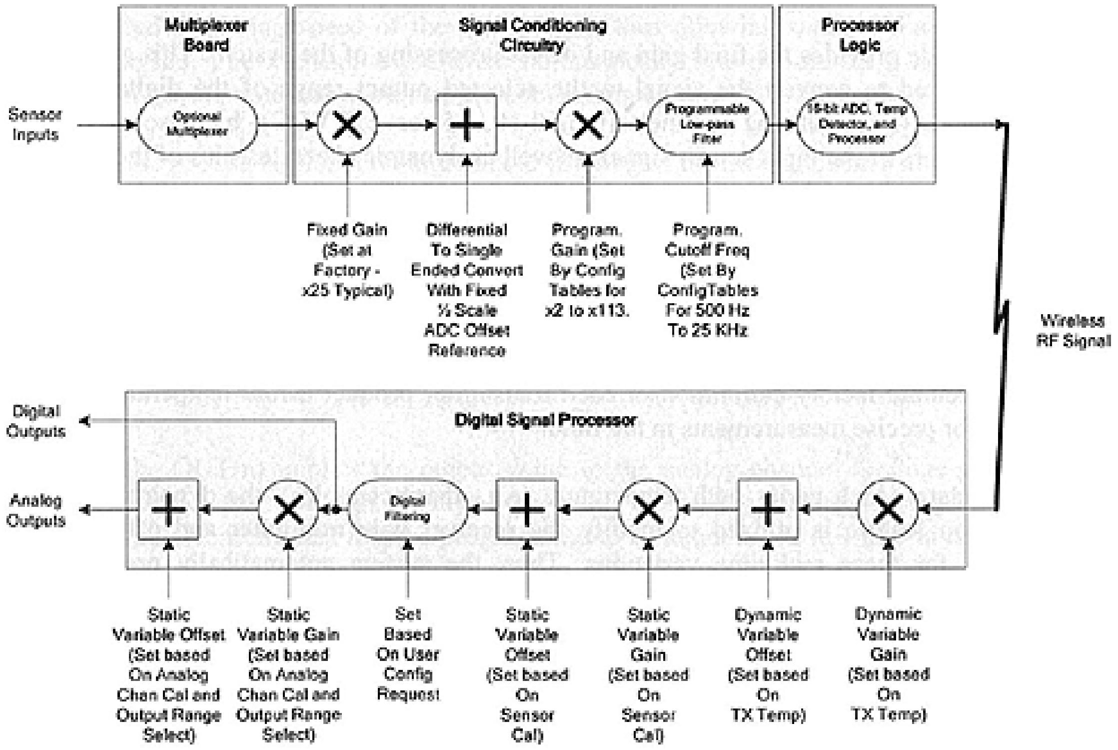

Figure 4.8: Data processing schematic (SRI/PMD, 2008)

4.7. Testing Procedure

With the exception of the wake mapping tests the procedure for obtaining the turbine thrust and radial forces, centre of pressure on the blades, and vibration response of the turbine was as follows. The first step in the data acquisition process was to manually balance each of the six Wheatstone bridges through a small slide wire resistor. This was done to ensure that the strain measurement did not exceed the upper or lower limit of the data acquisition system. Next, the turbine was driven to approx 100 RPM and allowed to spin for approx 5 minutes in order to relax any of the bolted joints between the struts and blades that may have been adjusted prior to the test (when changing blades or inserting pitch shims). If necessary, the Wheatstone bridges were manually balanced once again subsequent to relaxing the bolted joints. Having properly balanced the load sensors, a series of ‘spin-up’ test were then performed. For these tests, the turbine was driven at a series of rotational velocities from 20 RPM to 160 RPM by increments of 20 RPM. Loading data was recorded at each velocity setting for 30 seconds and was used to determine the loading component on the struts due to radial acceleration and blade drag in quiescent flow. This information was later used to approximate the centre of mass of the blades as well as the extent of blade bending due to radial acceleration.

Once the turbine was brought to rest, a 30 second recording of the Wheatstone bridge strains was obtained in order to determine any minor initial offset in the output voltages. The temperature within the tunnel was then recorded and the wind tunnel fans were brought up to speed. For a given wind velocity, the lowest rotational velocity at which the turbine was able to overcome frictional and aerodynamic losses was determined, and the first set of readings was taken. Readings at each rotational velocity were taken for a minimum of 30 revolutions. This meant that at low rotational velocities readings could take as long as 110 seconds, while for tests over 60 RPM the length of the recordings were kept constant at 30 seconds in order to provide enough time to acquire a sufficiently long torque measurement. The turbine rotational velocity was increased incrementally, recordings were taken at each setting, and the full operating range of the turbine configuration was mapped out. For these tests, maximum rotational velocity was limited either by excessive frictional and aerodynamic losses, such that the turbine was producing zero net power, or, the turbine vibration had grown to the extent that it was unwise to continue operation. Once this limit was reached, the wind tunnel was turned off, the turbine was brought to rest, and a final 30 second recording was taken in quiescent flow. Along with the initial non-rotating measurement, this data was used to account for any strain gauge drift during testing. Once all of these readings were taken, the bridges were balanced once again and the load measurement procedure was repeated for a higher wind velocity. Acceleration, blade position, and strain measurements were all acquired at a sampling rate of 1058 Hz.

A sketch of the entire wind turbine set-up within the wind tunnel with the force and vibration measurement instrumentation attached is given in Figure 4.9. Note that the accelerometer cables were run across the guy-wire support cables to allow for measurement of the vibration response at the top of the turbine where large amplitude deflections were observed in preliminary test cases.

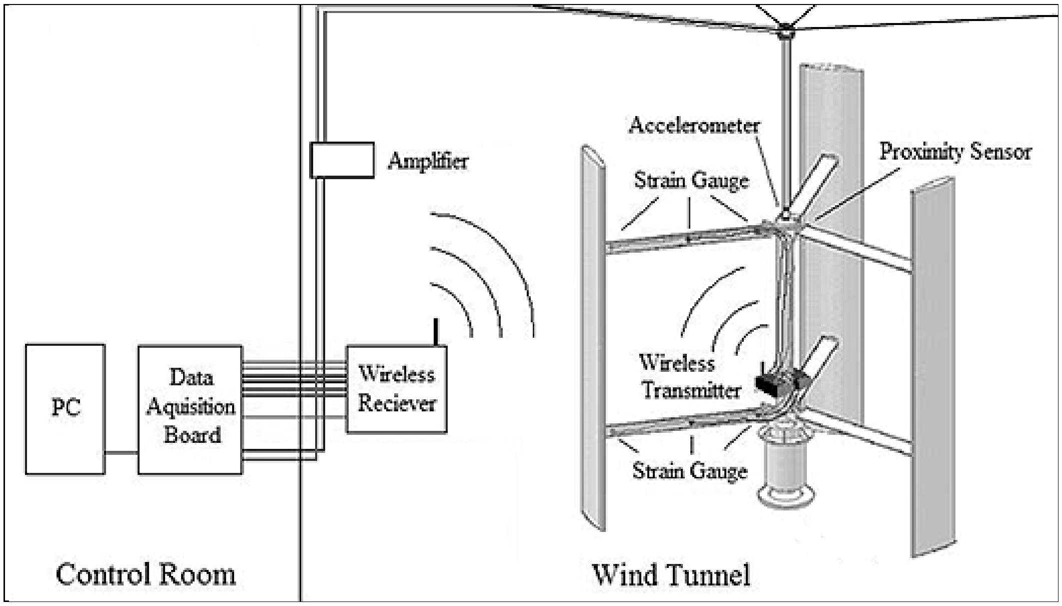

Figure 4.9: Wind tunnel test set-up. Note the accelerometers on the top of the turbine, the proximity sensor to detect angular position, the strain gauges for blade load measurement, and the wireless transmitter for data extraction

For the wake measurement tests, both the wind tunnel velocity and rotational velocity of the turbine were kept constant, and loading and vibration measurements were not recorded. For these tests, the sonic anemometer and its support structure were mounted atop a wooden skid such that a pallet jack could be used to move the system about the wind tunnel. Once the anemometer was set at its initial position upstream of the turbine, the wind tunnel was brought up to speed and the turbine rotational velocity was set. Recordings were then taken for 30 second intervals at each location as the anemometer was moved about the wind tunnel, upstream, beside, and downstream of the turbine. Once a complete mapping of the tunnel was completed at a given height above the floor, the height of the anemometer was adjusted and the tests were repeated. Wake velocity measurements were obtained at three different heights, the bottom, mid-height, and top of the turbine blades. Several other tests at intermediate and additional heights were recorded along the centreline of the turbine in order to determine the extent of flow divergence around the turbine. Sonic anemometer measurements were acquired at a sampling rate of 30 Hz.

CHAPTER 5

EXPERIMENTAL MEASUREMENTS

A series of full-scale experimental wind tunnel tests were performed to determine the aerodynamic loading behaviour on the airfoils of a high solidity, H-type, vertical axis wind turbine. During the course of this investigation, high vibration response of the turbine was observed over a wide range of test conditions. This large vibration response resulted in conditions that made it difficult or impossible to measure the underlying aerodynamic forces on the airfoils. As a result, in order to gain a greater understanding of the aerodynamic loading behaviour, a vibration mitigation methodology was developed to remove the effect of vibration from the measured aerodynamic forces on the blades. This included tests with two different support shaft end conditions over a range of flow velocities from 6 to 11 m/s, in order to isolate the numerous vibration modes and excitation mechanisms. Signal filtering techniques were also developed and employed in order to remove small amplitude remnant vibrations. In this way, an accurate and complete measurement of the aerodynamic loading on the turbine blades could be obtained to better understand the effects of dynamic stall and validate the results of numerical model predictions.

The contents of this chapter include a characterization of the turbine natural frequencies and mode shapes. The methods used to minimize the vibration response of the turbine during the course of this study, in order to maximize the amount of usable data from the recorded measurements, are also developed and explained. Finally, a sample of the aerodynamic force and power coefficient measurements obtained from these tests are given.

5.1. Turbine Vibration Response

5.1.1. Natural Frequency Characterization

Prior to performing any aerodynamic load measurements, a full characterization of the turbine natural frequencies was performed. This allowed for the identification of potential resonant response conditions. In order to characterize the natural frequency response of the wind turbine both with and without the guy wire system in place, a series of impact hammer tests were performed with three different accelerometer arrangements. First, the two accelerometers were mounted to the stationary inner shaft of the turbine in the streamwise and cross-stream directions. Due to the asymmetry of the turbine base support, excitation was then applied to the turbine in both the streamwise and cross-stream directions. Second, the accelerometers were mounted to the ends of the top and bottom support struts in the tangential direction and the turbine blades were excited tangentially. Finally, the accelerometers were mounted to the ends of the support struts in the vertical direction and the blades were excited vertically. Due to the effect of the turbine blade position on the system response, the impact hammer tests were performed first with one of the blades aligned in the streamwise direction, then again with one of the blades aligned in the cross-stream direction. Additionally, due to the change in stiffness introduced by the machining of the support struts to accommodate the Wheatstone bridges, all tests were performed on both the standard and instrumented struts. Because of the numerous test conditions required to isolate the effects of the cables, machined struts, blade position and turbine asymmetry, a vast array of vibration response was generated.

While the results of the impact hammer tests are subject to change somewhat with blade design, as well as cable tension, a summary of the general trends observed for the NACA0015, 420 mm chord blades can be found in Table 2.

Vibration Mode	Without Cables [Hz]	With Cables [Hz]
Streamwise Shaft Bending (Whirl)	4.0	6.8
Cross-Stream Shaft Bending (Whirl)	4.4	6.4
Bottom Instrumented Strut Horizontal Bending	8.1	8.3
Top Instrumented Strut Horizontal Bending	8.5	8.7
Instrumented Strut Blade Bouncing	9.0	9.0
Standard Strut Blade Bouncing	9.4	9.7
Bottom Standard Strut Horizontal Bending	10.9	10.9
Top Standard Strut Horizontal Bending	12.7	12.9

Table 2: Stationary turbine natural frequencies from impact hammer tests

The effect of the asymmetry of the turbine base support can clearly be seen in the splitting of the primary bending mode of the wind turbine at the closely spaced frequencies of 4.0 and 4.4 Hz without cables, and 6.8 and 6.4 Hz with cables. The most predominant effect of implementing the cable support system is to change the primary bending mode of the turbine from a fixed-free condition to a fixed-pinned condition. This results in an increase in the primary streamwise and cross-stream shaft bending frequencies by approximately 50%. Additionally, some increase in all of the higher turbine structural modes can be seen as a result of the implementation of the cable supports. Finally, due to the significant decrease in horizontal bending stiffness of the instrumented struts, an appreciable reduction in the horizontal bending frequency can be observed, while the vertical bending stiffness, and thus the blade bouncing frequency, has remained relatively unaffected. While the expected vibration excitation frequency range falls well below the higher natural frequencies, their effect on the vibration response of the turbine was closely monitored along with the primary shaft bending frequencies.

5.1.2. Primary Whirl Mode Excitation

In order to determine the frequency and magnitude of the vibration response of the turbine prototype for a given rotational velocity, the power spectral density (PSD) of the accelerometer measurements was calculated. The first step in determining the power spectral density was to divide the available data into as many 8 second intervals (2^{14} samples) as could be obtained. A Hamming window was then applied to each 8 second interval and the one-sided power spectral density was calculated.

$$One-sided\ PSD = \frac{2\left|FFT\big(a(t)\big)\right|^2}{0.54(\#\ of\ Samples)} \tag{5.1}$$

Note that the number of samples by which the fast Fourier transform (FFT) is normalized is scaled by a factor of 0.54 due to the application of the Hamming window. The power spectral densities calculated from each 8 second interval were then averaged to obtain the final power spectral density amplitude.

From the power spectral density measurements it was determined that the primary vibration response of the turbine prototype was resonance excitation of the dominant whirling mode. Significant deflection of the support shaft was observed at coincidence of this first natural frequency of the turbine and the blade pass frequency at which the turbine was operating. As an example, Figure 5.1 plots the power spectral density of the vibration response data in the streamwise direction both with and without the cable support system in place for the 420 mm NACA0015 blades, with a preset pitch angle of β = 0°. In this figure green lines indicate dominant natural frequencies obtained from impact hammer tests, while red lines are integer multiples of the rotational frequency. Despite some differences in the amplitude of the response in the streamwise and cross-stream directions, little difference is seen in the vibration response trends. As such, the cross-stream vibration response is not presented.

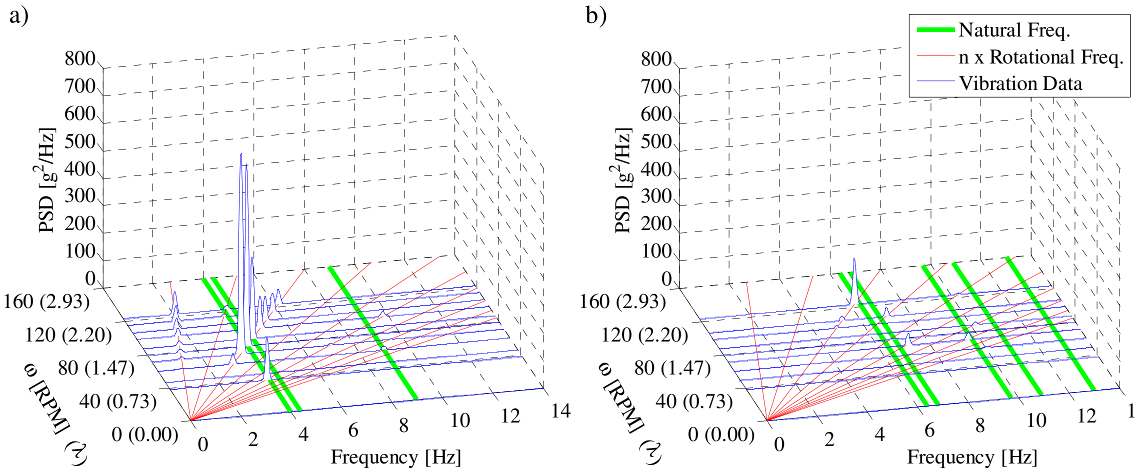

Figure 5.1: Power spectral density of turbine shaft vibration in the streamwise direction as a function of rotational velocity for a flow velocity of 8 m/s (NACA 0015, c = 420 mm, β = 0°). (a) without cables, (b) with cables

Without the guy wire system attached, the primary whirling frequency of the turbine is coincident with the blade pass frequency at 75 RPM. As per the power spectral density of the turbine vibration in the streamwise direction, this results in appreciable vibration excitation of the turbine over the typical power producing operating range of $1.4 \leq \lambda \leq 1.8$ (Figure 5.1a). As was the intention of the cable support system, pinning the upper end of the turbine support shaft stiffens the system and raises the primary whirl frequency. With the support cables in place, the primary structural mode of the turbine now coincides with the blade pass frequency at 135 RPM. While the first onset of a response to the whirling mode of the turbine is apparent at high blade speed ratios, little vibration response is seen throughout the typical operating range for any of the dominant turbine modes identified by the impact hammer tests (Figure 5.1b).

In order to demonstrate the vibration response of the turbine to the primary bending frequency, the normalized power spectral density amplitude for the blade pass frequency is calculated and plotted in Figure 5.2. Because the amplitude of vibration is a function of the amount of power available in the oncoming flow, normalizing the power spectral density amplitude by the product of the dynamic pressure and the flow rate through the turbine ($^1/_2 \rho U_\infty{}^3 2RH$) results in a collapse of the data. Figure 5.2a clearly demonstrates the exponential growth in vibration amplitude up to the resonance frequency without the cable system attached. With the cable support system in place (Figure 5.2b) the blade pass frequency amplitude is limited to the exponential growth region as the resonance frequency is at the upper limit of the operating capabilities of the wind turbine (Figure 5.1b). While not shown, this growth trend was also observed to exist in the cross-stream direction. Note that with the cable system in place, the growth rate of the response to the blade pass frequency is approximately one half of that observed without the cables attached. This is likely due to the change in mode shape and increase in energy required to excite the primary mode of the fixed-pinned shaft over the primary mode of the fixed-free shaft.

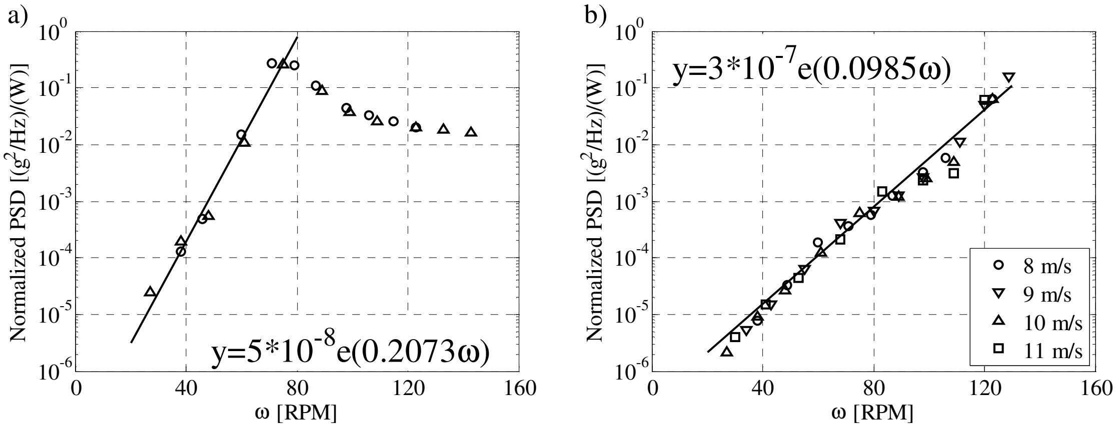

Figure 5.2: Power spectral density of the blade pass frequency normalized by the power available in the oncoming flow in the streamwise direction (NACA 0015, *c* = 420 mm, β = 0°). (a) without cables, (b) with cables

5.1.3. Strut Mode Excitation

While designed to measure the aerodynamic loading behaviour, the strain gauges mounted to the surface of the airfoil support struts also provided valuable information on the vibration response of the higher frequency structural modes. For a number of test cases, at coincidence of the strut mode natural frequencies with integer multiples of the rotational frequency of the turbine, the strain measurements became saturated with resonance response. This had a significant impact on the ability to ascertain the sensor output due to aerodynamic loading.

For each test case, data was recorded for a minimum of 30 revolutions and averaged over the total number of revolutions to produce a mean data set. This averaging technique effectively filters out all vibration response that is not occurring at an integer multiple of the rotational frequency. The mean output signal is then subtracted from the raw data in order to produce an additional data set. This data set represents the vibration component of the sensor output in response to the natural frequencies of the turbine, and is employed to determine the nature and severity of the excited structural mode.

As an example, a short segment of the sensor output for the strain gauge Wheatstone bridge mounted at the mid-point of the bottom strut without the cable system attached at two different blade speed ratios is given in Figure 5.3. In the case where there is no resonance response to the higher strut modes (Figure 5.3a), it can be seen that the raw data is relatively consistent from one revolution to the next, and that the difference between the mean and raw data is at a fixed frequency of approximately 8 Hz. As expected, this corresponds to the horizontal bending frequency of the instrumented strut without the cable system attached (Table 2).

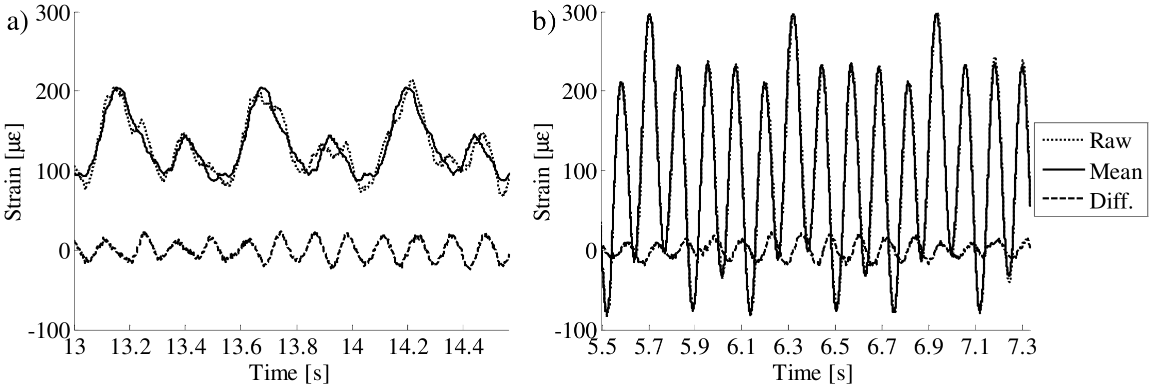

Figure 5.3: Sensor output for the strain gauge Wheatstone bridge mounted at the mid-point of the bottom strut without the cable system attached for a flow velocity of 8 m/s (NACA 0015, c = 420 mm, β = 0°). Three revolutions of the raw sensor data are shown along with the mean and vibration components. (a) without resonance (ω = 115 RPM, λ = 2.1), (b) with resonance (ω = 100 RPM, λ = 1.8)

However, in the case with resonance, the response to the natural frequency of the support strut at 8 Hz overwhelms the mean loading signal (Figure 5.3b). In this instance, the difference between the mean and raw data sets is small and represents minor changes in amplitude and phase from one revolution to the next. Note the considerable change in strain amplitude from the relatively small deflections of the non-resonant test case to the appreciable vibration of the resonant test case.

In order to better illustrate what modes are being excited, the PSD of the vibration component of the bottom mid-strut bending moment sensor output is calculated and plotted in Figure 5.4. In this figure, green lines indicate frequencies with high vibration response, while red lines are again integer multiples of the rotational frequency. From this figure it is clear that the primary vibration response of the turbine struts occurs at coincidence of all integer multiples of the turbine rotational frequency with the horizontal bending frequencies of the instrumented struts (8.1 Hz for test cases without cables and 8.3 Hz for test cases with cables). Additionally, some response to the top instrumented strut horizontal bending frequency (8.5 and 8.7 Hz) and bottom standard strut horizontal bending frequency (10.9 Hz) was also identified. As expected, negligible response to the blade bouncing frequencies was observed.

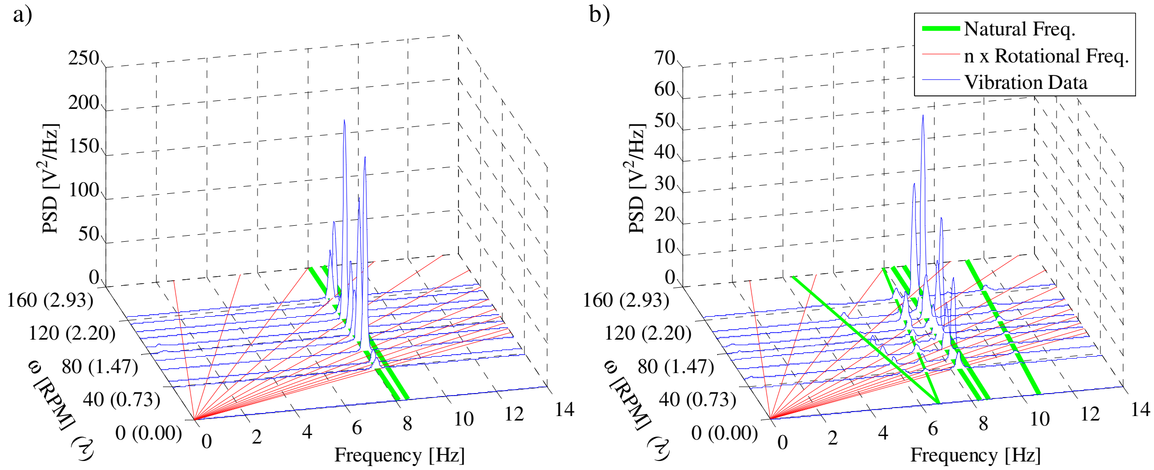

Figure 5.4: Power spectral density of the bottom mid-strut bending moment sensor vibration component as a function of rotational velocity for a flow velocity of 8 m/s. (NACA 0015, c = 420 mm, $\beta = 0°$). The 'vibration component' refers to the difference between the raw and mean signal output. (a) without cables, (b) with cables

With the addition of the cable support system, an overall reduction in the amplitude of the vibration component of the sensor output can be observed (Note the change in scale of the vertical axis in Figure 5.4). As was shown in Figure 5.1, the addition of the cable support system shifts the excitation of the primary whirling mode to the upper limits of the operational range of the turbine. As such, it is believed that this overall reduction in the vibration component amplitude is a result of a decrease in the amount of energy being transferred from the primary whiling mode to the higher structural modes of the support struts.

For cases without the cable system in place, while the response of the support strut to the primary whirling mode of the turbine is present, it is of such small relative amplitude that it does not appear in the strain gauge vibration response (Figure 5.4a). However, for cases with the cable support system, the whirling mode of the turbine is clearly present. As can be seen in Figure 5.4b, at zero rotational velocity, there is a single primary natural frequency of the turbine at approximately 6.7 Hz. However, as the rotational velocity of the turbine is increased, this natural frequency is split into two frequencies, presumably as a result of the gyroscopic effect.

The gyroscopic effect comes about due to the large moment of inertia of the turbine and the relatively low stiffness of the turbine base. Whirl of the turbine generates a moment, the reaction of which acts on the support structure in addition to the stiffness of the system (Den Hartog, 1956). The lower frequency represents the circumstance where whirl of the turbine is opposed to rotation, thus lowering the effective system stiffness. While, the higher frequency represents the instance where the effective stiffness of the system is increased as the direction of whirl is the same as the direction of turbine rotation (Den Hartog, 1956). Typically speaking, backward whirl, where the direction of whirl and rotation are opposed, cannot be excited by the unbalance force of a simple isotropic system. However, for systems with asymmetric supports, such as the present case, it is more likely to occur (Rao, 2000).

5.2. Data Maximization

Having identified the overwhelming prevalence of resonance excitation of the turbine throughout its entire operational range, it became clear that a vibration mitigation methodology would have to be developed in order to obtain the underlying aerodynamic loading free from turbine vibration response. As described above, the first step in removing vibration response from the data was to average the data over an extended duration. By averaging the data over a minimum of 30 revolutions, any vibration response that is not occurring at an integer multiple of the rotational frequency is effectively filtered from the data. While this approach removes some of the vibration response of the turbine, because the vibration excitation loading is applied at integer multiples of the rotational frequency, the largest resonant vibration responses still remain. As such, in order to maximize the amount of data obtained from the tests performed, the following vibration mitigation methodologies were developed.

5.2.1. Turbine Shaft End Conditions

The first step in maximizing the available data was to determine which test cases display resonance characteristics by calculating the PSD of the raw data and searching for large amplitude responses. As an example, Figure 5.5 shows the response of the bottom mid-strut bending moment and tension sensors without the cables attached at a wind velocity of 8 m/s. As for all previous and subsequent cases, the behaviour of the shaft side bending moment sensor closely resembles that of the mid-strut bending moment sensor and as such has been omitted.

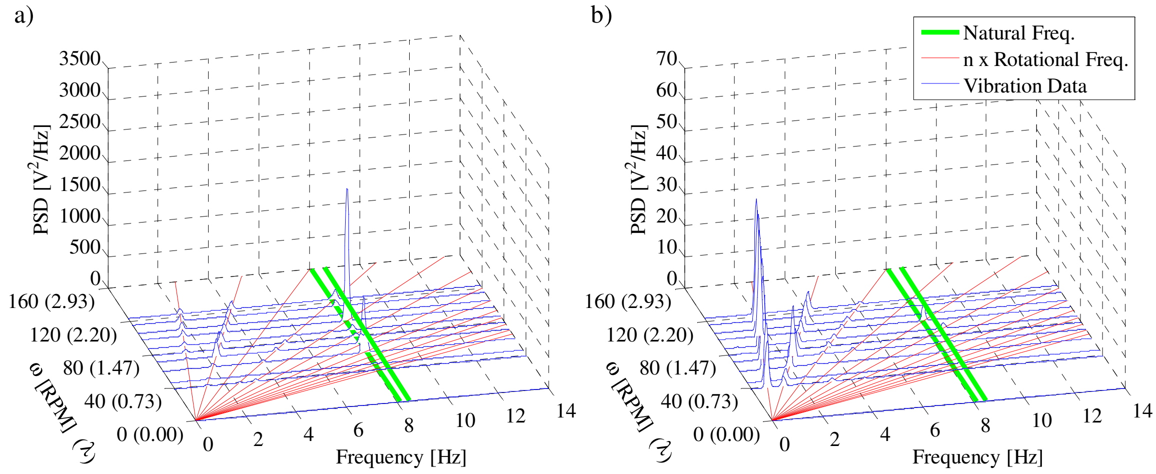

Figure 5.5: Power spectral density of the raw sensor data without cables as a function of rotational velocity for a flow velocity of 8 m/s (NACA 0015, *c* = 420 mm, *β* = 0°). (a) mid-strut bending moment sensor, (b) tension sensor

First and foremost, these figures display the considerable difference in the relative amplitude of response from each sensor. The mid-strut sensor, wired to measure bending strain in the horizontal plane, is very sensitive to the dominant horizontal bending frequencies of the struts. The tension sensor however, being wired to be responsive to tension rather than bending moment, has minimal response to this natural mode of vibration. Secondly, each of the sensors displays a response to the first and second multiples of the rotational frequency. Based upon the anticipated loading behaviour of the airfoils over a full rotation (Figure 3.6), this is entirely expected. Finally, a strong resonance response at 60 RPM and 100 RPM, where $\lambda = 1.1$ and $\lambda = 1.8$ respectively, dominates the mid-strut sensor output.

A sample of the thrust and radial forces calculated from the shaft side, mid-strut, and tension sensors provides a better understanding of the effect of this response on the ability to obtain the mean aerodynamic loads (Figure 5.6). For a very low blade speed ratio of $\lambda = 0.7$ the thrust loading displays many of the expected characteristics. A sharp increase in the thrust loading occurs on the upstream portion of the rotation, peaking at just 55° of rotation. Following this is a series of lower amplitude fluctuations in thrust loading throughout the duration of the downstream portion of the rotation. The radial force measurement for $\lambda = 0.7$ also reflects the expected loading behaviour, in that a decrease in radial load on the upstream portion of the rotation due to the considerable pressure gradient formed across the airfoil can be observed. Note the large mean offset due to centrifugal loading in the radial force measurements (Figure 5.6b).

For a blade speed ratio of $\lambda = 1.1$, a large spike in the vibration response for the bending moment sensor can be seen at a frequency of 8.1 Hz (Figure 5.5a). The response to this natural mode of vibration can clearly be seen in the thrust force measurement, where the support strut is unmistakably responding to the 8th multiple of the rotational frequency (Figure 5.6a). From an aerodynamic load measurement perspective this data sample is practically unusable in its present state.

At an intermediate blade speed ratio of $\lambda = 1.45$, a delay in the onset and severity of dynamic stall on the upstream portion of the rotation can be observed as the maximum thrust and radial loading now occurs at 77° of rotation (Figure 5.6a). Furthermore, the existence of a second peak in loading on the downstream portion of the rotation indicates that as expected, pronounced dynamic stall has occurred once again only to a lesser degree. Again, the radial loading closely resembles the expected loading behaviour with a marked increase in the mean loading component due to the increase in rotational velocity.

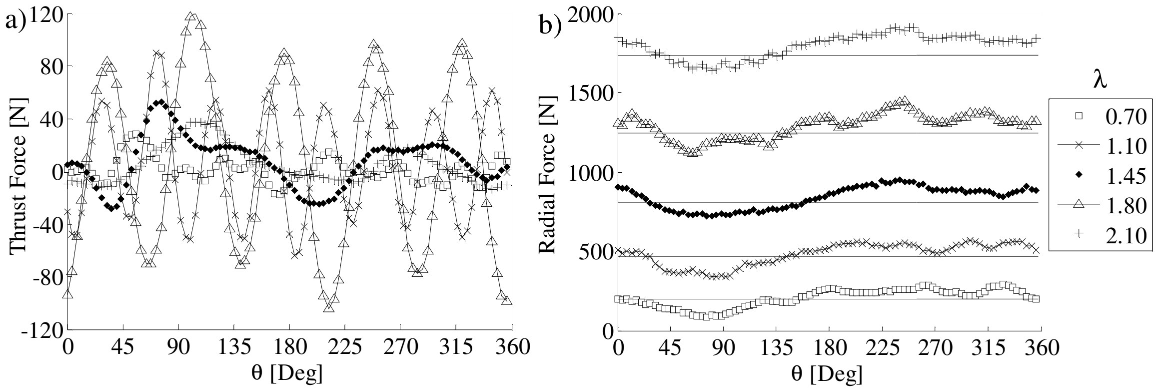

Figure 5.6: Applied force as a function of the angle of turbine rotation without the cable system attached for a flow velocity of 8 m/s (NACA 0015, c = 420 mm, β = 0°). Data has been averaged over a minimum of 30 revolutions. (a) thrust force, (b) radial force, solid lines indicate the loading component due to centrifugal force

For a blade speed ratio of λ = 1.8, resonance is once again encountered and response behaviour similar to a blade speed ratio of λ = 1.1 is observed. However, in this instance, it is the 5th multiple of the rotational frequency that coincides with the horizontal bending mode of the strut occurring at 8.1 Hz (Figure 5.5a). In this particular test case the vibration excitation is so large that a response to it can even be seen in the tension sensor output and radial force component (Figure 5.5b and Figure 5.6b).

Finally, for a blade speed ratio of λ = 2.1, resonance is avoided (Figure 5.5a) and the expected loading behaviour is once again observed. As anticipated, at much higher blade speed ratios dynamic stall is mainly suppressed and occurs gradually. This results in a single large thrust peak on the upstream portion of the rotation, with a second relatively lower amplitude peak occurring downstream.

In order to obtain aerodynamic loading data free from resonant vibration response at blade speed ratios of λ = 1.1 and 1.8, the primary support shaft was stiffened through the addition of the cable support system. As was observed in the natural frequency characterization, this results in an increase in the natural frequencies of the turbine, thus altering the conditions for coincidence. The PSD of the raw sensor outputs with the cables attached and a wind tunnel flow velocity of 8 m/s are shown in Figure 5.7. Again, the bottom support struts appear to be sensitive to the horizontal bending mode occurring under this configuration at a frequency of 8.3 Hz. In this instance however, due to the small change in natural frequency, resonance occurs at different rotational velocities than without cables. As such, high vibration response now occurs at 71 RPM and 123 RPM, or λ = 1.3 and 2.25 respectively. Due to relatively low vibration excitation at λ = 1.1 and 1.8 however, the forces calculated from these strain measurements can be used in place of the high vibration data sets obtained without the cable system.

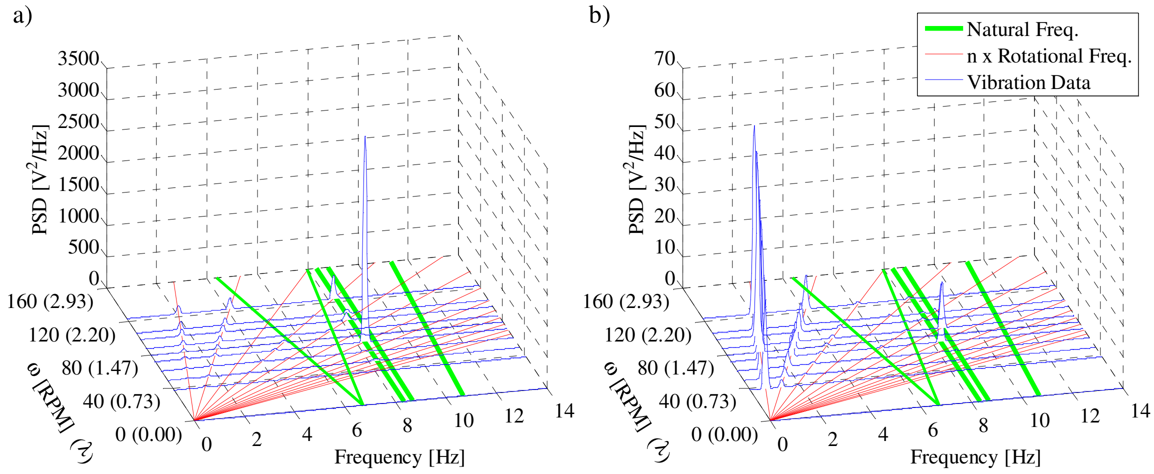

Figure 5.7: Power spectral density of the raw sensor data with cables as a function of rotational velocity for a flow velocity of 8 m/s (NACA 0015, *c* = 420 mm, *β* = 0°). (a) mid-strut bending moment sensor, (b) tension sensor

From Figure 5.8a, it can be seen that these results no longer exhibit the high amplitude resonance response observed without the cable system in place. The natural progression in the maximum thrust location is continued in the λ = 1.1 thrust force measurement, occurring at an angle of rotation of 74°. As was the case for λ = 0.7, this test case exhibits a series of low amplitude fluctuations in thrust loading on the downstream portion of the rotation, as it is predicted that a number of small vortices are shed from the airfoil surface.

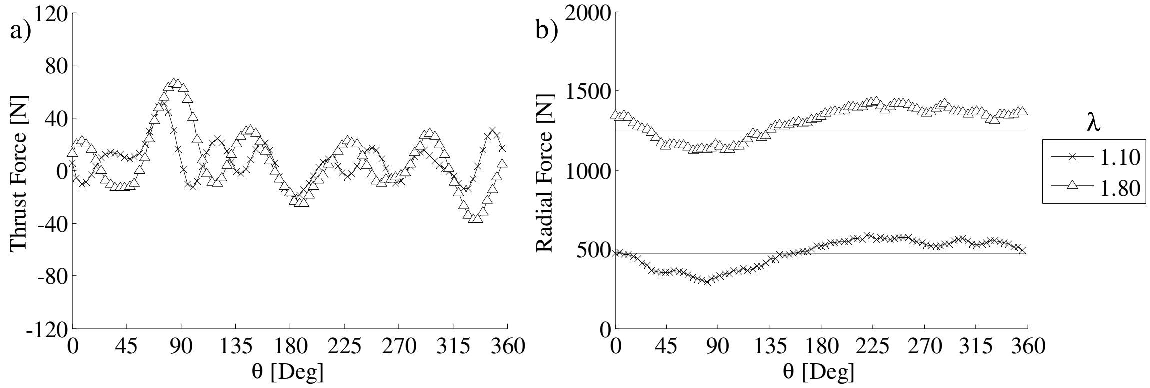

Figure 5.8: Applied force as a function of the angle of turbine rotation with the cable system attached for a flow velocity of 8 m/s (NACA 0015, *c* = 420 mm, *β* = 0°). Data has been averaged over a minimum of 30 revolutions. (a) thrust force, (b) radial force, solid lines indicate the loading component due to centrifugal force

For λ = 1.8, the maximum thrust value is reached within the expected range at θ = 86°. However, by inspecting the overall trend of the data output it appears that the resonance response of the turbine may still have been excited to some small degree. Both radial force measurements show considerable improvement over the test case results without the cables attached (Figure 5.8b).

By collecting the low vibration response test cases from the data sets with and without the cable system attached, a much clearer picture of the aerodynamic loading on the airfoil can now be obtained. However, despite having been able to avoid or minimize the resonant response of the turbine in most instances, some vibration component was still observed to exist even under ideal test conditions. As a result, additional methods to avoid coincidence of integer multiples of the turbine rotational frequency with the natural frequencies of the turbine were explored.

5.2.2. Multiple Wind Speeds

An alternate approach to maximizing the aerodynamic load measurements free of vibration response, is to test at various flow velocities. By normalizing the forces by the product of the dynamic pressure and the planform area of the blade ($^1/_2\rho U_\infty{}^2cH$) the effect of a change in flow velocity on aerodynamic loading can be appropriately accounted for. Defining the loading in this way allows for direct comparison of the measurements at a particular blade speed ratio over a range of wind velocities, where the non-dimensionalized aerodynamic wind loading is the same, but the rotational velocity, and thus the excitation frequency, is different. Just like a change in turbine end condition, a change in flow velocity results in a shift in the rotational velocities at which coincidence between the turbine natural frequencies and the integer multiples of the rotational frequency occur. However, because tests can be performed over a wide range of flow velocities, rather than just two potential end conditions, this method provides a greater data set from which potentially vibration free aerodynamic loading data can be obtained. As an example, Figure 5.9 contains the thrust and radial force coefficients with the cable system attached at a blade speed ratio of λ = 0.7 for flow velocities of 8, 9, 10 and 11 m/s.

Note that the data from the 6 m/s test case is not included as the chord Reynolds number (Re_c = 160,000) is below the Reynolds number independence threshold (Re_c = 210,000).

While the agreement between the thrust coefficients is quite good on the upstream portion of the rotation where aerodynamic loading is highest, considerable discrepancies can be seen throughout the remainder of the rotation. Despite the fact that for all flow velocities the PSD of the bending strain measurements displayed little response to the dominant natural frequencies of the turbine, some influence of the structural modes can still be seen in each of the thrust coefficient curves. However, because the turbine is operating at a different rotational velocity for each wind speed in order to maintain a constant blade speed ratio, the same structural mode is being excited at different integer multiples of the rotational frequency for each test case.

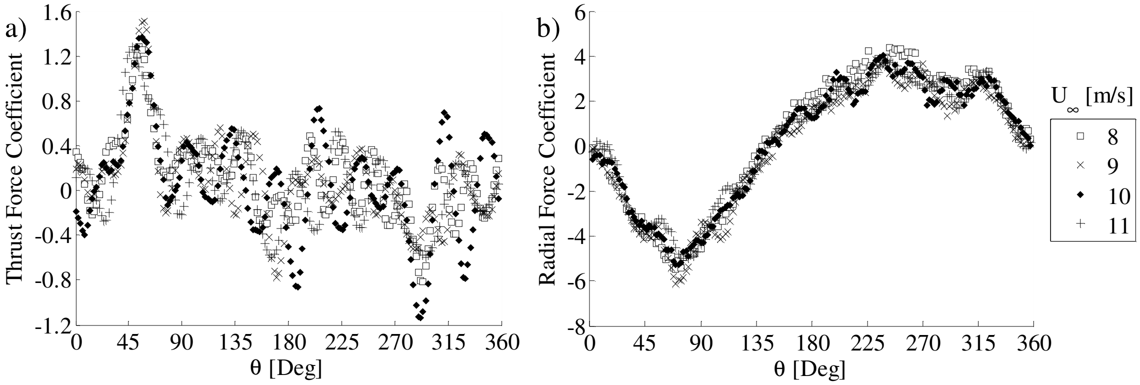

Figure 5.9: (a) Thrust force coefficient, and (b) radial force coefficient with cable system attached normalized by dynamic pressure force, λ = 0.7 (NACA 0015, c = 420 mm, β = 0°)

From Figure 5.9a, the dominant vibration response is at 14, 12, 11, and 10 cycles per revolution for the test cases at 8, 9, 10, and 11 m/s respectively. The radial force coefficients however, show very good agreement between test cases for all angles of rotation. The mean offset of the radial force coefficient measurements due to the applied centrifugal forces has been accounted for in each of the radial force measurements.

Because no dominant resonance vibration response exists in any of the sample test case measurements (as was the case in the end condition example), it is not obvious which measurement is the more accurate representation of the true underlying aerodynamic loading. Hence, while testing at different flow velocities will often allow for resonant conditions to be identified and avoided, some vibration component is likely to persist. As such, some form of vibration filtering must still be applied to even the least corrupted aerodynamic load measurements.

5.2.3. Filtering Techniques

5.2.3.a Band-Stop Filter

As described in McLaren et al. (2010), one method of eliminating vibration response from aerodynamic load measurements is to obtain data at multiple wind velocities, apply a narrow band-stop filter to any resonance response, and then average the filtered aerodynamic force coefficients. An equivalent approach to determining the average force coefficients would be to average the filtered data within the frequency domain prior to calculating the force coefficients. While this method would produce identical results, averaging of the force coefficients themselves provides a more physical understanding of the effect of the band-stop filtering, and as such will be the approach described here in detail.

The band-stop filtering (BSF) method takes advantage of the fact that for a given blade speed ratio, the aerodynamic load normalized by the dynamic pressure force ($½\rho U_\infty^2 cH$) is independent of wind velocity (beyond a chord Reynolds number of $Re_c = \rho U_\infty c/\mu \geq 210{,}000$). However, as wind velocity is increased, in order to maintain a constant blade speed ratio, the rotational velocity of the turbine must also be increased. As a result, the natural frequencies of the turbine, in terms of cycles/revolution, decrease. This means that for a given blade speed ratio, each of the different natural frequencies of the turbine can either coincide with an integer multiple, n, of the rotational frequency, f, and be excited, or can be far enough removed from these excitation frequencies that they do not influence the loading data, dependant on wind velocity.

As an example, Figure 5.10 plots the amplitude of the real component of the frequency content of the thrust force coefficient measurements for the bottom support strut at a blade speed ratio of $\lambda = 1.32$. The vertical green lines indicate the location of the turbine natural frequencies. Because the aerodynamic loading is periodic at *nf*, averaging the data over a minimum of thirty revolutions of the turbine effectively filters out all vibration content at non-integer multiples of the rotational frequency. From Figure 5.10a it is clear that at 8 m/s, the 7th multiple of the rotational frequency, 7*f*, is exciting the resonance mode of the turbine, while at 11 m/s (Figure 5.10d) this same natural frequency of the turbine (horizontal bending of the bottom support strut) is now excited by the 5th multiple of the rotational frequency, 5*f*. At 9 and 10 m/s, no strong resonant excitation is observed. While similar response behaviour is observed in the radial force coefficients, because the magnitude of the radial force is much greater than the thrust force, and because the excited structural mode is primarily the bending mode of the support struts, the resonant response is far less apparent. The loading data obtained from the top support strut exhibits similar vibration response trends, and thus is not presented herein.

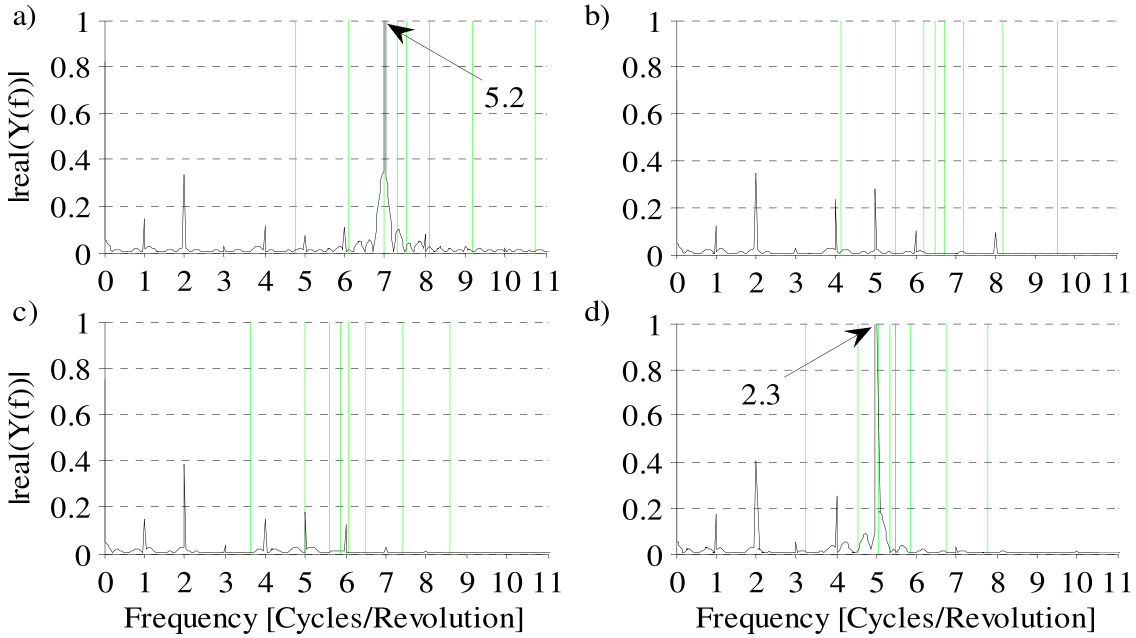

Figure 5.10: Single-sided amplitude spectrum of thrust coefficients for the bottom support strut, $\lambda = 1.32$ (NACA 0015, c = 420 mm, $\beta = 0°$). U_∞ [m/s] a) 8, b) 9, c) 10, and d) 11. Vertical green lines indicate turbine natural frequencies

A comparison of the thrust and radial force coefficients for the entire blade as a function of the angle of rotation, θ, at a blade speed ratio of $\lambda = 1.32$ highlights the effect of the resonant response of the turbine (Figure 5.11). The large resonant response observed in the frequency domain for $U_\infty = 8$ and 11 m/s results in saturation of the thrust force measurements with large amplitude vibration response behaviour (Figure 5.11a). As stated previously, the radial force coefficient measurement is far less affected by the vibration response of the turbine due to the nature of the structural modes being excited, and the much larger relative amplitude of the aerodynamic radial load component (Figure 5.11b). Plotted along with the experimental results is the average of the force coefficients as well as the radial loading component due to centrifugal loading.

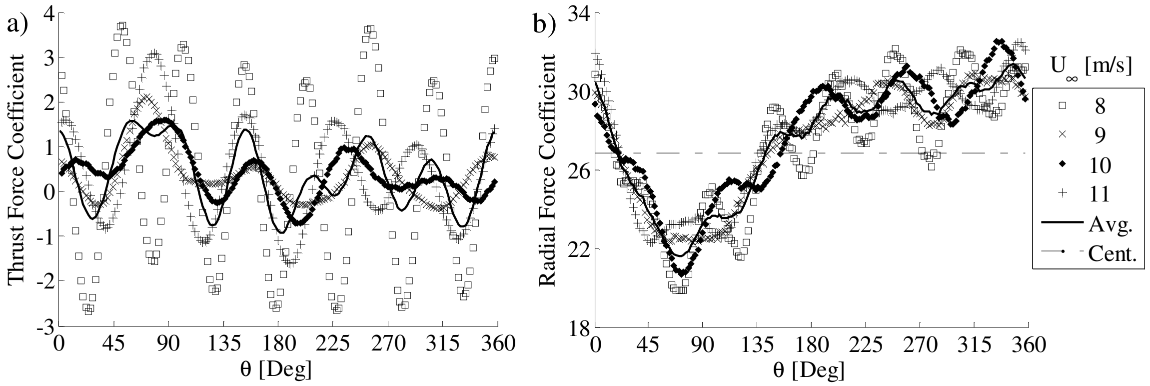

Figure 5.11: Total (a) thrust force coefficient, and (b) radial force coefficient, as a function of the angle of rotation *θ*, *λ*=1.32 (NACA 0015, *c* = 420 mm, *β* = 0°)

Because the resonant behaviour exists over a very narrow region surrounding a given multiple of the rotational frequency, *nf*, the use of a narrow band-stop filter to remove the effect of the vibration response is an attractive solution to the problem at hand. As such, when a natural frequency of the turbine is within ± 0.1 cycles/revolution of an integer multiple of the rotational frequency, a simple Butterworth band stop filter is applied to the force coefficient data. The Butterworth filter used in this study has pass-band frequencies of $nf \pm 0.2$, and stop-band frequencies of $nf \pm 0.1$. In order to ensure that there is no phase shift introduced by the application of the band-stop filter, it is applied to the data in both the forward and backward directions, such that any phase-shift introduced on the forward pass is exactly cancelled out on the backward pass (Mitra, 1998).

Figure 5.12 plots the thrust and radial force coefficients after having been filtered in this manner. Note that the results from the $U_\infty = 9$ m/s test case have been removed due to the close proximity of the backward whirl frequency to the 4th multiple of the rotational frequency, $4f$ (Figure 5.10b). By observing the behaviour of the other test cases it is clear that filtering this frequency content from the data would remove a fundamental component of the underlying aerodynamic loading. From Figure 5.12, while some discrepancy between the measurements obtained at the various flow velocities still exists, considerable improvement in their agreement is achieved by filtering the resonant vibration response from the experimental data. The true thrust and radial force coefficient behaviour can now be readily discerned from the average of the remaining three data sets. This procedure can then be repeated for all blade speed ratios within the operational range of the turbine.

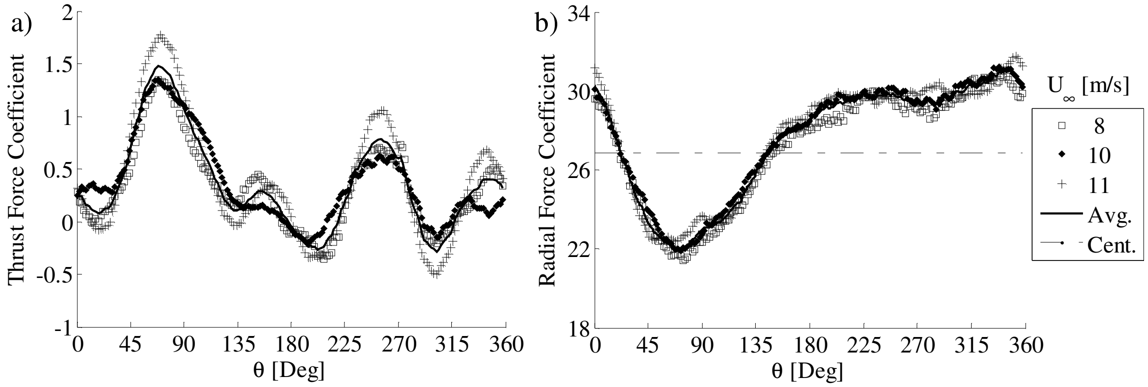

Figure 5.12: Total band-stop filtered (a) thrust force coefficient, and (b) radial force coefficient, λ=1.32 (NACA 0015, c = 420 mm, β = 0°)

One of the advantages of employing this method is that as long as the natural frequencies are well removed from the fundamental aerodynamic loading components, data is only required at a single wind speed. For example, had data only been recorded at a wind velocity of 8 m/s (where resonant vibrations were initially large), a clear picture of the thrust and radial force coefficient behaviour could still be obtained through the use of this filtering method. One major disadvantage of this method however, is that some knowledge of the aerodynamic loading behaviour must be known a priori in order to ensure that none of the underlying aerodynamic loading components are inadvertently removed by the application of the filter. Furthermore, locating and filtering each of the resonant vibration responses from each of the tests cases is a time consuming and manually intensive process. It is for these two reasons that the frequency content minimization technique, described below, was developed.

5.2.3.b Vibration Minimization Technique

As with the band-stop filtering method, the frequency content minimization technique relies on the characteristic that the aerodynamic force coefficients are independent of wind speed beyond a threshold chord Reynolds number. In contrast to the band-stop filtering method however, this technique amalgamates the minimum frequency content of the raw data obtained at different flow velocities, rather than the filtered load coefficients, in order to remove the resonant vibration response of the turbine. In essence, for each blade speed ratio, a fast Fourier transform (FFT) of all the loading signals is calculated, and the minimum amplitude of the real component at each frequency is determined. An inverse fast Fourier transform (IFFT) is then performed on the obtained amplitude lower bound along with its corresponding phase angle. This can be defined as, z = IFFT{min[FFT(y_8,y_9,y_{10},y_{11})]}, where z is the amalgamated force coefficient data, and $y_{U\infty}$ is the force coefficient data at flow velocity U_∞. The results of this calculation for the sample case of $\lambda = 1.32$ are shown in Figure 5.13 and Figure 5.14.

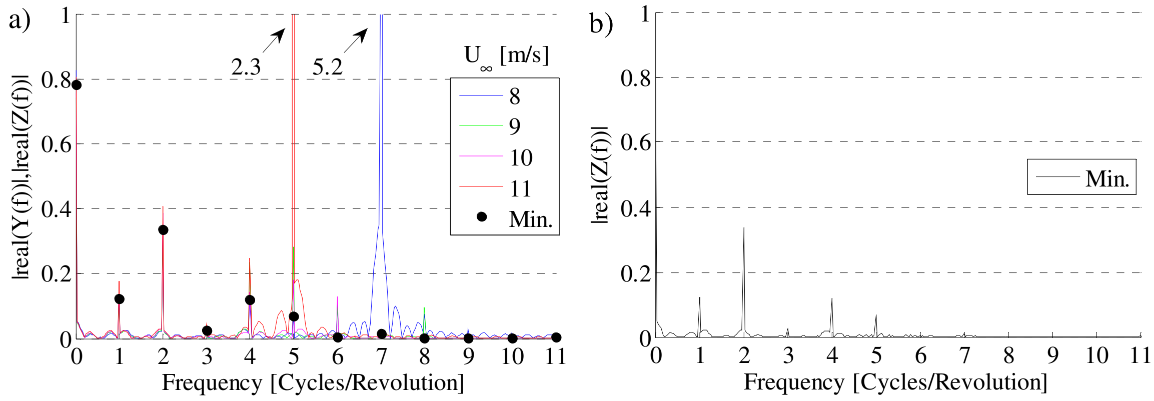

Figure 5.13: Single-sided amplitude spectrum of thrust coefficients for the bottom support strut, $\lambda = 1.32$ (NACA 0015, c = 420 mm, $\beta = 0°$). a) U_∞ = 8, 9, 10, and 11 m/s, as well as minimum values at nf, b) entire amalgamated force coefficient data

Figure 5.13a plots the frequency content of the data from the four wind speeds along with the minimum values at the integer multiples of the rotational frequency, *nf*. From Figure 5.13a it is clear that the largest resonant vibration responses at n = 5 and 7, and to a lesser degree at the other integer multiples of the rotational frequency, have effectively been removed. Figure 5.13b plots the frequency content for the entire amalgamated force coefficient data set alone. It is this data set to which the IFFT is applied. This procedure is repeated for the top support strut, which behaves in a similar manner, to determine the total aerodynamic load coefficients for the entire blade. Figure 5.14 plots the thrust and radial force coefficients calculated from the IFFT of the amalgamated minimized data for λ = 1.32, along with the average force coefficients calculated from the band-stop filtering (BSF) technique (refer to Figure 5.12).

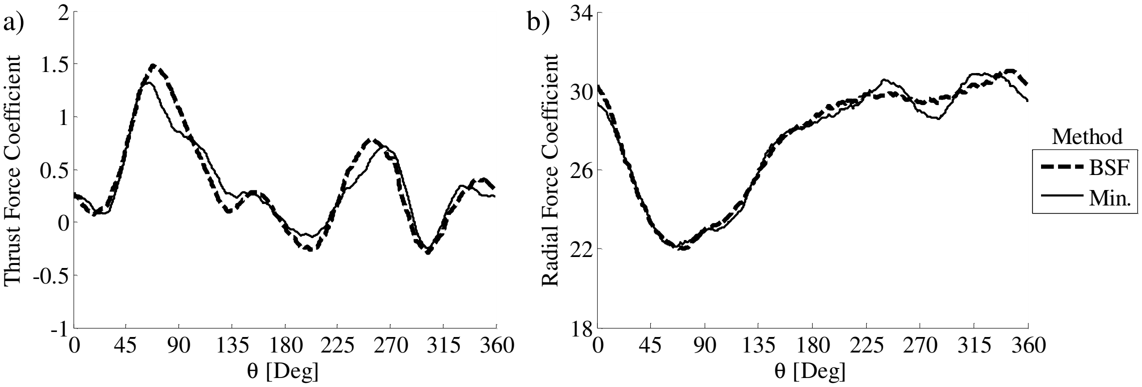

Figure 5.14: Total (a) thrust force coefficient, and (b) radial force coefficient for the band-stop filter and frequency content minimization techniques, λ=1.32 (NACA 0015, *c* = 420 mm, β = 0°)

From Figure 5.14 it is clear that while the two filtering methods produce similar results, some small discrepancies can be observed. One possible reason for these discrepancies stems from a fundamental limitation of the frequency content minimization technique. This method is only effective when a sufficiently large number of tests cases at various flow velocities are performed such that it can be guaranteed that at least one test case does not resonate at any integer multiple of the rotational frequency. Provided that this condition is satisfied, the minimum amplitude values obtained from the minimization technique can then be said to reliably represent the underlying aerodynamic loading.

As previously described, an equivalent approach to calculating the average thrust and radial force coefficients for the band-stop filtering method would be to perform the IFFT of the average value of the filtered frequency content for U_∞ = 8, 10 and 11 m/s (z = IFFT{Avg[filt(FFT(y_8,y_{10},y_{11}))]}). This identity can be utilized to gain greater insights into the discrepancies between the two filtering methods. Comparing the frequency content obtained using the two alternate techniques at the integer multiples of the rotational frequency reveals that large relative discrepancies exist at n = 4 and 5 (Figure 5.15). This is likely due to the fact that these two multiples of the rotational frequency tend to fall between the forward and backward whirl frequencies. Because the turbine is switching between these two modes of vibration during the course of a single measurement, any integer multiple of the rotational frequency falling between them may have a tendency to be excited to some unknown extent. In turn, the two filtering methods may be treating this effect in different ways.

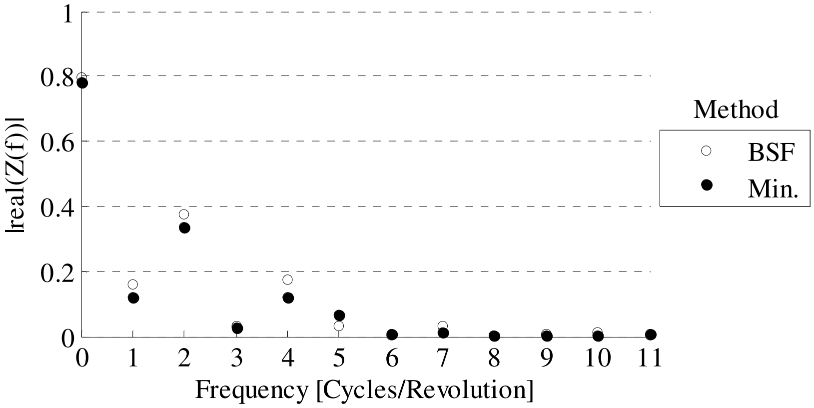

Figure 5.15: Single-sided amplitude spectrum of thrust coefficients for the bottom support strut obtained from the two alternate filtering techniques at *nf*, λ = 1.32 (NACA 0015, *c* = 420 mm, β = 0°)

The increased peak amplitude of the thrust force coefficient measurements at an angle of attack of $\theta \approx 70°$ for the band-stop filtering technique (Figure 5.14a) can likely be attributed to the increase in magnitude of the 1st , 2nd and 4th integer multiples of the rotational frequency.

From this analysis, the following conclusions can be drawn regarding the capabilities of the two alternate filtering techniques. Ultimately, both methods produce similar results when the number of available test cases is sufficient (≥ 3 in this particular sample case). The band-stop filtering technique can be applied to a data set obtained at a single flow velocity. However, it is manually intensive, time consuming, and requires a priori knowledge of the expected loading behaviour to ensure that no component of the underlying aerodynamic loading is eliminated due to filtering. The frequency content minimization technique requires a large set of data at multiple flow velocities in order to ensure that at least one case does not resonate at any given integer multiple of the rotational frequency The number of test cases necessary to obtain reliable results is a function of the distribution and number of turbine natural frequencies as well as the wind speed interval at which the data is recorded. However, it is fast and easy to apply and does not require any advanced knowledge of the expected loading behaviour. Therefore, when the number of test cases is limited the band-stop filtering (BSF) method is more appropriate, while the frequency content minimization technique (Min.) produces more consistent results when a large number of test cases are available.

5.3. Experimental Results

5.3.1. Thrust and Radial Force Coefficients

Having determined the primary sources of vibration excitation, and developed several methods to minimize or eliminate the effect of vibration response from the aerodynamic load measurements, investigation of the experimentally obtained loading behaviour can now be carried out. Figure 5.16 plots the thrust and radial force coefficients for the NACA0015, c = 420 mm, R = 1400 mm, β = 0°, test case over a range of blade speed ratios within the operational boundaries of the turbine prototype. Note that for both the thrust and radial force coefficients the mean loading component due to centrifugal loading of the blade has been removed (refer to Appendix A.4).

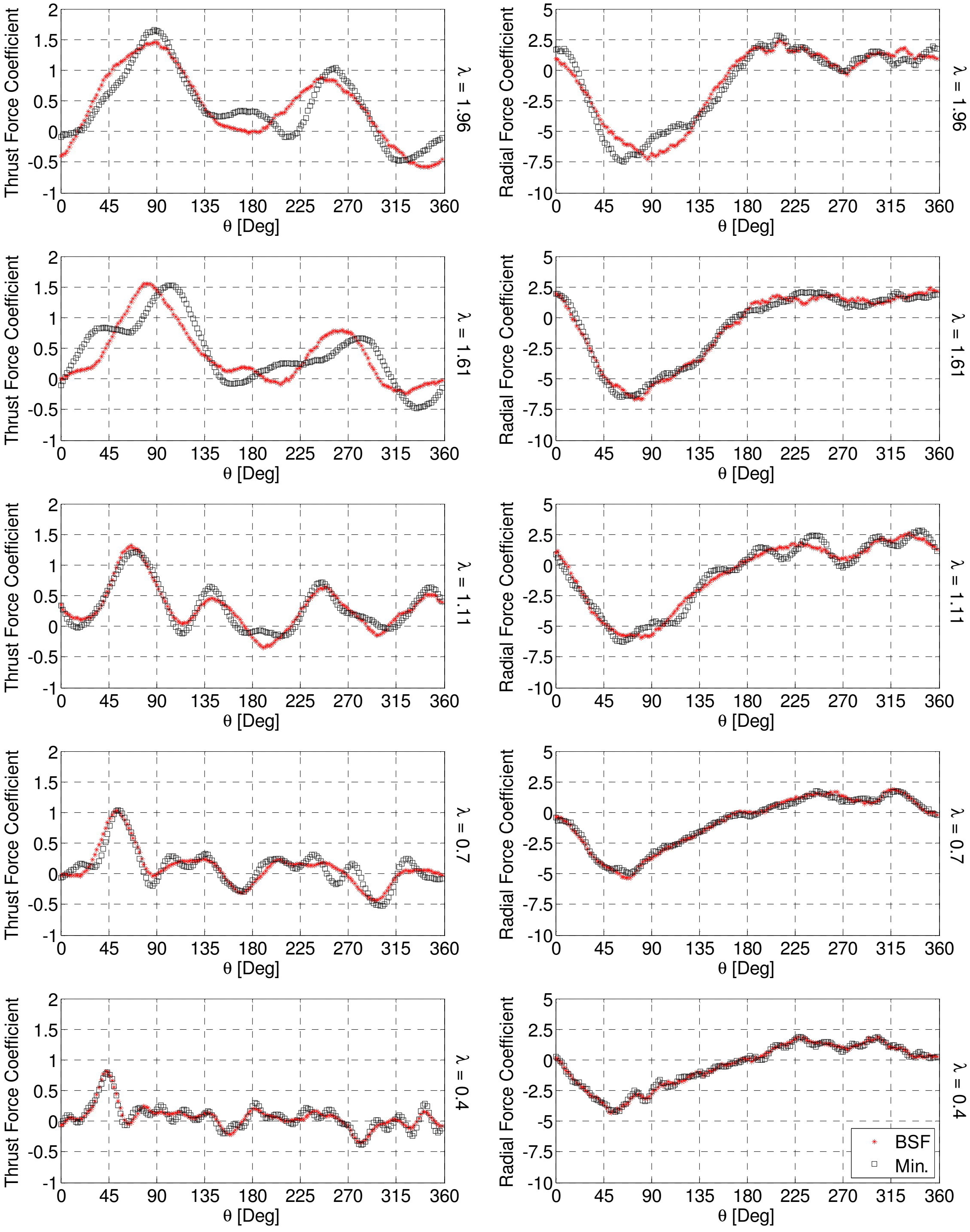

Figure 5.16: Total thrust and radial force coefficients for a single blade for the band-stop filter and frequency content minimization techniques (NACA 0015, c = 420 mm, β = 0°, with cables)

As with the preliminary numerical model results, one of the most important loading features is the primary thrust peak due to dynamic stall. This feature is consistent between the two filtering techniques for low blade speed ratios, despite some high frequency noise in the minimization technique results (λ = 0.40), and exhibits the trend of increasing amplitude and angle of attack predicted by the numerical model. At high blade speed ratios, the agreement between the two filtering techniques begins to break down, in particular because of a more erratic behaviour from the minimization technique results. The large dip in thrust loading on the primary dynamic stall peak for λ = 1.61, and the large overshoot for λ = 1.96, indicates that the conditions required to satisfy the minimization technique are not being met. Either the same integer multiple of the rotational frequency is being excited in all cases (λ = 1.61), or there are two few test cases to ensure a sufficiently diverse sample (λ = 1.96). The radial force coefficients obtained from the two filtering techniques are generally in good agreement, with the minimization technique displaying a slightly more unsteady behaviour for a number of test cases.

Based upon these results it was determined that due to its inconsistent nature, particularly at the upper and lower operational limits of the turbine where the amount of data is limited, the minimization filtering technique results will not be analysed further in this study. However, due to its ease of application, the minimization filtering technique will be used as a first approximation of the thrust and radial loading components. In doing so, the minimization technique will be used as a guide from which the band-stop filtering method can be directed. This helps to ensure that the underlying aerodynamic loading behaviour is not removed during the filtering process. Henceforth, the band-stop filtered data will be referred to simply as the ‘experimental results’.

5.3.2. Power Coefficient

As described in the Two-Dimensional Numerical Model Results section (3.3.3), the power coefficient of the turbine can be calculated directly from the average thrust force of the three turbine blades. From the experimental results, an interesting phenomenon was identified when this calculation was performed (Figure 5.17).

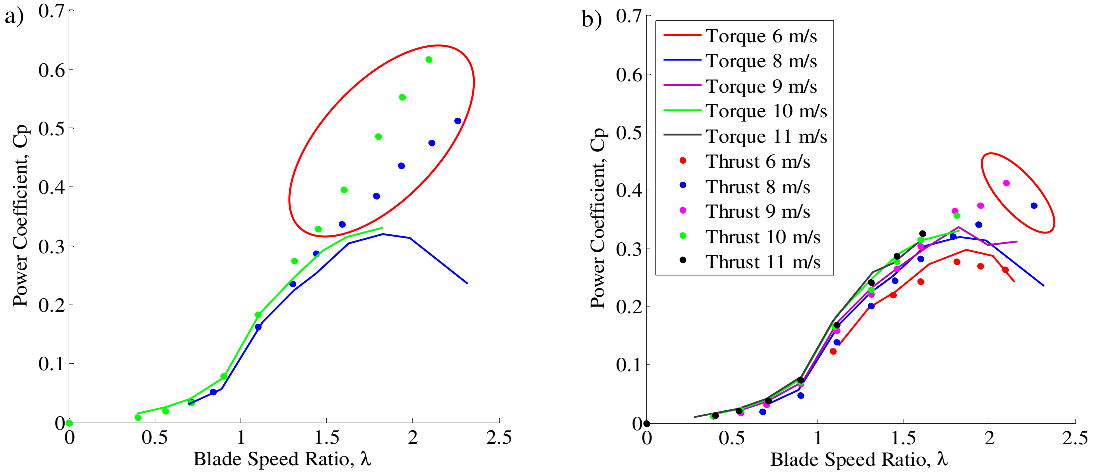

Figure 5.17: Power coefficient (a) without cables, (b) with cables. (NACA 0015, *c* = 420 mm, *β* = 0°) Red ellipses indicate regions of dynamic amplification

When the cable supports are not attached, the power coefficients calculated from the aerodynamic thrust force far over-predict those determined from the torque measurements at high blade speed ratios. However, with the cable system attached (all other conditions remaining the same), good agreement between the power coefficients measured from the shaft torque (Fiedler, 2009), and those calculated from the aerodynamic thrust, were obtained (refer to Appendix A.4 for a full description of the Centre of Gravity correction). Nevertheless, some amplification of the turbine power output calculated from the aerodynamic thrust force can also be observed for the test cases with the cables attached at very high blade speed ratios (Figure 5.17b).

Close inspection of the filtered frequency content of the thrust force measurements without and with the cable system attached reveals the reason for this discrepancy. As can be seen in Figure 5.18a, without the cables attached the second integer multiple of the rotational frequency, 2*f*, falls between the backward and forward whirl frequencies for the upper 7 test cases. This produces a strong excitation of what is expected to be a large component of the underlying aerodynamic thrust loading at high blade speed ratios (refer to Figure 3.6 and Figure 5.16). However, with the cables attached, the lower whirl frequency only approaches the second integer multiple of the rotational frequency at very high blade speed ratios ($\lambda = 2.26$).

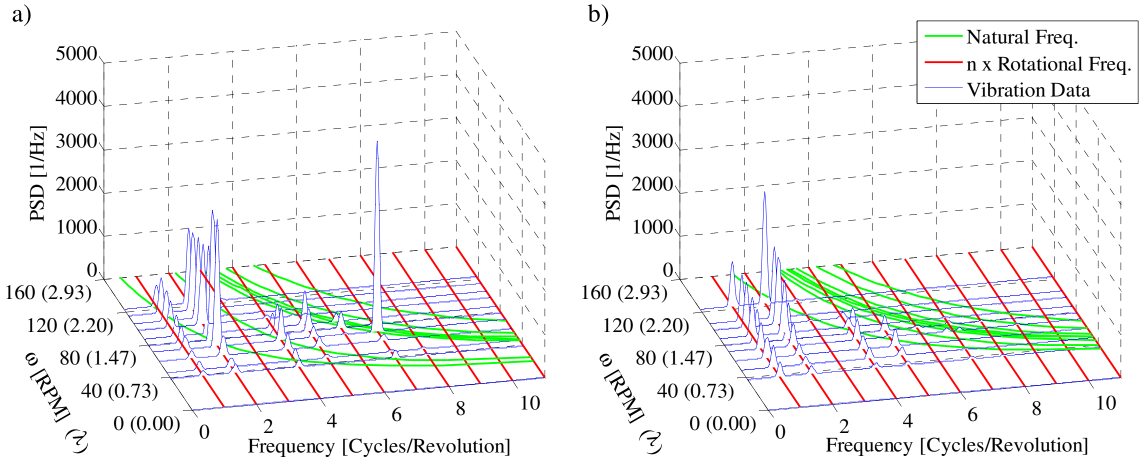

Figure 5.18: Filtered frequency content of the bottom strut thrust force (NACA 0015, c = 420 mm, β = 0°, U_∞ = 8 m/s). (a) Without cables, (b) with cables

A comparison of the thrust force measurements at a blade speed ratio of λ = 1.80, where the discrepancy is greatest, demonstrates the effect that dynamic amplification has on the loading signal (Figure 5.19). From this figure it is evident that without the cable system attached, the strut vibration has locked-in to the second integer multiple of the rotational frequency, resulting in large amplitude thrust peaks at greater angles of rotation. In turn, this results in a substantial increase in the average thrust force measured by the instrumented struts, and thus the turbine power measurement.

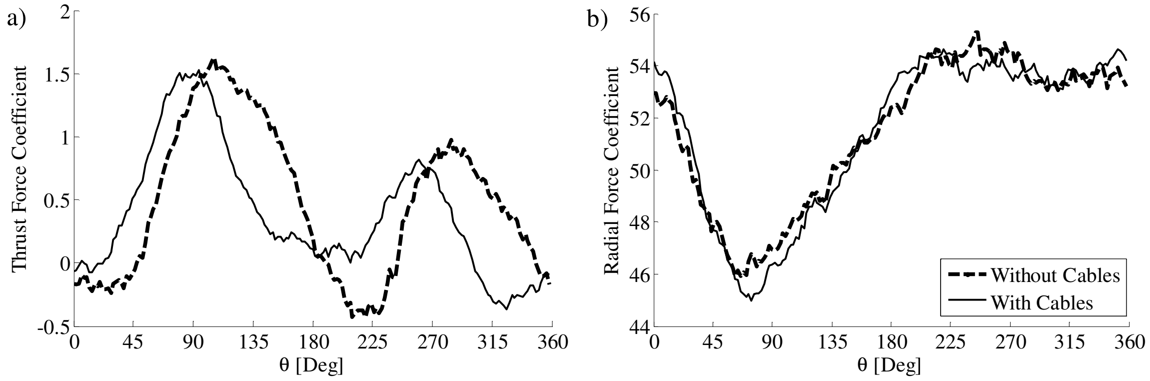

Figure 5.19: Total filtered (a) thrust, and (b) radial force measurement with and without cables, λ = 1.80. (NACA 0015, c = 420 mm, β = 0°, U_∞ = 8 m/s)

While this vibration response of the turbine has a rather profound effect on turbine thrust force, the radial force component is relatively unaffected. However, in order to avoid damaging the turbine and the thrust force measurement instrumentation in particular, as well as maximize the amount of vibration-free data, very few tests cases were performed without the cable system attached. As such, the results presented within the remainder of the thesis will be exclusively from the tests cases where the cable support system is in place.

5.4. Summary

Based upon a series of preliminary studies, it was determined that the aerodynamic load measurements were going to be difficult to obtain as they were being contaminated by the very vibration response of the turbine that was being investigated. In order to overcome this challenge, a series of vibration mitigation methods were developed. The cable guy-wire system, while not practical under normal operating conditions, allowed for the natural frequencies of the turbine to be shifted so that the resonance response conditions were altered. This also greatly reduced the incidences of dynamic amplification of the force coefficient measurements. In a similar manner, by testing over a wide range of flow velocities, the resonant response conditions of the turbine could be avoided. Finally, two unique filtering techniques were developed to remove any remaining vibration component from the aerodynamic load measurements. From this analysis it was concluded that while the vibration minimization technique could be used to obtain a quick first approximation of the aerodynamic forces, use of the band-stop filtering (BSF) technique resulted in more reliable and repeatable results.

By developing and applying these vibration mitigation methodologies, the true underlying aerodynamic forces on the turbine blades were determined. This is an important contribution of this research as the available experimental database was appreciably expanded as a result. In particular, aerodynamic force coefficient data and turbine vibration response for full-scale, high solidity VAWTs operating at low blade speed ratios and high Reynolds numbers were obtained.

CHAPTER 6

NUMERICAL MODEL VALIDATION AND APPLICATION

Having overcome the complications involved in obtaining measurements free from the effects of turbine vibration response, a reliable representation of the true underlying aerodynamic loading has now been obtained. It is this data to which the numerical model can be compared in order to assess its capabilities.

The following chapter will include an analysis of the numerical model's ability to properly determine the effect of dynamic stall on the aerodynamic force coefficients, vibration excitation loading, turbine power output, and wake behaviour. An in-depth investigation into the sources and scales of three-dimensional flow effects, including flow divergence around the turbine and parasitic losses, will then be undertaken. Finally, the effects of a change in the preset pitch of the blade, β, and the blade thickness ratio, t/c, on the power producing loads and vibration excitation and response behaviour of the turbine will be thoroughly explored.

6.1. Initial Comparison

6.1.1. Thrust and Radial Force Coefficients

A sample comparison of the thrust and radial force coefficients predicted by the numerical model against those measured experimentally for the NACA0015, $c = 420$ mm, $R = 1400$ mm, $\beta = 0°$ test case are given in Figure 6.1 below. While the agreement between the numerical predictions and the experimental results is in general quite good, some discrepancies can be seen to exist. The location of the peak in the thrust force coefficient on the upstream portion of the rotation ($0 \leq \theta < 180$) is well modelled, however higher than experimental amplitudes are predicted. Additionally, at high blade speed ratios ($\lambda \geq 1.4$) the experimental results indicate the presence of a second large thrust peak on the downstream half of the rotation ($180 \leq \theta < 360$), while the numerical model predicts a more constant thrust force. Due to the fact that large vortex structures are being shed from the airfoil surfaces and convected downstream along with the blades (refer to Figure 3.8 and Fiedler, 2009), it is not unexpected that the numerical model will encounter difficulties in solving the highly separated, complex flows in this region.

In general, the radial force coefficient predictions are quite accurate, despite the existence of some high frequency fluctuations predicted by the numerical model at low blade speed ratios. Note that due to an inherent variability in turbine rotational velocity (refer to section 4.2.2), for a given blade speed ratio the mean radial force component due to centrifugal loading fluctuated somewhat from one test case to another. In order to minimize this discrepancy, the mean value of the experimental radial force coefficient measurement was corrected for by setting it equal to the mean aerodynamic radial force coefficient predicted by the numerical model. Streamwise and cross-stream force coefficients are not a function of the mean radial loading component, and as such are unaffected by this minor correction.

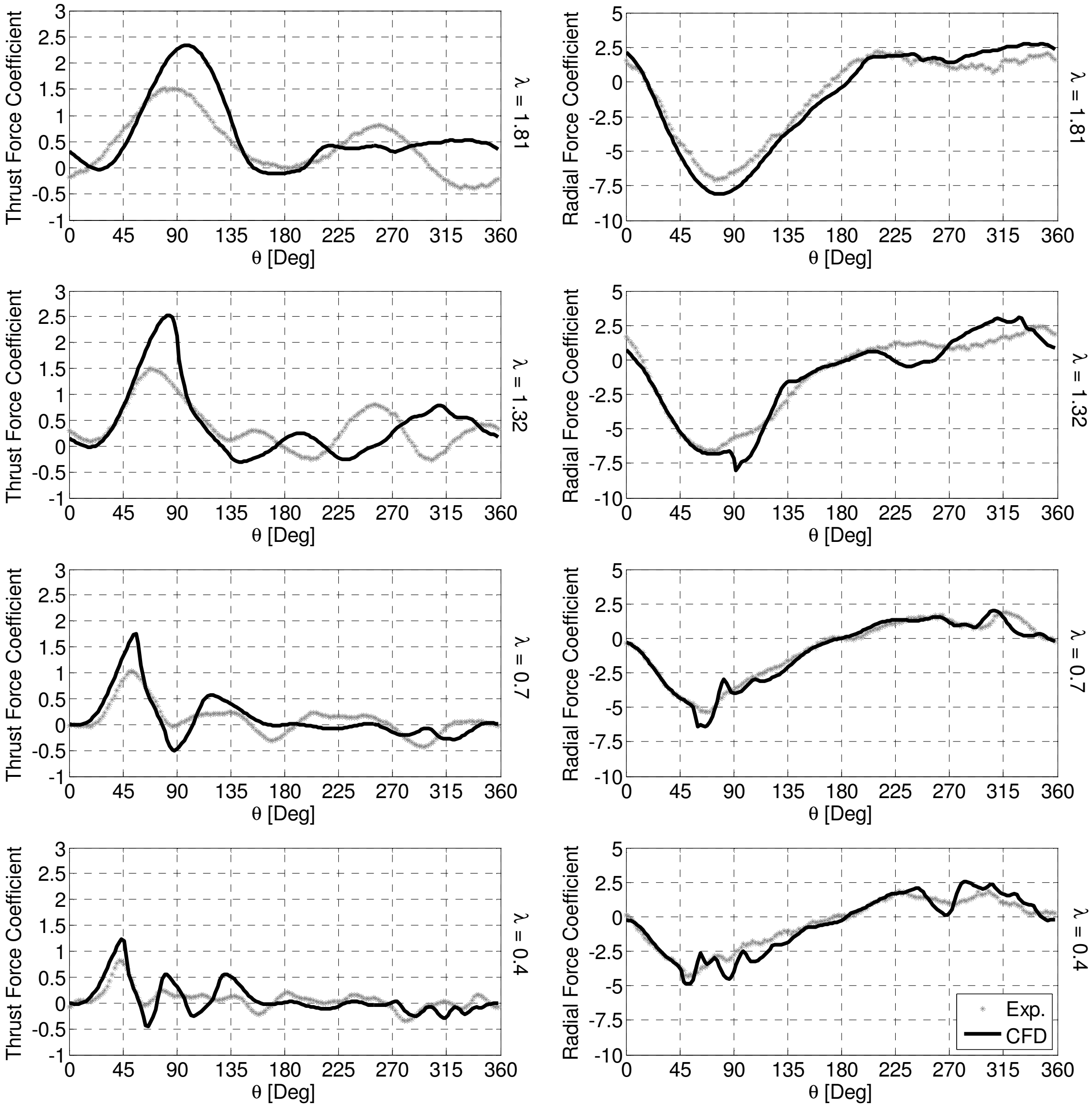

Figure 6.1: Numerical and experimental thrust and radial force coefficients for λ = 1.81, 1.32, 0.7, and 0.4 (NACA 0015, *c* = 420 mm, *β* = 0°)

The thrust and radial force coefficients over the entire operating range of the turbine can be illustrated as a contour plot to more clearly show the change in loading behaviour with blade speed ratio. As can be seen in Figure 6.2, the numerical model predicts the increase in amplitude, angle of rotation, and broadness of the primary dynamic stall peak that accompany an increase in the blade speed ratio, and thus a decrease in the relative angle of attack. The over-prediction of the magnitude of the thrust peak by the numerical model at high blade speed ratios can also be seen.

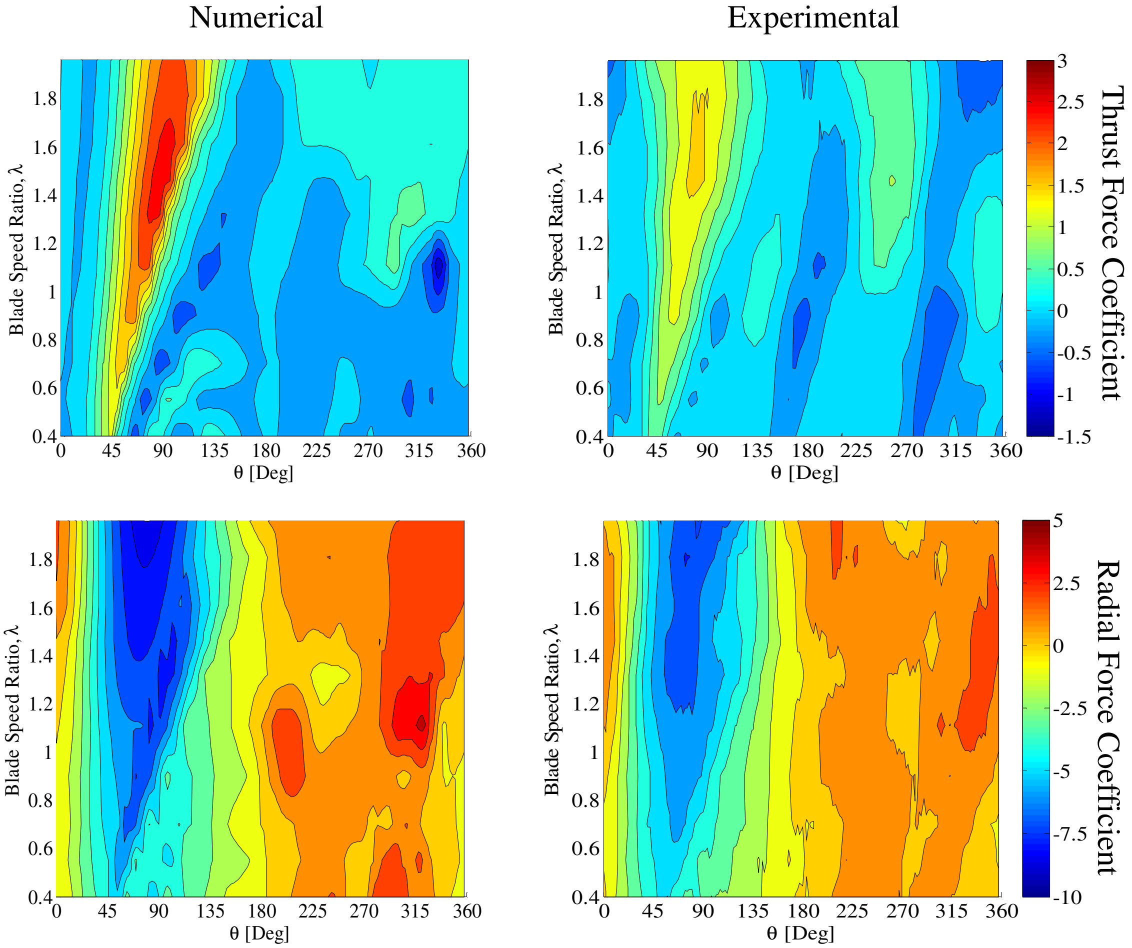

Figure 6.2: Contour plot of numerical and experimental thrust and radial force coefficients, (NACA 0015, c = 420 mm, $\beta = 0°$)

6.1.2. Vibration Excitation Loads

As with the preliminary numerical model results, the vibration excitation loads applied to the entire turbine can be calculated by performing a vector summation of the streamwise and cross-stream force coefficients applied to the three turbine blades. While the force coefficients were only measured on one blade, it can be assumed that there is equivalent loading behaviour on the other two blades, simply offset by 120 and 240° of rotation. A sample of the vector summation of the loading on all three blades predicted by the numerical model, and measured experimentally, is given in Figure 6.3.

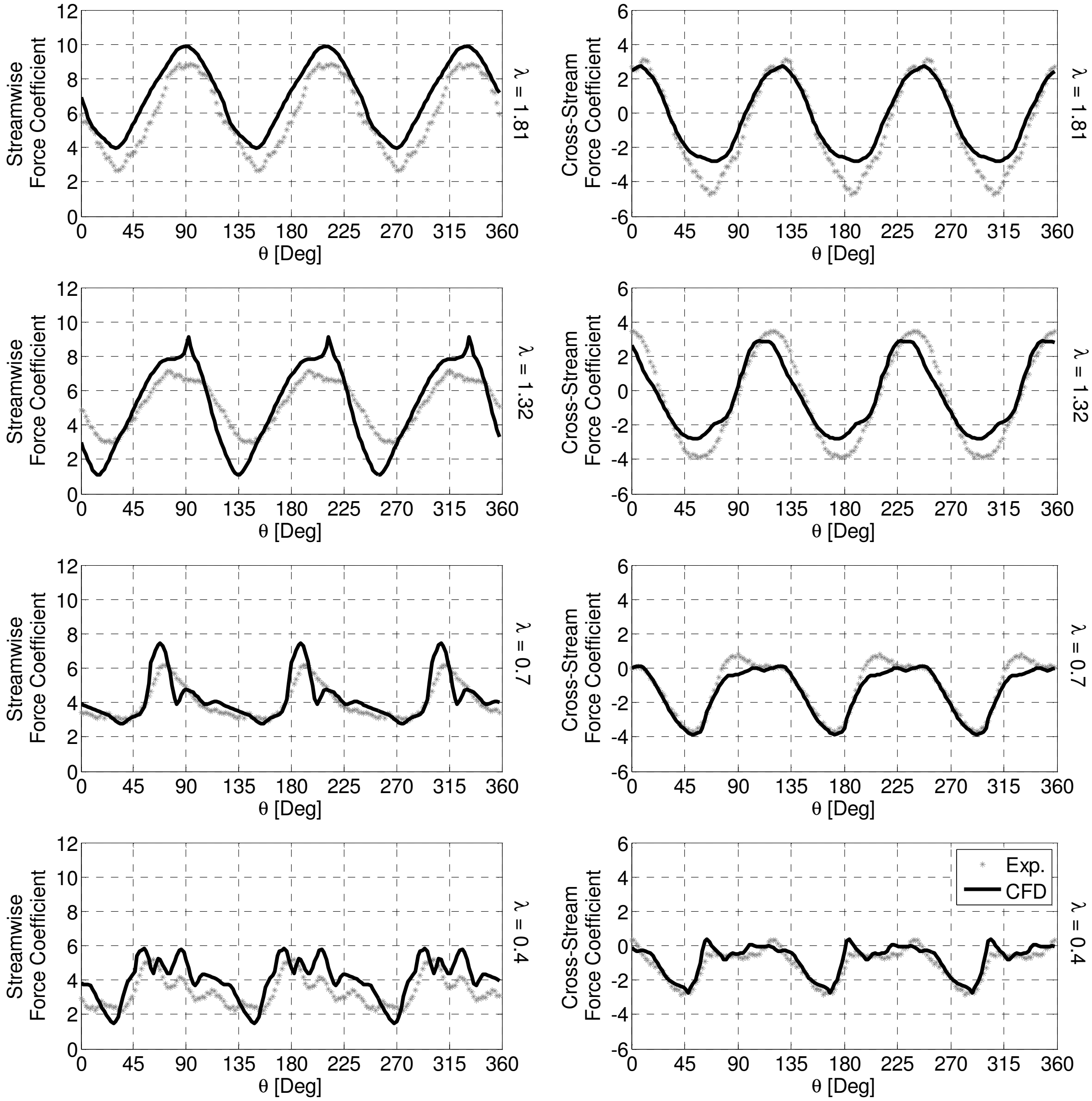

Figure 6.3: Numerical and experimental streamwise and cross-stream force coefficients for λ = 1.81, 1.32, 0.7, and 0.4 (NACA 0015, *c* = 420 mm, *β* = 0°)

The predictive capabilities of the numerical model are shown to be quite good when comparing the CFD vibration excitation loads to those obtained experimentally. The nearly sinusoidal loading at high blade speed ratios, and more impulsive loading behaviour at low blade speed ratios, is generally well modelled. However, the transition in this behaviour in the streamwise loading component at a blade speed ratio of $\lambda = 1.32$ is not well predicted. Additionally, the mean value of the streamwise force component is over-predicted for nearly all blade speed ratios tested. The prediction of the cross-stream loading component however is good for all blade speed ratios within the operational capabilities of the turbine prototype. In order to look at the effect that the streamwise and cross-stream loading components will have on excitation of the turbine structural modes, Figure 6.4 plots the two vibration excitation loads against one another. As expected, the phase lag between the streamwise and cross-stream loading peaks results in an orbital loading pattern applied at a rate of three cycles per revolution. This will undoubtedly contribute to excitation of the primary whirling mode of the turbine.

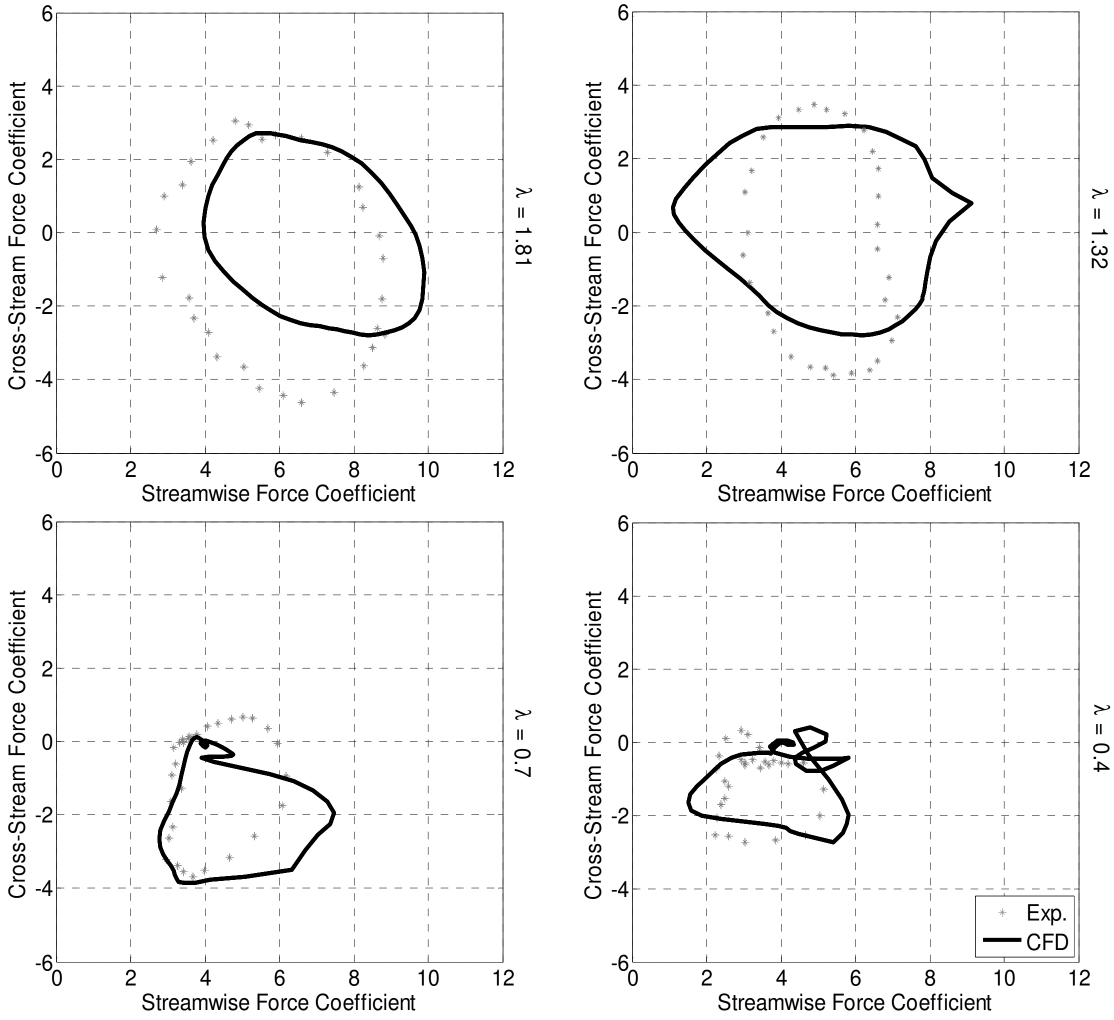

Figure 6.4: Numerical and experimental streamwise and cross-stream force coefficients for λ = 1.81, 1.32, 0.7, and 0.4 (NACA 0015, *c* = 420 mm, *β* = 0°)

6.1.3. Power Coefficient

While the streamwise and cross-stream force coefficients illustrate the total vibration excitation loading, which is primarily a function of the radial force component; the turbine power coefficient demonstrates the gross effect of thrust loading. When the power coefficients calculated from the thrust force measurements are compared to the CFD simulation results, it is clear that the maximum power coefficient, as well as the blade speed ratio at which it occurs, is considerably over-predicted (Figure 6.5), as was observed by Howell et al. (2010). Note that because of the high vibration response of the turbine prototype at high blade speed ratios ($\lambda > 2$), thrust force measurements were not obtained beyond this threshold. However, power coefficients obtained from turbine torque measurements indicate that peak gross power output does occur at a blade speed ratio of $\lambda \approx 1.9$ (refer to Figure A.18).

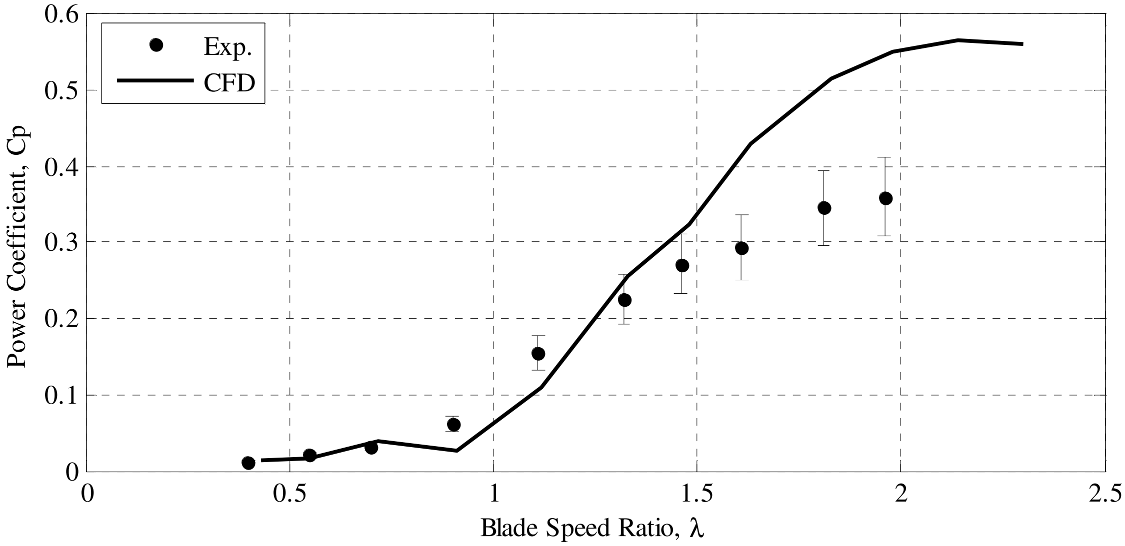

Figure 6.5: Numerical and experimental gross power coefficients (NACA 0015, c = 420 mm, β = 0°)

It is hypothesised that this discrepancy in power coefficient amplitudes is primarily a result of the finite height of the wind turbine prototype, resulting in two distinct three-dimensional flow mechanisms not modeled in the CFD simulations. Firstly, due to the finite aspect ratio of the entire turbine, flow is able to pass both above and below the turbine swept area, effectively reducing the oncoming wind velocity, and thus the power available in the flow (McLaren et al., 2011). Secondly, because of the finite aspect ratio of the blades themselves as well as the presence of the support struts, parasitic drag in the form of induced drag from tip-vortices (Howell et al., 2010) and interference drag, is expected to occur. Because of the substantial impact that these two three-dimensional flow mechanisms will have on the predictive capabilities of the numerical model, a detailed investigation of the relative scale of their effects will be carried out (Section 6.2).

6.1.4. Wake Measurements

Analysis of the flow velocity through, around, and downstream of the turbine allows for further understanding of the conversion of flow momentum to mechanical power by the turbine. Figure 6.6 depicts the time averaged streamwise velocity profiles for a series of stream-wise positions near peak turbine power production (λ = 1.7), normalized by U_∞. While Figure 6.6 only plots the velocity profiles within 2 radii of the turbine in the cross-stream direction, the simulation domain extends 8 radii on either side of the turbine central shaft. At this distance, the velocity and pressure profiles asymptote to their respective free-stream values.

In the numerical model predictions, significant flow momentum extraction occurs through the turbine; reducing the bulk flow velocity by up to 40% of its free-stream value just one chord length downstream of the upstream pass ($0.7R$ Upstream), by 50% at the centreline of the turbine (Mid Turbine), and by 60% one chord length upstream of the downstream pass ($0.7R$ Downstream). Furthermore, a region of nearly stagnant flow is predicted just two radii downstream of the central shaft ($2.0R$ Downstream). While this indicates that a significant amount of flow momentum has been extracted by the turbine as mechanical power, this has large negative implications for the prospect of placing numerous turbines within close proximity of one another. This decrease in streamwise flow velocity through the turbine is partially due to the effective blockage of the turbine which also results in local flow acceleration around the turbine of up to 20%. Disturbances in the normalized time averaged flow velocities at the centreline of the turbine (at $y = 0$ and ± $1R$), one chord length downstream of the upstream pass (at $y = \pm 0.7R$), and one chord length upstream of the downstream pass (at $y = \pm 0.7R$) are a result of the displacement of fluid by the central support shaft and the turbine blades as they pass.

Experimental streamwise velocity measurements obtained at mid-height of the turbine are plotted with the numerical model predictions in Figure 6.6. From this figure it is clear that the numerical model wake predictions agree particularly well with the experimental results on the side of the turbine where the blades are travelling downstream and shedding vortices into the turbine wake. As the flow reaches $2.0R$ downstream of the turbine, both the experimental and numerical results show that the velocity profile amplitude decreases substantially. Experimental measurements confirm that a large region of nearly stagnant flow is present at just $2.0R$ downstream of the turbine centreline, a testament to the drastic reduction in flow momentum through a very high solidity turbine. However, the numerical model predicts considerably higher flow velocities on the side of the turbine where the blades are travelling upstream ($0.5R \leq y \leq 1R$). On average, the streamwise flow velocity predicted by the numerical model is 20% higher than the experimental measurements at this downstream position. As the flow progresses further downstream to $3.0R$, the numerical velocity profile prediction begins to evolve into a more top-hat distribution as per the experimental measurements. At this downstream location, the high local flow velocity through the turbine predicted at $2.0R$ downstream (centred at $y = 0.3R$) has been greatly reduced. However, the numerical model is now predicting an average streamwise flow velocity 25% higher than the experimental measurements.

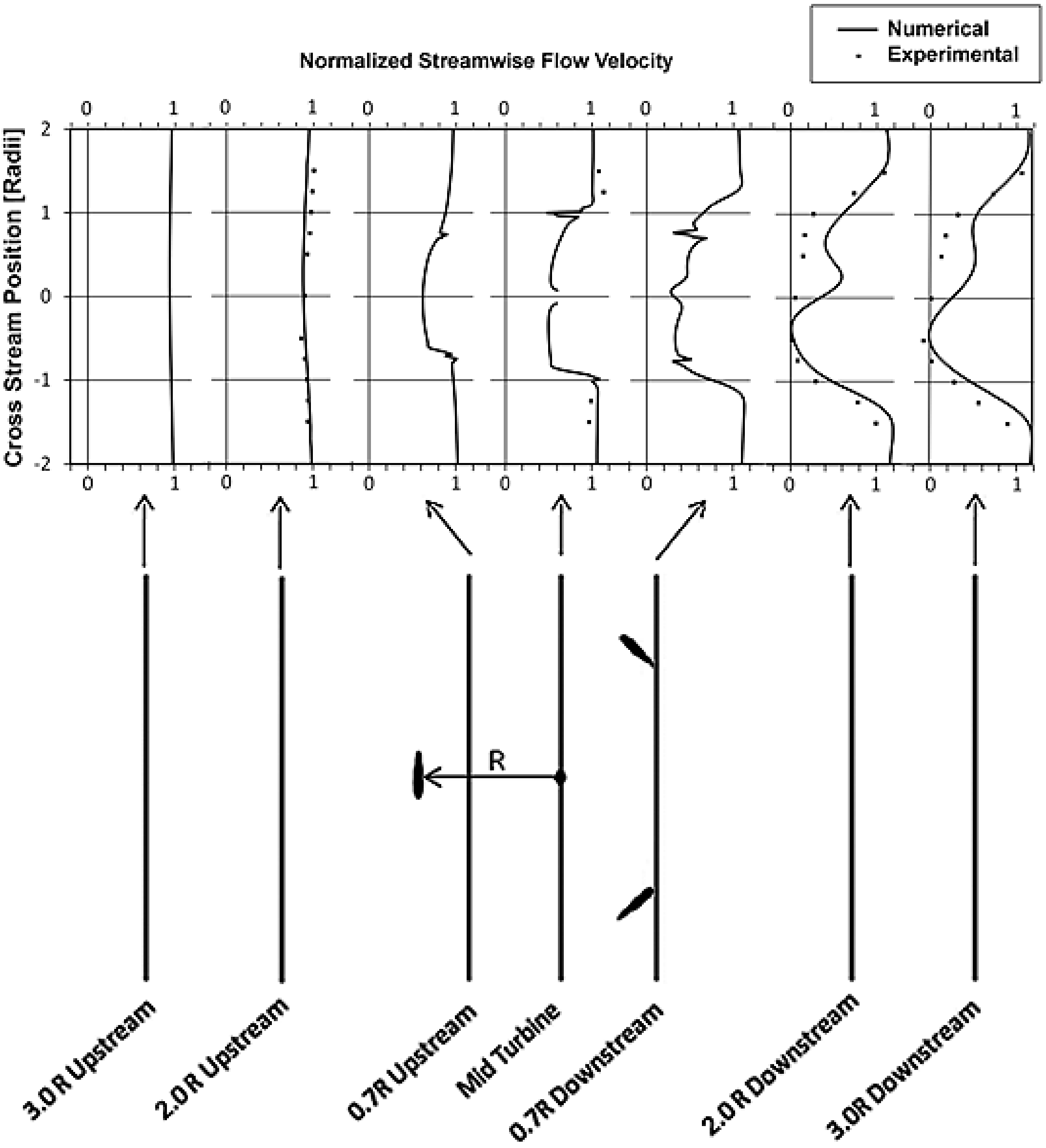

Figure 6.6: Numerical and experimental normalized time averaged flow velocity profiles about the turbine, displaying momentum extraction through the turbine and flow acceleration around the turbine (NACA 0015, c = 420 mm, λ = 1.7, U_∞ = 8 m/s, β = -3.34°). Profiles are labelled according to their distance upstream or downstream of the turbine centre

6.2. Three-Dimensional Effects

Early on in the development of the numerical model, it was identified that the analysis domain would have to be limited to a two-dimensional cross-section of the turbine. This is due to the computational requirements imposed by the high mesh density necessary to properly resolve the flow field close to the surface of the blade and satisfy the conditions of the turbulence model. As noted by Hamada et al. (2008), in order to solve a three-dimensional unsteady flow for a full-scale VAWT at flow velocities of practical interest, a substantial increase in the number of mesh nodes and simulation time would be required. In order to sufficiently resolve the solution domain for a three-dimensional turbine simulation, it is predicted that the number of nodal points would have to be increased by a factor of at least 50 times the current number of nearly 500,000. For the present two-dimensional numerical model, simulation of one rotation at a single blade speed ratio takes approximately one day. Thus, in order to simulate the five rotations necessary to overcome initial condition effects for a much larger three-dimensional model, a total of approximately 250 days would be required to simulate just one blade speed ratio. While some effort has been made to increase the resources with which to perform these simulations, even a 10 fold increase in the computing power would only reduce the simulation time to approximately 1 month.

From a turbine design perspective, given the current realizable computational resources, simulation of the entire three-dimensional domain is not a practical endeavour. As such, the three-dimensional flow effects encountered experimentally must now be identified and corrected for if an objective comparison to the two-dimensional numerical model is to be made.

6.2.1. Flow Divergence (Effective Velocity)

As the upstream flow approaches the wind turbine, due to the effective blockage introduced by the rotating blades, flow will tend to diverge around the entire turbine. For the two-dimensional numerical model, this effect is restricted so that the flow is only capable of diverging around either side of the turbine. For the finite aspect ratio turbine prototype however, the flow is not restricted in this manner and is able to pass both above and below the swept area of the turbine.

From Figure 6.7a it can be seen that the streamtube approaching the two-dimensional turbine model expands horizontally directly upstream of the turbine. Due to the condition of conservation of mass within a streamtube, this must result in a decrease in the average upstream flow velocity, $U_{Upstream}$. For the finite aspect ratio turbine (Figure 6.7b), these flow divergence effects are exaggerated by the fact that the flow can pass above and below the turbine. As a result, the increase in the area of the streamtube upstream of the turbine is far greater, resulting in a much more substantial decrease in average upstream flow velocity, and thus the power available to the turbine. Downstream of the finite aspect ratio turbine, the streamtube area has again increased considerably and as a result the average flow velocity is much less than that downstream of the infinite aspect ratio model, as seen in the turbine wake measurements (Figure 6.6). The primary effect of the finite aspect ratio of the turbine prototype is to reduce the average flow velocity entering the turbine in comparison to that predicted by the infinite aspect ratio numerical model, despite having the same far upstream average flow velocity, U_∞.

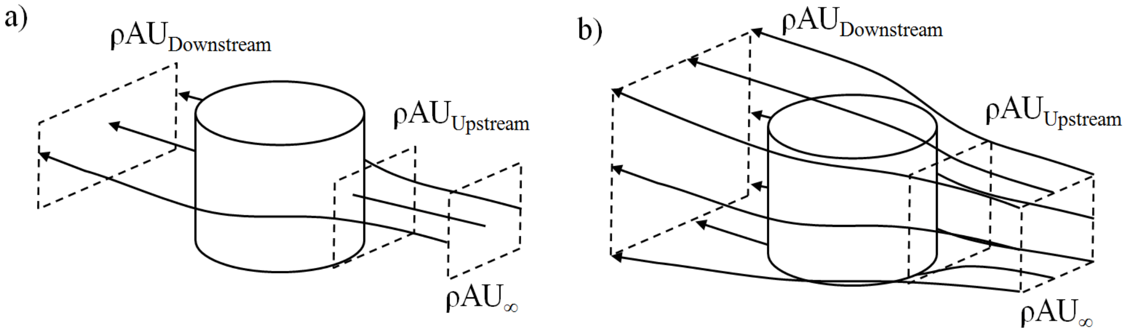

Figure 6.7: Streamtube divergence around the (a) two-dimensional, and (b) three-dimensional wind turbine

Based upon the simple streamtube analysis given above, it can be concluded that as a result of flow diverging above and below the turbine prototype, the two-dimensional numerical model cross-section is subjected to an effectively higher flow velocity. In turn, this would result in the higher force coefficients (Figure 6.1), turbine power output (Figure 6.5), and downstream wake velocities (Figure 6.6) observed. In order to correct for these differences, a flow velocity correction factor, κ, can be applied to more correctly describe the upstream velocity seen by the two-dimensional numerical model, prior to normalizing the numerical model results.

$$U_{Eff} = \kappa U_{\infty} \tag{6.1}$$

The result of applying a velocity correction factor (increasing the numerical model's effective flow velocity) is to increase the effective dynamic pressure force as well as the effective power available in the oncoming flow. In turn, this decreases the effective blade speed ratio of the turbine as well as the amplitude of the force and power coefficient predictions.

$$\lambda = \frac{\omega R}{U_{\infty}}\,; \qquad \lambda_{Eff} = \frac{\omega R}{U_{Eff}} = \frac{\lambda}{\kappa} \tag{6.2}$$

$$C_F = \frac{F}{\frac{1}{2}\rho U_{\infty}^2 cH}; \qquad C_{F\,Eff} = \frac{F}{\frac{1}{2}\rho U_{Eff}^2 cH} = \frac{C_F}{\kappa^2} \tag{6.3}$$

$$C_P = \frac{P_T}{\frac{1}{2}\rho U_{\infty}^3 2RH}\,; \qquad C_{P\,Eff} = \frac{P_T}{\frac{1}{2}\rho U_{Eff}^3 2RH} = \frac{C_P}{\kappa^3} \tag{6.4}$$

Because the average turbine streamwise force is a direct function of the velocity deficit through the turbine, this velocity correction factor can be determined by calculating the ratio of the average turbine streamwise force coefficients predicted by the numerical model to those measured experimentally. This process is complicated by the fact that the blade speed ratio at which the comparison is being made is also scaled by the velocity correction factor. As such, a second order polynomial was fit to the experimental results and the correction factor was iteratively applied to the numerical model results until the least-squares error was obtained. This calculation was performed for all blade speed ratios, blade shapes, and preset pitch angles for which experimental data was available. In order to determine the validity of these results, a reference calculation of the velocity correction factor was also performed for a perforated circular cylinder of 40% open area with an infinite aspect ratio to that with an aspect ratio of 1.2 (Blevins, 1984). From this analysis, the velocity correction factors given in Table 3 were determined.

Test Case		κ
Perforated Circular Cylinder (40% open area)		1.13
Blade Type	Chord length [mm]	
NACA0015	420	1.10
NACA0015	400	1.14
NACA0021	400	1.07

Table 3: Velocity correction factors

While there is some variation between the three different airfoils tested, likely due to a change in the effective blockage of the turbine, good agreement is observed in comparison to the perforated circular cylinder reference case. This correction factor also agrees well with the increase in average streamwise flow velocity predicted by the numerical model in the near wake field of the turbine (Figure 6.6). With this correction factor applied, an improvement in the average cross-stream force coefficient predictions can also be observed (Figure 6.8b).

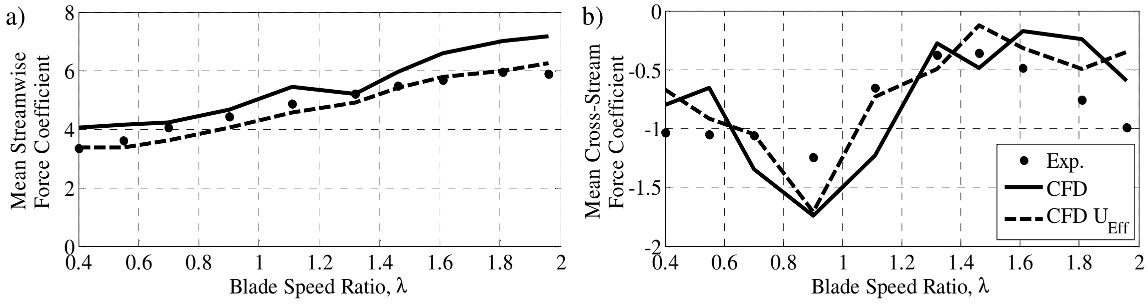

Figure 6.8: Average numerical and experimental (a) streamwise, and (b) cross-stream force coefficients (NACA 0015, *c* = 420 mm, *β* = 0°)

The impact of the velocity correction factor is substantial when comparing the effective thrust and radial force coefficients (Figure 6.9). In general, peak thrust force amplitudes have been reduced by as much as 20%, resulting in improved agreement in the primary dynamic stall peak behaviour. While the initial radial force coefficient predictions were quite good, effective numerical model predictions are now extremely accurate throughout the entire rotation for all blade speed ratios.

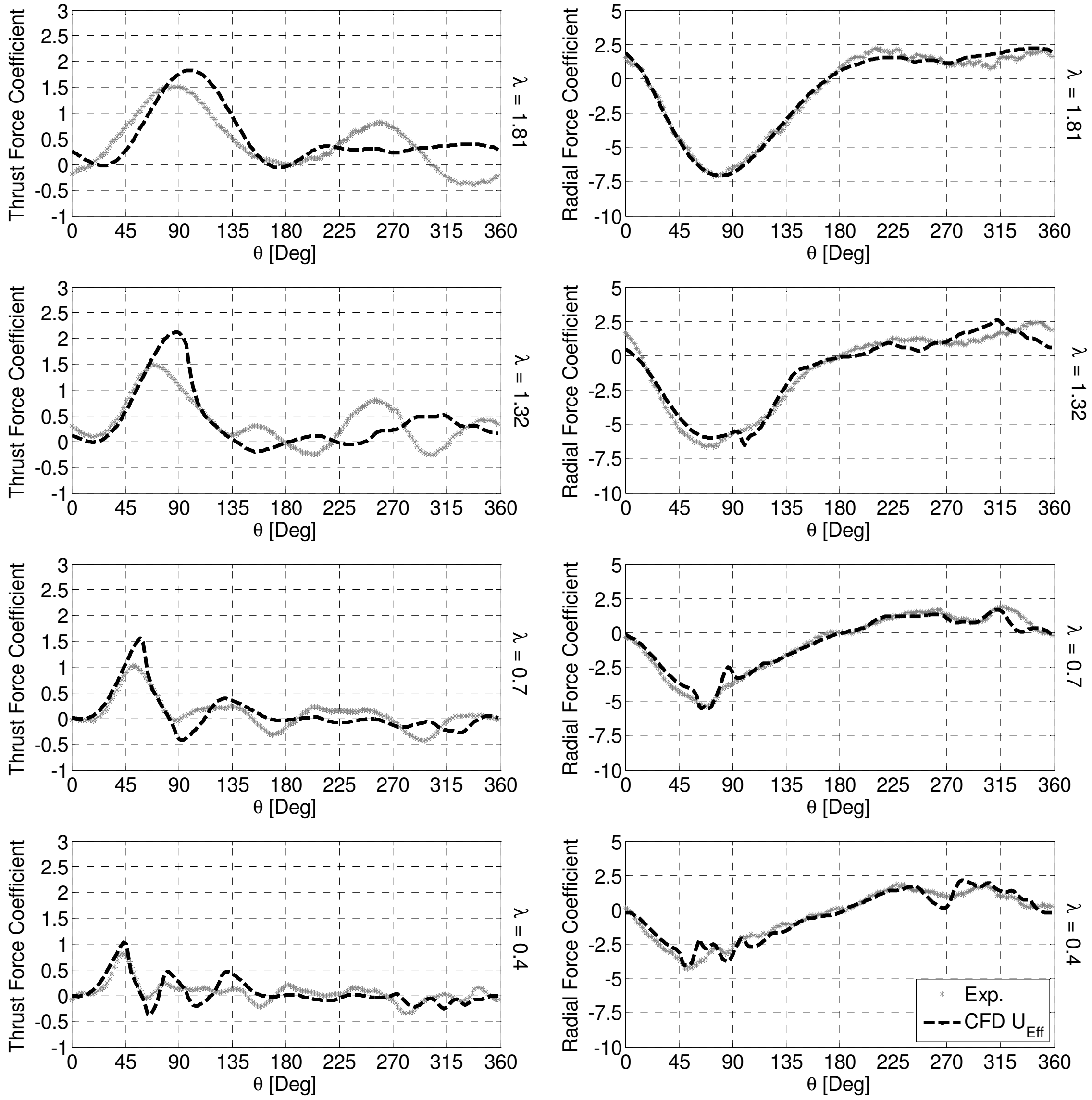

Figure 6.9: Effective numerical (κ = 1.10) and experimental thrust and radial force coefficients for λ = 1.81, 1.32, 0.7, and 0.4 (NACA 0015, c = 420 mm, β = 0°)

Note that because of the change in blade speed ratio imposed by a change in the effective inlet flow velocity, a revised set of numerical model simulations were performed in order to make a direct comparison with existing experimental results. As an example, experimental results were obtained at a blade speed ratio of $\lambda = 0.70$ for the NACA 0015, $c = 420$ mm, $\beta = 0°$, test case. In order to compare the effective numerical model to these results, a simulation at $\lambda = 0.77$ was performed so that when the velocity correction factor was applied, the two test cases would be at the same effective blade speed ratio ($0.77 / \kappa = 0.70$).

The numerically predicted streamwise and cross-stream force coefficients, which are mainly a function of radial loading, are also considerably improved by the application of a velocity correction factor (Figure 6.10). In particular, a change in the effective blade speed ratio has resulted in a more accurate prediction of the transition in the streamwise force coefficient behaviour at a blade speed ratio of $\lambda = 1.32$. The transition from the impulsive loading behaviour at low blade speed ratios to the sinusoidal loading behaviour at high blade speed ratios is now more accurately reproduced by the effective numerical model.

Applying the velocity correction factor to the turbine power coefficient calculation has an even more profound effect on the predictive capabilities of the numerical model. While the force coefficient amplitudes have been reduced by a factor of $1/\kappa^2$, power coefficient amplitudes have been reduced by a factor of $1/\kappa^3$. Additionally, the blade speed ratio has been reduced by a factor of $1/\kappa$. As a result, the blade speed ratio and amplitude of the peak power coefficient predicted by the numerical model are now more representative of the experimentally measured values (Figure 6.11).

Note that, in addition to flow divergence due to the finite aspect ratio of the turbine, a velocity correction factor also accounts for flow divergence due to the turbine components not included in the numerical model. These features include the struts, wireless telemetry system, generator, and steel frame upon which the turbine is mounted.

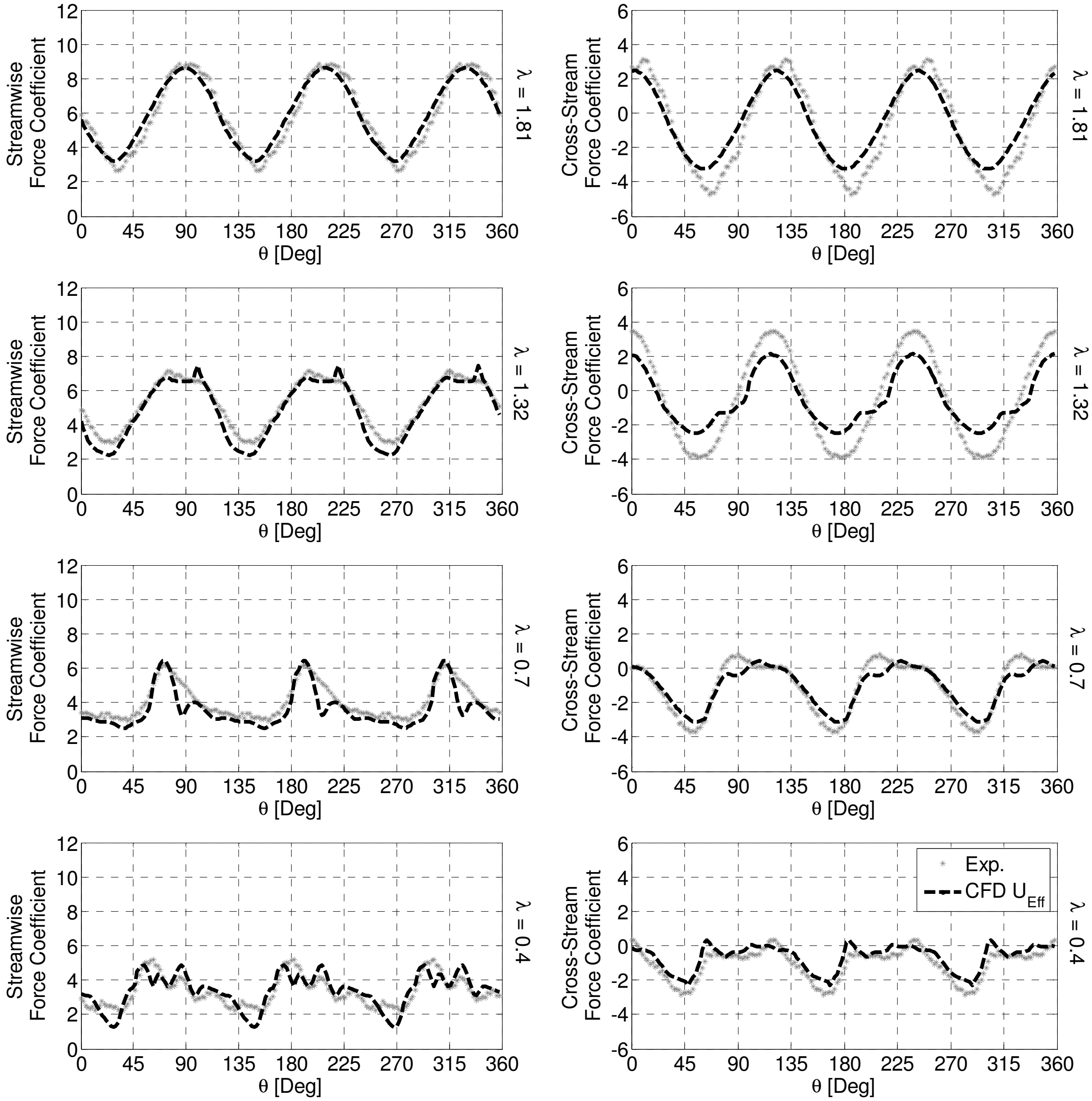

Figure 6.10: Effective numerical (*κ* = 1.10) and experimental streamwise and cross-stream force coefficients for λ = 1.81, 1.32, 0.7, and 0.4 (NACA 0015, *c* = 420 mm, *β* = 0°)

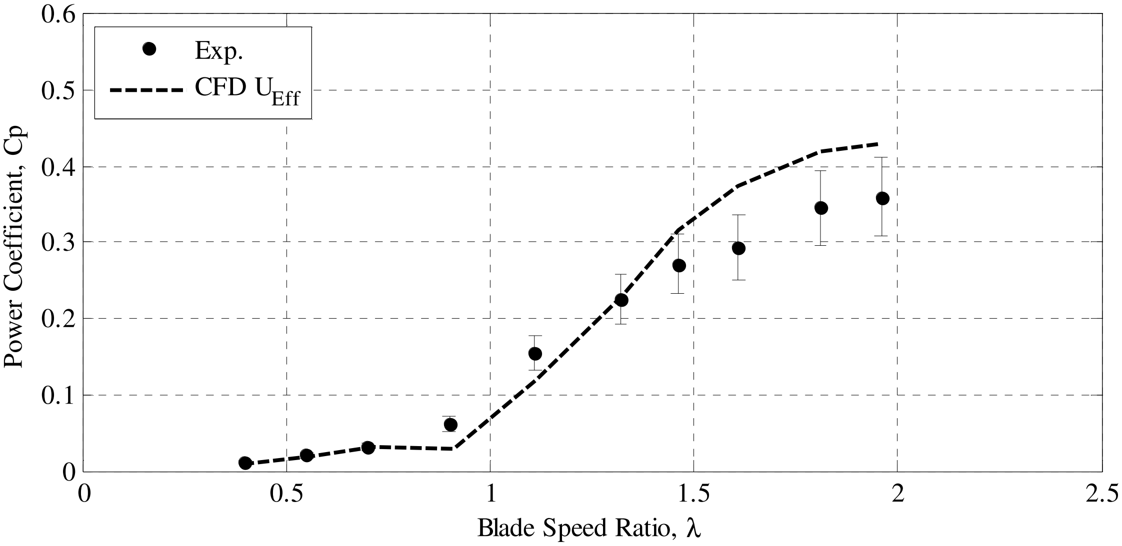

Figure 6.11: Effective numerical (*κ* = 1.10) and experimental gross power coefficients (NACA 0015, *c* = 420 mm, *β* = 0°)

While the application of a velocity correction factor, *κ*, to the numerical model inlet velocity improves the agreement in the force and power coefficient predictions, considerable discrepancy still exists in the power coefficient amplitudes at high blade speed ratios. For example, for the sample NACA 0015, *c* = 420 mm, *β* = 0°, test case, the peak power coefficient was initially over-predicted by 57%. With the velocity correction factor applied, this discrepancy has been reduced, but peak power output of the turbine is still over-predicted by approximately 20%. It is believed that this remaining discrepancy exists in part as a result of induced and parasitic drag forces. As such, these additional three-dimensional flow effects must be taken into consideration in order to improve the quality and accuracy of the numerical model predictions.

6.2.2. Induced and Parasitic Drag Forces (Effective Height)

The velocity correction factor takes into account the effect of the finite aspect ratio of the entire turbine on the blade speed ratio, force, and power coefficients. However, additional three-dimensional flow effects exist as a result of the finite length of the blades themselves, as well as the turbine structure. These three-dimensional flow features result in induced and parasitic drag forces which primarily affect the thrust force, and thus the power coefficient measurements. Conversely, these drag forces have relatively little effect on the radial loads, and thus the streamwise and cross-stream vibration excitation forces.

Induced drag, or ‘drag due to lift’, is generated from the presence of vortices at the blade tips. Due to the large pressure gradient formed between the pressure and suction sides of the airfoil that generates the characteristic lift force, fluid will flow around the ends of the airfoil from the high to low pressure regions. This results in the formation of blade-tip vortices, and a downwash of flow behind the airfoil, w (Figure 6.12).

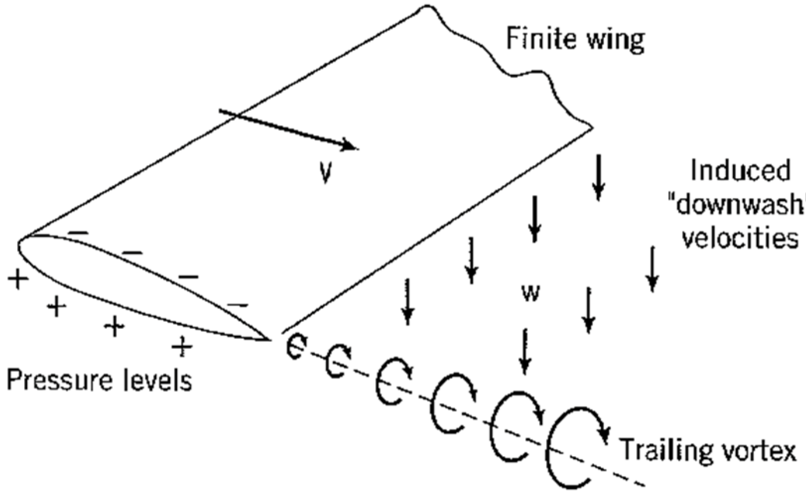

Figure 6.12: Schematic representation of the trailing vortex system of a finite wing, adapted from (Fox, McDonald, & Pritchard, 2004)

As described by the Lanchester-Prandtl wing theory for airfoils in steady flow (Abbott & Von Doenhoff, 1959), this downward component of flow causes a decrease in the effective angle of attack of a finite aspect ratio airfoil. The lift vector is tilted backward by the induced angle of attack, α_i, as a result. While the decrease in the effective angle of attack has negligible effect on the airfoil lift force component (primarily radial loading), the rearward component of the tilted lift vector causes a substantial increase in drag force (negative thrust).

As an example, Figure 6.13 plots the effect of a change in aspect ratio on both the geometric angle of attack and the total drag force coefficient for a typical airfoil predicted by the incompressible flow theory. For an aspect ratio of 7.1, characteristic of the high solidity wind turbine prototype airfoil geometry (H/c = 3000/420 = 7.1), the increase in the geometric angle of attack at peak lift is only 3°. However, the total drag force coefficient increases by a factor of approximately 5 at peak lift. Not surprisingly, this will have a substantial impact on the total thrust force, and thus power output, produced by the wind turbine airfoils.

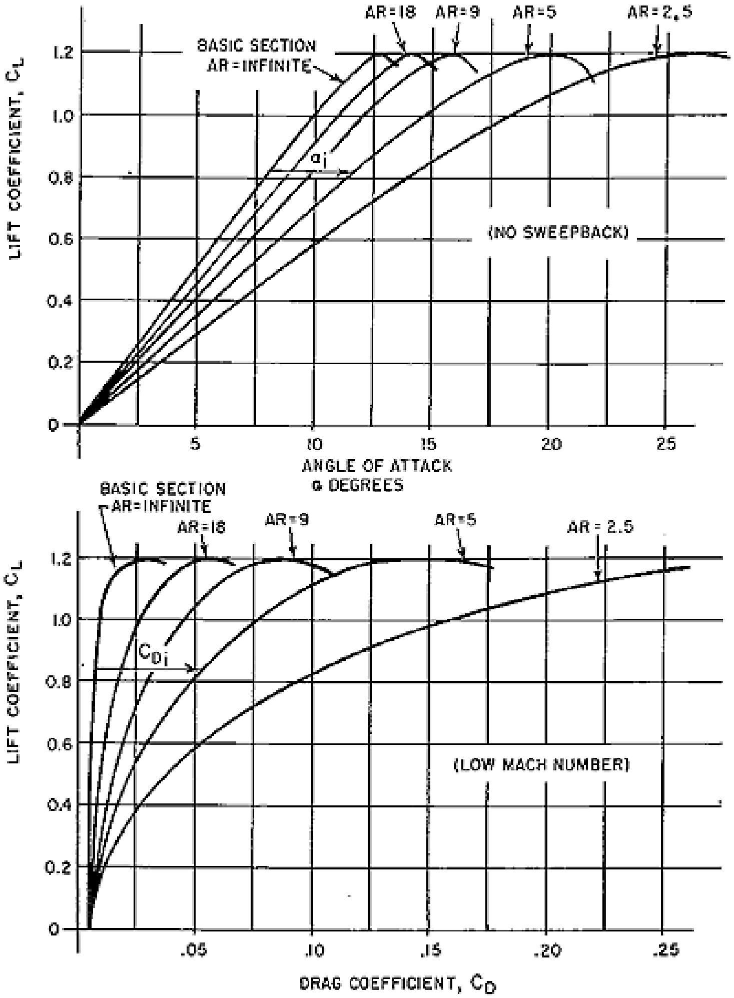

Figure 6.13: Effect of aspect ratio on airfoil characteristics, adapted from (Dole, 1981)

While this ‘lift induced drag’ theory has been developed and verified for airfoils in steady flow at low angles of attack, it is presumed that a similar three-dimensional flow mechanism exists for VAWT airfoils effectively pitching at extreme angles of attack. Clearly, for high solidity VAWTs, the pitching motion of the airfoil and the resultant formation of large vortex structures due to deep dynamic stall will have a substantial impact on the prevalence of this induced drag effect. However, some speculation on the magnitude of parasitic drag due to blade-tip losses has been discussed in previous VAWT studies (Howell et al., 2010), and some numerical models have employed the finite-wing theory for airfoils in steady flow to estimate their effects (Paraschivoiu, 2002). Ultimately, from a high solidity VAWT perspective, tip vortices can be considered as primarily a loss in the potential thrust force of the airfoil, with a rather negligible effect on radial loading.

The major source of parasitic drag is known as ‘interference drag’ and arises as a result of the support strut mounting geometry. At the end of each support strut is a relatively large rectangular aluminum block to which the blades are bolted. This block is 20 mm thick, 110 mm high, 150 mm wide, and is offset from the surface of the blade by approximately 15 mm (Figure 6.14). While the effect of the aerodynamic losses introduced by the strut and end plates themselves have been accounted for in the calculation of the experimental thrust force (refer to Appendix A.2), the interaction of the flow over the surface of the airfoil with the strut end plate and mounting bolts has not been considered. Due to the interference of the boundary layers from the airfoil and strut end plate, a small portion of the airfoil near the two support struts will not be operating at the ideal infinite aspect ratio conditions as imposed by the two-dimensional numerical model (Dole, 1981). As a result of the interference drag generated at these locations, the total thrust force produced by the airfoil experimentally will be reduced from the numerical model predictions. As with the induced drag, it is expected that this behaviour will have a relatively small effect on the airfoil radial force coefficients.

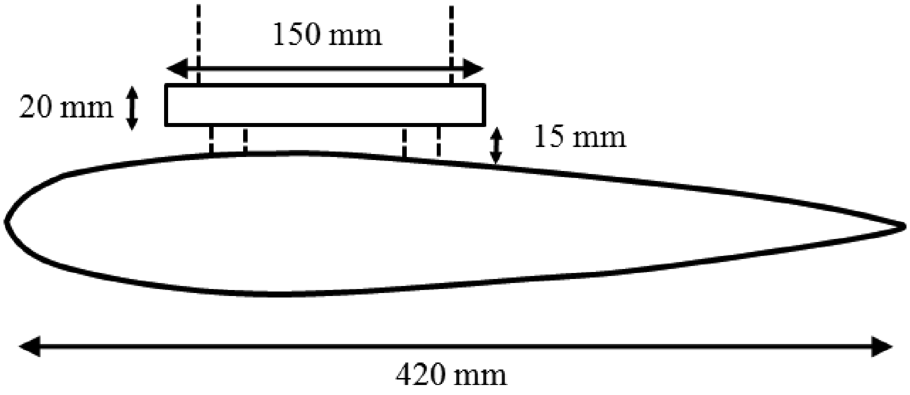

Figure 6.14: Airfoil and strut end plate cross-section at the airfoil mounting location

While the above sources of induced and parasitic drag are relatively easily understood, the individual contribution of each is difficult to predict (Dole, 1981). This challenge is further compounded given the current understanding of the influence of dynamic stall on their behaviour. As such, the effect of both induced and interference drag on the turbine thrust force and power coefficient calculations will be incorporated through the use of a simple all encompassing turbine height correction factor, τ.

When calculating the thrust force and power coefficients, it is implied that the dynamic pressure force acts along the entire length of the blade. If it is assumed that the induced and parasitic drag forces effectively reduce the length of the airfoil producing thrust, then a multiplication factor, τ, applied to the two-dimensional numerical model height will account for the additional thrust production. As indicated, because the induced and parasitic drag forces primarily effect the airfoil thrust force, this correction factor will only be applied to the thrust force and power coefficients, and not to the radial force coefficients (see Equations 6.5, 6.6, 6.7, and 6.8).

$$H_{Eff} = \tau H \qquad 6.5$$

$$C_R = \frac{F_R}{\frac{1}{2}\rho U_\infty^2 cH}; \qquad C_{R\,Eff} = \frac{F_R}{\frac{1}{2}\rho U_{Eff}^2 cH} = \frac{C_R}{\kappa^2} \qquad 6.6$$

$$C_T = \frac{F_T}{\frac{1}{2}\rho U_\infty^2 cH}; \qquad C_{T\,Eff} = \frac{F_T}{\frac{1}{2}\rho U_{Eff}^2 cH_{Eff}} = \frac{C_T}{\kappa^2 \tau} \qquad 6.7$$

$$C_P = \frac{P_T}{\frac{1}{2}\rho U_\infty^3 2RH}; \qquad C_{P\,Eff} = \frac{P_T}{\frac{1}{2}\rho U_{Eff}^3 2RH_{Eff}} = \frac{C_P}{\kappa^3 \tau} \qquad 6.8$$

Because of the difficulty associated with accurately determining the individual contributions of the induced and parasitic drag forces, the turbine height correction factor was determined by performing a least squares error analysis between the experimental power coefficients and the numerical model results with the velocity correction factor applied. The velocity and height correction factors can be determined in this sequential manner due to the nature of their formulation. The velocity correction factor is calculated based upon the average turbine drag coefficient, which is almost exclusively a function of the radial force component. Thus, application of the turbine height correction factor, which is not applied to the radial force component, has a negligible effect on the average turbine drag coefficient, and consequently the determination of the velocity correction factor. As such, the velocity correction factor can be calculated and applied independent of the turbine height correction factor.

Because of the nature of the induced and parasitic drag forces, they are not expected to be a function of the blade design or preset pitch. As such, the turbine height correction factor was calculated for all blade designs and preset pitch angles, and a universal value of τ = 1.15 was determined and applied to all numerical simulation results. Based upon the relatively low aspect ratio of the turbine airfoils ($H/c \approx 7$), and the fact that the two strut end plates cover a total of 7.3% of the blade length, this value appears to be physically realistic. The power coefficients calculated from the turbine blade thrust force measurements are plotted in Figure 6.15 against the numerical results with both the velocity and height correction factors applied for the sample NACA 0015, c = 420 mm, β = 0°, test case.

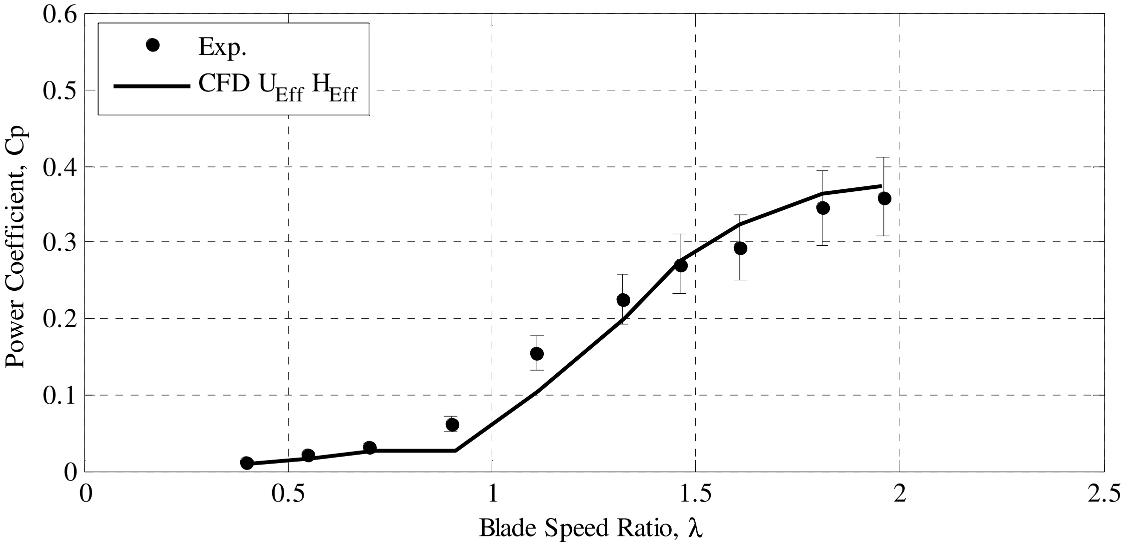

Figure 6.15: Effective numerical (κ = 1.10, τ = 1.15) and experimental gross power coefficients (NACA 0015, c = 420 mm, β = 0°)

As demonstrated by Equation 6.8, by effectively increasing the height over which the numerical model's power producing thrust force is applied, a substantial decrease in the predicted power coefficients is observed. As compared to the original, unmodified numerical model predictions, the effective numerical model results have vastly improved agreement with experimental measurements in both the peak amplitude (just 4% over-prediction) and the blade speed ratio at which it occurs ($\lambda \approx 1.9$). Clearly, calculating the power coefficient and blade speed ratio based upon an inflated effective flow velocity and accounting for additional three-dimensional losses through a turbine height correction factor, results in better overall agreement. The low power output region for $\lambda \leq 0.9$, the rapid increase in power production for $0.9 < \lambda < 1.32$, and the maximum power output plateau at $\lambda \approx 1.9$ are all well captured by the effective numerical model.

With the application of a turbine height correction factor to the predicted turbine thrust force coefficients, a proportionate decrease in amplitude is observed (Figure 6.16). Because it was identified that the radial force coefficients are independent of induced and parasitic drag forces, and thus unmodified by the turbine height correction factor, they remain unchanged (Figure 6.16). By applying both the velocity and height correction factors, the dominant three-dimensional flow effects are now taken into account and the agreement between the experimental and effective numerical model thrust and radial force coefficient predictions is vastly improved for all blade speed ratios.

For the high blade speed ratio of λ = 1.81, the gradual increase in thrust force loading predicted by the preliminary numerical studies is observed. Both the effective numerical model and the experimental results indicate a very broad, gradual increase in thrust loading on the upstream portion of the rotation, despite the nearly 14° lag in the angle of rotation predicted by the effective numerical model. The second peak in thrust loading on the downstream portion of the rotation measured experimentally is not predicted by the numerical model. Despite the discrepancies in the thrust force coefficient predictions, for this high blade speed ratio the radial force coefficients are extremely well reproduced by the effective numerical model. The very high amplitude loading upstream (peak-to-peak $C_R \approx 8.6$), as well as the nearly constant radial loading downstream ($C_R \approx 1.4$), is well predicted in both amplitude and duration.

For the moderate blade speed ratio of λ = 1.32, the rising side of the primary dynamic stall peak is accurately predicted by the effective numerical model. The peak thrust force amplitude however is somewhat over-predicted as well as the angle of rotation at which it occurs. This likely contributes to the substantial discrepancies observed in the downstream thrust loading behaviour as the dominant vortex structure formed by exposure of the airfoil to the deep dynamic stall regime will have a large impact on the subsequent turbine aerodynamics. Again, the radial force coefficient predictions highlight the dominance of the primary dynamic stall peak, with negative aerodynamic radial loading occurring over the very broad range of 10 to 180° of rotation.

The sharp peak in thrust force loading at very low blade speed ratios ($\lambda \leq 0.7$) is well modelled in duration, amplitude, and angle of rotation at which it occurs. The relatively constant, low-amplitude thrust force loading for the remainder of the rotation is also well predicted. At these low blade speed ratios, the radial force coefficient amplitude is relatively small, however the response to the high relative angle of attack and dominant dynamic stall on the upstream portion of the rotation is still very evident. Small peaks in radial loading at θ = 300 and 320° for blade speed ratios of λ = 0.4 and 0.7 respectively, have also been accurately reproduced by the effective numerical model. Comparison of the effective numerical model thrust and radial force coefficient predictions to the experimental measurements for additional blade speed ratios, and alternative blade designs, can be found in Appendix A.5.

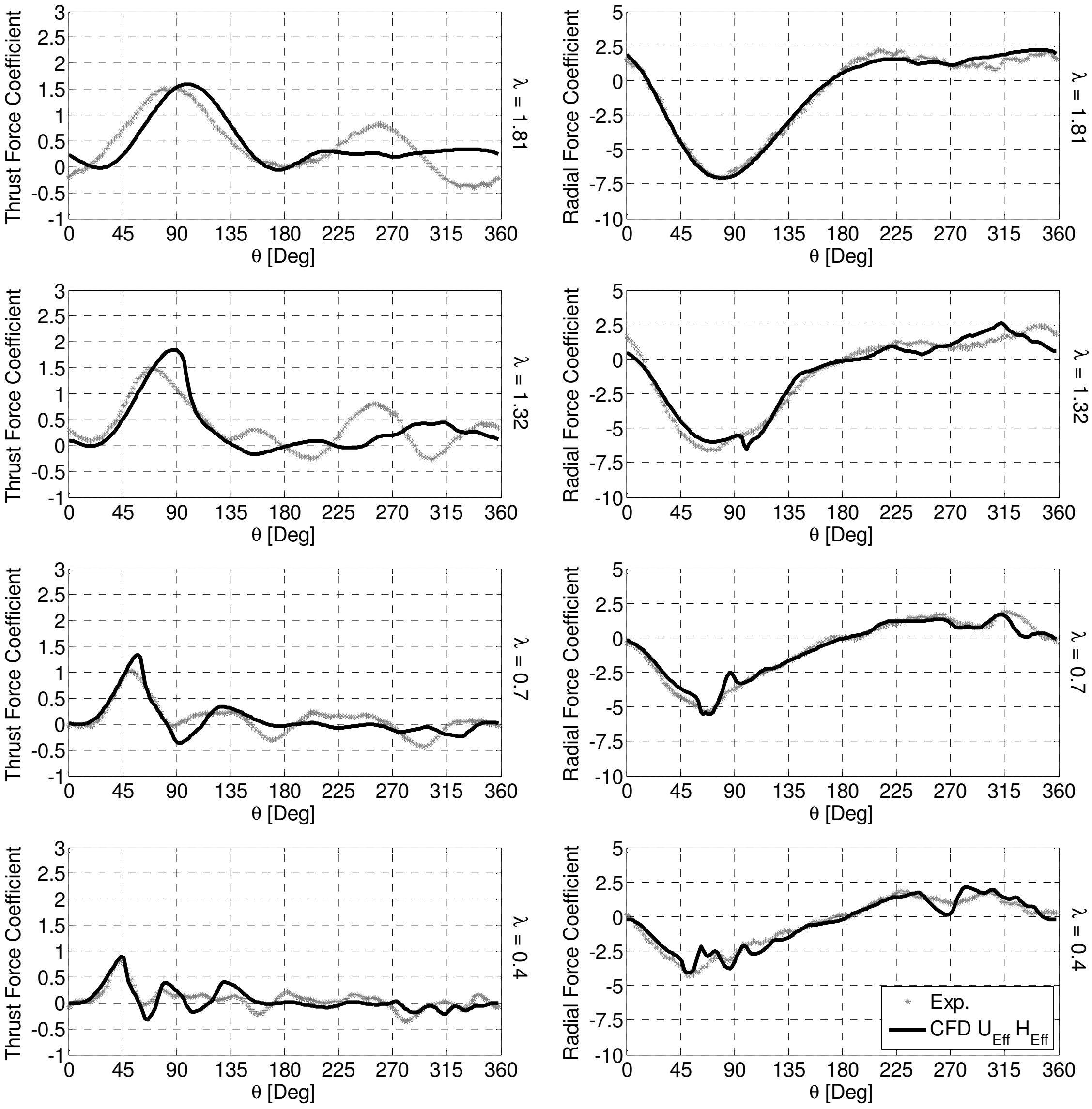

Figure 6.16: Effective numerical (κ = 1.10, τ = 1.15) and experimental thrust and radial force coefficients for λ = 1.81, 1.32, 0.7, and 0.4 (NACA 0015, c = 420 mm, β = 0°)

As identified in the literature review and preliminary studies, the most dominant feature of the thrust and radial loading behaviour is the existence of a large peak in loading on the upstream pass due to the presence of dynamic stall. This primary dynamic stall peak is the main source of power production of the turbine as well as the dominant source of vibration excitation loading. As such, it is crucial that the numerical model is able to predict the onset and magnitude of this loading feature if accurate power and vibration excitation loads are to be obtained. The maximum thrust coefficient amplitude of the primary dynamic stall peak, as well as the angle of rotation at which it occurs for both the experimental results and the effective numerical model is given in Figure 6.17.

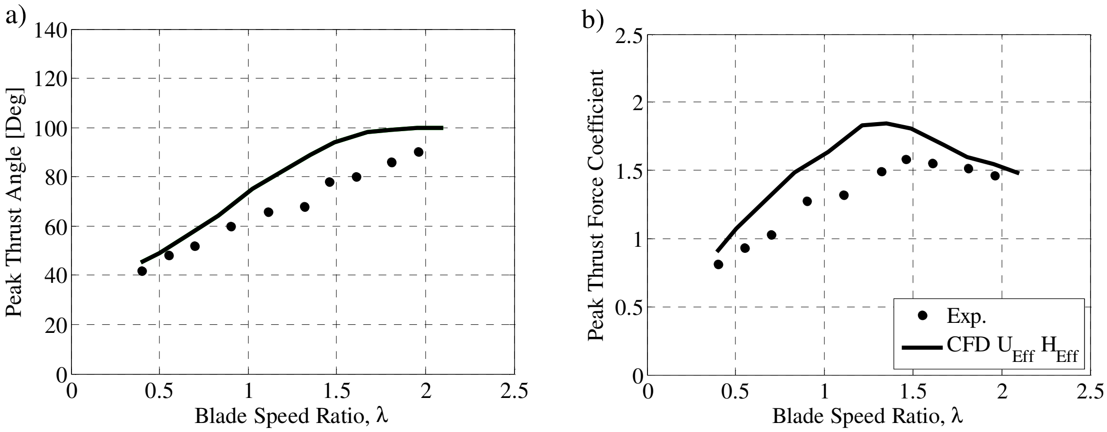

Figure 6.17: Peak thrust force coefficient (a) angle of rotation, and (b) amplitude (κ = 1.10, τ = 1.15, NACA 0015, c = 420 mm, β = 0°)

For $\lambda < 1$, the effective numerical model is able to predict the angle of rotation at which maximum thrust force is obtained quite well. However, for $\lambda > 1$ the numerical model considerably over-predicts the primary dynamic stall peak angle of rotation. Nevertheless, the trend in the dynamic stall location with a change in blade speed ratio is relatively well modelled by the effective numerical model simulations. By applying the flow velocity and turbine height correction factors, excellent agreement in the peak thrust force amplitude, and the trend with a change in blade speed ratio, is obtained. On average, the effective numerical model only over-predicts the experimental measurements by 15%. Note that this discrepancy is relatively constant over the operational range of the turbine (Figure 6.17b). This over-prediction of the dynamic stall peak location and amplitude by the effective numerical model is likely due to the over-prediction of the static stall amplitude and angle of attack by the SST turbulence model (Appendix A.1).

While thrust and radial force coefficients are a conventional and convenient method of comparing results, it is the vibration excitation loads that are the primary interest in this study (Figure 6.18).

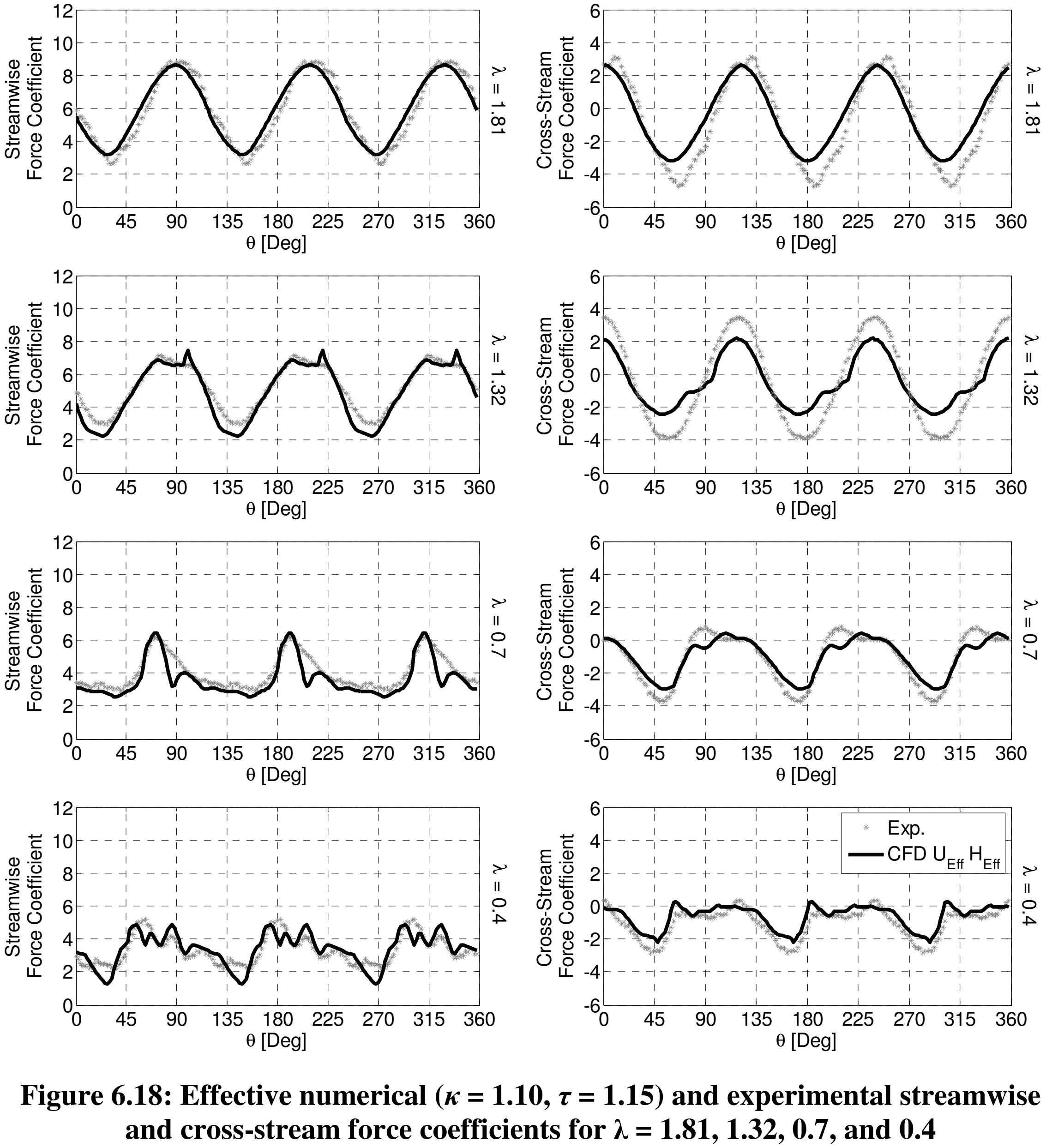

Figure 6.18: Effective numerical (κ = 1.10, τ = 1.15) and experimental streamwise and cross-stream force coefficients for λ = 1.81, 1.32, 0.7, and 0.4 (NACA 0015, c = 420 mm, β = 0°)

As expected, because the streamwise and cross-stream force coefficients are almost exclusively a function of radial loading, applying the height correction factor to the thrust force coefficients has an almost negligible effect on vibration excitation loads, and excellent agreement is still observed (refer to Figure 6.10). As previously described, it is for this reason that the correction factors can be applied in a sequential manner.

6.2.3. Half-Blade Tests

In order to gain a greater understanding of the relationship between the turbine aspect ratio ($H/2R$) and the three-dimensional flow effects, a series of 'half-blade' tests were performed. For these tests, a set of three shorter, NACA 0015, c = 400 mm blades, each 1400 mm in length, were mounted to the top support struts of the turbine. Because of the non-uniform loading along the length of the blade observed during the full-blade test cases, aerodynamic force coefficient measurements were not obtained for these half-blade tests, but shaft torque measurements were used to determine the gross turbine power coefficients.

Figure 6.19 plots the power coefficients calculated from the turbine shaft torque for both the 'full-blade' ($H/2R$ = 1.07) and 'half-blade' ($H/2R$ = 0.50) test cases. As expected, for the half-blade tests both the peak power coefficient amplitude and the blade speed ratio at which it occurs are reduced from the full-blade test results. From Figure 6.19, it is estimated that the peak power coefficient for the full-blade test cases is 0.345, at a blade speed ratio of $\lambda \approx$ 1.77, while the half-blade test cases have a peak power coefficient of approximately 0.32, at a blade speed ratio of $\lambda \approx$ 1.70.

It is anticipated that as the aspect ratio of the turbine is increased, the power coefficient amplitudes will asymptote towards the two-dimensional numerical model predictions (peak Cp = 0.538, at λ = 2.14). However, because the relationship between the turbine aspect ratio and the three-dimensional flow divergence and individual blade effects is very complex, it is difficult to predict the rate at which this will occur.

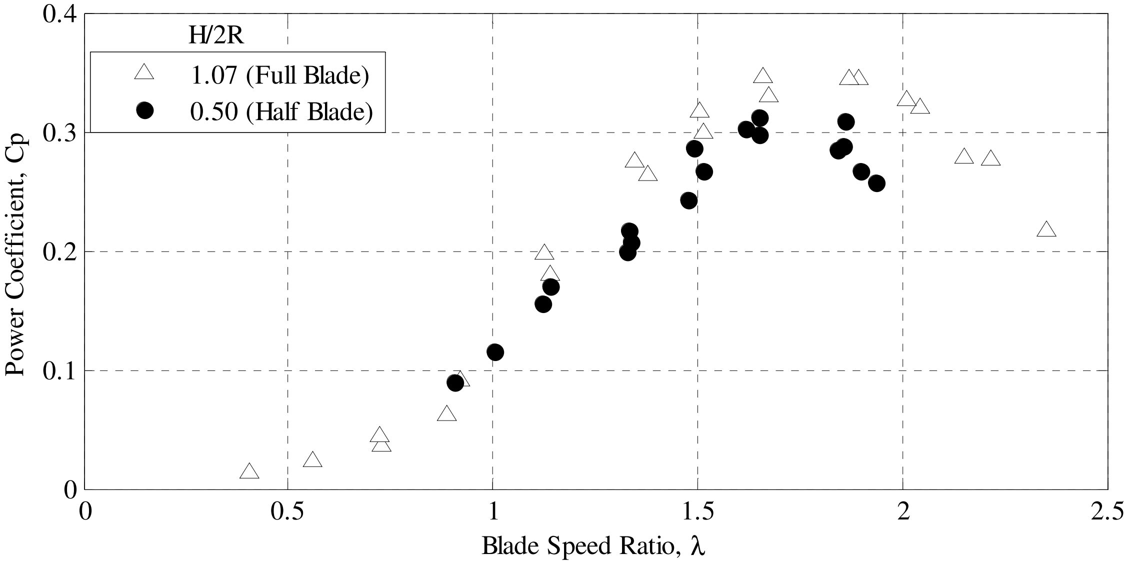

Figure 6.19: Gross turbine power coefficient for 'full-blade' and 'half-blade' test cases (NACA 0015, c = 400 mm, β = 0°, R = 1400 mm)

However, what is clear is that by halving the turbine aspect ratio, the amount of flow divergence around the top and bottom of the turbine has increased, and thus the velocity correction factor would increase as well. In fact, the observed decrease in the blade speed ratio at which peak power output is obtained corresponds to an increase in κ of approximately 4%. This would result in a decrease of 12% in the predicted peak power output of the turbine. However, this behaviour is somewhat offset by the fact that the turbine support structure (generator, stand, telemetry system) no longer contributes to the divergence of flow around the turbine. As a result, the experimentally observed decrease in power output is only approximately 7%.

Note that for the half-blade test cases, the bottom support strut was removed, such that the relative interference drag of the turbine is unchanged from the full-blade test cases. However, the aspect ratio of the airfoils was reduced to H/c = 3.5, and as a result the induced drag from blade-tip vortices was increased. Because it is difficult to estimate how much of a contribution each of these sources of drag has on the total thrust force of the turbine, the net change in the turbine height correction factor is unclear, but expected to be small.

6.3. Blade Preset Pitch Effect

For a high solidity VAWT, it has been identified that a small change in the preset pitch angle of the blades can have a relatively large impact on the dynamic stall behaviour, and thus the gross turbine power production (Fiedler, 2009). Based on the present research findings, it is expected that due to its dominance over both the streamwise and cross-stream loading, changes in dynamic stall behaviour will also affect the vibration excitation loading on the turbine. Considering both of these factors together, design decisions can be made to maximize power output while minimizing vibration loading. However, in order to employ the current effective numerical model as a design tool, its behaviour as a function of the preset pitch angle of the blades must first be validated against experimental results.

Initial qualitative analysis of the effects of preset pitch have indicated that the two-dimensional numerical model is capable of predicting the dynamic stall behaviour and power output trends over the range of β = -12 to 6° (Fiedler, 2009), where negative values of β refer to the condition of toe-out. However, because of the two-dimensional nature of the original, unmodified numerical model, it was unable to quantitatively determine the turbine power output. By measuring the aerodynamic loading components on the turbine, the importance of adjusting the two-dimensional numerical model through the use of both a velocity and height correction factor is now apparent. As described above, by determining the scale of these correction factors and applying them to the numerical model predictions, an objective comparison of the experimental power coefficients to the effective numerical model predictions can now be made.

Additionally, a quantitative analysis of the aerodynamic loading components on the turbine blade, as well as the vibration excitation loading on the turbine as a whole, can now be performed. Note that due to wind tunnel time limitations, thrust and radial force measurements were obtained for only two preset pitch configurations ($\beta = 0$ and 2.66°).

6.3.1. Power Performance

The most evident change in behaviour accompanying a change in the preset pitch angle of the airfoil is in the turbine power coefficients. Prior to performing the preset pitch effect test cases, it was postulated that adding a toe-in angle of β = 2.66° would result in dynamic stall occurring earlier on in the rotation, and a decrease in the amplitude of the primary dynamic stall peak. It was anticipated that this would result in a decrease in power output. A comparison of the results obtained for the NACA 0015, c = 420 mm airfoils with β = 0 and 2.66° is given in Figure 6.20. For both preset pitch angles, the numerical model correction factors were calculated to be κ = 1.10 and τ = 1.15.

With these correction factors applied, excellent agreement between the effective numerical model predictions and the experimental measurements is obtained for both preset pitch angles. Below a blade speed ratio of $\lambda \approx 1.1$, the effective numerical model is able to predict that the power output of the turbine is practically independent of the preset pitch of the airfoil. Above this threshold, the effective numerical model predicts the nearly constant change in power coefficient of $\Delta Cp \approx 0.04$ measured experimentally.

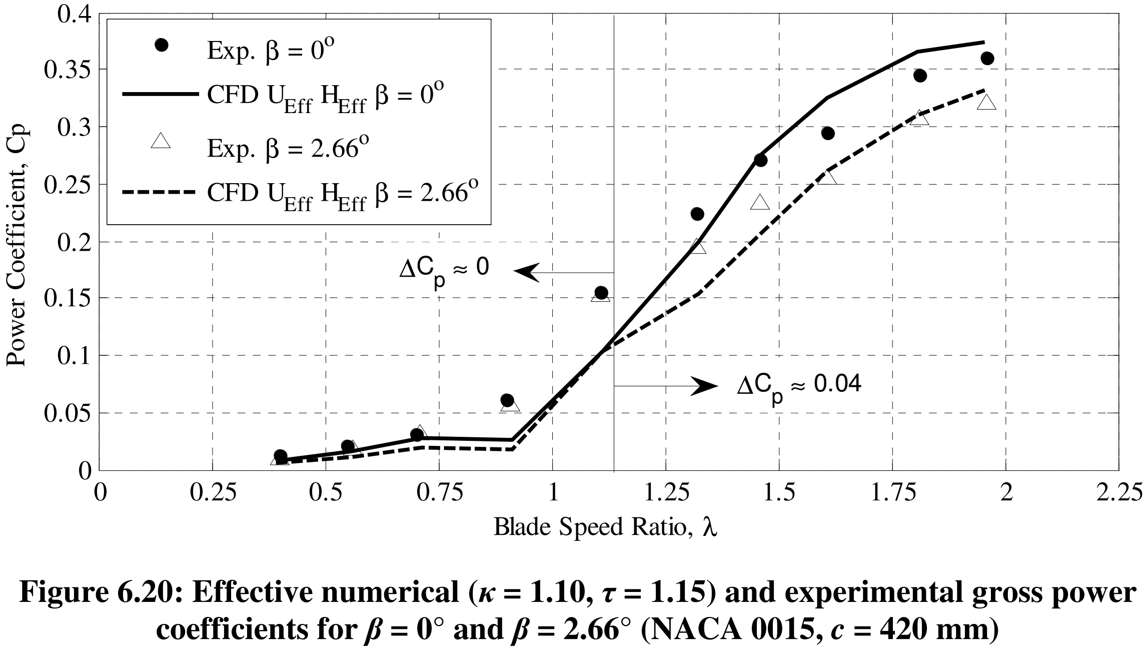

Figure 6.20: Effective numerical (κ = 1.10, τ = 1.15) and experimental gross power coefficients for β = 0° and β = 2.66° (NACA 0015, c = 420 mm)

6.3.2. Thrust and Radial Force Coefficients

A small change in the preset pitch of the airfoil generally has a relatively small impact on the large scale flow structures formed throughout a rotation of the turbine. However, the effect on the primary dynamic stall peak is substantial enough that an appreciable change in power coefficient is produced at high blade speed ratios (Figure 6.20). The effect of a small change in the preset pitch ($\Delta\beta = 2.66°$) on the aerodynamic force coefficients at low ($\lambda < 1.1$) and high ($\lambda \geq 1.1$) blade speed ratios is demonstrated through a set of sample results for $\lambda = 0.9$ and 1.81.

Figure 6.21 plots the thrust force coefficients for a blade speed ratio of $\lambda = 0.9$ for the $\beta = 0$ and 2.66°, NACA 0015, $c = 420$ mm test cases. For a change in the preset pitch angle from 0 to 2.66° toe-in, the effective numerical model captures the 4° decrease in the primary dynamic stall peak angle of rotation, and associated drop in peak thrust force amplitude, measured experimentally. These results also demonstrate that at low blade speed ratios ($\lambda < 1.1$) the addition of a toe-in angle of $\beta = 2.66°$ reduces both the dynamic stall peak amplitude and width, reducing the power output on the upstream portion of the rotation.

However, in order to produce an equivalent overall power output to the $\beta = 0°$ test cases (Figure 6.20), this implies that an increase in the average thrust force loading on the downstream portion of the rotation must occur. In fact, by adding a toe-in angle of 2.66° the average thrust force coefficient on the downstream portion of the rotation ($180° \leq \theta \leq 360°$) predicted by the numerical model increases by 0.07, which agrees well with the experimentally measured increase of 0.05. While this may appear to be a trivial increase in the thrust force coefficient, it is applied throughout the entire downstream portion of the rotation, and is sufficient to make up for the reduction in thrust force from the primary dynamic stall peak.

This behaviour can be explained based upon a simple analysis of the relative angle of attack that the airfoil is subjected to throughout a full rotation. For a preset pitch of β = 0°, the airfoil is in general subjected to lower relative angles of attack on the upstream portion of the rotation, resulting in delayed dynamic stall and higher average thrust force coefficients. However, on the downstream portion of the rotation the relative angle of attack of the airfoil is higher than the β = 2.66° test case, and dynamic stall occurs more rapidly, resulting in reduced thrust force from the airfoil.

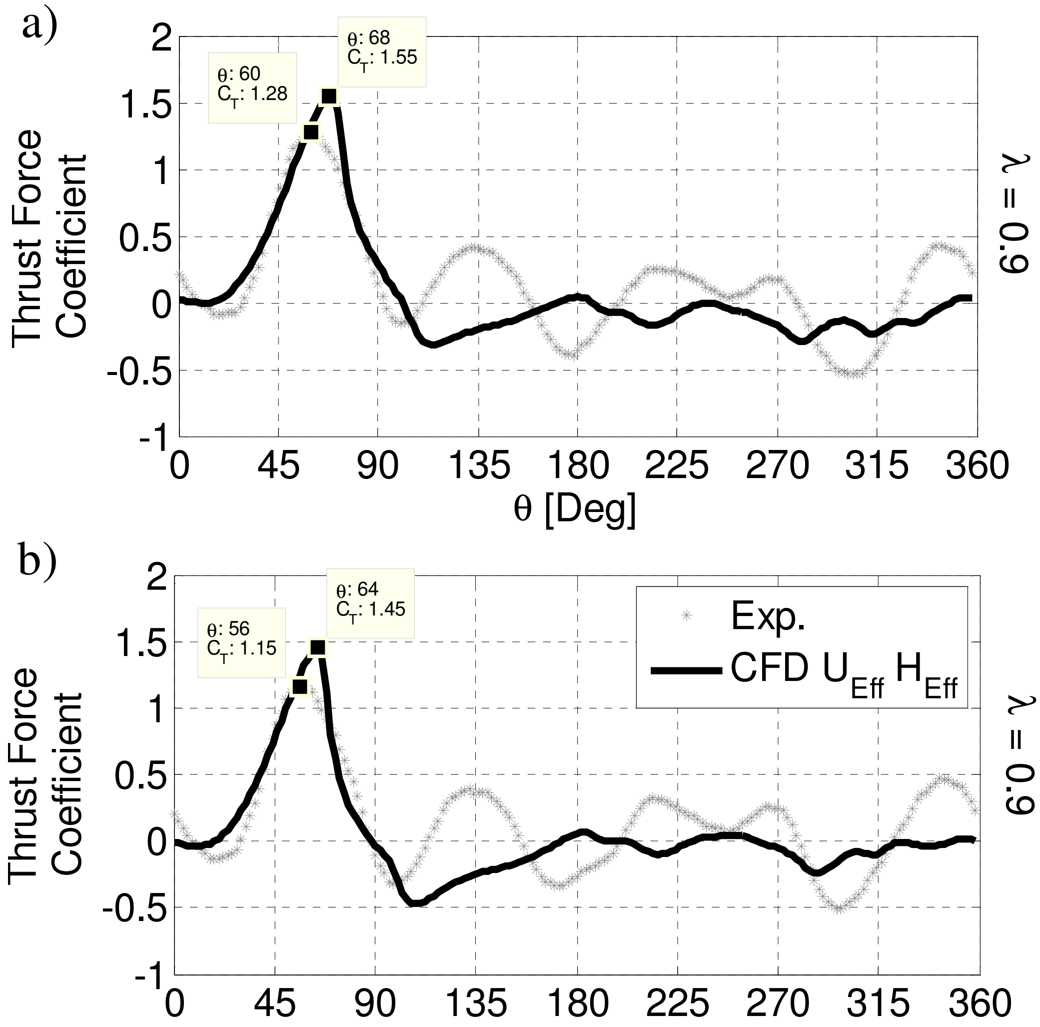

Figure 6.21: Effective numerical (κ = 1.10, τ = 1.15) and experimental thrust force coefficients (a) β = 0° (b) β = 2.66° (NACA 0015, c = 420 mm, λ = 0.9)

The corresponding radial force coefficients for the λ = 0.9 test cases are plotted in Figure 6.22. From this figure it can be seen that the numerical model is also able to predict the experimentally measured decrease in the angle of rotation of the peak radial force coefficient, when the preset pitch is increased to 2.66°. Otherwise, there are only minor changes in loading behaviour between the two cases, both experimentally and as predicted by the effective numerical model.

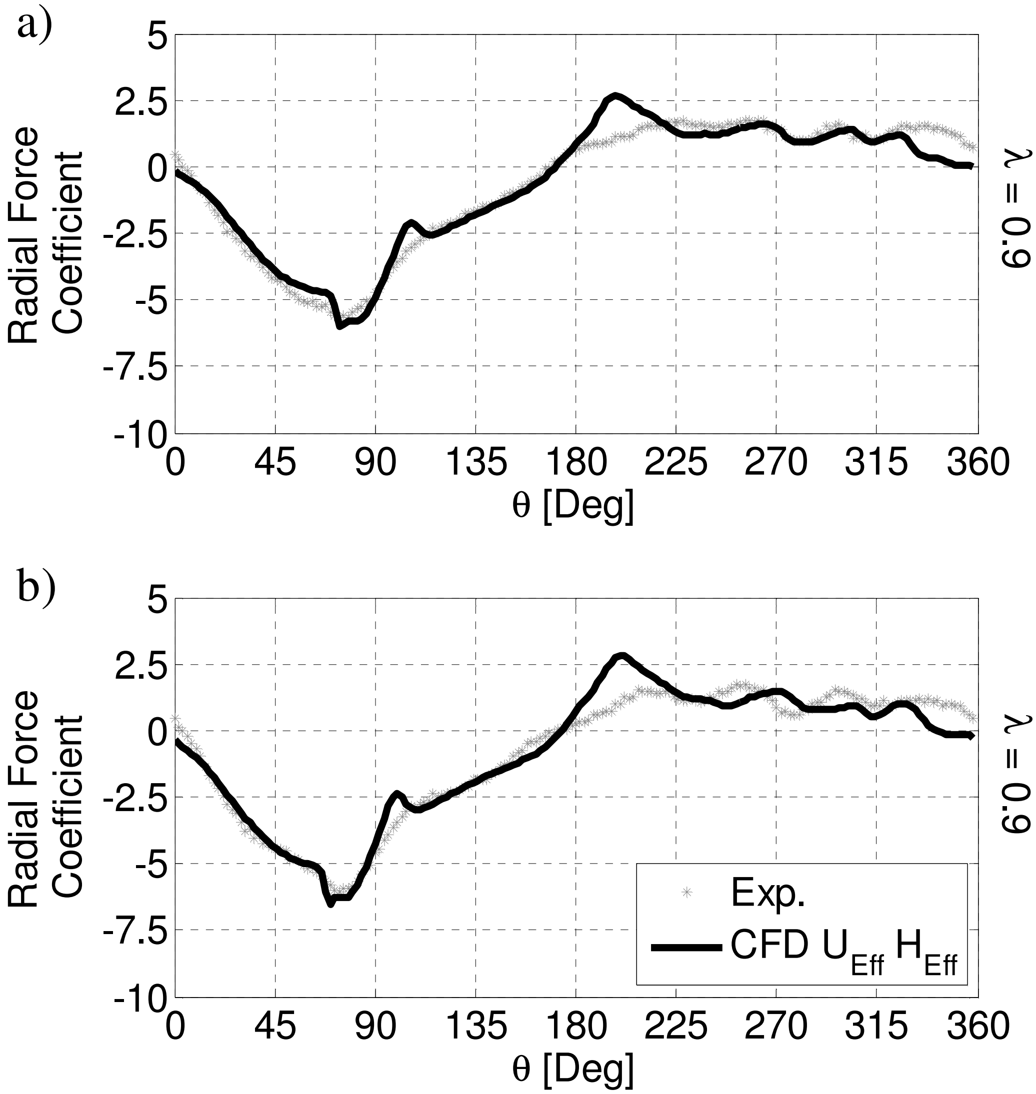

Figure 6.22: Effective numerical (*κ* = 1.10, *τ* = 1.15) and experimental radial force coefficients (a) *β* = 0° (b) *β* = 2.66° (NACA 0015, *c* = 420 mm, *λ* = 0.9)

For λ = 1.81, the addition of a toe-in angle of β = 2.66° continues to narrow and hasten the appearance of the dynamic stall peak. But, unlike at lower blade speed ratios, an *increase* in the dynamic stall peak amplitude is experimentally observed, and predicted by the effective numerical model. However, the narrowing of the dynamic stall peak offsets the increase in the peak thrust force amplitude, such that the average thrust force coefficient on the upstream portion of the rotation (0° ≤ θ ≤ 180°) continues to decrease (Figure 6.23).

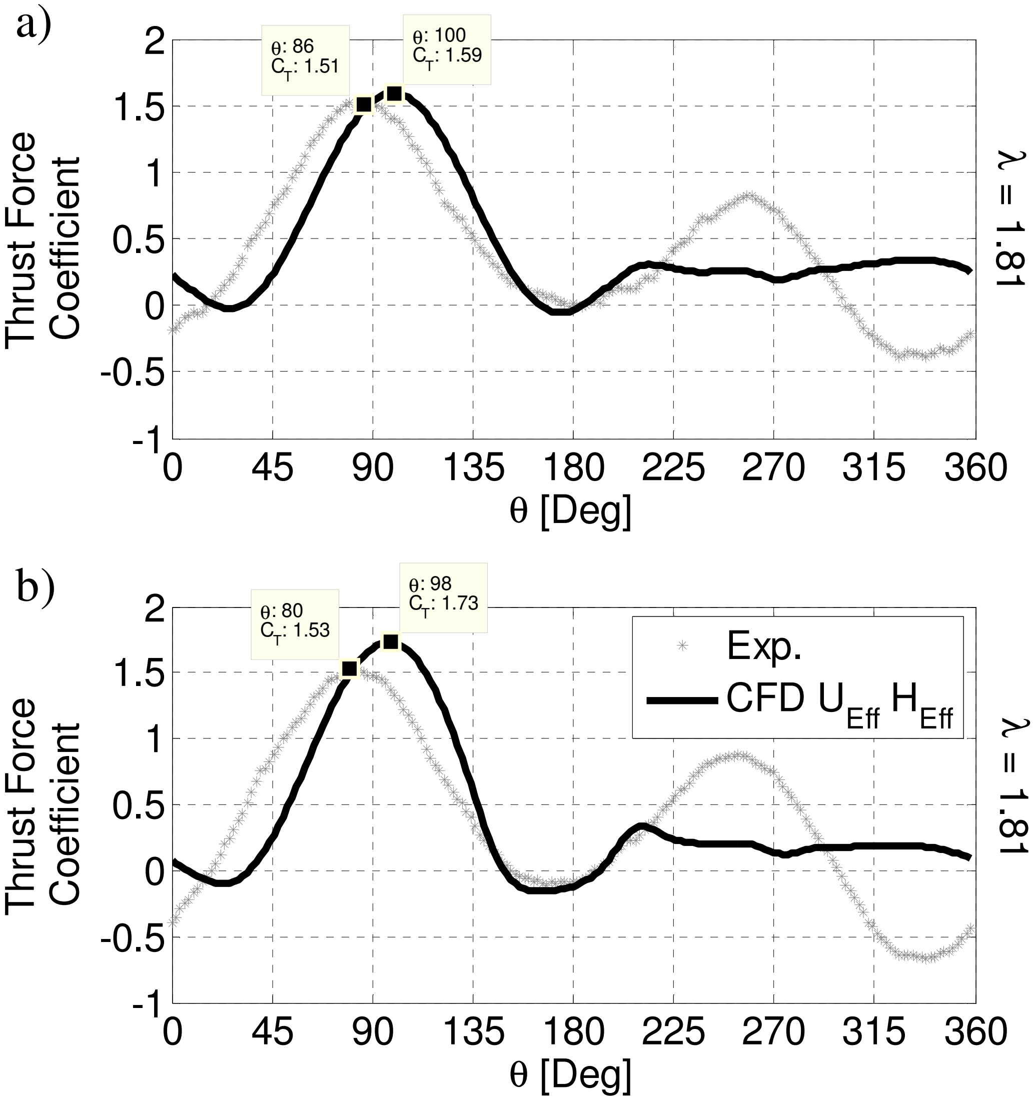

Figure 6.23: Effective numerical (κ = 1.10, τ = 1.15) and experimental thrust force coefficients (a) β = 0° (b) β = 2.66° (NACA 0015, c = 420 mm, λ = 1.81)

At this high blade speed ratio, an increase in the preset pitch angle to 2.66° decreases the average thrust force coefficient on the downstream portion of the rotation as well, resulting in a substantial reduction in the turbine's gross power output (Figure 6.20).

The experimentally measured change in radial force coefficient behaviour is again well predicted by the effective numerical model when the preset pitch angle is increased to 2.66° (Figure 6.24). For the β = 0° test case, the non-zero radial force component at θ = 0°, and the more constant downstream radial load, are accurately modelled.

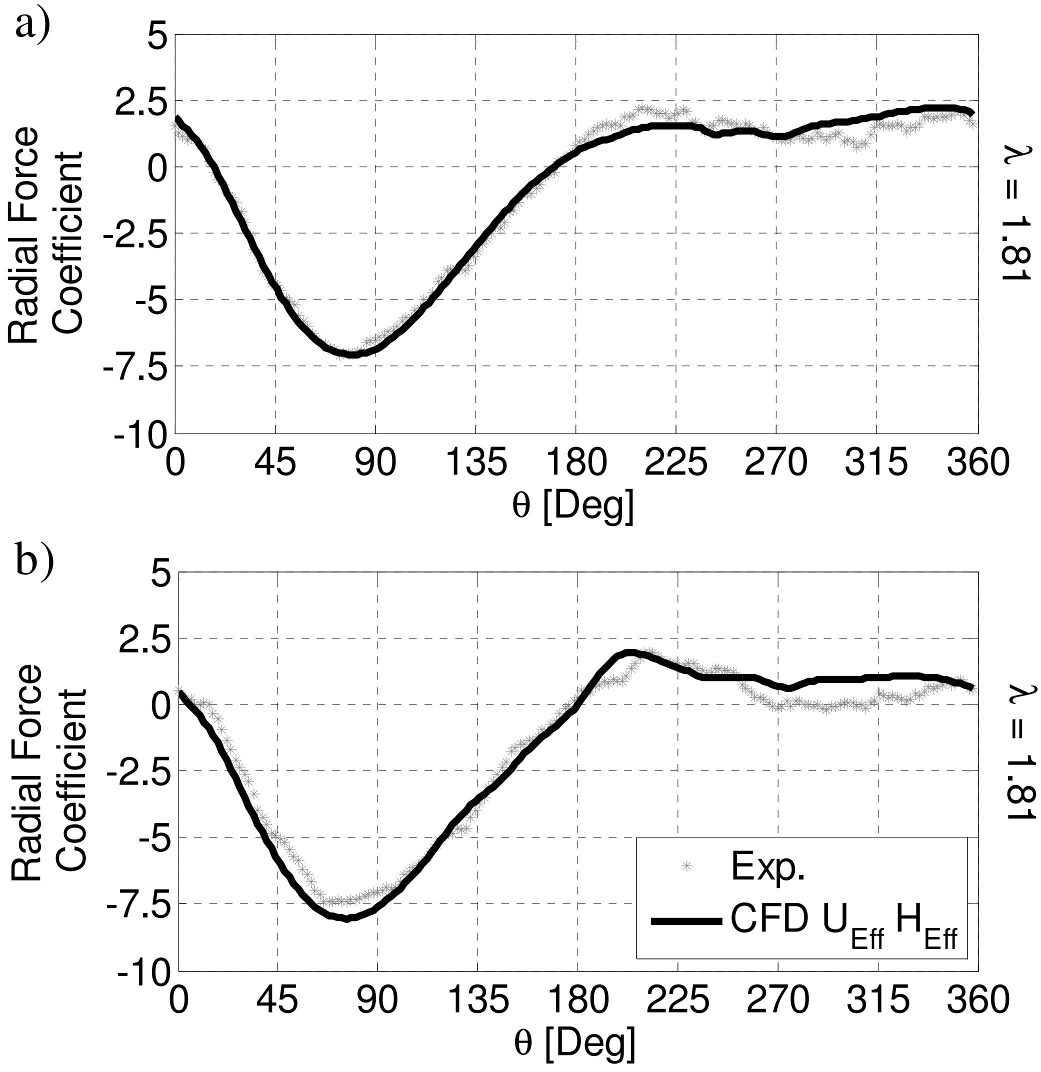

Figure 6.24: Effective numerical (κ = 1.10, τ = 1.15) and experimental radial force coefficients (a) β = 0° (b) β = 2.66° (NACA 0015, c = 420 mm, λ = 1.81)

Figure 6.25 shows the change in the angle of rotation at which the primary dynamic stall peak occurs, and the ratio of the peak thrust force coefficient amplitudes over the entire operational range of the turbine ($0.4 \leq \lambda \leq 1.95$). Over this range of blade speed ratios, even a small change in the preset pitch angle from $\beta = 0$ to 2.66° toe-in, results in an average decrease of 4° in the experimentally measured angle of rotation at which dynamic stall first occurs (Figure 6.25a). This onset of dynamic stall earlier in the rotation due to the added toe-in preset pitch is captured by the effective numerical model predictions. Based upon an increase in the effective angle of attack of the airfoil on the upstream portion of the rotation, this behaviour is not unexpected. However, it does confirm that the effective numerical model is properly simulating the effect of a change in the preset pitch angle for the small range investigated.

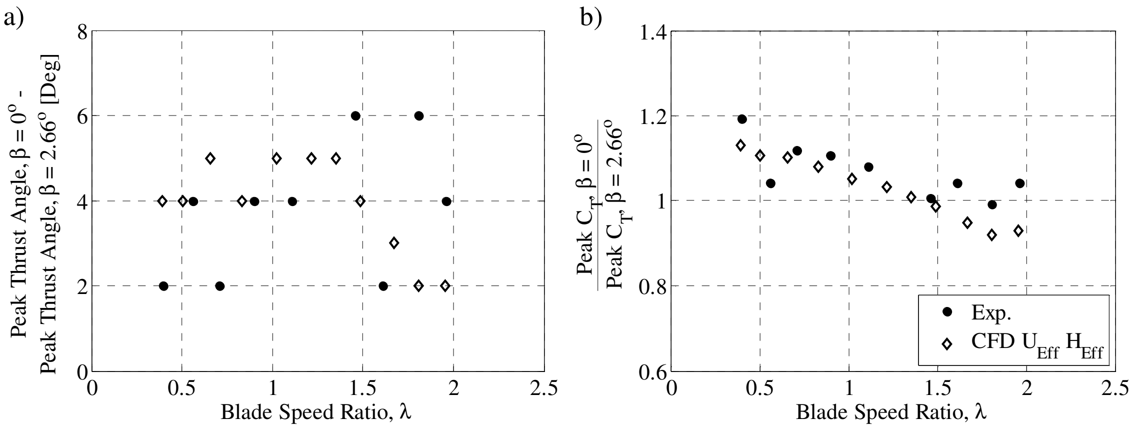

Figure 6.25: Primary dynamic stall peak (a) change in angle of rotation, and (b) amplitude ratio, for a change in preset pitch from $\beta = 0°$ to $\beta = 2.66°$ (NACA 0015, $c = 420$ mm)

The ratio of the peak thrust force coefficient for the $\beta = 0°$ test cases to those of the $\beta = 2.66°$ test cases is given in Figure 6.25b. Experimentally, adding a toe-in angle of $\beta = 2.66°$ results in a significant decrease in the peak thrust force coefficient amplitude at blade speed ratios of 1.1 or less. However, for $\lambda > 1.1$, the peak thrust force coefficient amplitude remains relatively constant with the addition of a preset pitch of $\beta = 2.66°$. Note that the results for $\lambda = 1.32$ have been omitted due to vibration response at all wind velocities for the $\beta = 2.66°$ test case.

The downward trend in the peak thrust force coefficient amplitude ratio with blade speed ratio is well predicted by the effective numerical model for $\lambda \leq 1.5$ (Figure 6.25b). Beyond a blade speed ratio of 1.5, as observed experimentally, the effective numerical model does predict a levelling off in the amplitude ratio. However, considerably higher peak thrust force coefficient amplitudes for the $\beta = 2.66°$ test cases are predicted, resulting in much lower amplitude ratios then are measured experimentally.

Overall, these results highlight the ability of the effective numerical model to predict very small changes in aerodynamic loading behaviour as a result of even smaller changes in geometry. For additional comparisons of the effective numerical model predictions of the thrust and radial force coefficients to those measured experimentally over the entire operational range of the turbine ($0.4 \leq \lambda \leq 1.96$), refer to Appendix A.5.

6.3.3. Vibration Excitation Loads

Because the change in both thrust and radial force coefficients with the addition of a toe-in angle of just 2.66° are quite small, their impact on the vibration excitation loads on the turbine are minimal. The streamwise and cross-stream force coefficients predicted numerically and measured experimentally are plotted for both preset pitch angles in Figure 6.26 and Figure 6.27 respectively. Note that while the vibration response conditions at $\lambda = 1.32$ prevented an accurate measurement of the peak thrust force amplitude and angle of rotation for the $\beta = 2.66°$ test case, the best available aerodynamic force coefficient measurements have been included here for continuity.

In the streamwise direction, there is little change in the experimentally measured loading behaviour with the addition of a preset pitch angle of $\beta = 2.66°$. The effective numerical model captures this behaviour, in that little change in the streamwise loading predictions is seen for a change in preset pitch from 0 to 2.66°. However, at high blade speed ratios ($\lambda \geq 1.8$), the numerical model does predict lower amplitude fluctuations than were measured experimentally. Additionally, for $\beta = 2.66°$, the effective numerical model predicts higher amplitude fluctuations at intermediate blade speed ratios ($1.32 \leq \lambda \leq 1.46$).

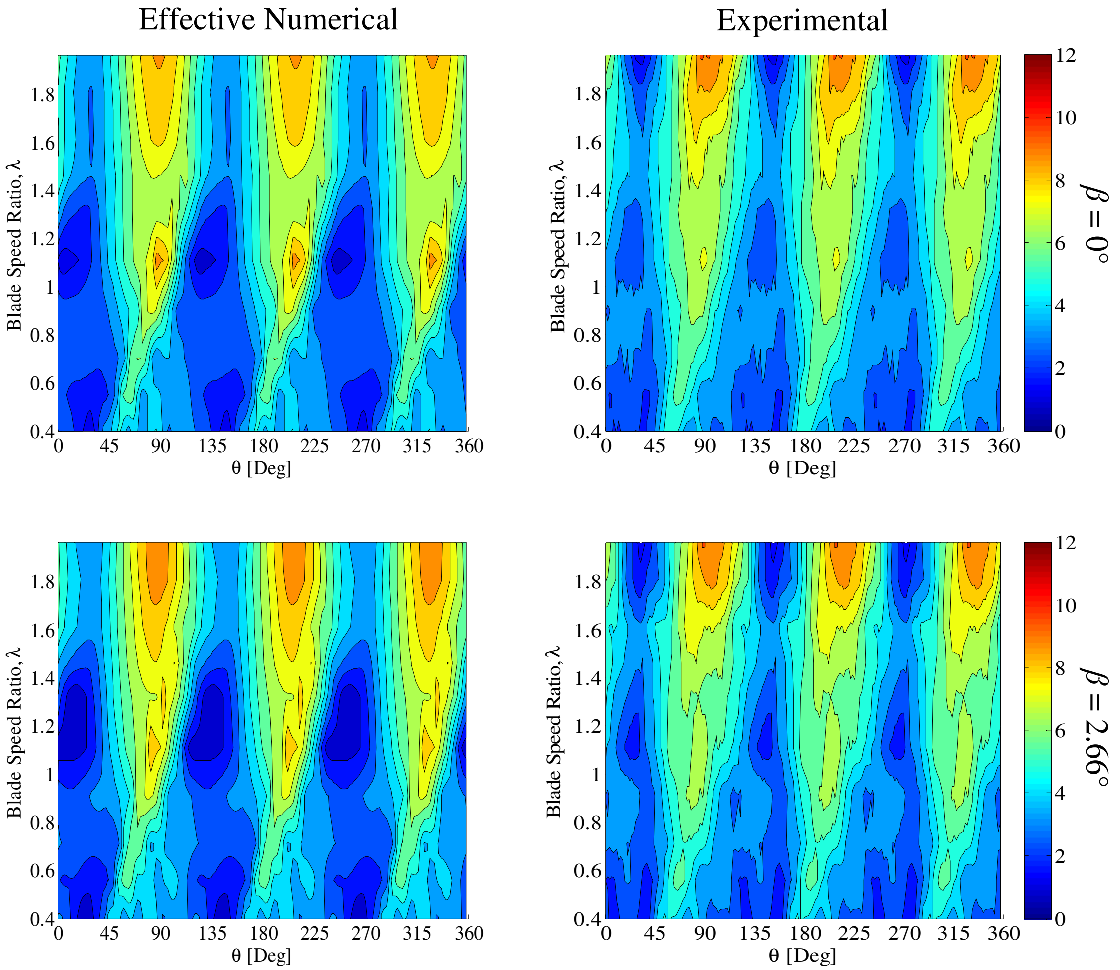

Figure 6.26: Contour plot of effective numerical (κ = 1.10, τ = 1.15) and experimental streamwise force coefficients, (NACA 0015, c = 420 mm)

As expected, there is also little difference in the experimentally measured cross-stream loading behaviour with a change in the preset pitch angle (Figure 6.27). For low blade speed ratios ($\lambda \leq 1.1$), the effective numerical model reproduces the experimentally measured loading behaviour quite well. In particular, the sharp peaks in loading at a blade speed ratio of $\lambda = 0.9$ are accurately reproduced. At higher blade speed ratios ($\lambda > 1.1$), the effective numerical model under predicts the amplitude of the cross-stream aerodynamic loading variations, particularly for $\beta = 0°$. However, it is able to capture the decrease in the mean cross-stream loading component with an increase in β of 2.66°.

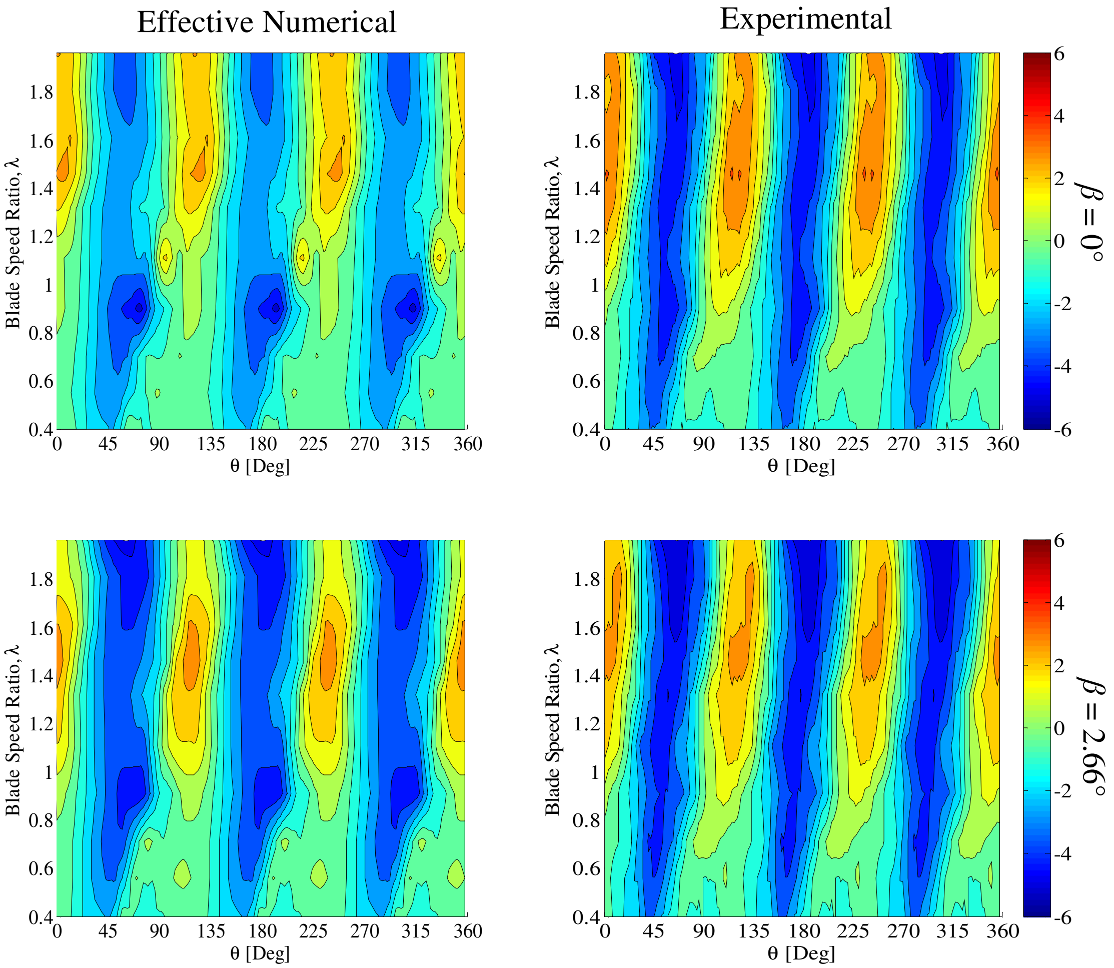

Figure 6.27: Contour plot of effective numerical (*κ* = 1.10, *τ* = 1.15) and experimental cross-stream force coefficients, (NACA 0015, *c* = 420 mm)

From Figure 6.28 it is clear that at blade speed ratios of 1.1 or less the mean cross-stream loading component is primarily unchanged by a change in the preset pitch angle. However, for blade speed ratios greater than 1.1, the β = 2.66° experimental measurements exhibit consistently lower mean cross-stream loading coefficients. The effective numerical model reproduces this trend in a somewhat exaggerated manner. While it is important that the effective numerical model is able to properly capture this behaviour, in terms of vibration excitation loading on the turbine, this trend has no effect as it is the magnitude of the loading amplitude that is the driving force for vibration.

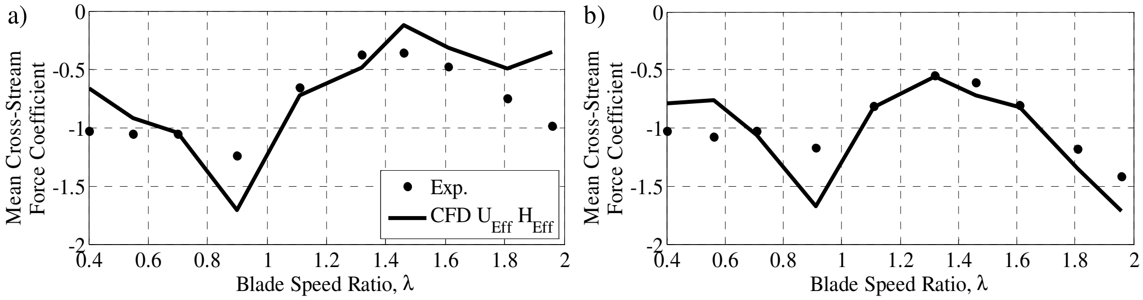

Figure 6.28: Average effective numerical and experimental cross-stream force coefficient (a) *β* = 0° (b) *β* = 2.66° (NACA 0015, *c* = 420 mm)

6.3.4. Vibration Response

One method to assess the susceptibility of a particular blade design to vibration excitation is to measure the vibration response of the turbine. While the vibration response of any particular turbine will be dependent on the stiffness of the system, and thus the natural frequencies, a relative measure of the vibration amplitudes can be made. As discussed in section 4.4, the vibration response data was obtained from two accelerometers mounted directly above the upper set of support struts. Because of the difficulty in measuring the aerodynamic force coefficients without the cable system, a limited number of test cases were performed with the turbine in its typical operating condition. As such, the effect of a change in the vibration response with a change in preset pitch from 0 to 2.66° can only be analysed based upon the much lower amplitude vibration response of the turbine with the cable system in place. The normalized vibration response behaviour for the blade pass frequency is plotted in Figure 6.29 below. In the streamwise direction, an increase in the preset pitch to 2.66° slightly increases the vibration response amplitude over the entire operational range of the turbine by 4 to 13%. In the cross-stream direction, the vibration response is decreased at high RPM by nearly 5%, but increases by up to 16% at low rotational velocities.

From these results it can be concluded that the β = 0° design is superior as it produces 13% more power than the β = 2.66° design at peak power production, and in general has somewhat lower vibration response behaviour. From a design perspective there appears to be no advantage to operating the turbine with a toe-in angle of 2.66°.

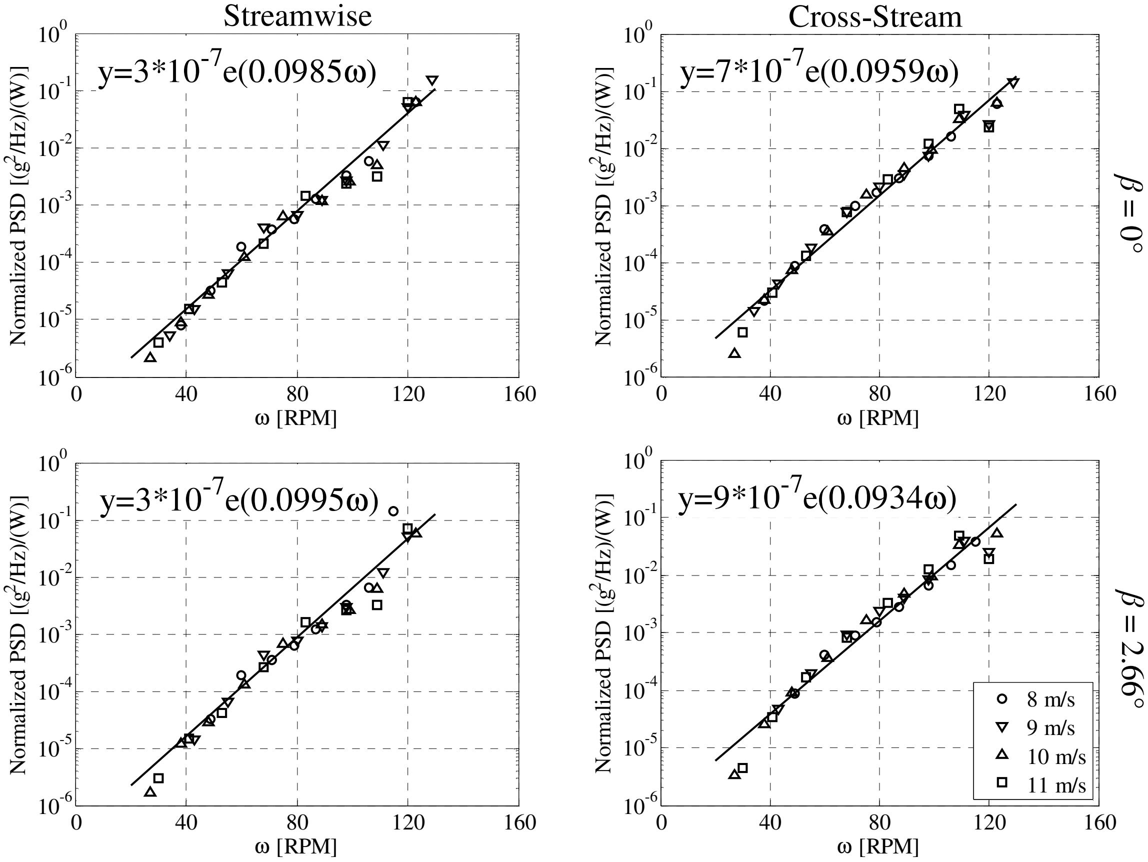

Figure 6.29: Power spectral density of the blade pass frequency with cables normalized by the power available in the oncoming flow (NACA 0015, c = 420 mm)

6.4. Blade Shape Effect

In addition to a change in the preset pitch angle of the airfoil, there are several other methods to modify the dynamic stall behaviour of the wind turbine blade. One such approach is to modify the thickness of the airfoil. In order to accomplish this, two different sets of tests were performed. The first of which was with the 420 mm chord length NACA 0015 blades at a preset pitch angle of β = 0°, as described above. The second was with the 48% thicker NACA 0021 airfoils with a chord length of 400 mm and thus a more blunt trailing edge, also mounted at a preset pitch angle of β = 0°. The effect of this change in geometry is two-fold. The most obvious effect is a change in the thickness ratio of the airfoil, and is partially a result of the increase in chord length. For the sharp trailing edge NACA 0015 airfoils, the thickness ratio is t/c = 0.156, while for the bunt trailing edge NACA 0021 airfoils, the thickness ratio is $t/c = 0.231$. Second, as previously noted, in order to accommodate its sharp trailing edge, the chord length of the thinner NACA 0015 blades was increased. For a given support strut radius, this slightly increases the solidity ratio of the turbine, such that for c = 400 mm, turbine solidity is 0.424, whereas for c = 420 mm, turbine solidity is 0.450.

6.4.1. Power Performance

Based on the trends found within the literature review and during the preliminary tests, it is expected that an increase in solidity ratio due to an increase in chord length will result in a decrease in the blade speed ratio at which maximum power output occurs. For the two test cases performed the change in solidity ratio is quite small (≈ 6%), and this effect is expected to be minimal. In fact, from Figure 6.30 it is clear that the effect of a change in airfoil thickness ratio is far greater than the effect of a change in solidity ratio, as the opposite behaviour occurs. For the thicker NACA 0021 airfoils, the maximum power coefficient of 0.355 measured experimentally occurs at a blade speed ratio of approximately 1.8. For the thinner NACA 0015 airfoils, maximum power output of Cp = 0.360 occurs at a blade speed ratio of $\lambda \approx 1.95$.

However, the effective numerical model predicts relatively little difference in the blade speed ratio at which maximum Cp occurs ($\lambda \approx 1.96$). This is despite the fact that the original, unmodified CFD model predicts that the maximum power coefficient for the NACA 0021 airfoils occurs at a slightly lower blade speed ratio than for the NACA 0015 airfoils (as observed experimentally). It is because a smaller velocity correction factor is applied to the NACA 0021 results ($\kappa = 1.07$) than the NACA0015 results ($\kappa = 1.10$), that the effective numerical model prediction of the blade speed ratio at which maximum Cp occurs is very similar for the two test cases. Nevertheless, the effective numerical model is capable of predicting the broader range of blade speed ratios over which higher turbine power output is produced for the NACA 0021 blade design. Overall, the effective numerical model does predict the correct change in the power coefficient trends with blade speed ratio due to a change in airfoil thickness ratio, only in a less severe manner.

In terms of the maximum gross power coefficient amplitude, the experimental measurements indicate that there is negligible change with respect to the airfoil thickness ratio (for the given range). While the original, unmodified CFD model predicts considerably higher power output from the NACA 0015 airfoils (Max. Cp = 0.565) as compared to the NACA 0021 airfoils (Max. Cp = 0.523), the effective numerical model successfully accounts for this initial difference through the application of different flow velocity correction factors. In doing so, the effective numerical model is able to predict that there is no change in the maximum power output with a change in thickness ratio. This is further confirmation of the method used to calculate the velocity correction factor.

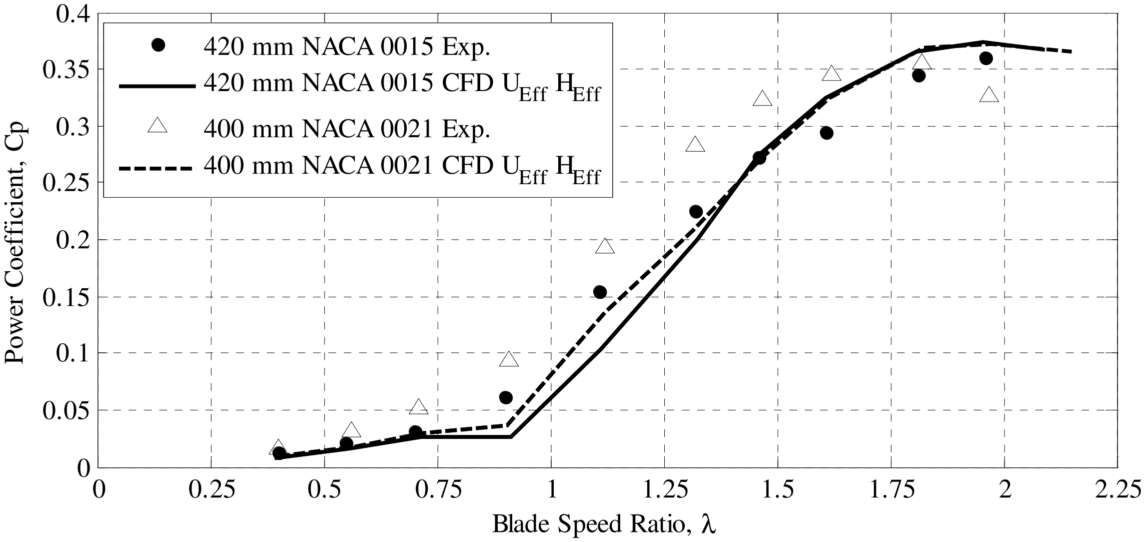

Figure 6.30: Effective numerical and experimental gross power coefficients for the 420 mm NACA 0015 (κ = 1.10, τ = 1.15), and 400 mm NACA 0021 (κ = 1.07, τ = 1.15) airfoils (β = 0°)

6.4.2. Thrust and Radial Force Coefficients

As with a change in preset pitch, blade speed ratios of λ = 0.9 and 1.81 will be used as sample demonstrations of the change in behaviour with a change in airfoil thickness ratio. Figure 6.31 plots the experimentally measured thrust force coefficients against the effective numerical model predictions for λ = 0.9.

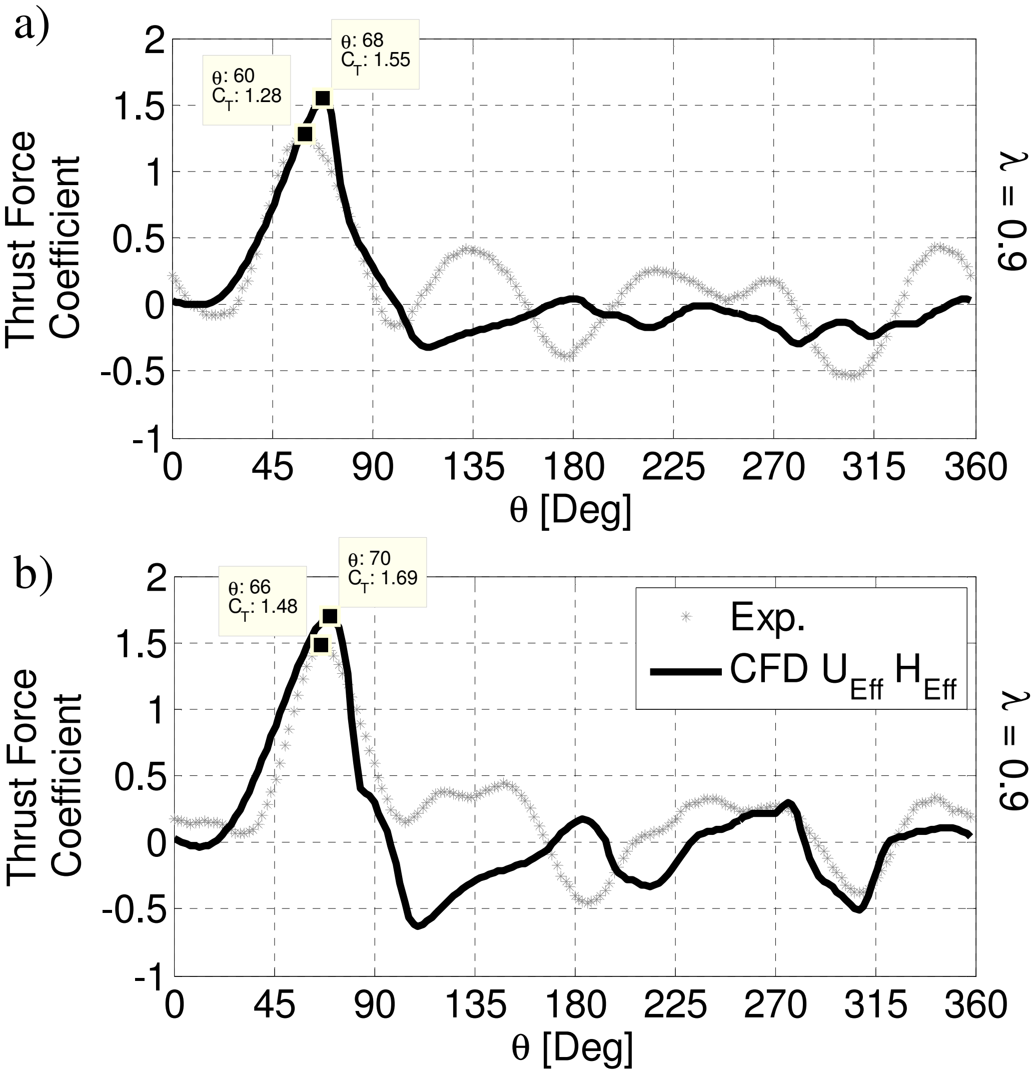

Figure 6.31: Effective numerical and experimental thrust force coefficients (a) 420 mm NACA 0015 (b) 400 mm NACA 0021 ($\beta = 0°$, $\lambda = 0.9$)

As predicted by the effective numerical model, an increase in airfoil thickness ratio increases the experimentally measured angle of attack at which the main dynamic stall peak occurs, as well as the peak thrust force coefficient amplitude. For the blunter NACA 0021 airfoils, the numerical model does not predict the formation of a leading edge vortex immediately after the primary dynamic stall peak. Instead, due to the fact that the thicker airfoils are more prone to trailing-edge dynamic stall (section 2.2.1.c), the initial trailing edge vortex (1-b) propagates towards the leading edge of the airfoil.

For the downstream portion of the rotation ($180° < \theta < 360°$) the effective numerical model prediction of the thrust loading behaviour for the NACA 0021 airfoil design is better than for the NACA 0015 airfoils. In particular, the large dip in thrust force loading centred at $\theta = 308°$ is well represented in both amplitude and location. However, while the experimental measurements indicate only small differences in loading behaviour between the two blade designs on the downstream portion of the rotation, the numerical model predicts much larger variations in thrust force loading for the NACA 0021 airfoils as compared to the NACA 0015 airfoils.

For a blade speed ratio of $\lambda = 0.9$, the experimentally measured change in the radial force coefficients with a change in thickness ratio is small (Figure 6.32). The effective numerical model captures this behaviour with the exception of some larger amplitude, small scale fluctuations in loading for the NACA 0021 airfoil design (Figure 6.32b). Particularly, immediately after dynamic stall at $\theta \approx 85°$, and on the downstream pass from $\theta = 270$ to 320°, where interestingly the effective numerical model well predicts the large drop in thrust force coefficient (Figure 6.31b).

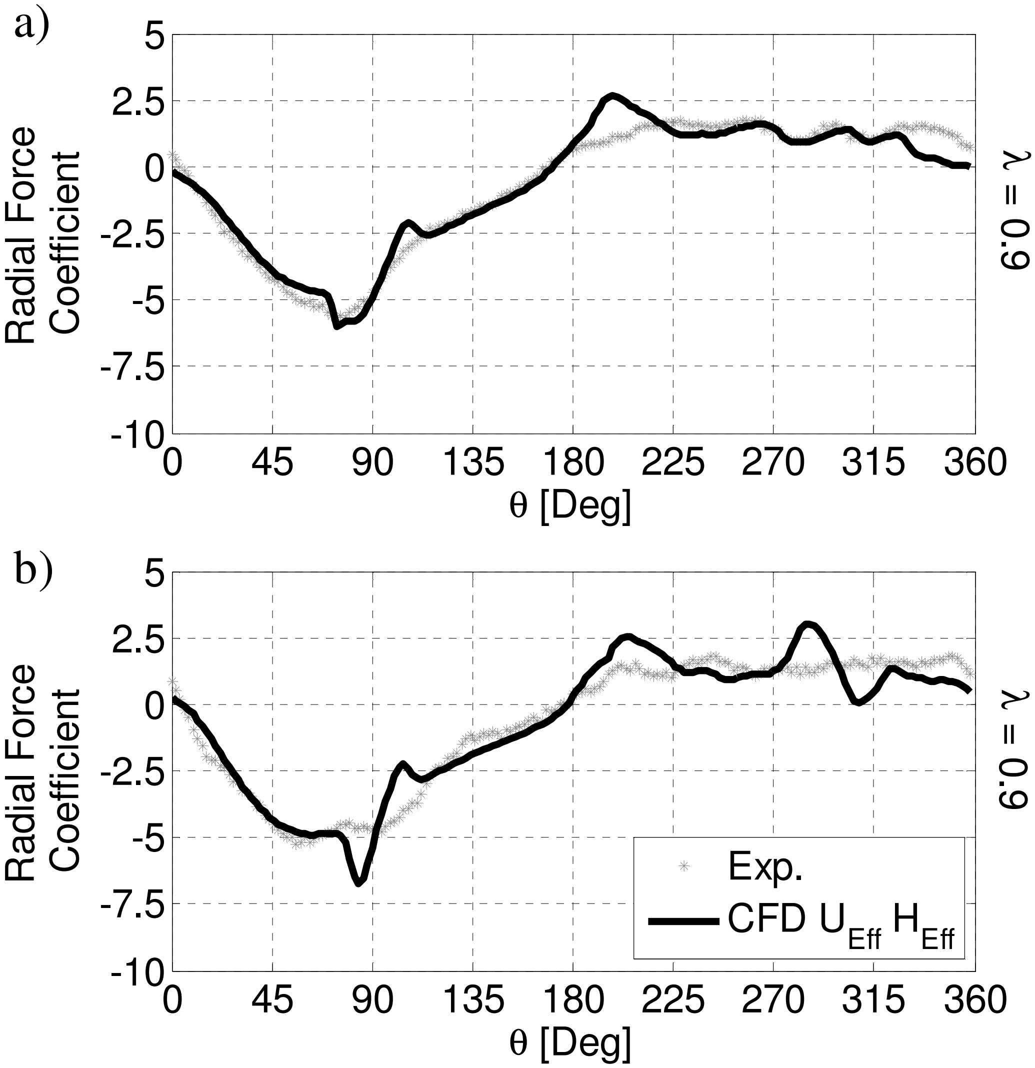

Figure 6.32: Effective numerical and experimental radial force coefficients (a) 420 mm NACA0015 (b) 400 mm NACA0021 (β = 0°, λ = 0.9)

For a high blade speed ratio of $\lambda = 1.81$, the experimentally measured peak thrust force coefficient amplitude increases slightly with an increase in airfoil thickness ratio (Figure 6.33). However, unlike at low blade speed ratios, the NACA 0021 airfoils stall earlier in the rotation than the NACA 0015 design (≈ 10°). The thicker NACA 0021 airfoils then experience a more rapid increase in thrust loading on the upstream side of the rotation. This narrows the primary dynamic stall peak, and counteracts the increase in power output that accompanies an increase in peak thrust force amplitude.

This increase in peak thrust force coefficient amplitude and decrease in stall location measured experimentally is predicted by the effective numerical model. Overall, the change in total power production between the two blade designs measured experimentally is minimal at a blade speed ratio of λ = 1.81, as predicted by the effective numerical model (Figure 6.30).

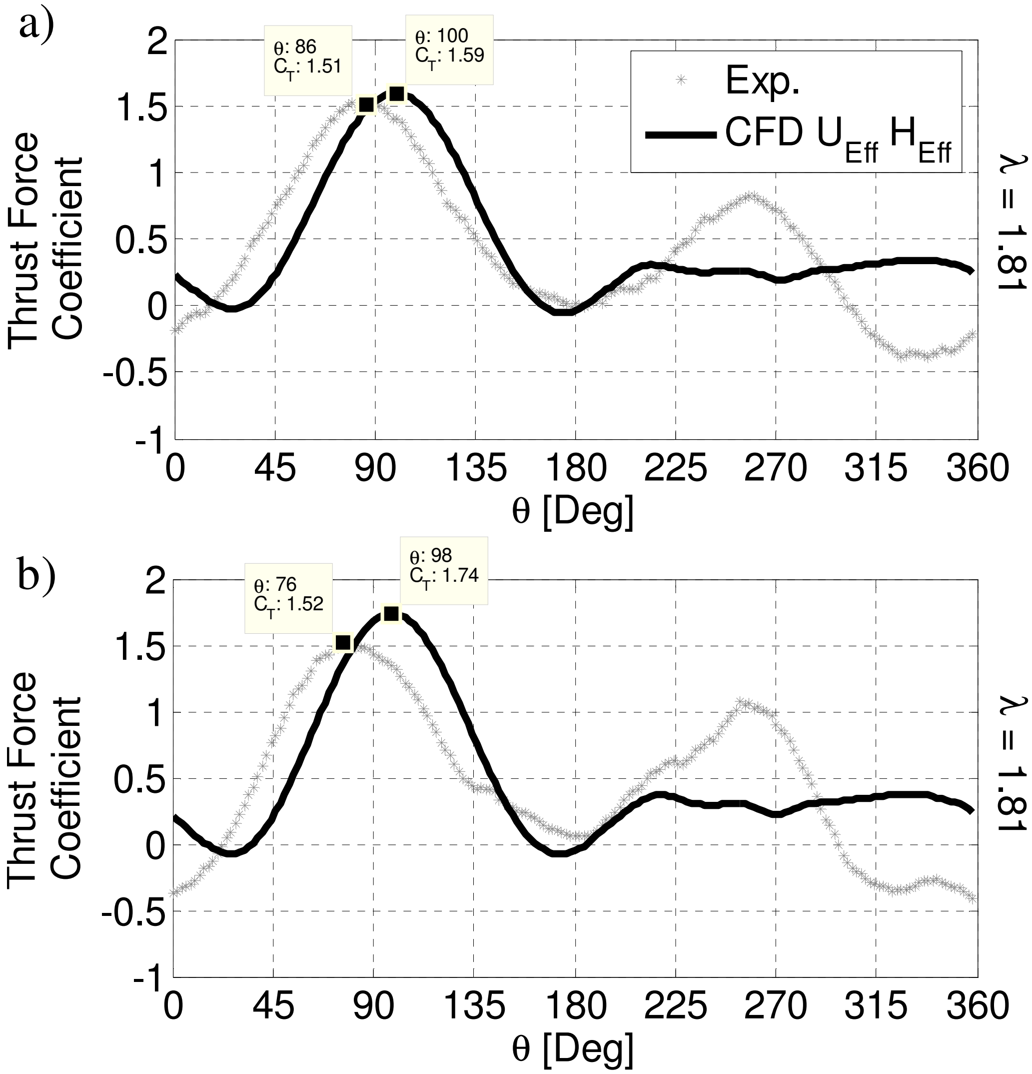

Figure 6.33: Effective numerical and experimental thrust force coefficients (a) 420 mm NACA 0015 (b) 400 mm NACA 0021 (β = 0°, λ = 1.81)

For a blade speed ratio of λ = 1.81, the change in radial force coefficient with an increase in blade thickness ratio is primarily limited to a slight increase in the peak radial force for the NACA 0021 blade design. At this blade speed ratio, the radial force coefficient predictions for both the NACA 0021 and the NACA 0015 blade designs are excellent (Figure 6.34). The effective numerical model predictions capture the location, amplitude, and duration of the main peak in the radial force component for both blade designs. The nearly constant radial force component on the downstream portion of the rotation is also well predicted by the effective numerical model.

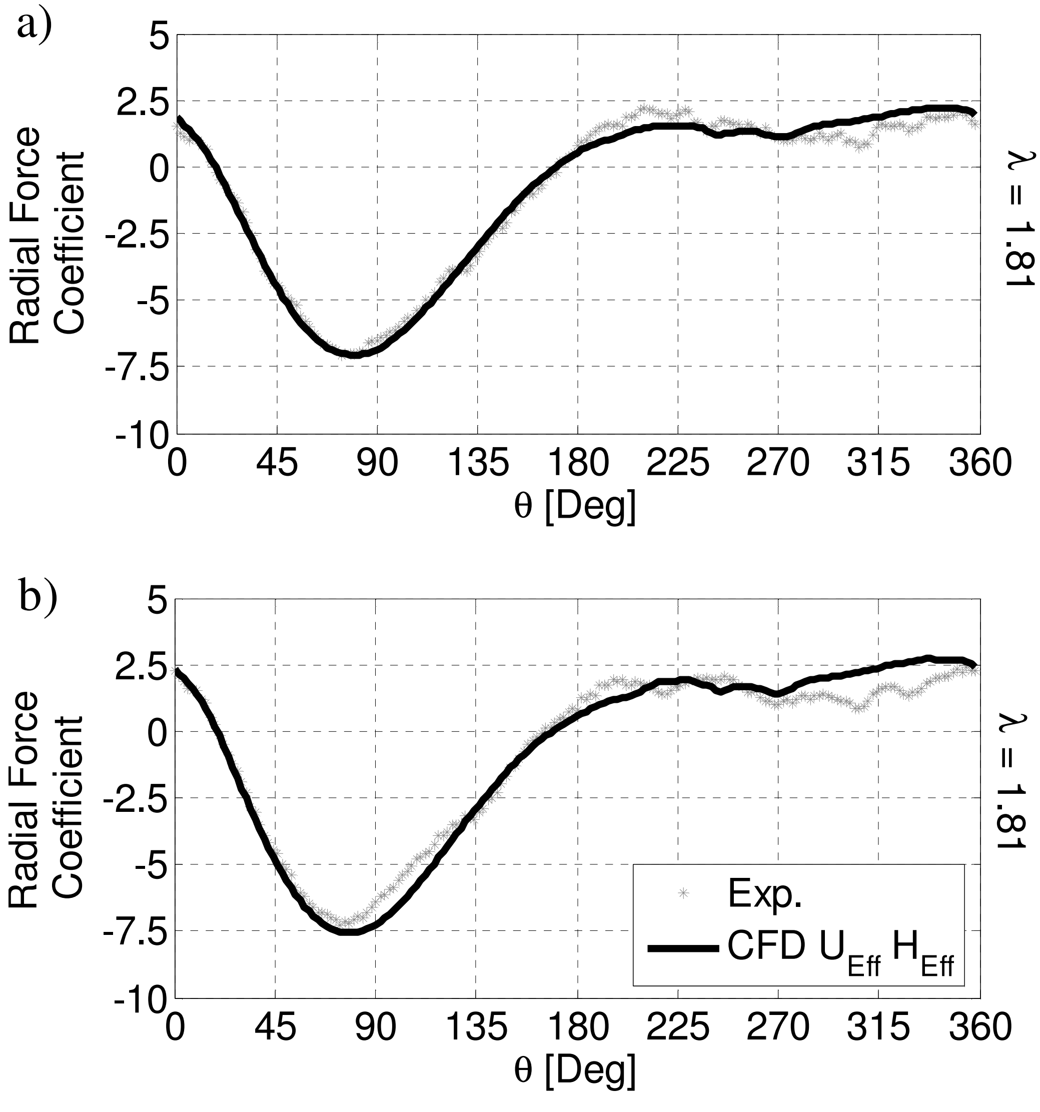

Figure 6.34: Effective numerical and experimental radial force coefficients (a) 420 mm NACA 0015 (b) 400 mm NACA 0021 (β = 0°, λ = 1.81)

As before, the primary vibration excitation load is due to the main dynamic stall peak on the upstream portion of the rotation, and as such this will be the principal focus of the following analysis. From Figure 6.35a, it can be seen that at low blade speed ratios the thinner NACA 0015 airfoil stalls at an earlier angle of attack, while for high blade speed ratios the opposite is true. This behaviour is observed both experimentally and in the effective numerical model predictions. However, as with the blade speed ratio at which maximum power output is obtained, the effective numerical model predicts a considerably smaller difference between blade designs than is measured experimentally.

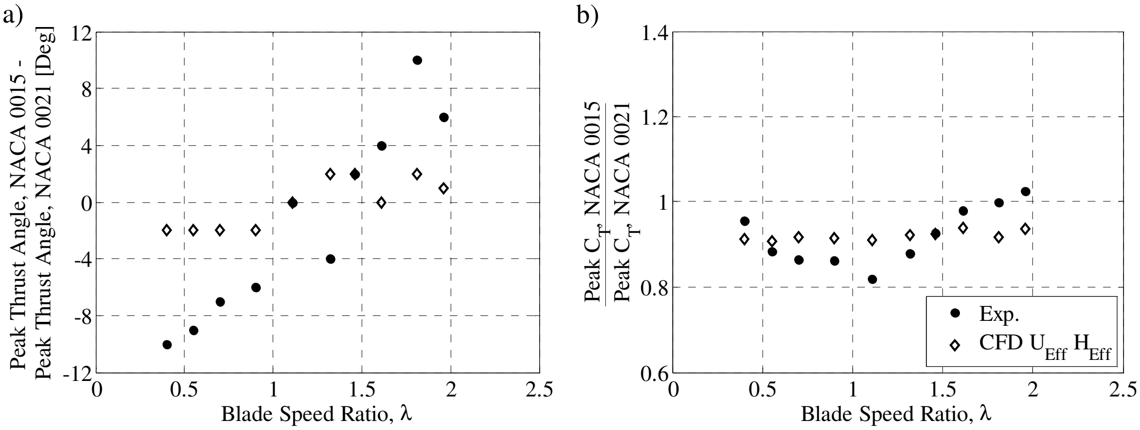

Figure 6.35: Primary dynamic stall peak (a) change in angle of rotation, and (b) amplitude ratio, for a change in blade design from the 420 mm NACA 0015 airfoils to the 400 mm NACA 0021 design ($\beta = 0°$)

While there is some scatter in the experimental data, an increase in blade thickness ratio results in an increase in the peak thrust force coefficient amplitude for nearly all blade speed ratios tested (Figure 6.35b), over the operational range of the turbine ($0.4 \leq \lambda \leq 1.96$). At higher blade speed ratios ($\lambda > 1.32$), the primary dynamic stall peak is attained more gradually (Figure 6.33), and this increase is less significant. Numerically, the effective CFD model predicts this increase in the peak thrust force amplitude that the thicker NACA 0021 airfoils will have over the NACA 0015 design. This increase in peak thrust force is predicted to be nearly constant over the entire operational range of the turbine.

6.4.3. Vibration Excitation Loads

Figure 6.36 below plots the streamwise force coefficients predicted by the effective numerical model against those obtained experimentally for the c = 420 mm NACA 0015 blades and the c = 400 mm NACA 0021 blades. While at first glance the differences in streamwise loading behaviour as a result of a change in airfoil thickness ratio may be difficult to determine, a closer look at a few sample test cases will highlight the dominant loading patterns.

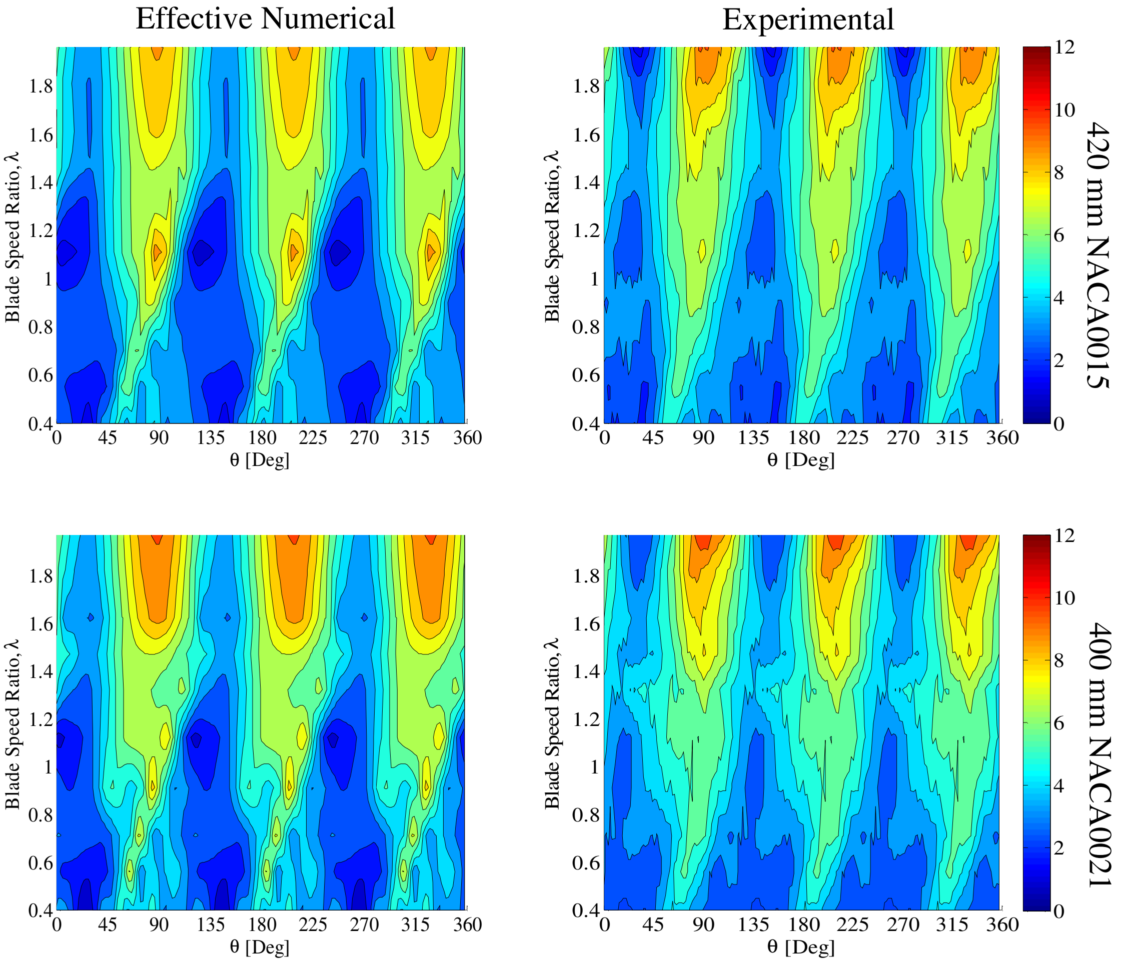

Figure 6.36: Contour plot of effective numerical and experimental streamwise force coefficients for the 420 mm NACA 0015 (κ = 1.10, τ = 1.15) and 400 mm NACA 0021 (κ = 1.07, τ = 1.15) airfoils (β = 0°)

From the sample of results presented in Figure 6.37, it can be seen that for high blade speed ratios ($\lambda > 1.4$), the thinner NACA 0015 airfoils have a distinctive triangular wave form, while the NACA 0021 airfoils have a more rounded, sinusoidal streamwise loading pattern. For intermediate blade speed ratios ($1.0 < \lambda < 1.4$), the thicker airfoils have much lower amplitude variations as compared to the thinner NACA 0015 blades, producing a more constant streamwise loading component. Finally, for low blade speed ratios ($\lambda < 1.0$) the thicker NACA 0021 airfoils have more distinctive peaks in streamwise loading. These changes in behaviour are well represented by the effective numerical model for all blade speed ratios.

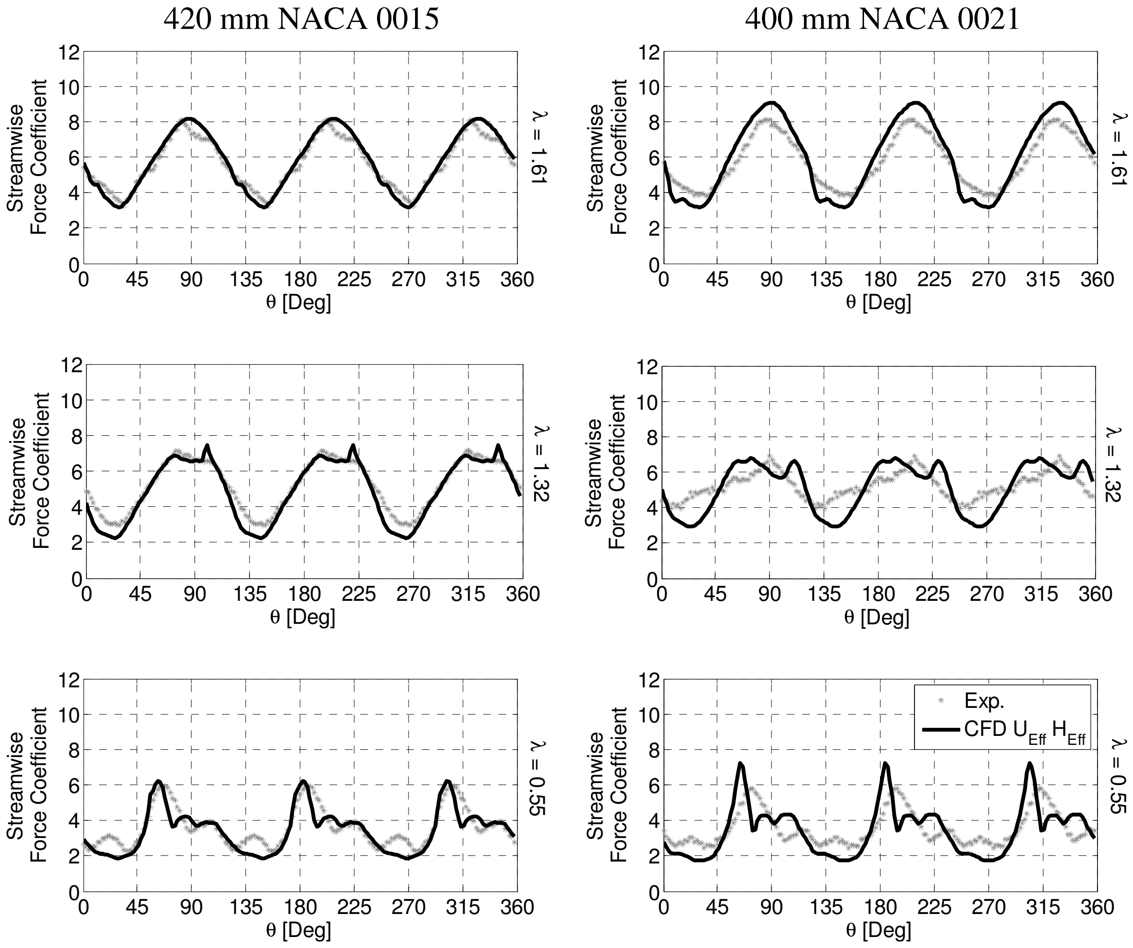

420 mm NACA 0015

400 mm NACA 0021

Figure 6.37: Effective numerical and experimental streamwise force coefficients for the 420 mm NACA 0015 and 400 mm NACA 0021 airfoils ($\beta = 0°$, $\lambda = 1.61, 1.32$, and 0.55)

The cross-stream force coefficients predicted by the effective numerical model and those obtained experimentally for the c = 420 mm NACA 0015 blades and the c = 400 mm NACA 0021 blades, are plotted in Figure 6.38. The most apparent change in cross-stream loading behaviour with an increase in thickness ratio is the minor drop in loading amplitude for $\lambda \approx 1.6$. This feature is well modelled by the effective numerical predictions. Beyond this change in behaviour however, there is little difference in cross-stream loading with a change in thickness ratio.

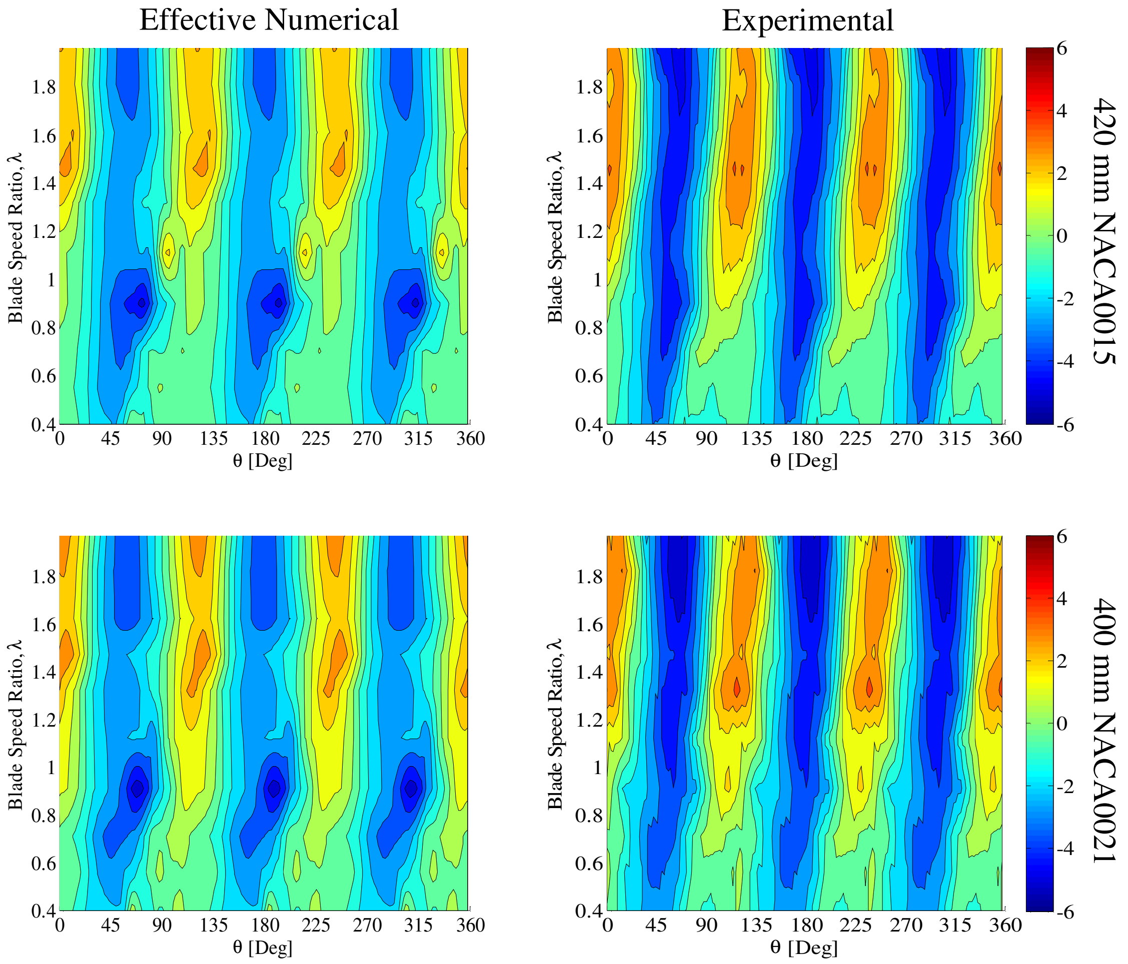
Effective Numerical

Experimental

Figure 6.38: Contour plot of effective numerical and experimental cross-stream force coefficients for the 420 mm NACA 0015 (κ = 1.10, τ = 1.15) and 400 mm NACA 0021 (κ = 1.07, τ = 1.15) airfoils (β = 0°)

From Figure 6.38, and the series of sample results given in Figure 6.39, it is clearly evident that the cross-stream loading behaviour is mainly unaffected by an increase in blade thickness ratio. The loading pattern of the cross-stream force is very similar for the two test cases in terms of amplitude, phase, and wave form. The one minor exception is the slightly higher positive force coefficient amplitudes measured experimentally at intermediate blade speed ratios, which is well predicted by the effective numerical model. In general, the effective numerical model predicts this component of the vibration excitation loading behaviour with considerable accuracy for both blade types throughout the entire operational range of the turbine.

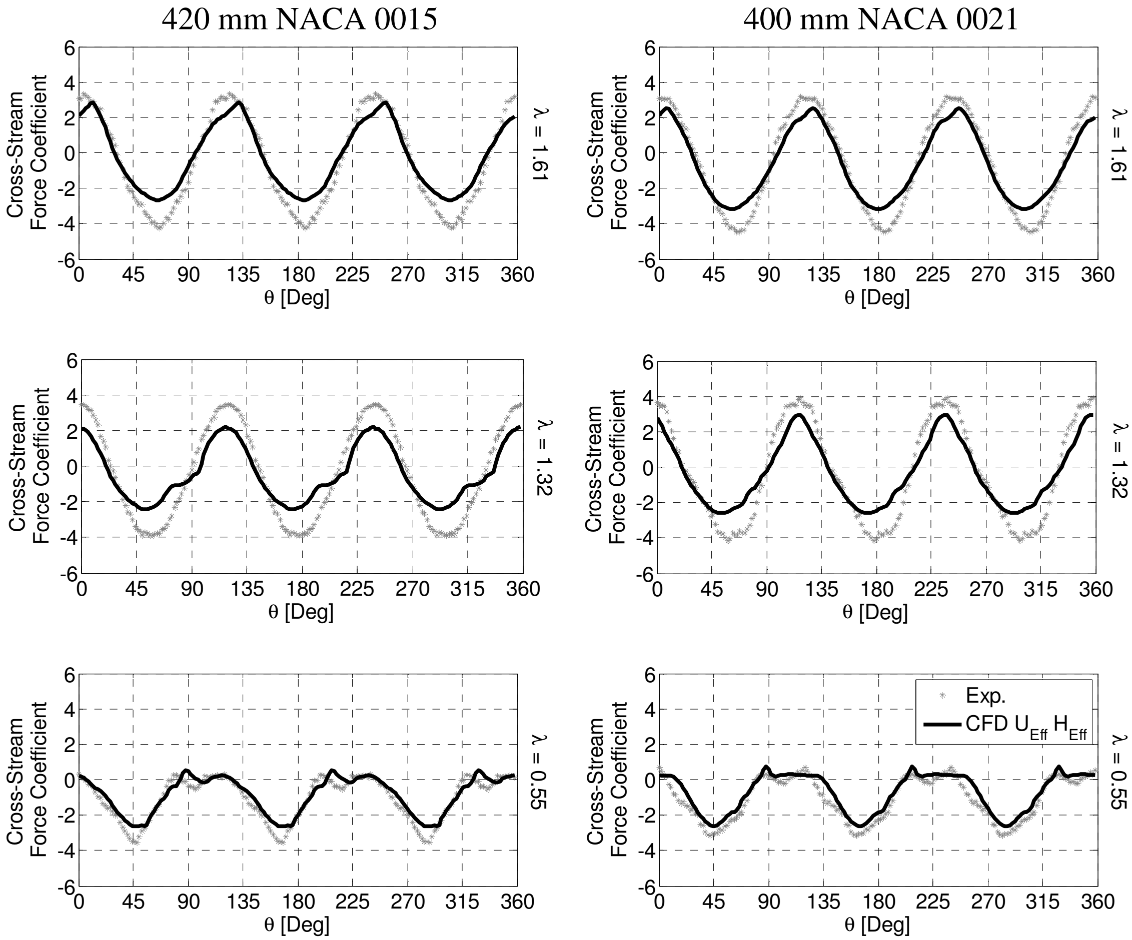

Figure 6.39: Effective numerical and experimental cross-stream force coefficients for the 420 mm NACA 0015 and 400 mm NACA 0021 airfoils (β = 0°, λ = 1.61, 1.32, and 0.55)

6.4.4. Vibration Response

Measurements of the turbine force coefficients and vibration response were obtained without the cable support system in place for a limited set of blade designs. As previously noted, without the cable system attached, resonant excitation of the primary whirl frequency of the turbine shaft occurs directly within the operational range of the turbine. This resulted in high vibration response of the turbine, such that the force coefficient measurements obtained from these test cases were practically unusable. Nevertheless, the turbine must operate in the field without the guy wire support system in place. As such, the vibration measurements obtained without the cable support system are a more realistic representation of the vibration response of the turbine under normal operating conditions. As a result, where available, these measurements will be analysed in order to determine the vibration response characteristics of the different blade designs.

In addition to the NACA 0015, c = 420 mm and NACA 0021, c = 400 mm blades, vibration response measurements were also obtained for the intermediate NACA 0015, c = 400 mm blade design (t/c = 0.169). Unfortunately, force coefficient data is not available for this blade design, and as such the vibration excitation characteristics could not be analysed.

Normalized vibration response data for the blade pass frequency of the turbine (as performed in section 5.1.2) are plotted in Figure 6.40, where linear line segments have been interpolated between the 8 and 10 m/s data sets in order to more clearly demonstrate the vibration response behaviour of the turbine. From this figure, it can be seen that the resonant vibration response of the turbine occurs at a rotational velocity of approximately 75 RPM for all blade designs, indicating that there is little effect of the blade type on the turbine structural dynamics. This corresponds to blade speed ratios of λ = 1.37 and 1.11, for wind speeds of 8 and 10 m/s respectively. Note that it is over this range of blade speed ratios that appreciably lower amplitude variations in streamwise loading were measured experimentally and predicted by the effective numerical model for airfoils with greater thickness ratio.

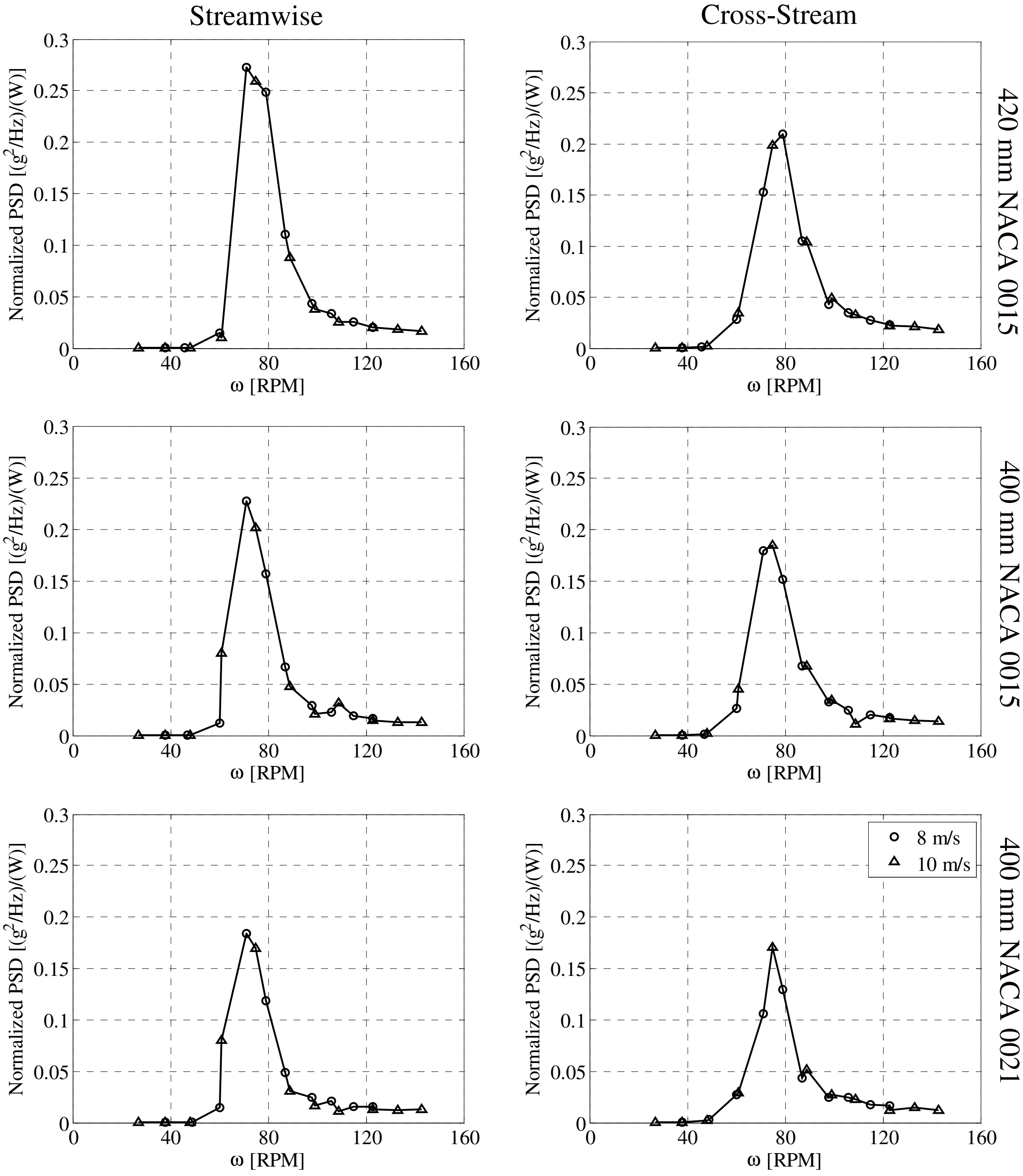

Figure 6.40: Power spectral density of the blade pass frequency without cables normalized by the power available in the oncoming flow ($\beta = 0°$)

Table 4 below lists the peak normalized power spectral density amplitude of the streamwise and cross-stream accelerometer measurements for the three blade designs described above. Due to the smaller amplitude fluctuations in the streamwise force coefficients for the thicker airfoils at intermediate blade speed ratios, the vibration response of the turbine is considerably smaller in the streamwise direction. However, despite having slightly larger amplitude fluctuations in the cross-stream force coefficients over this same range of blade speed ratios, the thicker blades also experienced a decrease in the cross-stream peak normalized power spectral density. This is likely due to a coupling with the streamwise vibration response through the whirl mode of the turbine, resulting in higher cross-stream vibration responses for the thinner blades. While this is a simplified method of comparing the vibration response of the turbine for the different blade designs, these values are a good representation of the primary vibration response behaviour of the turbine.

Test Case			Peak Normalized PSD Amplitude	
Blade Design	Chord Length [mm]	t/c	Streamwise	Cross-stream
NACA 0015	420	0.156	0.273	0.209
NACA 0015	400	0.169	0.227	0.185
NACA 0021	400	0.231	0.184	0.171

Table 4: Peak normalized power spectral density amplitude in the streamwise and cross-stream directions as a function of blade thickness ratio

6.5. Summary

The third phase of this research consisted of using the experimental measurements (Chapter 5) to validate the transient results obtained from the numerical model developed at the onset of this study (Chapter 3). After an initial comparison of the experimental data to the simulation results it was clear that the two-dimensional numerical model considerably over-predicted the turbine power output, aerodynamic force coefficients, and turbine wake velocities.

Based upon these results it was concluded that due to the finite aspect ratio of the turbine prototype, the effective flow velocity across the turbine must be considerably less than that of the ideal two-dimensional numerical model. To compensate for this discrepancy in the effective inlet flow velocity, a velocity correction factor was developed. This factor was determined based upon the ratio of the mean streamwise force coefficient of the numerical model, to that of the experimental results. By applying the velocity correction factor, the power coefficient amplitudes, as well as the blade speed ratios at which they occur, showed far better agreement with the experimental data.

Ultimately, while the velocity correction factor did account for a major source of disagreement between the finite aspect ratio turbine prototype and the infinite aspect ratio numerical model, some discrepancy still existed in the thrust and power coefficient predictions. It was postulated that the formation of blade-tip vortices and boundary layer interference at the support strut mounting locations were contributing to this loss in thrust force, and thus power output of the turbine prototype. In order to account for the induced and parasitic drag forces, a simplified turbine height correction factor was applied to the numerical simulation results. This effectively increased the blade area by which the numerical results were normalized, thereby reducing the thrust and power coefficient amplitudes of the effective numerical model.

In conjunction, these two correction factors successfully accounted for the dominant three-dimensional flow effects present in the experimental measurements, and vastly improved the effective numerical model aerodynamic force coefficient predictions. This is an important finding of this research as it demonstrates that through the proper application of a set of simple correction factors, two-dimensional numerical model results can be applied to determine the aerodynamic loading behaviour on a three-dimensional turbine. This means that the computational expense of a full three-dimensional numerical model can be avoided, and the two-dimensional numerical model can be quickly employed to simulate numerous blade designs and turbine configurations.

Once the appropriate velocity and height correction factors had been determined, the numerical model was then validated for a number of different blade designs. In particular, the effect of a change in the preset pitch angle of the blades on the development of dynamic stall and overall turbine performance was investigated. From this analysis it was found that considerable increases in turbine power production (13%) could be obtained while decreasing the vibration response of the turbine by simply decreasing the preset pitch of the airfoils. While the range over which this behaviour was validated was small, parallel studies have indicated that the numerical model is capable of determining the change in performance that accompanies a change in the preset pitch angle with considerable accuracy (Fiedler, 2009).

Further examinations revealed the effects of a change in the thickness ratio of the airfoil on the aerodynamic loading components. By increasing the relative thickness of the blade an equivalent peak power output could be obtained, while significantly decreasing the vibration excitation loads, and thus the primary resonance vibration response of the turbine (33%). These findings can be directly applied to the design of the present VAWT prototype to reduce the vibration excitation and response behaviour, and optimize the structural requirements of the turbine and its support structure.

CHAPTER 7

CONCLUSIONS AND RECOMMENDATIONS

This research was initially motivated by an interest in the vibration and noise production of Cleanfield Energy's small-scale, high-solidity, VAWT. Because the turbine is installed within the urban environment, noise production is a primary concern for the manufacturer. A preliminary study was performed where the noise level of the turbine installed in a typical rooftop setup was measured (Appendix A.6). From this study it was concluded that even at high flow velocities the noise production of the turbine was insignificant (20 dBA). However, during the course of this investigation, high amplitude, low frequency vibrations were observed under nearly all operating conditions.

Due to the urban environment within which the turbine is typically installed, a conventional guy-wire system to support the turbine is often impractical to implement. As such, in order to isolate the turbine dynamics from the building upon which it is mounted, a large support structure needs to be employed. However, the cost associated with the turbine support structure is often on the same scale as the expense of the turbine itself. As such, the cost effectiveness of the turbine is greatly reduced by the need to account for the presence of high amplitude vibrations through the use of a robust support system.

Based upon this observation it was concluded that a study on the flow induced vibration excitation and response mechanisms of high solidity VAWTs needed to be performed. The core motivation for this research being to better understand the aerodynamics of the flow through and around the turbine in order to be able to make design changes that could minimize the flow induced excitation of the turbine. The original contributions of this work include: design of an aerodynamic force measurement system, development of vibration mitigation methodologies, measurement of aerodynamic forces on a high solidity VAWT operating at low blade speed ratios, development of two correction factors to account for three-dimensional flow effects, and the development of a VAWT design tool. A summary of these findings are given below.

7.1. Conclusions

The first major contribution of this research was the development of a system capable of obtaining accurate, repeatable measurements of the aerodynamic loading on the airfoils of a high solidity VAWT. This system consisted of extensively calibrated load measurement instruments and a wireless telemetry device capable of remotely capturing the aerodynamic force data from the rotating turbine. Chapter 4 and Appendix A.2 present and summarize the development of the aerodynamic load measurement system. The utilization of a wireless telemetry system avoids the use of slip-rings for transmitting data and reduces signal noise. Additionally, by measuring the integrated aerodynamic force through the use of strain measurements rather than pressure distributions on the airfoil surface, the error introduced by pressure integration of sparse measurements is circumvented.

Because of the very high vibration response of the turbine, aerodynamic load measurements were very difficult to obtain. In order to be able to measure the underlying aerodynamic forces on the turbine blades, a series of vibration mitigation methodologies were developed (Chapter 5). First, a cable guy-wire system was developed to shift the natural frequencies of the turbine, so that the resonance response and dynamic amplification conditions of the turbine were altered. In a similar manner, tests were performed over a wide range of flow velocities, so that the resonant response conditions of the turbine could be avoided. Finally, two unique filtering techniques were developed to remove any remaining vibration component from the aerodynamic load measurements. While the vibration minimization technique was easily applied, due to insufficient amounts of data at the upper and lower operational capabilities of the turbine, inconsistent and unreliable results were obtained. Conversely, while more manually intensive, the band stop filtering technique proved to be an appropriate method to remove the remnant vibration component from the aerodynamic load measurements for all blade speed ratios. By developing and applying these vibration mitigation techniques, the true underlying aerodynamic forces on the turbine blades could be determined.

Application of the load measurement system and vibration mitigation methodologies to obtain the aerodynamic forces on the blades of a high solidity VAWT operating at low blade speed ratios is the third major contribution of this work. Previous research has been limited to low solidity turbines ($\sigma \leq 0.20$) operating at high blade speed ratios ($\lambda \geq 2.0$), where dynamic stall effects are minimal. The present aerodynamic load measurements however were obtained for a very high solidity ratio design ($\sigma = 0.424$ and 0.45) such that the turbine was operating at very low blade speed ratios ($0.4 \leq \lambda \leq 2.3$). These measurements were obtained for three different blade designs at two different preset pitch angles. This is an important contribution of this research as the available experimental database was appreciably expanded as a result. In particular, aerodynamic force coefficient data, wake velocity measurements, and turbine vibration response for a full-scale, high solidity VAWT operating at low blade speed ratios and high Reynolds numbers were obtained. Not only was this data used for the validation of the present two-dimensional numerical model, it can also be directly employed to validate any future three-dimensional numerical models of high solidity VAWTs.

The range of blade speed ratios over which experimental data was obtained is particularly important in regards to the unsteady aerodynamic loading behaviour of VAWTs, due to a combination of two factors. First, because the airfoils are subjected to high relative angles of attack and high pitch rates, deep dynamic stall and the production of large scale flow structures was identified throughout the rotation. Second, over this range of blade speed ratios the ambient wind velocity is nearly the same as the rate at which the blades are travelling downstream. The combination of these two conditions results in a situation where large intervals of blade/vortex interaction is occurring as the vortices formed during dynamic stall are convected downstream with the blades.

The next major contribution of this research was the validation of the two-dimensional URANS model with the experimentally obtained aerodynamic force and wake measurements (Chapter 6). Initial comparison of the experimental results to the numerical model predictions revealed a considerable over-prediction of the aerodynamic forces on the blades. This resulted in an over-prediction of the vibration excitation amplitudes and turbine power coefficients. This was an immediate indicator of the magnitude of the three-dimensional flow effects on the experimental force measurements.

Comparison of the wake velocity measurements to the numerical streamwise velocity profiles revealed that the two-dimensional numerical model predicted higher downstream flow velocities. This indicated that as a result of the two-dimensional nature of the numerical model, flow was being restricted to pass through the turbine rather than above or below it. These measurements also highlighted the significant loss in flow momentum through the turbine as a result of the effective blockage of the turbine and mechanical power extraction. An inlet velocity correction factor, κ, was developed to account for the three-dimensional flow divergence effects due to the finite aspect ratio of the turbine as a whole.

The effects of blade-tip vortices and boundary layer interference at the strut mount locations were accounted for through the use of a turbine height correction factor, τ. This scaling factor corrected for the induced and parasitic drag forces not modelled in the two-dimensional numerical representation of the turbine prototype. Application of this correction factor assumed that the induced and parasitic drag forces shortened the effective length of the turbine prototype blades, such that the dynamic pressure force was reduced from the numerical model predictions.

The magnitude of these two correction factors highlighted the relative scale of the dominant three-dimensional flow effects for the given turbine and blade aspect ratios ($\kappa \approx 1.1$, $\tau \approx 1.15$). Combined, the velocity and height correction factors were capable of properly scaling the numerical model predictions, such that considerably improved agreement with the experimental measurements of the aerodynamic force were obtained. This is an important finding as it demonstrates that through the proper application of a set of simple correction factors, two-dimensional numerical model results can be applied to determine the aerodynamic loading behaviour on a three-dimensional turbine.

The effective numerical model was first validated against a base wind turbine configuration with good agreement. After which, a number of different blade designs were simulated in order to examine the performance of the model on other turbine configurations. First, the effect of a change in the preset pitch angle of the blade, β, on the turbine power production, onset of dynamic stall, and the resultant vibration excitation and response behaviour, was investigated. For the small decrease in β from 2.66 to 0°, an increase in turbine power production of approximately 13% was realized. This finding is of particular interest as this change in the preset pitch angle also resulted in a small decrease in the primary vibration response behaviour of the turbine.

Second, the effect of a change in the thickness ratio of the airfoil, t/c, was explored. By increasing the thickness ratio of the blades from 0.156 to 0.231, a nearly equivalent peak power output (within 1%) was obtained. The vibration excitation loads were reduced, resulting in a decrease in the turbine vibration response of up to 33%. This finding can be directly applied to the design of the present VAWT prototype to reduce the vibration excitation and response behaviour, and optimize the structural requirements of the turbine and its support structure. In doing so, the cost of installation for the turbine can be reduced, along with the likelihood of fatigue failure. Ultimately, this will increase both the lifespan and the cost effectiveness of the turbine.

The culmination of this research is the development of a two-dimensional CFD model corrected for three-dimensional flow effects which can be employed as a VAWT design tool. From the knowledge gained from this research a design tool has been created which can be used to accurately model the highly dynamic flows of a high solidity VAWT. This model has been extensively validated against aerodynamic force coefficient data, wake velocity measurements, turbine power output, and vibration response measures. The importance of three-dimensional flow phenomenon on the turbine loads and effective blade speed ratio has been thoroughly explored and is incorporated in the VAWT design tool. From the information contained within this thesis this design tool can easily be recreated and applied to study numerous other flow conditions, blade designs, and blade configurations for turbines of varying aspect ratios.

7.2. Recommendations

Based upon the findings and conclusions of this research the following recommendations can be made. In regards to the advancement and development of the two-dimensional numerical model, the use of turbulence transition models is encouraged. Due to the transitional Reynolds numbers at which high solidity, low rotational velocity turbines operate, flow is transitioning from laminar to turbulent over the surface of the airfoils. The location of this transition along the airfoil chord will have a direct impact on the onset and severity of dynamic stall, as a laminar boundary layer has less flow momentum near the airfoil surface, and thus is more prone to separation. It should be noted however that the development and validation of turbulence transition models is a research field in itself.

One of the primary findings of this research was the considerable impact that three-dimensional flow effects have on both the thrust and radial force coefficients, and consequentially the power output and vibration excitation of the turbine.

Due to the finite aspect ratio of the turbine, flow diverges above and below the swept area, reducing the effective oncoming flow velocity and thus turbine power. While it is impractical to manufacture a ducting system to prevent flow from diverging around the turbine, this behaviour can be minimized by close-surface mounting, reducing the effective blockage of the turbine, or by increasing the turbine aspect ratio. One method of reducing turbine blockage effects is to minimize the total frontal projected area of the turbine support structure and generator. By reducing resistance to flow, the oncoming flow will have a greater propensity to pass through the swept area of the turbine, rather than around it.

The second approach which can be employed to minimize flow divergence is to increase the aspect ratio of the turbine. In doing so, the turbine will be subjected to a higher effective flow velocity, increasing the power available in the oncoming flow, and maximizing the power output of the turbine. One issue with this approach however is the potential change in the aerodynamic and structural properties of the turbine that will accompany an increase in aspect ratio. If the turbine aspect ratio is increased by decreasing the turbine radius, the solidity ratio of the turbine will increase. This will decrease the optimal rotational velocity, further increasing the airfoils' relative angle of attack, and promoting dynamic stall and vibration excitation. This behaviour can be further investigated through the use of the effective numerical model. Conversely, if the turbine aspect ratio is increased by increasing the length of the airfoils, the span over which the blades are supported must also increase, or additional struts may need to be added to support the blades. Because of the large fluctuating radial forces applied to the blades throughout each rotation, an increase in blade span between support struts may increase their vulnerability to failure in the bending mode. Alternatively, an increase in the number of support struts will increase the turbine's aerodynamic and interference drag, reducing net power output. One final consideration is the change in turbine dynamics that would accompany an increase in turbine height. By raising the centre of gravity of the turbine, and increasing its total mass moment of inertia, the turbine will be considerably more prone to the already dominant whirl mode.

Several approaches can be taken to decrease the losses introduced by the turbine support struts and blade-tip vortices, thereby reducing the turbine height correction factor. Because the radial forces applied to the turbine are independent of the parasitic losses introduced by these three-dimensional flow effects, the vibration excitation loads on the turbine are relatively unaffected by the turbine height correction factor. As such, any decrease in the height correction factor will increase the power output of the turbine, without any significant increase in turbine vibration excitation.

Interference drag introduced by the strut mounting geometry is a large source of parasitic drag. Because of the large rectangular block located directly opposite the suction side of the airfoil, it is unable to produce the ideal thrust force predicted by the numerical model. Integrating the struts into the blades, such that the transition from blade to strut is less dramatic, would help to reduce these losses. This could be achieved by placing a faring around the existing mount location, such that the airfoil thickness is increased at each strut. While this could be applied as a retrofit to the existing turbine prototype, it is recommended that a redesign of the interface between the strut and blade is made in future turbine models. To better understand how the strut/end plate boundary layer interaction affects the lift and drag properties of the airfoil, further two-dimensional numerical studies that incorporate the strut mounting plate could be performed.

An increase in blade aspect ratio will reduce the relative impact of blade-tip vortices on the power output of the turbine. This can be accomplished by increasing the blade length, as described above, or by suppressing flow around the ends of the airfoils, thereby increasing their effective aspect ratio. While there are end plates on the blades tested in this study, they extend only 2 cm beyond the surface of the airfoil and present relatively little resistance to flow around the end of the blade. Increasing the size of the end plates could help to prevent the formation of blade-tip vortices, and have been proven effective in other applications such as those found at the tips of aircraft wings. One trade-off which must be considered is the increase in skin drag introduced by an increase in end plate area. As an alternative, blended winglets could be added to the blades to take advantage of the blade-tip vortices and produce additional lift, and thus thrust force, on the blades. This method has been applied to aircraft and horizontal axis wind turbines with considerable success. However, the design of winglets is highly sensitive to the flow conditions over the surface of the airfoil. Because of the rapidly changing flow direction, relative angle of attack, and dynamic stall behaviour of the VAWT airfoils, optimizing winglets for this application would likely be an extremely involved procedure.

From the analysis of the experimentally measured force and power coefficients and turbine vibration response, as well as the effective numerical model predictions, a series of high potential blade design parameters can be developed. First, as was identified by Fielder (2009), by reducing the preset pitch of the airfoils, greater turbine power output can be obtained. The second blade design aspect that was investigated was the effect of a change in the relative airfoil thickness. An increase in the thickness ratio of the airfoil resulted in a decrease in vibration excitation and response of the turbine. Further investigation of the potential vibration excitations loads over a wider range of preset pitch angles and thickness ratios of the airfoils should be carried out through the use of the numerical model to determine if there is an optimal value which both maximizes power output, while minimizing vibration excitation. In the end, some compromise between the maximum power output of the airfoil design and the vibration response of the turbine may need to be made in order to maximize the total power output of the turbine; where the total power output is the product of the turbine lifespan and the average turbine power output.

Another design aspect which could be investigated now that a reliable, validated VAWT design tool has been developed is the use of asymmetric airfoils to improve turbine performance. Asymmetric airfoils could be applied to optimize the airfoil performance on both the upstream and downstream portions of the rotation, such that a more regulated thrust and radial force is applied to the airfoil throughout its entire rotation. This would minimize vibration excitation of the turbine, and has the potential to produce equivalent or increased power output.

Finally, the numerical model could be expanded to investigate the interaction of multiple wind turbines, as found in wind farm installations. In doing so, a greater understanding of the effects of a highly dynamic, low momentum turbine wake velocity on downstream turbines could be determined. This would include an investigation of the power output and vibration excitation of wind turbines subjected to large scale vortex structures shed from upstream turbines. This would aid in the development of a set of guidelines necessary to determine the optimal spacing of high solidity VAWTs in wind farm configurations.

REFERENCES

Abbott, I. H., & von Doenhoff, A. E. (1959). *Theory of wind sections: Including a summary of airfoil data*. Mineola, Dover Publications, Inc.

Ahmadi, S. A., Sharif, S., & Jamshidi, R. (2009). A numerical investigation on the dynamic stall of a wind turbine section using different turbulent models. *World Academy of Science, Engineering and Technology, 58*, 290-296.

Akins, R. E., Klimas, P. C., & Croll, R. H. (1983). Pressure distributions on an operating vertical axis wind turbine blade element. *Proceedings of the American Solar Energy Society Annual Meeting, Sixth Biennial Wind Energy Conference*, 455-462.

Allet, A., Halle, S., & Paraschivoiu, I. (1999). Numerical simulation of dynamic stall around an airfoil in Darrieus motion. *Journal of Solar Energy, 121,* 69-76.

Anderson, J. D., Jr. (1989). *Introduction to flight* (3rd ed.). New York: McGraw-Hill.

ANSYS CFX-Solver Theory Guide. (2009). ANSYS Inc. Canonsburg, PA.

Armstrong, S. (2011). Power performance, flow behaviour and excitation response of canted blades for a vertical axis wind turbine. M.A.Sc. Thesis McMaster University.

Armstrong, S., Fiedler, A. J., & Tullis, S. (2011). Flow separation on a high Reynolds number, high solidity vertical axis wind turbine with straight and canted blades and canted blades with fences. *Accepted for publication in Renewable Energy.*

Ashwill, T. D., (1989). Initial structural response measurements for the Sandia 34-meter test bed. *Proceedings of the Eighth ASME Wind Energy Symposium, 7,* 47-54.

Ashwill, T. D., Sutherland, H. J., & Veers, P. S. (1990). Fatigue analysis of the Sandia 34-meter vertical axis wind turbine. *Proceedings of the Ninth ASME Wind Energy Symposium, 9,* 109-115.

Ashwill, T. D., & Veers, P. S. (1990). Structural response measurements and predictions for the Sandia 34-meter test bed. *Proceedings of the Ninth ASME Wind Energy Symposium, 9,* 101-108.

Baldwin, B. S., & Barth, T. J. (1991). A one-equation turbulence transport model for high Reynolds number wall-bounded flows. *AIAA.* (Paper 91-0610).

Baldwin, B. S., & Lomax, H. (1978). Thin layer approximation and algebraic model for separated turbulent flows. *AIAA*. (Paper 78-0257).

Barth, T. J., & Jesperson, D. C. (1989) The design and application of upwind schemes on unstructured meshes. *AIAA.* (Paper 89-0366).

Batchelor, G. K. (1967). *An Introduction to Fluid Dynamics.* Cambridge: Cambridge University Press.

Baudu, N., Sagner, M., & Souquet, J. (1973). Modelisation du déchrochage dynamic d'un profil oscillant, *Association Aéronautique et Astronautique de France 10th Colloque d'Aéronautique Appliquée,* France.

Berton, E., Allain, C., Favier, D., & Maresca, C. (2002) Experimental methods for subsonic flow measurements. *Notes on Numerical Fluid Mechanics and Multidisciplinary Design, 81,* 251–260.

Betz, A. (1920). Das Maximum der theoretisch möglichen Ausnützung des Windes durch Windmotoren. *Zeitschrift für das gesamte Turbinenwesen, 26,* 307–309.

Blackwell, B. F., Sheldahl, R. E., & Feltz, L. V. (1976). *Wind tunnel performance data for the Darrieus wind turbine with NACA 0012 blades.* (SAND76-0130). Albuquerque, NM: Sandia National Laboratories.

Blades, E. L., & Marcum, D. L. (2007). A sliding interface method for unsteady unstructured flow simulations, *Int. J. Numer. Meth. Fluids, 53,* 507–529.

Blevins, R. D. (1984). *Applied fluid dynamics handbook*, Van Nostrand Reinhold.

Bourdet, S., Braza, M., Hoarau, Y., Akoury, R. E., Ashraf, A., Harran, G., Chassaing, P., & Djeridi, H., Prediction and physical analysis of unsteady flows around a pitching airfoil with the dynamic mesh approach. *European Journal of Computational Mechanics, 16,* 451–476.

Bravo, R., Tullis, S., & Ziada, S. (2007). Performance testing of a small vertical-axis wind turbine. *Proceedings of the 21st Canadian Congress of Applied Mechanics (CANCAM)*, 470-471.

Brochier, G., Fraunié, P., Béguier, C., & Paraschivoiu, I. (1986). Water channel experiments of dynamic stall on Darrieus wind turbine blades. *AIAA Journal of Propulsion and Power, 2*, 445-449.

Burg, D. E., Klimas, P. C., & Stephenson, W. A. (1990). Aerodynamic design and initial performance measurements for the Sandia 34-m diameter vertical-axis wind turbine. *Proceedings of the Ninth ASME Wind Energy Symposium, 9,* 93-99.

Carne, T. G., Lauffer, J. P., Gomez, A. J., & Ashwell T. D. (1989). Model validation of the Sandia 34-meter test bed turbine using substructured modal-testing. *Proceeding of the Eighth ASME Wind Energy Symposium (ASME)*, *7*, 39-45.

Carta, F. O., Commerford, G. L., Carlson, R. G., & Blackwell, R. H. (1972). *Investigation of airfoil dynamic stall and its influence on helicopter control loads.* (U.S. Army AMRDL-Eustis Directorate Report TR-72-51) East Hartford, CT.

Cebeci, T., & Smith, A.M.O. (1974). *Analysis of turbulent boundary layers.* New York: Academic Press.

Chien, K.-Y., (1982). Predictions of channel and boundary layer flows with a low-Reynolds-number turbulence model. *AIAA Journal, 20*, 33–38.

Crimi, P., & Reeves, B. L. (1972) *A method for analyzing dynamic stall of helicopter rotor blades* (NASA-CR-2009). Retrieved from http://ntrs.nasa.gov/

Den Hartog, J. P. (1956). *Mechanical vibrations*. New York: McGraw-Hill Book Company, Inc.

Devaud, C. B., Weisinger, J., Johnson, D. A., and Weckman, E. J. (2009) Experimental and numerical characterization of the flow field in the large-scale UW fire research facility. *Int. J. Numer. Meth. Fluids*, *60*, 539-564.

Dodd, H. M. (1990). Performance predictions for an intermediate-sized VAWT based on performance of the 34-m VAWT test bed. *Proceedings of the Ninth ASME Wind Energy Symposium, 9,* 131-136.

Dohnmann, C. R., & Veers, P. S. (1989). Time domain structural response calculations for vertical axis wind turbines. *Proceedings of the Eighth ASME Wind Energy Symposium, 7,* 11-17.

Dole, C. E. (1981). *Flight theory and aerodynamics*. New York: Wiley.

Fanucci, J. B., & Walters, R. E. (1976). Innovative wind machines: The theoretical performances of a vertical axis wind turbine (SAND 76-5586). *Proceedings of the Vertical Axis Wind Turbine Technology Workshop*, 61-93.

Fiedler, A. J. (2009) The effects of blade pitch and mount point offset on vertical axis wind turbine performance. M.A.Sc. Thesis McMaster University.

Fiedler, A. J., & Tullis, S. (2009). Blade offset and pitch effects on a high solidity vertical axis wind turbine. *Wind Engineering, 33*(3), 237–246.

Ferreira, C. J. S., Bijl, H., van Brussel, G., & van Kuik, G. (2007). Simulating dynamic stall in a 2D VAWT: Modeling strategy, verification and validation with particle image velocimetry data. *Journal of Physics: Conference Series, 75.*

Ferreira, C., van Kuik, G., & van Bussel, G. (2006). Wind tunnel hotwire measurements, flow visualization and thrust measurement of a VAWT in skew (AIAA 2006-1368). *44th AIAA Aerospace Sciences Meeting and Exhibit.*

Fox, R. W., McDonald, A. T., & Pritchard, P. J. (2004). *Introduction to fluid mechanics* (6th ed.). Hoboken: Wiley.

Fujisawa, N., & Shibuya, S. (2001). Observations of dynamic stall on Darrieus wind turbine blades. *J Wind Eng Ind Aerod, 89,* 201-214.

Giesing, J. P. (1968). Nonlinear two-dimensional potential flow with lift. *Journal of Aircraft, 5*(2), 135-143.

Glauert, H. (1948). *The elements of airfoil and airscrew theory*, 2^{nd} Edition. Cambridge University Press.

Gormont, R. E. (1973) *A mathematical model of unsteady aerodynamics and radial flow for application to helicopter rotors* (Report No. DAAJO2-71-C-0045). Philadelphia, PA.

Guerri, O., Sakout, A., & Bouhadef, K. (2007). Simulation of the fluid flow around a rotating vertical axis wind turbine. *Wind Engineering, 31*(3), 149-163.

Ham, N. D. (1968). Aerodynamic loading on a two-dimensional airfoil during dynamic stall, *AIAA Journal*, *6* (10), 1927-1934.

Hamada, K., Smith, T., Durrani, N., Qin, N., & Howell, R. (2008). Unsteady flow Simulation and dynamic stall around vertical axis wind turbine blades. *46th AIAA Aerospace Sciences Meeting and Exhibit.*

Howell, R., Qin, N., Edwards, J., & Durrani, N., (2010). Wind tunnel and numerical study of a small vertical axis wind turbine. *Renewable Energy, 35*, 412-422.

Hofemann, C., Ferreira, C. S., Dixon, K., van Brussel, G., van Kuik, G., & Scarano, F. (2008). *3D stereo PIV study of the tip vortex evolution on a VAWT*. Retrieved from http://www.ewec2008proceedings.info/

Holmes, O. (1976). A contribution to the aerodynamic theory of the vertical axis wind turbine. *Proceedings of the Int. Symposium on Wind Energy Systems*, 55-72.

Islam, M., Ting, D.S.K., & Fartaj, A. (2008). Aerodynamic models for Darrieus-type straight-bladed vertical axis wind turbines. *Renewable and Sustainable Energy Reviews, 12,* 1087-1109.

Jacobs, E. N., & Sherman, A. (1937). *Airfoil section characteristics as affected by variations in the Reynolds number* (naca-report-586). Retrieved from http://naca.central.cranfield.ac.uk/

Jacobs, E. N., Ward, K. E., & Pinkerton, R. M. (1933). *The characteristics of 78 related airfoil sections from tests in the variable-density wind tunnel* (naca-report-460). Retrieved from http://naca.central.cranfield.ac.uk/

Johnson, D. A., & King, L. S. (1985). A mathematically simple turbulence closure model for attached and separated turbulent boundary layers. *AIAA Journal, 23*, 1684.

Jones, W. P., & Launder, B. E. (1972). The prediction of laminarization with a two-equation model of turbulence. *Int. J. Heat Mass Transfer, 15*, 301-314.

Klimas, P. C. & Sheldahl, R. E. (1978). *Four aerodynamic prediction schemes for vertical-axis wind turbines: A compendium.* (SAND78-0014). Albuquerque, NM: Sandia National Laboratories.

Kline, S. J., Cantwell, B. J., & Lilley, G. M. (1981). *AFOSR-HTTM Stanford conference on complex turbulent flows: Comparison of computation and experiment*, Stanford University, Stanford, CA,

Kroll, N., Rossow, C. C., Schwamborn, D., Becker, K., & Heller G. (2002) MEGAFLOW– a numerical flow simulation tool for transport aircraft design. *Proceedings of the ICAS 2002 Congress*, Paper No. 1105.

Kuethe, A., & Chow, C. (1986). *Foundations of aerodynamics* (4th ed.). New York: Wiley.

Lapin, E. E. (1975). *Theoretical performance of vertical axis wind turbines* (ASME paper, 75-WA/Ener-1), The winter annual meeting, Houston, TX, USA.

Larsen, H. C., (1975). Summary of a vortex theory for the Cyclogiro. *Proceedings of the Second U.S. National Conference on Wind Engineering Research, 8*, 1-3.

Leishman, J. G. (2000). *Principles of helicopter aerodynamics.* Cambridge: Cambridge University Press.

Leishman, J. G. (2002). Challenges in modelling the unsteady aerodynamics of wind turbines. *Wind Energy*, 5, 85-132.

Loftin, L. K., Jr., & Smith, H. A. (1949). *Aerodynamic characteristics of 15 NACA airfoil sections at seven Reynolds numbers for 0.7 x* 10^6 *to 9.0 x* 10^6 (naca-tn-1945). Retrieved from http://naca.central.cranfield.ac.uk/

Martinat, G., Braza, M., Hoarau, Y., & Harran, G. (2008). Turbulence modelling of the flow past a pitching NACA 0012 airfoil at 10^5 and 10^6 Reynolds numbers. *Journal of Fluids and Structures, 24*(8), 1294-1303.

Mathur, S. R. (1994). Unsteady flow simulations using unstructured sliding meshes. *AIAA Fluid Dynamics Conference*. AIAA: Washington, DC.

McAlister, K., Carr, L., & McCroskey, W. (1978) *Dynamic stall experiments on the NACA 0012 airfoil.* (NASA-TP-1100). Retrieved from http://naca.larc.nasa.gov

McCroskey, W. J. (1981). *The phenomenon of dynamic stall* (NASA Technical Memorandum 81264). Moffett Field: Ames Research Center.

McCroskey, W. J. (1982). Unsteady airfoils. *Annual Review of Fluid Mechanics*, *12*, 285-311.

McCroskey, W. J., McAlister, K. W., Carr, L. W., Pucci, S. L., & Lambert, O. (1980) *Dynamic stall on advanced airfoil sections*. (American Helicopter Society Preprint 80-01). Moffett Field: Army research and technology labs.

McCroskey, W. J., & Pucci, S. L. (1982) Viscous-inviscid interaction on oscillating airfoils in subsonic flow, *AIAA Journal, 20*, 167 - 174.

McLaren, K., Tullis, S., & Ziada, S. (2007a). CFD Simulation of dynamic thrust and radial forces on a vertical axis wind turbine blade. *15th Annual Conference of the Computational Fluid Dynamics Society of Canada - CFD 2007.*

McLaren, K., Tullis, S., & Ziada, S. (2007b). Vibration analysis of a vertical axis wind turbine blade. *21st Canadian Congress of Applied Mechanics*. 762-763.

McLaren, K., Tullis, S., & Ziada, S. (2010) Measurement of high solidity vertical axis wind turbine aerodynamic loads under high vibration response conditions, Submitted to *Journal of Fluids and Structures*, (YJFLS-D-10-00192).

McLaren, K., Tullis, S., & Ziada, S. (2011). Computational fluid dynamics simulation of the aerodynamics of a high solidity, small scale vertical axis wind turbine, *Wind Energy* (in press).

Menter, F. (1992). *Improved two-equation k-ω turbulence models for aerodynamic flows.* (NASA Technical Memorandum 103975). Moffett Field: Ames Research Center.

Menter, F. (1994). Two-equation eddy-viscosity turbulence models for engineering applications, *AIAA Journal, 32*, 1598-1605.

Mitra, S. K., (1998) *Digital Signal Processing*, New York: McGraw-Hill Book Company, Inc.

Newman, B. G. (1983) Actuator-disk theory for vertical-axis wind turbines. *J Wind Eng Ind Aerod, 15,* 347.

Oler, J. W., Strickland, J. H., Im, B. J., & Graham, G. H. (1983). *Dynamic stall regulation of the Darrieus turbine* (SAND83-7029). Albuquerque, NM: Sandia National Laboratories.

Ono, K., Kuwahara, K., & Oshima, K. (1980). Numerical analysis of dynamic stall phenomena of an oscillating airfoil by discrete vortex approximation, *7th International Conference on Numerical Methods in Fluid Dynamics*, California.

Paraschivoiu, I. (1981). *Double-multiple streamtube model for Darrieus wind turbines.* Second DOE/NASA wind turbines dynamics workshop, (NASA CP-2186), 19-25.

Paraschivoiu, I. (1983). Predicted and experimental aerodynamic forces on the Darrieus rotor. *Journal of Energy, 7,* 610-615.

Paraschivoiu, I. (1988). Double-multiple streamtube model for studying vertical-axis wind turbines. *AIAA Journal of Propulsion and Power, 4,* 370-378.

Paraschivoiu, I. (2002). *Wind turbine design: With emphasis on Darrieus concept.* Montreal: Presses Intl. Polytechnique.

Paraschivoiu, I., & Allet, A. (1988) Aerodynamic analysis of the Darrieus wind turbines including dynamic-stall effects, *AIAA Journal of Propulsion and Power, 4*, 472-477.

Paraschivoiu, I., Desy, P., & Masson, C. (1988). Blade-tip, finite-aspect ratio and dynamic-stall effects of the Darrieus rotor. *AIAA Journal of Propulsion and Power, 2*, 73-80.

Paraschivoiu, I., & Delclaux, F. (1983). Double-multiple streamtube model with recent improvements. *AIAA Journal of Energy, 7,* 250-255.

Piziali, R. A. (1994) *2-D and 3-D oscillating wing aerodynamics for a range of angles of attack including stall* (NASA Technical Memorandum 4632). Moffett Field: Ames Research Center.

Rao, J. S. (2000). *Vibratory condition monitoring of machines.* New Delhi: Narosa Publishing House.

Raw, M. J. (1996) Robustness of coupled algebraic multigrid for the Navier-Stokes Equations. *AIAA.* (Paper 96-0297), 34th Aerospace and Sciences Meeting & Exhibit, Reno, NV.

Rodi, W. & Scheurer, G. (1986). Scrutinizing the k-ε model under adverse pressure gradient conditions. *Journal of Fluids Engineering, 108,* 174-179.

Scheurich, F., Fletcher, T. M., & Brown, R. E. (2011). Simulating the aerodynamic performance and wake dynamics of a vertical-axis wind turbine. *Wind Energy, 14,* 159-177.

Shankar, P. N. (1976). On the aerodynamic performance of a class of vertical shaft windmills. *Proceedings Royal Society of London,* A.349, 35-51.

Sheldahl, R. E., & Klimas, P. C. (1978). *Four aerodynamic prediction schemes for vertical-axis wind turbines: A compendium* (Sandia National Laboratories Unlimited Release) Albuquerque, NM: Sandia National Laboratories.

Sheldahl, R. E., & Klimas, P. C. (1981). *Aerodynamic characteristics of seven symmetrical airfoil sections through 180-degree angle of attack for use in aerodynamic analysis of vertical axis wind turbines.* (SAND80-2114) Albuquerque, NM: Sandia National Laboratories.

Sheldahl, R. E., Klimas, P. C., & Feltz, L. V. (1980). *Aerodynamic performance of a 5-metre-diameter Darrieus turbine with extruded aluminum NACA-0015 blades.* (SAND80-0179). Albuquerque, NM: Sandia National Laboratories.

Sorensen, N. N., Michelson, J. A., & Schreck, S. (2002). Navier-Stokes predictions of the NREL phase VI rotor in the NASA Ames 80 ft x 120 ft wind tunnel. *Wind Energy, 5,* 151-169.

South, P., & Rnagi, R. S. (1975). *An experimental investigation of a 12-ft diameter high-speed vertical-axis turbine*. (Report No. LTRLA-166) National Research Council of Canada, Ottawa.

Spalart, P. R.,& Allmaras, S. R. (1992). A one-equation turbulence model for aerodynamic flows. *AIAA.* (Paper 92-0439).

Spalart, P.R., Jou, W.-H., Strelets, M., & Allmaras, S.R. (1997). Comments on the feasibility of LES for wings, and on a hybrid RANS/LES approach. In: Liu, C., Liu, Z. (Eds.), First AFOSR International Conference on DNS/LES, Ruston, LA, Advances in DNS/LES, Greyden Press, Columbus, OH.

Srinivasan, G. R., Ekaterinaris, J. A., & McCroskey, W. J. (1995). Evaluation of turbulence models for unsteady flows of an oscillating airfoil. *Computer and Fluids, 24*, 833-861.

SRI/PMD. (2008). *Operations and maintenance manual: Enhanced series 500e digital telemetry equipment* (70-SS510-00), Melbourne, Florida.

Strickland, J. H. (1975). *The Darrieus turbine: A performance prediction model using multiple streamtubes* (SAND 75-0431). Albuquerque, NM: Sandia National Laboratories.

Strickland, J. H., Webster, B. T., & Nguyen, T. (1979). A vortex model of the Darrieus turbine: An analytical and experimental study. *Journal of Fluid Engineering, 101*, 500-505.

Strickland, J. H., Smith, T., & Sun, K. (1981). *A vortex model of the Darrieus turbine: An analytical and experimental study* (SAND 81-7017). Albuquerque, NM: Sandia National Laboratories.

Tanaka, E., & Nakata, S. (1975). The interference of two-dimensional parallel jets. *Bulletin of the JSME, 18,* 1134-1141.

Templin, R. J. (1974). *Aerodynamic performance theory for the NRC vertical axis wind turbine* (National Research Council of Canada Report LTR-LA-160).

Tsang, K. K. Y., So, R. M. C., Leung, R. C. K., & Wang, X. Q. (2008). Dynamic stall behaviour from unsteady force measurements. *Journal of Fluids and Structures*, *24*, 129-150.

Veers, P. S. (1983). *A general method for fatigue analysis of vertical axis wind turbine blades* (SAND82-2543). Albuquerque, NM: Sandia National Laboratories.

Vittecoq, P., & Laneville, A. (1983). The aerodynamic forces for a Darrieus rotor with straight blades: Wind tunnel measurements. *J Wind Eng Ind Aerod, 15,* 381-388.

Webster, N. T. (1978). A study of an airfoil undergoing cycloidal motion, MS Thesis, Texas Tech University.

Weisinger, J. (2004). Characterization of the University of Waterloo live Fire Research Facility wind generation system, University of Waterloo, Waterloo.

Wilcox, D. C. (1993a). *Turbulence modeling for CFD*. La Canada, CA: DCW Industries.

Wilcox, D. C. (1993b). Comparison of two-equation turbulence models for boundary layers with pressure gradients. *AIAA Journal, 31,* 1414-1421.

Wilson, R. E. (1978). Vortex sheet analysis of the giromill. *Journal of Fluids Engineering, 100*(3), 340-342.

Wilson, R. E. & Lissaman, P.B.S. (19740. Applied aerodynamics of wind Power machines, Oregon State University.

Worstell, M. H. (1978). *Aerodynamic performance of the 17 meter diameter Darrieus wind turbine* (SAND78-1737). Albuquerque, NM: Sandia National Laboratories.

Worstell, M. H. (1982). *Aerodynamic performance of the 17 meter diameter Darrieus wind turbine in the three-bladed configuration: An addendum* (SAND79-1753). Albuquerque, NM: Sandia National Laboratories.

Zervos, A. (1988). Aerodynamic evaluation of blade profiles for vertical axis wind turbines. *European Community Wind Energy Conference,* 611-616.

Zervos, A., & Morfiadakis, E. (1990). Instantaneous pressure distribution measurements on the blades of a vertical axis wind turbine. *European Community Wind Energy Conference*, 247-251.

Zervos, A., Morfiadakis, E., & Stefanatos, N. (1989). Testing of blade profiles for vertical axis wind turbines. *Proc. of the EWEC*, 193-197.

APPENDICES

A.1. Steady State Model

In order to determine an appropriate mesh sizing and turbulent-viscosity model for use with the dynamic VAWT cross-section numerical model, a series of steady-state validation tests were performed. These tests consisted of simulation of experimental wind tunnel conditions for a NACA 0015 airfoil (Sheldahl & Klimas, 1981).

A.1.1. Numerical Domain

In order to ensure the proper interaction of the pressure field with the walls of the wind tunnel, a dynamically scaled flow domain was designed. Due to the elliptic nature of the flow, the overall length of the domain was 20 metres long in order to ensure the outlet condition did not affect the results of the simulation. The overall height of the domain was set to 5.6 metres. The 0.4 metre long NACA0015 airfoil is located at the centre of a circular sub-domain contained within the stationary rectangular domain. The circular sub-domain is 3.6 metres in diameter and its centre (corresponding to the centre of the blade) is located 5.0 metres from the inlet. The circular sub-domain was created in order to allow for adjustment to the angle of attack without the need to reproduce and re-mesh the entire domain. Figure A.1 shows the dimensions of the flow domain.

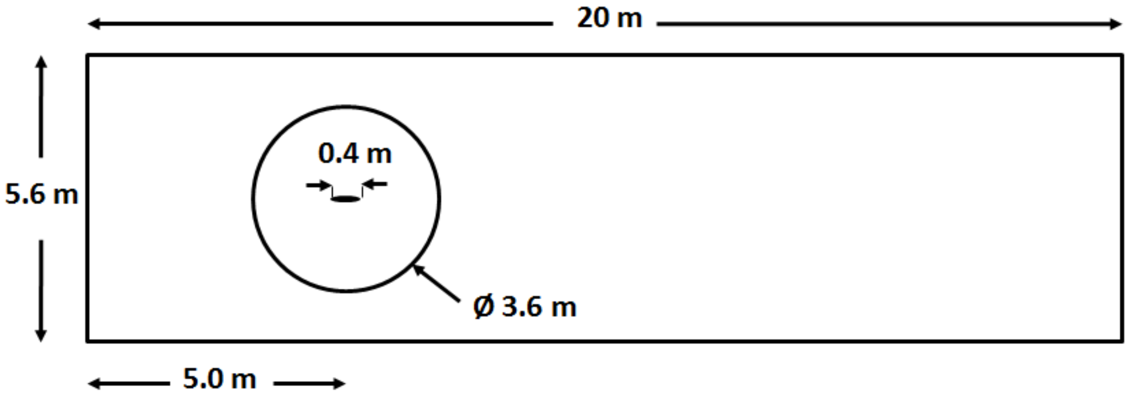

Figure A.1: Wind tunnel flow domain dimensions

The normal flow velocity was set to 13.45 m/s at the inlet of the rectangular domain, with turbulence intensity of 1%. The resulting Reynolds number based on free-stream velocity and airfoil chord length is Re_c = 360,000. The condition imposed at the outlet of the domain was a static pressure over the entire face with an average static pressure of 1 atm. The upper and lower surfaces of the domain, as well as the surface of the airfoil, were given a smooth, no-slip wall condition. Finally, a conservation of mass and momentum flux condition was imposed at the interface of the large rectangular domain and the small circular sub-domain in order to guarantee continuity. The location of these flow conditions is shown below in Figure A.2.

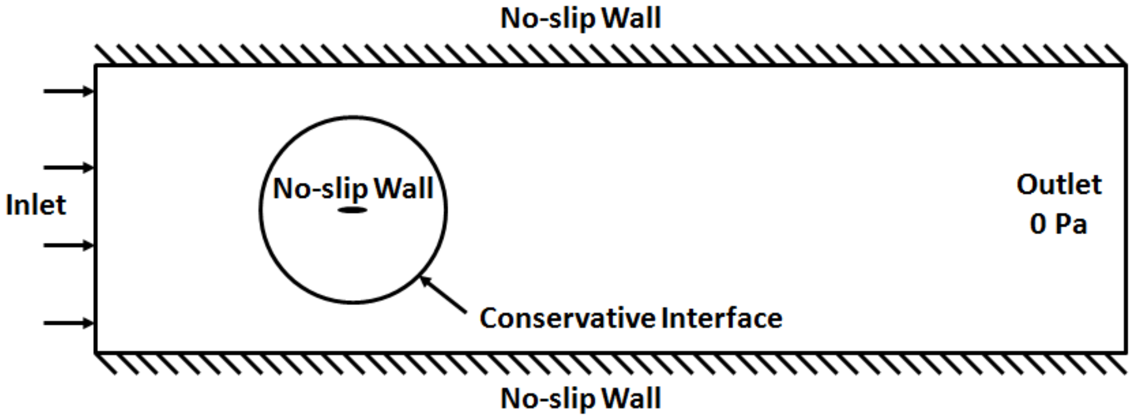

Figure A.2: Wind tunnel boundary conditions

A.1.2. Mesh Characteristics

The mesh imposed on the domain was generated based on a series of grid independence tests. Initially an angle of attack of α = 7° was selected as a gauge with which to measure the accuracy of the model. Once a suitable mesh had been settled upon further independence tests were performed at additional angles of attack ranging from α = 0° to α = 90°. The final mesh was composed of a structured boundary layer imposed at the surface of the blade and walls and an unstructured mesh within the bulk of the flow domain (Figure A.3).

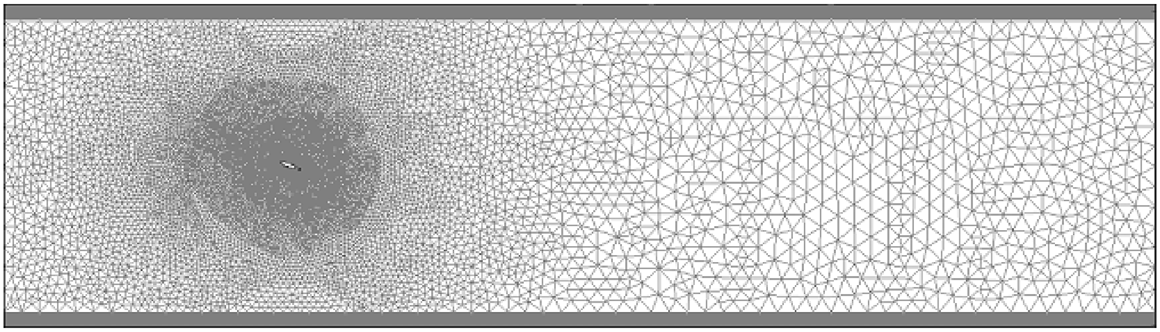

Figure A.3: Wind tunnel domain mesh

The boundary layer mesh was governed by the following restrictions; the length of the boundary layer segments was 0.8 mm, the thickness of the boundary layer was 6 mm, and the boundary layer consisted of 40 layers with a spreading rate of 1.1. The average y^+ value of the nearest nodal points from the surface of the blade was 0.64. The mesh size external to the boundary layer varied from 0.75 mm at the interface to the boundary layer, to 250 mm at the outlet of the domain. Figure A.4 and Figure A.5 show the mesh as it appears in close proximity to the blade and within the boundary layer itself, respectively.

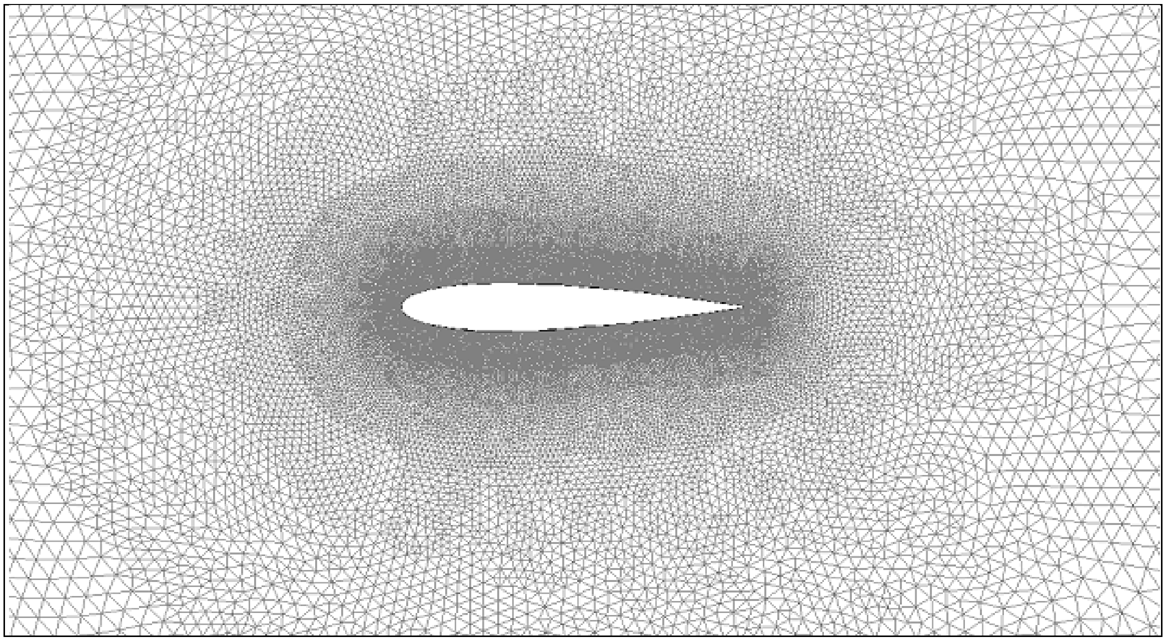

Figure A.4: Wind tunnel mesh surrounding the blade

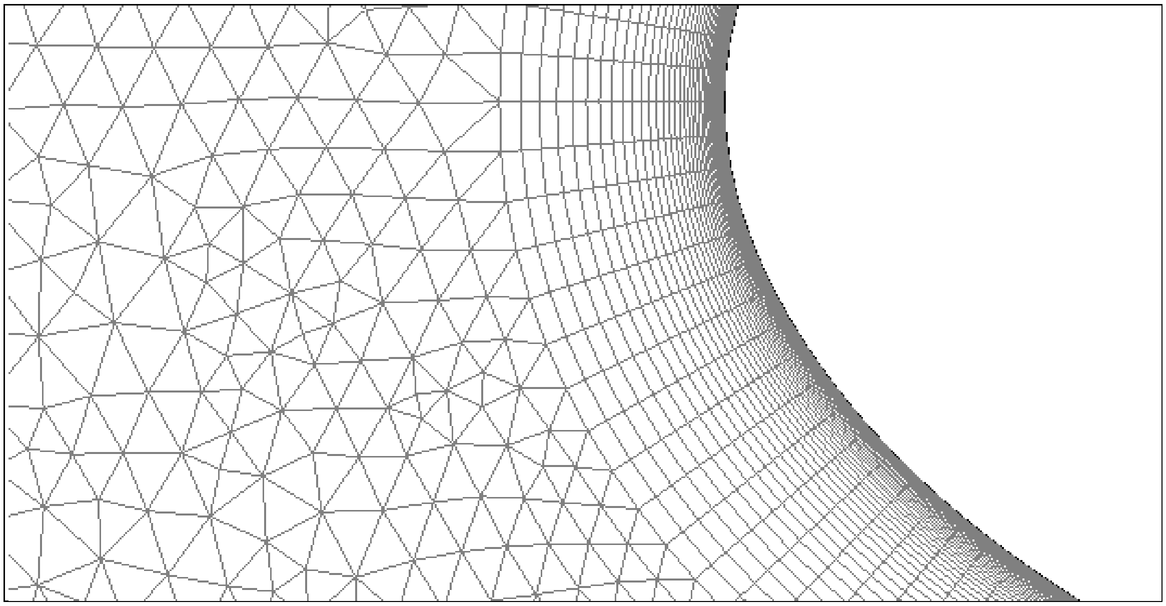

Figure A.5: Boundary layer mesh highlighting the highly refined structured mesh within close proximity of the airfoil surface

A.1.3. Turbulence Model Selection

As discussed in the literature review, the most widely used and well known turbulent-viscosity models are the k-ε model of Jones and Launder (1972) and the k-ω model developed by Wilcox (1993a). Due to the considerable successes of these two models, they were used as the baseline with which to compare the Shear Stress Transport (SST) model of Menter (1994). The SST model has been shown to perform well for highly separated aerodynamic flows, and was the primary candidate for the appropriate turbulence model.

From Figure A.6 it can be seen that due to the limitations of the k-ε model in the near-wall region (Wilcox, 1993b), the sharp rise in drag caused by flow separation at $\alpha \approx 16^{\circ}$ is not resolved. As a result, the k-ε model under-predicts the drag coefficient for $\alpha > 16^{\circ}$. In contrast, the superior treatment of the viscous near-wall region by Wilcox's k-ω model, allows for accurate prediction of the drag coefficient over the entire range of interest, even in highly adverse pressure gradients (Wilcox, 1993b). Not surprisingly, due to the formulation of the SST model, the solution within the viscous near-wall region is nearly identical to Wilcox's k-ω model, resulting in similar drag coefficient predictions.

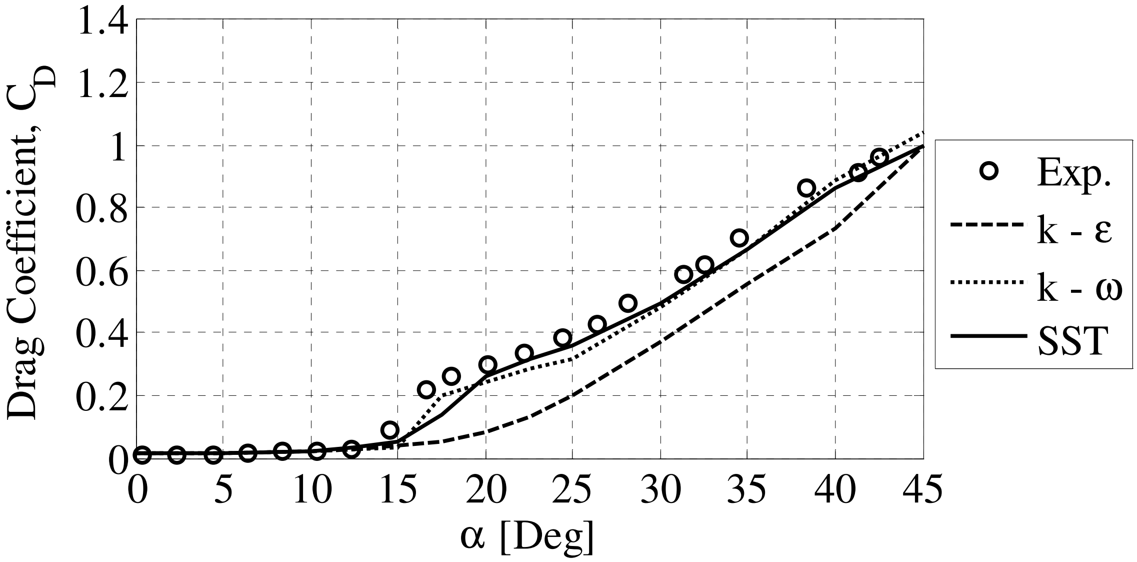

Figure A.6: Wind tunnel turbulence model drag coefficients. Exp. from Sheldahl and Klimas (1978)

Figure A.7 shows a dramatic difference between the lift coefficient values predicted by the k-ε, k-ω, and SST turbulence models. Up to an angle of attack of 10º, the pressure gradient is favourable, and separation of the flow from the blade surface is minimal. Within this region, the turbulence model predictions are nearly identical and reproduce the experimental values well. However, as the angle of attack increases further, the lift characteristics of the three models begin to deviate considerably.

At an angle of attack of α = 17.5°, the k-ω model predicts a large counter-clockwise vortex on the suction side of the blade. This causes the flow to accelerate over the trailing edge of the upper surface, producing a large low pressure region, and excessive lift. Conversely, the k-ε model predicts minimal flow recirculation, and for the most part the flow remains attached to the airfoil surface. As identified by Kline, Cantwell, and Lilley (1981), this is a result of an over-prediction of shear-stress levels in adverse pressure gradient flows due in turn to an over-prediction of the turbulent length scale (Rodi & Scheurer, 1986). Finally, the SST model, modified from the standard k-ω formulation in the near-wall region to account for the transport effects of the principal turbulent shear stress, predicts a moderate zone of clockwise rotational flow midway up the blade, resulting in a substantial drop in lift, as is observed experimentally.

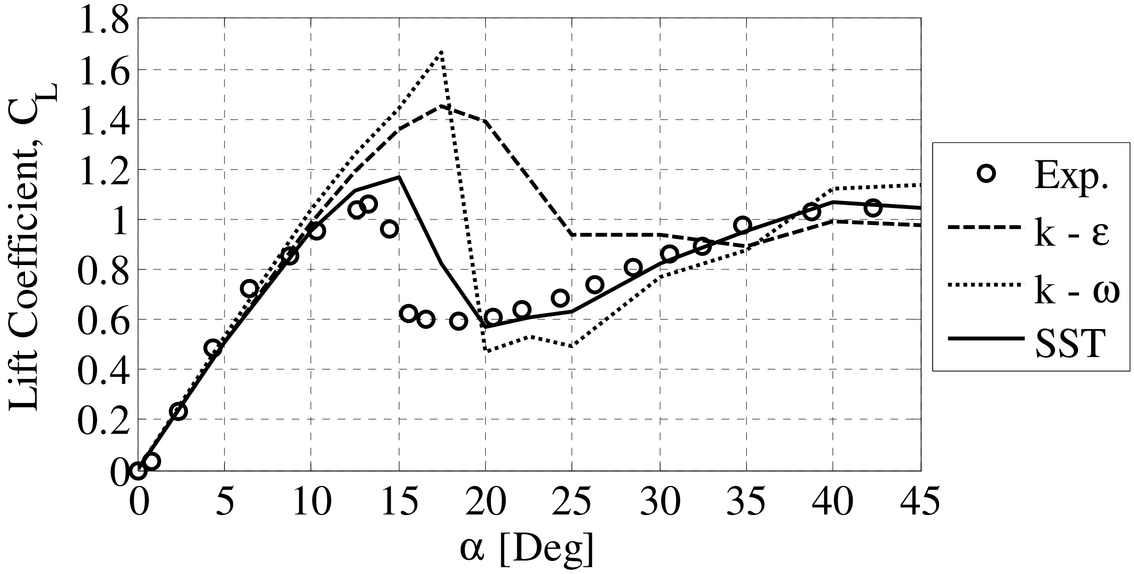

Figure A.7: Wind tunnel turbulence model lift coefficients. Exp. from Sheldahl and Klimas (1978)

At an angle of attack of α = 20°, the k-ε model continues to simulate the flow poorly, with only a moderate amount of flow recirculation, i.e. the blade has still not yet experienced stall. Both the k-ω and SST model do a satisfactory job of simulating the large recirculation zone on the upper surface of the blade and flow acceleration around the bottom of the trailing edge of the blade at this angle of attack. The k-ω and SST models perform better then the k-ε model within the stall region due in part to their ability to account for the effects of streamwise pressure gradients (Menter, 1992). Beyond an angle of attack of α = 35°, all three models begin to behave in the same manner once again. At an angle of attack of this magnitude the blade begins to operate like a bluff body, with the separation point located at the leading-edge. Having simulated the steady-state flow over the blade with the k-ε, k-ω, and SST models, it is clear that as per the literature reviewed, the SST model provides superior results.

A.2. Strain Gauge Data Processing

A.2.1. Pre-processing

1. The proximity sensor signal is processed in order to determine the instant at which the proximity sensor is triggered (θ = 0°) and the indices of these impulse locations are recorded. For the 0 RPM case where no proximity sensor data is available the impulse locations are generated at evenly spaced intervals of 1 second.
2. Based upon the location of the indices generated above, the signal is then divided into single rotation segments. At the same time, the proximity sensor signal is converted into a degree of rotation indicator varying from 0 to 360°.
3. The single rotation segment data is then linearly interpolated at the specified degree interval size (1°) and averaged over the total number of rotations recorded.

A.2.2. Correction Factor Application

1. Due to the nature of a strain gauge Wheatstone bridge there is a natural tendency for drift of the mean voltage output to occur. Prior to each experimental test set, a 0 RPM signal was recorded in quiescent flow. After completing the test set, a second 0 RPM signal was obtained, again at no flow velocity. The average voltage output from each sensor was then calculated and linearly interpolated over the duration of the test set. These voltages were then subtracted from the raw data in order to account for any initial offset in voltage due to bridge balancing as well as any signal drift during the duration of the test set.
2. Due to the self weight, radial load, and drag of the turbine strut segments during operation, a voltage output will be observed from each sensor prior to the application of any additional external loads. In order to accommodate for this, the turbine was driven over a range of RPM at various temperatures (0, 8, 13, 18, and 23 °C) with only the turbine struts attached to the shaft.

3. A second order curve fit was then applied to the data obtained from each sensor and the two coefficients were recorded. Based upon the temperature of the experimental test performed, a linear interpolation of the ‘strut only’ coefficients was applied and the voltage output due to only the strut at any given RPM was generated from the calibration coefficients. This voltage was then subtracted from the raw data in order to account for the ‘strut only’ load at each RPM.
4. As a result of the relatively low stiffness of the turbine blades and the concentration of radial load at the mid-height of the turbine, a certain amount of bowing of the blade is expected. As a result of this deflection of the blade, a horizontal torque and vertical load will be applied to the end of each of the turbine struts. Because the top and bottom struts are extensively calibrated independently, a correction factor needs to be applied in order to account for voltage output due to this loading component which comes only as a result of the connection between the struts. Hence, the turbine was driven over a range of RPM at various temperatures (12 and 20 °C) with a blade that had been cut in half attached to each of the struts. In order to ensure that there were no end effects at the gap formed at the mid-height of the blade a small guard of negligible mass was wrapped around the joint and secured to one half of the blade. Based upon the RPM, radius, and blade mass a voltage/radial force relationship was then developed for these ‘half-blade’ calibration tests for each sensor. A first order curve fit was then applied to the data obtained from each sensor and the coefficient was recorded. Based upon the temperature of the experimental test performed a linear interpolation of the ‘half blade’ coefficient was applied and the voltage outputs were obtained. Prior to performing an experimental test set, the turbine was driven over a range of RPM to produce a ‘pre-test’ data set. Again, for each sensor a voltage/radial force relationship was developed based upon the RPM, radius, and blade mass and a first order curve fit was applied to the data. For each of the sensors, a radial load results in bending of the blade and thus a voltage error due to the horizontal torque and vertical load. As a result, the

correction factor added to the raw data of the sensors is a function of the tension sensor voltage output and is calculated as the difference between the 'half blade' and 'pre-test' voltages corresponding to the experimentally obtained tension sensor voltage.

A.2.3. Force Calculation

1. Having averaged and corrected all of the voltage outputs from the strain gauge Wheatstone bridges, the next step is to calculate the loads that result in this output. An extensive set of calibration tests were performed over a large range of temperatures (0, 8, 13, 18, and 23 °C) in order to develop the relationships between thrust force, radial force, and vertical torque on the blades to the voltage output of the sensors (where it has been assumed that the thrust force acts through the chord-line of the blade and thus does not generate vertical torque of the blade). To calibrate both of the instrumented struts a calibration fixture was developed that consisted of two lengths of angle aluminum (1.2m) mounted back to back and secured to the free end of the turbine strut in place of the blade. Along the length of this fixture were a series of holes through which small steel cables were threaded. Along with a large A-frame stand and a low friction pulley, these cables formed a block and tackle system which was employed to apply fixed loads to the instrumented strut. Both negative and positive thrust loads were applied to the ends of the fixture, while radial loads were applied along the length of the fixture in order to determine the effect of an offset in radial load. In order to apply large radial loads at the centreline of the struts, the fixture was removed and replaced with a 15.24 cm diameter, 6 cm thick, steel disk, the weight of which is equivalent to that of ½ of a turbine blade. The two struts were mounted opposite to one another, and the turbine was driven over a range of rotational velocities. Based upon the nature of the Wheatstone bridge, these relationships are primarily linear, but due to minor geometric differences in the mount location of the gauges as well as non-uniformity of the strut geometry, some second order dependence was

observed. Furthermore, due to some cross-talk between sensors each voltage is a function of both the first and second powers of each loading component.

2. Based upon the experimental test temperature the calibration coefficients were linearly interpreted to determine the correct voltage/load relationships. Finally, in order to solve for the loading components the roots needed to be found for the eighth order polynomial generated from the loading components, calibration coefficients and voltage outputs. While the majority of these solutions appear in the imaginary domain, a select few produce real value solutions. Filtering out extraneous solutions produces the solution to the loading on the turbine blade. Because the vertical torque applied to the blade is only a function of the radial load, the position along the chord-line that the radial load is being applied could also be calculated.
3. Effects of centrifugal load on both the radial and thrust loading components can then be accounted for. A negative thrust component arises due to a rearward offset of the centre of mass of the turbine blade. Finally, the thrust and radial loads can be non-dimensionalized by the ambient dynamic pressure and planform area of the blade.

A.3. Experimental Error Analysis

While the random error of the experimental measurement devices has been stated explicitly in Chapter 4, the systematic error introduced through imperfect calibration of the measurement instruments (zero error) will be given herein. The steps taken to minimize error within the experimental measurements will also be given.

A.3.1. Angle of Rotation

One of the initial steps taken prior to obtaining experimental measurements of the aerodynamic forces on the wind turbine blades was the calibration of the angular position sensor. This was carried out to ensure that the trigger pin was activating the proximity sensor at the proper location ($\theta = 0°$). First, the instrumented struts were aligned normal to the wind tunnel structure. In particular, the two rail lines used to move equipment and measurement devices the length of the wind tunnel were used as a reference. Once the blade was properly aligned, the trigger pin was rotated about the stationary inner shaft until the proximity sensor was activated. The trigger pin was then firmly secured to the stationary inner shaft of the turbine.

It is estimated that the alignment of the instrumented turbine struts could be off by as much as ± 50 mm at the blade radius, R. This equates to a measurement error of approximately ± 2° for all aerodynamic force measurements. Because the trigger pin location was unchanged for all of the test cases performed, this error will be constant for all measurements. As such, any comparisons made between experimental aerodynamic force measurements in reference to the angular position will not be influenced by this source of error. For example, the change in the angle of rotation at which dynamic stall occurs is not dependent on the absolute angular position, and thus is unaffected by any error introduced by misalignment of the trigger pin.

A.3.2. Preset Pitch Angle

In order to account for the offset in the blade mounting location, the airfoils had to be pitched by 2.66° for the 420 mm chord length blades, and 2.25° for the 400 mm chord length blades. To adjust the preset pitch angle of the airfoils, a set of small metal shims were inserted between the leading edge mounting locations of the blades and the ends of the support struts. The steel shims were each approximately 0.5 mm thick, and the gap size that needed to be filled for the 420 and 400 mm chord length blades was 3.7 and 2.75 mm, respectively. If it is conservatively assumed that the maximum error introduced by the shims is equal to 50% of the thickness of one shim (0.25 mm), than the error in the preset pitch angle is at most 0.2° for both blade designs.

A.3.3. Flow Velocity

Calibration of the wind tunnel was performed every other day during the wind tunnel testing program in order to ensure that ambient atmospheric conditions did not influence the reference wind tunnel flow velocity. Calibration was performed by measuring the flow velocity with the propeller anemometer while the wind tunnel fans operated at 0, 20, 40, and 60 Hz, for 60 second intervals at each fan speed.

Unfortunately, because of the multi-fan design of the wind tunnel, there is a propensity for a spatially non-uniform flow velocity distribution at a given downstream position. As identified by Weisinger (2004), the major source of this non-uniformity in the velocity distributions of the wind tunnel used in this study is characteristic of merging parallel jets. Because of the limitations of the fan control system, the flow velocity produced by each fan is slightly different from all others. As a result, lower velocity jets will tend to merge with higher velocity jets, resulting in an increase in flow velocity over a small region within the flow field (Tanaka & Nakata, 1975). Measurements of the flow velocity distribution over the core region of the wind tunnel clearly demonstrate this behaviour (Figure A.8), where three distinct high velocity regions can be identified (y = -2, z = 2.5; y = 1, z = 0.5; y = 1, z = 3.8; refer to Figure 4.1 for coordinate system).

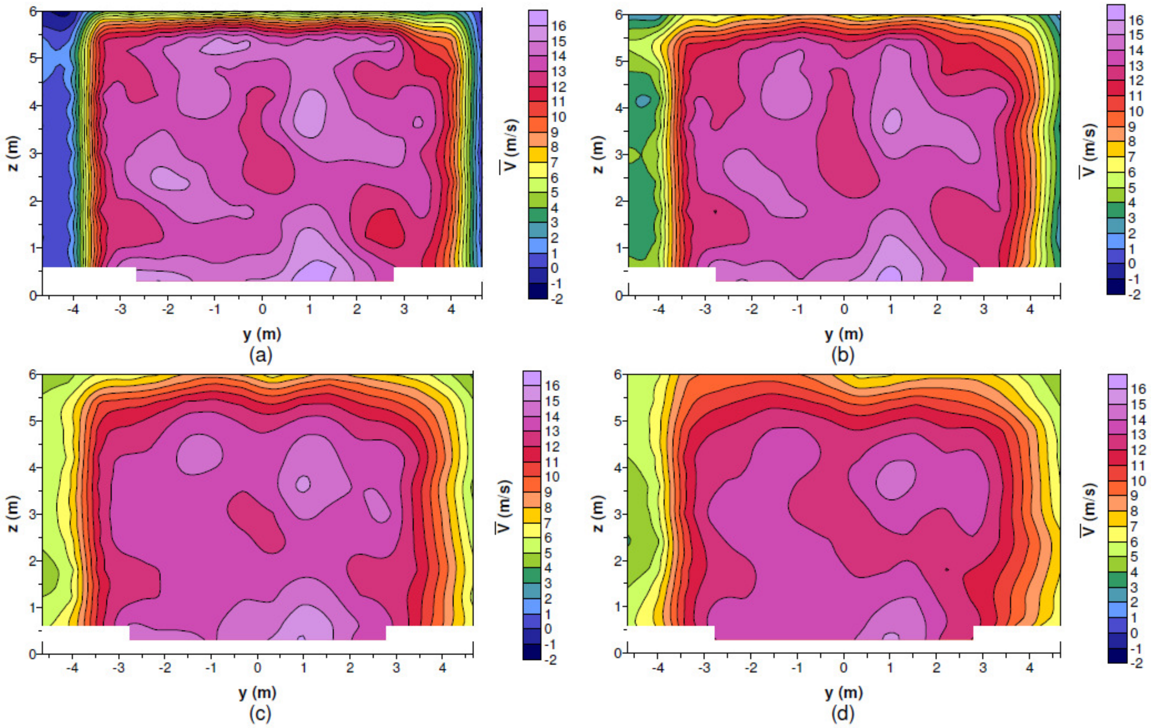

(a) (b)

(c) (d)

Figure A.8: Time-averaged velocity contours in the wind tunnel test section with fans operating at peak output (a) x = 2 m; (b) x = 5 m; (c) x = 10 m; and (d) x = 15 m (Weisinger, 2004)

Because a single point measurement is being used to represent the average flow velocity entering the entire wind turbine swept area, any non-uniformity in the inlet flow velocity may result in a bias in the measured value. In order to minimize the error introduced by this non-uniformity in the velocity distribution, wind velocity calibration measurements were recorded at two different upstream locations. These measurements were made at mid-height of the stationary turbine (z = 2.1 m) in order to best represent the average flow velocity entering the turbine. During all calibration tests the turbine was orientated to present minimum frontal projected area from the turbine blades and equipment mounted at the base of the turbine, in order to minimize blockage effects.

The first calibration was performed with the propeller anemometer located 3 radii upstream of the turbine's axis of rotation (x = 3.8 m, where x is the distance downstream of the plenum), at the turbine's outer radius (y = -1.5 m, where y is the cross-stream distance from the centreline of the wind tunnel). However, it was quickly identified that due to the high local velocity at this location that the calibration obtained from these measurements would likely be skewed towards higher velocities (Figure A.8). As such, the three subsequent wind velocity calibrations were performed with the propeller anemometer located approximately midway between the plenum exit and the upstream surface of the turbine ($x \approx 3.3$ m), on the opposite side of the wind tunnel ($y = 1.5$ m). At this location, the flow velocity is more uniform and better represents the average flow velocity over the core of the wind tunnel (Figure A.8). Placing the anemometer at the outer radius of the turbine ($y = \pm 1.5$ m) ensured that the anemometer and its support structure had a minimal impact on the flow entering the wind turbine. This was an important consideration as the anemometer was used to monitor wind velocity during the aerodynamic force measurements. In both instances, special care was taken to ensure that the anemometer was not positioned in the wake of the flow straightening vanes.

From these calibration tests the coefficient that relates the rotational frequency of the wind tunnel fans to the flow velocity was obtained ($U_\infty = 0.1835*f$, where U_∞ is in m/s and f is in Hz). The maximum deviation of this coefficient between calibration tests was just 2.1%, while the R^2 value for all four calibrations performed was at least 0.9982. While the calibration test results appear to be nearly independent of the ambient atmospheric conditions and upstream location at which the measurements were recorded, a conservative approach was taken to calculating the potential error in the inlet flow velocity. By calculating the deviation in velocity at the anemometer locations interpolated from the wind velocity profiles given by Devaud et al. (2009), a measure of the error introduced by the non-uniformity in the inlet flow velocity can be made. For this analysis, flow velocity was averaged over the height of the turbine ($0.6 \leq z \leq 3.6$) and width of the wind tunnel for which experimental data with minimal error exits ($-2.8 \leq y \leq 2.8$, equivalent to two turbine diameters).

The deviation of the flow velocity from the average was calculated within a small region surrounding the anemometer position (Figure A.9). This averaging technique was performed for the following reasons. First, the anemometer has a propeller diameter of 0.2 m, and thus is an integrated measurement over the area of the propeller. Second, some adjustment in the anemometer position about the nominal location was required in order to ensure that it was not placed directly downstream of the flow straightening vanes. Third, experimental error in the velocity profile measurements introduces some uncertainty in the location and strength of the high velocity regions. And finally, this technique was employed because of the error introduced by the linear interpolation of the velocity profiles required to obtain velocities at the necessary locations (Figure A.9).

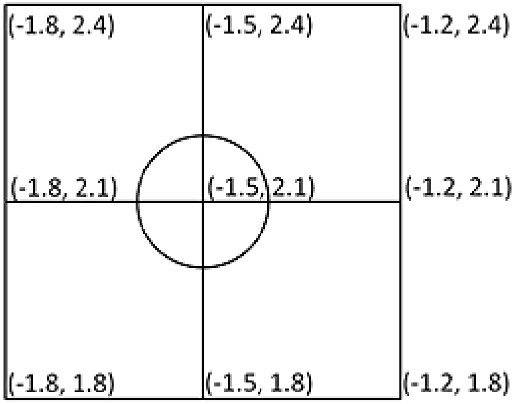

Figure A.9: Locations at which the deviation in flow velocity from the average were calculated (y, z). The circle represents the frontal area of the propeller anemometer.

Based upon the available wind velocity profile measurements (Figure A.10 and Figure A.11), the maximum deviation from the average flow velocity within 0.3 m of the first anemometer location (x = 3.8 m, y = -1.5 m, z = 2.1 m) is 7.1% higher than the average flow velocity at this downstream location. This behaviour is not unexpected based upon the initial assessment of the flow velocity contours at this location of the wind tunnel (x = 3.8 m, y = -1.8 m, z = 2.4 m). The magnitude of this maximum error is also consistent with that reported by Armstrong (2011) for lower velocity flows. The average deviation of the velocity measurement at this location is considerably lower at 4.1%, with a standard deviation of 1.9%, based upon the nine locations shown in Figure A.9.

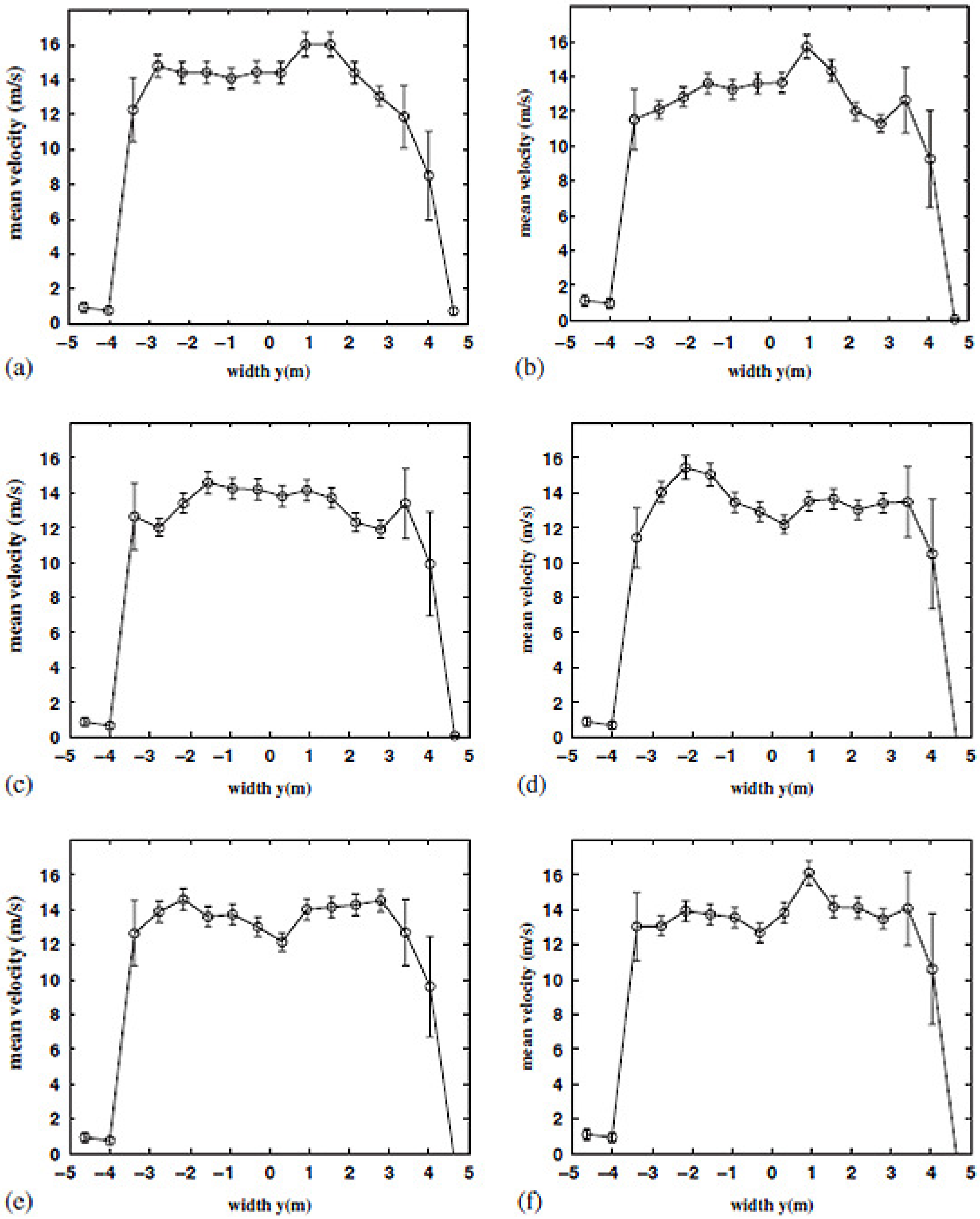

Figure A.10: Time-averaged velocity profiles at x = 2 m, Exp: line with open symbols and LES: solid line. (a) z = 0.6 m; (b) z = 1.2 m; (c) z = 1.8 m; (d) z = 2.4 m; (e) z = 3.0 m; (f) z = 3.6m, adapted from (Devaud et al., 2009)

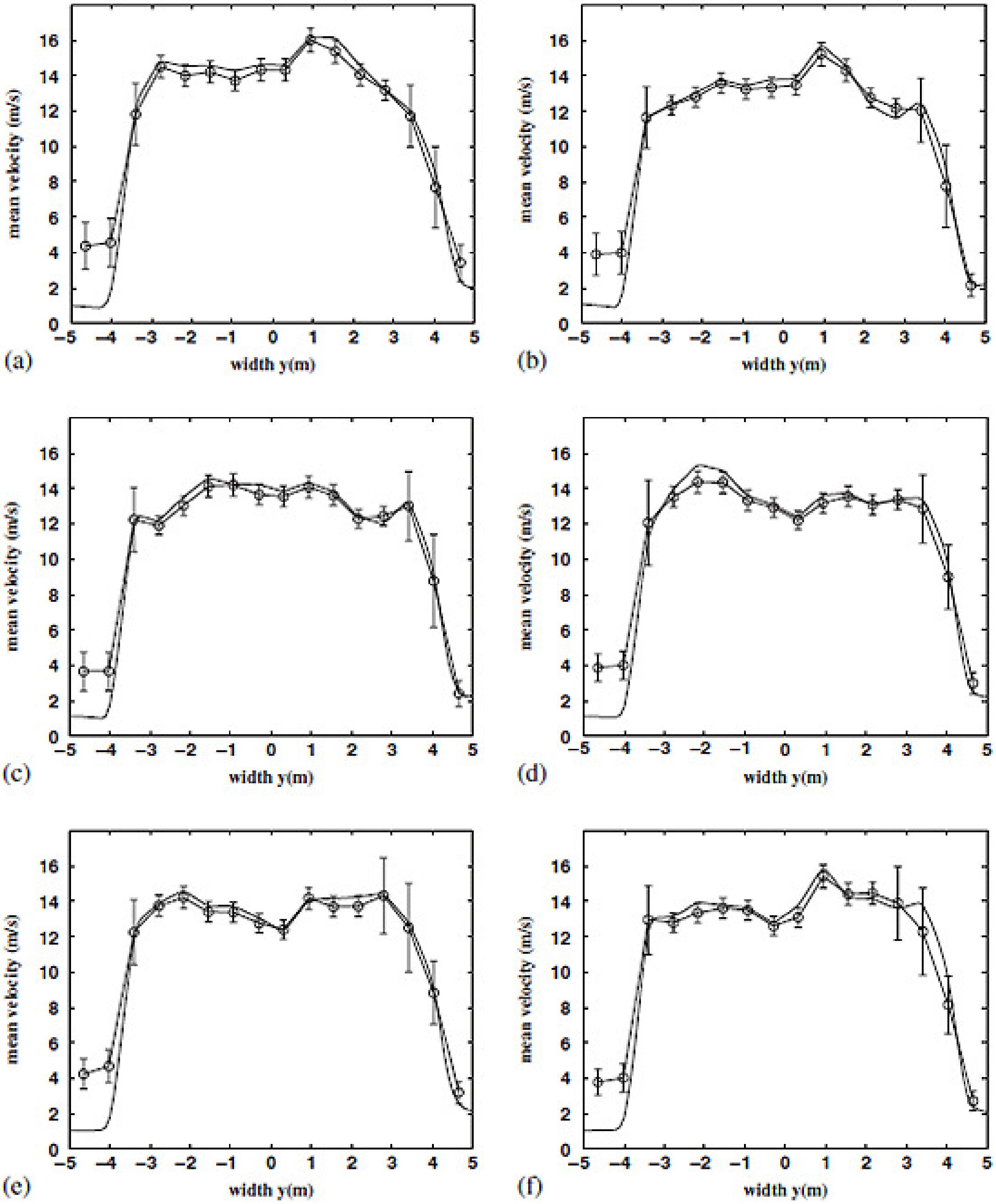

Figure A.11: Time-averaged velocity profiles at x = 5 m, Exp: line with open symbols and LES: solid line. (a) z = 0.6 m; (b) z = 1.2 m; (c) z = 1.8 m; (d) z = 2.4 m; (e) z = 3.0 m; (f) z = 3.6m, adapted from (Devaud et al., 2009)

Conversely, the maximum deviation from the average flow velocity within 0.3 m of the second anemometer location (x = 3.3 m, y = 1.5 m, z = 2.1 m) is 4.5% *lower* than the average flow velocity. The average deviation of the velocity measurement at this location is just -1.4% with a standard deviation of 1.9%, again based upon the nine locations shown in Figure A.9. While the standard deviation at this position is the same as the first anemometer location, the amplitude of the average deviation of the velocity measurement is reduced from 4.1 to 1.4%. As anticipated, this confirms that due to the more uniform flow velocity distribution at the second anemometer position, it is a good location to perform the wind tunnel calibrations. It is for this reason that the anemometer was moved to this location to perform the wind tunnel calibrations.

The greatest impact of an error in the flow velocity measurement lies in the non-dimensionalization of both the aerodynamic forces and turbine power output. Because the power coefficient is proportional to U_∞^3 any error in flow velocity will have an especially large impact on the power coefficient amplitude. Fortunately, the power coefficient measurements obtained from this and previous studies performed in this wind tunnel (Fiedler, 2009; Armstrong, 2011) agree well with measurements for a similar turbine configuration obtained at the more spatially uniform inlet flow, 9 m x 9 m, NRC wind tunnel in Ottawa, Canada (Bravo et al., 2007). This confirms the accuracy of the wind velocity measurements.

A.3.4. Temperature

The air temperature within the wind tunnel was measured through the use of a commercially available wireless digital thermometer. While the thermometer was capable of displaying the temperature at increments of 0.1°C, as a conservative estimate it was assumed that the measurement was only accurate to the nearest whole degree.

One of the impacts of the temperature measurement accuracy is in the calculation of the air density. For this study, air density was not measured directly, but was rather calculated from standardized tabulated values at sea-level and atmospheric pressure. The calculation used to determine air density in kg/m^3 is given as, ρ = (-0.004*T + 1.29), where T is the air temperature in °C. As such, an error in temperature of ±1°C, translates to an error in air density of just ± 0.3%.

The primary effect of an error in temperature is the change in calibration coefficients used to convert the strain gauge outputs to thrust and radial force measurements, and will be discussed in detail in the following section.

A.3.5. Force Measurement Calibration

In order to minimize the error in the aerodynamic force measurements, a number of important steps were taken in the data acquisition and pre-processing of the Wheatstone bridge outputs. First, as stated in the Pre-processing section (A.2.1), the signal outputs are averaged over the total number of rotations for which data was obtained. As described in the Filtering Techniques section (5.2.3), this eliminates any turbine vibration component from the signal that is not at an integer multiple of the rotational frequency. More importantly however, this reduces signal error considerably as it minimizes any cycle-to-cycle variability within the output. As an example, Figure A.12 plots the raw and average output for the bottom strut middle bending moment and tension sensors for the NACA 0015, c = 420 mm, β = 0° blades operating at λ = 1.45.

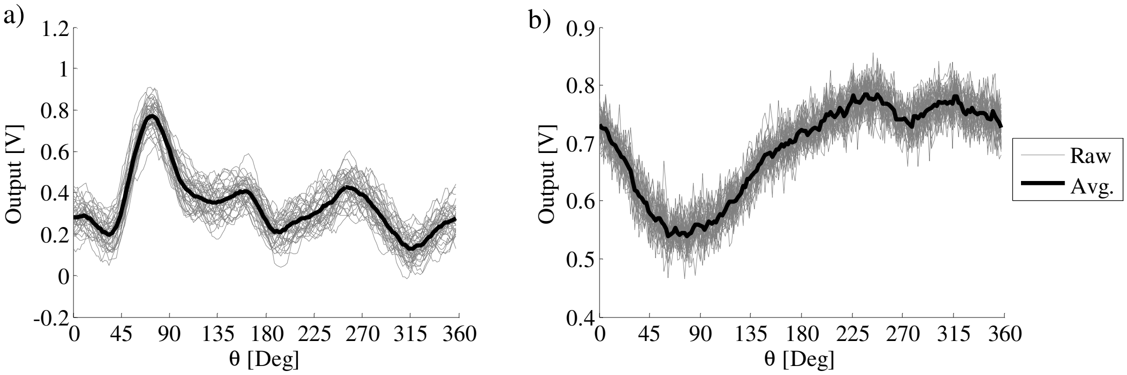

Figure A.12: Raw and averaged bottom strut (a) middle bending moment, and (b) tension sensor output (NACA 0015, c = 420 mm, β = 0°, U_∞ = 8 m/s, λ = 1.45)

For this test case, when the number of revolutions per average is doubled from 15 to 30, the percent difference in the peak middle bending moment sensor amplitude is just 0.5%. Thus, by averaging the data over a minimum of 30 revolutions, the error introduced by cycle-to-cycle variations and signal noise can be minimized.

Error introduced by imperfect balancing of the Wheatstone bridges, as well as linear strain gauge drift, is then accounted for through the use of measurements taken prior to and following the aerodynamic force measurement tests. In general, the initial and final voltage output of the Wheatstone bridge sensors is on the order of ± 0.02 V. This equates to an error of approximately 4% of a typical full scale measurement. However, by subtracting a linear interpolation of the initial and final voltage output of the sensors from each of the Wheatstone bridge signals, the initial signal bias, as well as the bias introduced by linear signal drift, is removed from the sensor outputs.

A series of correction factors to account for the self weight, radial load, and drag of the struts was then developed. In order to accomplish this, a second order polynomial fit to the sensor outputs of the 'strut only' tests was made. For any given rotational velocity of the turbine, the 'strut only' sensor output could then be calculated and subtracted from the total sensor output, to produce the output due exclusively to blade loading. As an example, the outputs from the top and bottom strut sensors are given in Figure A.13 for the 'strut only' calibration test performed at 13 °C. From this figure it can be seen that the forces imposed on the strut due to its self weight, centrifugal acceleration, and aerodynamic drag account for as much as 0.2 V of the total sensor output at 140 RPM (the turbine's upper operating capability). Left unaccounted for, the 'strut only' output could introduce as much as 40% error in a typical full scale measurement. However, by subtracting the 'strut only' outputs from the raw data this error is reduced considerably.

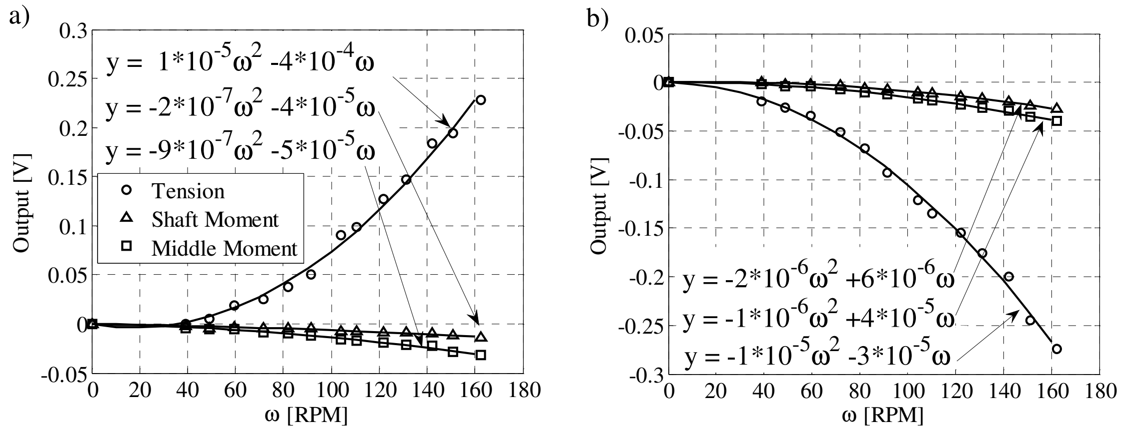

Figure A.13: (a) Top and (b) bottom 'strut only' sensor outputs (13°C)

Because the calibration coefficients obtained from these tests are a function of temperature, 'strut only' tests were performed at 0, 8, 13, 18, and 23 °C. A linear interpolation of the calibration coefficients was then required in order to obtain the values at the specific temperature at which the aerodynamic force measurements are recorded. As a result, some error is introduced into the 'strut only' correction factors. For most of the sensors the difference in the 'strut only' measurements over the calibration temperature range is limited to ± 10%. However, as a conservative approach, due to the large number of calibration coefficients required, the estimated error is based upon a 50% change in the 'strut only' sensor outputs over the range of 0 to 23 °C. This is equivalent to an error in the 'strut only' calibration coefficients of 2% / °C, and introduces an error of approximately 1% / °C in terms of a typical full scale sensor output.

A series of correction factors to account for bending of the blade about the airfoil chord line, and the resultant blade shortening, were also developed. From the 'blade-bending' tests it was determined that the error introduced into the calibration coefficients by blade bending and shortening is typically on the order of 5%, but can reach values upwards of 25%, dependant on the sensor. This change in behaviour is most notably observed in the tension sensors, as a horizontal bending moment is perceived as a tension or compression force on the support struts. As with the 'strut only' correction factors, the error introduced by blade bending and shortening is accounted for by subtracting the additional voltage output due to blade bending and shortening calculated at the given rotational velocity from the raw sensor outputs.

The change in the 'blade bending' sensor outputs over the range of 12 to 20 °C is typically on the order of just 0.06 V at 140 RPM. This equates to an error of 12% of a typical full scale measurement over this temperature range. Because all of the aerodynamic force measurements were obtained between 9 and 17 °C, and because the change in behaviour over this range was found to be very small, only two calibrations tests were performed. From these tests, it can be approximated that the blade bending correction factor introduces an error of 1.5% / °C in the sensor outputs.

Having developed the necessary correction factors to account for the effects of 'strut only' and 'blade bending' loads, the calibration coefficients used to calculate the aerodynamic forces on the blades could then be applied. From the extensive calibration tests performed through the use of the block and tackle system, a large array of calibration coefficients were developed. Because the strain gauge Wheatstone bridges were wired to be sensitive to either horizontal bending or tension, the sensor outputs will be particularly responsive to a given aerodynamic loading component. Despite this fact, due to sensor cross-talk, there are two coefficients which relate the first and second order terms of all three loading components (thrust force, radial force, and vertical torsion) to a given sensor output.

$$V_A = A_1 F_T y + A_2 (F_T y)^2 + A_3 F_R + A_4 (F_R)^2 + A_5 F_R x + A_6 (F_R x)^2 \qquad \text{A.1}$$

where V_A is the voltage output of sensor A, F_T is the thrust force, y is the distance from the sensor to the airfoil chord line, F_R is the radial force, x is the offset of the centre of pressure from the sensor datum line, and A_i are the calibration coefficients for sensor A. Here it is assumed that the thrust force is applied on the chord line of the airfoil.

Overall, this equates to 6 calibration coefficients per sensor, for each of the 6 sensors, for a total of 36 calibration coefficients for a given temperature. Figure A.14 below plots the voltage/force relationships for the bottom strut middle bending moment and tension sensors for the five calibration temperatures. Note that the shaft side bending moment sensor outputs demonstrate similar behaviour to the middle bending moment sensors and as such have been omitted for the sake of clarity.

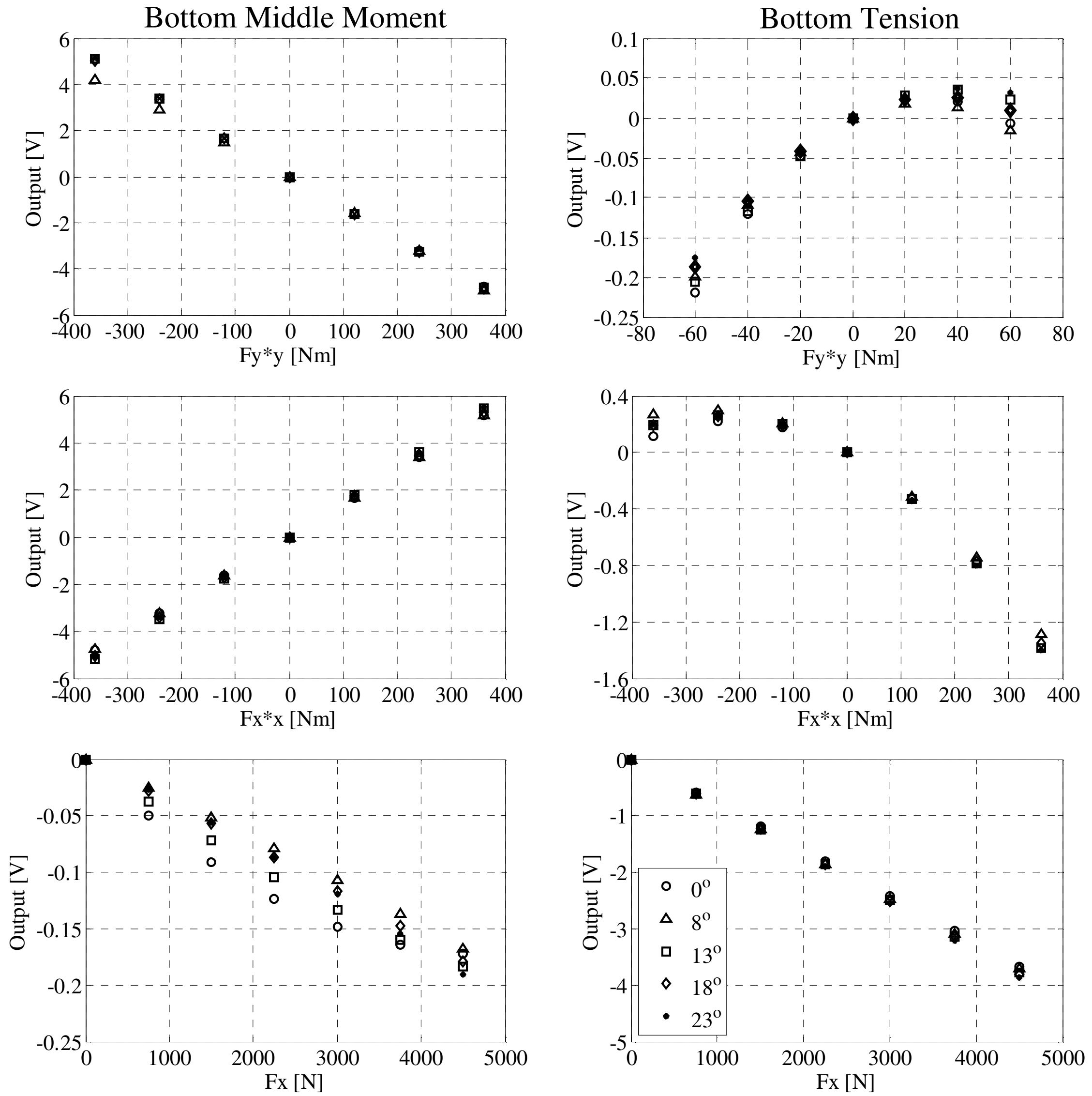

Figure A.14: Bottom strut middle moment and tension sensor voltage/force relationship over a range of temperatures

From Figure A.14 it is clear that, as per its design, the middle bending moment sensor is very sensitive to both the thrust force applied at the airfoil chord line as well as the vertical torsion component. It is because of this behaviour that two bending moment sensors, mounted at different lengths from the airfoil chord, are required in order to discern which loading component is producing the observed output. These two relationships are both strongly linear and differ by just 10% with respect to temperature over the expected loading range. Conversely, the bending moment sensor is relatively independent of the radial force component. The sensor output due to radial loading is just 4% of that due to thrust and vertical torsion over the expected loading ranges. Thus, while the variability in the middle bending moment sensor output due to radial force is quite large with respect to temperature (± 100%), this equates to just 1% of the voltage output due to the dominant thrust force component.

The tension sensor, having been wired to be sensitive to tension and compression loads, is relatively insensitive to thrust force applied to the airfoil. In fact, the tension sensor output due to thrust loading is just 5% of that due to radial force over the expected loading ranges. The vertical torsion component however has a much greater impact on the tension sensor output. Fortunately, this behaviour is well represented by a second order curve fit to the data and has a scatter of just 0.2 V with respect to temperature over the expected loading range. This is equivalent to just 5% of the maximum voltage output due to radial force. Finally, a strongly linear relationship is developed for the tension sensor with respect to radial load, as was the initial design objective. The variation in the tension sensor output as a result of radial loading over the range of temperatures tested is just 5%.

Overall, the error introduced by cross-talk between sensor outputs has been substantially reduced by incorporating the effects of all three loading components into the calculation of each. Thus, while the number of calibration coefficients is large, the total variation with respect to temperature is generally relatively small with respect to the dominant loading components. Conservatively, it is approximated that this error is on the order of (3% / °C). One other consideration is the error introduced by the block and tackle system used to obtain the calibration coefficients. Because the pulley and cable system used to apply the loads to the instrumented struts is not perfectly frictionless, it is expected that the voltage/force relationships may be in error by an additional ± 2%.

One final step was performed in order to reduce the amount of error present in the aerodynamic force coefficients. By measuring the aerodynamic force at different flow velocities, aerodynamic force coefficient measurements, which are independent of wind speed, could then be averaged for a given blade speed ratio. While the number of data sets available varies with blade speed ratio, there are typically two or three test cases within the turbine's operational capabilities, and without considerable turbine vibration response, for a given blade speed ratio. As an example, Figure A.15 plots the thrust and radial force coefficients for a blade speed ratio of $\lambda = 0.55$ for the NACA 0015, $c = 420$ mm, $\beta = 0°$ test case. While some variation exists between measurements, the repeatability in the force coefficients is quite good regardless of the change in wind velocity and magnitude of the aerodynamic forces.

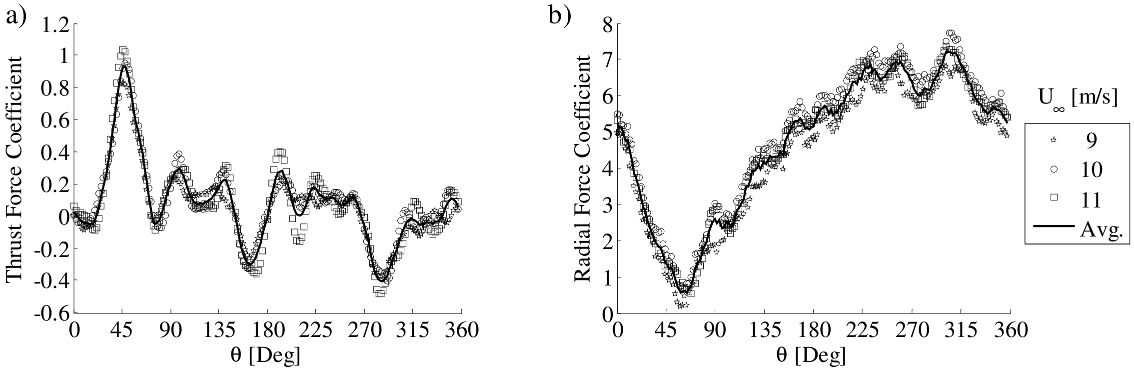

Figure A.15: (a) Thrust and (b) radial force coefficients as a function of wind velocity (NACA 0015, $c = 420$ mm, $\beta = 0°$, $\lambda = 0.55$).

A.3.6. Cumulative Error

The cumulative error in the primary variables in this study can be calculated through the use of standard error propagation techniques. The product and quotient of variables which are dependently related will have their percentage errors summed, while independent variables will have their percentage errors added in quadrature. Values for which a power is calculated are treated as dependent variables and as such will have their percentage errors multiplied by the magnitude of the exponent. Note that a conservative approach has been taken in the estimation of any sources of error where required.

θ; error in rotational position = $\pm 2°$

β; error in preset pitch angle = $\pm 0.2°$

U_∞; error in flow velocity = $\sqrt{1^2 + 4.5^2} = \pm 4.6\%$

ω; error in rotational velocity = $\pm 2\%$

F; error in aerodynamic force = $\sqrt{1^2 + 1.5^2 + 3^2 + 2^2}\% = \pm 4\%$

$\lambda = \omega R / U_\infty$; error in blade speed ratio $= \sqrt{2^2 + 4.6^2}\,\% = \pm 5\%$

$C_F = F/\left(\frac{1}{2}\rho {U_\infty}^2 cH\right)$; error in force coefficient $= \sqrt{4^2 + 0.3^2 + (2 \cdot 4.6)^2} = \pm 10\%$

$C_P = \dfrac{\omega RN \frac{1}{360}\int_0^{360} F_T d\theta}{\frac{1}{2}\rho U_\infty^3 2RH}$;error in power coefficient = $\sqrt{2^2 + 4^2 + 0.3^2 + (3 \cdot 4.6)^2}$

$= \pm 14.5\%$

A.4. Blade Centre of Gravity Correction

Initially, it was assumed that the centrifugal loading applied to the struts from the mass of the rotating blades was contributing only to a mean radial loading component. However, due to the design of the wind turbine blades, and the location along the chord at which they are mounted to the support struts, an offset exits between the blade's centre of gravity and the load measurement system datum. As can be seen in Figure A.16, because of this offset in the centre of gravity, Δx, the centrifugal load will result in both a radial force $F_R = F_C[cos(tan^{-1}(\Delta x/R))]$, and a thrust force $F_T = -F_C[sin(tan^{-1}(\Delta x/R))]$.

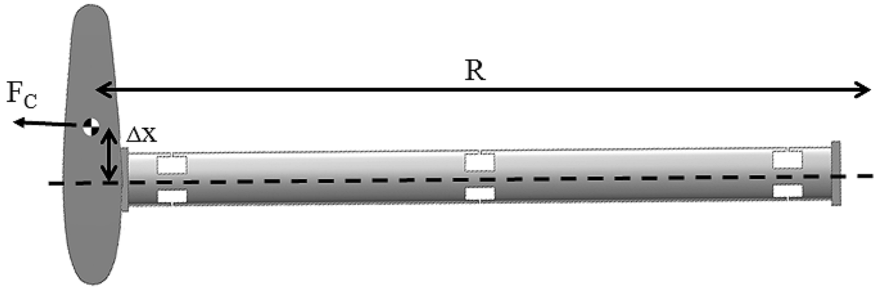

Figure A.16: Blade centre of gravity offset from measurement system datum line

From a series of preliminary 'spin-up' tests it was determined that this offset was on the order of 33 to 35 mm, depending on the blade type and mounting configuration. For a turbine radius of 1400 mm, and an offset of 34 mm, centrifugal loading results in a radial force of $F_R = F_C[0.9997]$ and a thrust force of $F_T = -F_C[0.0243]$. Obviously, this offset in the centre of gravity has a relatively small effect on the expected magnitude of the mean radial force, but a profound effect on the mean thrust force. As an example, for a blade mass of 17kg, and a rotational velocity of 140 RPM (near the typical upper operational capabilities of the turbine), the centrifugal load results in a mean thrust force of -124 N. Because this load is being applied throughout the entire rotation, and because the expected thrust force rarely exceeds 120 N at this rotational velocity, this will result in a negative power coefficient measurement.

As an example, Figure A.17 plots the power coefficients predicted from the thrust force measurements without having accounted for the effect of centrifugal loading, against those obtained from the shaft torque measurements obtained by the method of Fiedler (2009). While this effect has little impact at low rotational velocities (and thus low blade speed ratios), at high rotational velocities the mean thrust load component overwhelms the aerodynamic thrust force component.

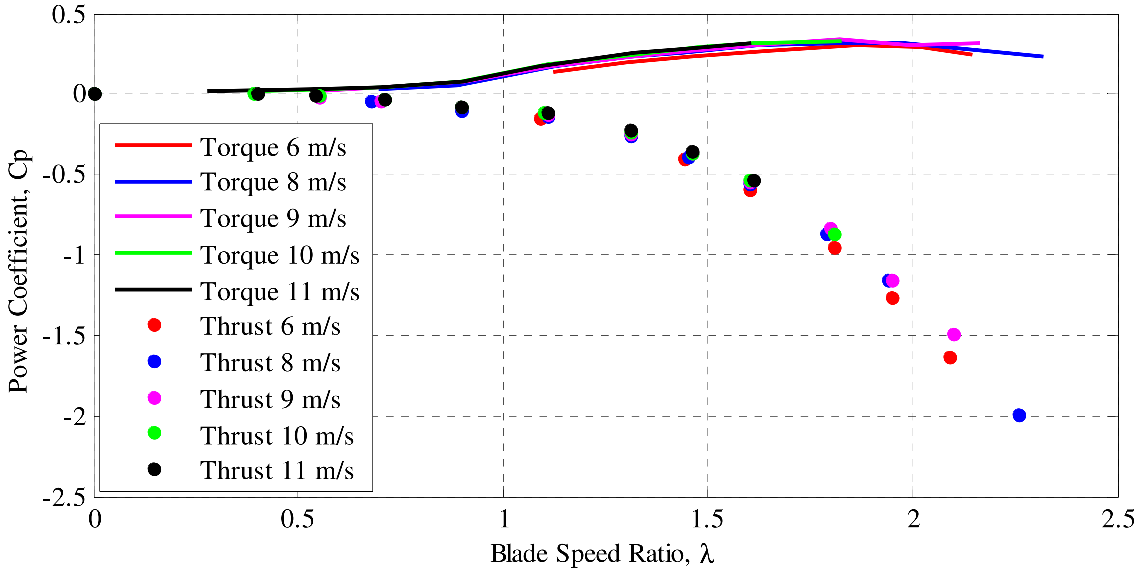

Figure A.17: Gross power coefficients calculated directly from thrust force measurements, compared to those obtained from torque measurements (NACA 0015, c = 420 mm, $\beta = 0°$).

Fortunately, an offset in the centre of gravity of the blade only affects the mean loading component and is independent of the aerodynamic loading. As such, accounting for the mean offset in the thrust force measurements, and thus the turbine power calculations, is a simple matter of adding the effect of centrifugal loading onto the measured values. Unfortunately, the offset in centre of gravity calculated from the 'spin-up' tests is merely an approximation. Additionally, because of the size and geometry of the blades, an accurate measurement of the centre of gravity could not be made directly. As such, the centre of gravity is determined such that the power coefficients calculated from the thrust force measurements agree well with those obtained from the torque measurements (Figure A.18), where some discrepancy at high blade speed ratios occurs due to dynamic amplification effects discussed above. The offset in the centre of gravity calculated in this manner differs somewhat from those obtained from the 'spin-up' tests, typically on the order of 10 mm. Some variation between the centres of gravity calculated for the bottom and top struts also exists due to minor differences in the custom designed sensors and turbine geometry. However, because the power coefficients calculated from the thrust force measurements are very sensitive to this value, this is not unexpected.

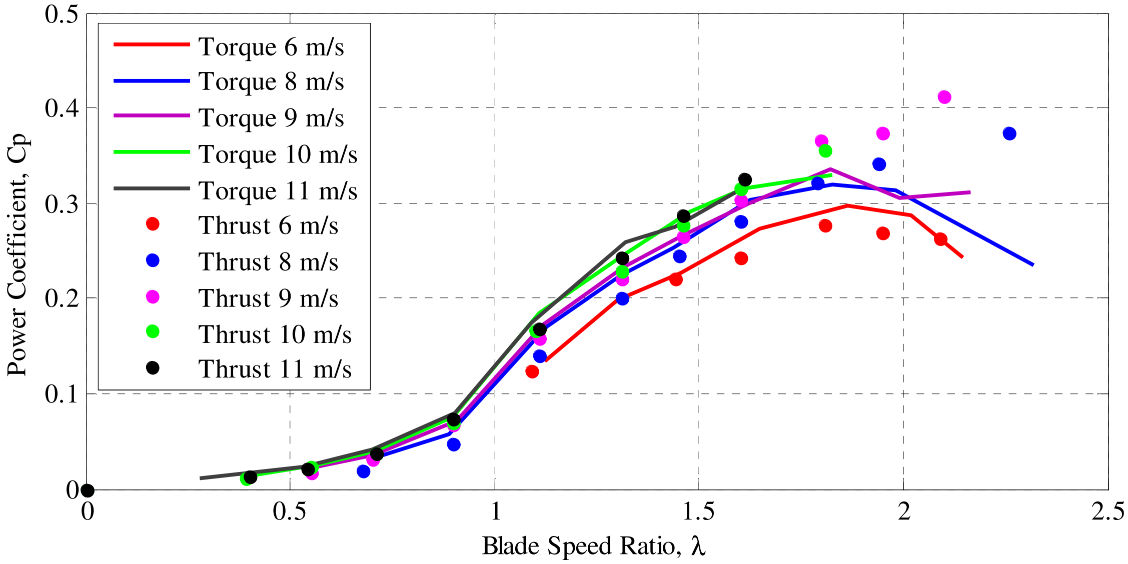

Figure A.18: Gross power coefficients calculated from thrust force measurements corrected for centrifugal loading, compared to those obtained from torque measurements (NACA 0015, *c* = 420 mm, *β* = 0°).

A.5. Complete Test Case Data

Figure A.19 through Figure A.23 plot the experimentally measured thrust and radial force coefficients against those predicted by the effective numerical model over the entire operational range of the turbine ($0.4 \leq \lambda \leq 1.96$), for the five blade configurations tested (Table A.1).

Blade Design	Chord Length [mm]	β [Deg]	κ	τ
NACA 0015	420	0	1.10	1.15
NACA 0015	420	2.66	1.10	1.15
NACA 0021	400	0	1.07	1.15
NACA 0021	400	2.25	1.07	1.15
NACA 0015	400	2.25	1.14	1.15

Table A.1: Blade configurations tested

Note that while the effect of a change in preset pitch for the NACA 0021 blade design was not described within the thesis, similar trends to the NACA 0015 airfoils were observed (section 6.3). However, the change in loading behaviour was less dramatic, due in part to the fact that the change in preset pitch was smaller for the NACA 0021 airfoils.

Additionally, because the change in thickness ratio between the c = 400 mm, $\beta = 2.25°$, NACA 0015 blade design, and the c = 400 mm, $\beta = 2.25°$, NACA 0021 blade design was smaller than the described sample case (section 6.4), a comparison was not made within the thesis. However, the application of the inlet velocity and turbine height correction factors did prove to effectively scale the turbine power and force coefficients for this blade design.

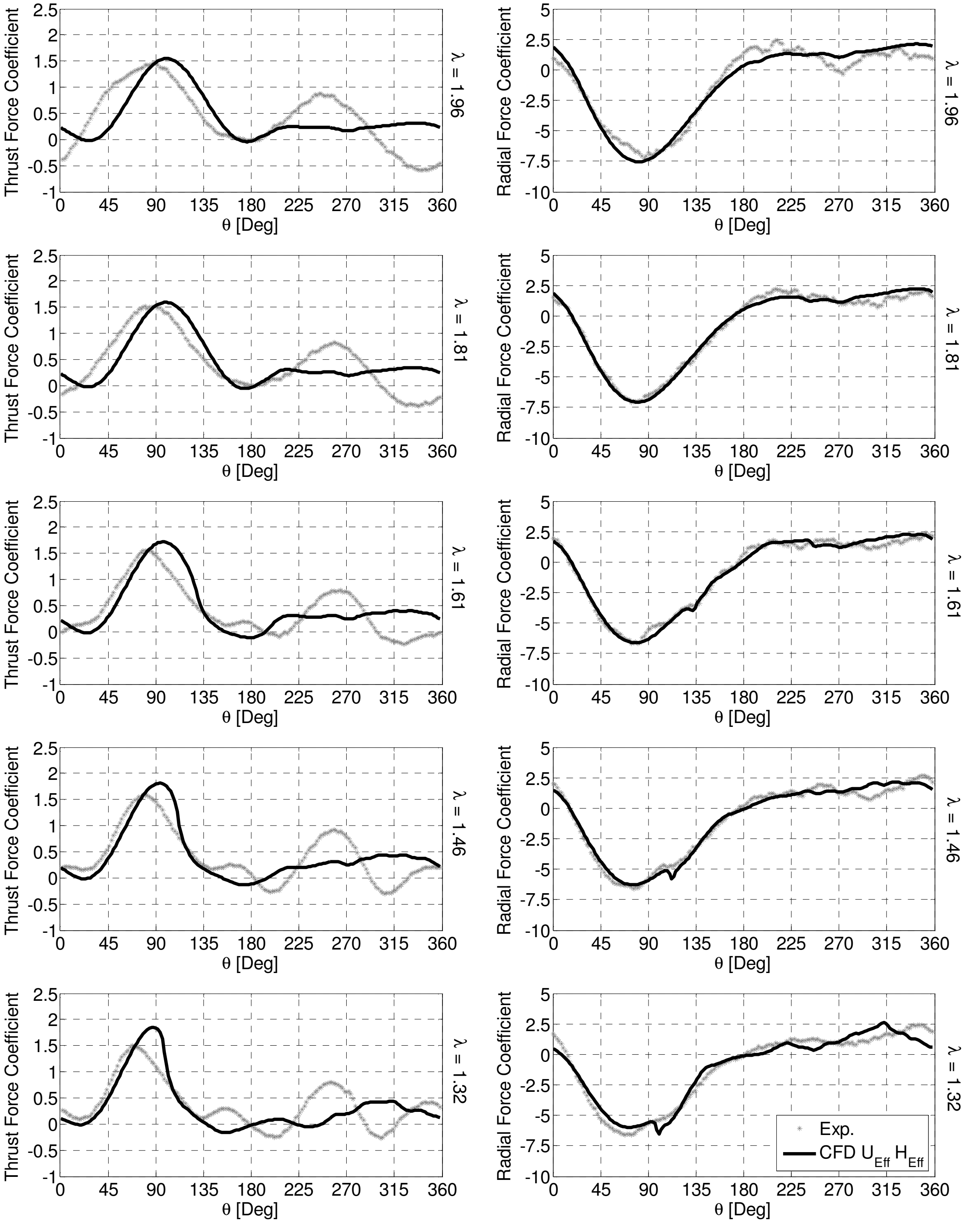

Figure A.19: Aerodynamic force coefficients (NACA 0015, *c* = 420 mm, *β* = 0°)

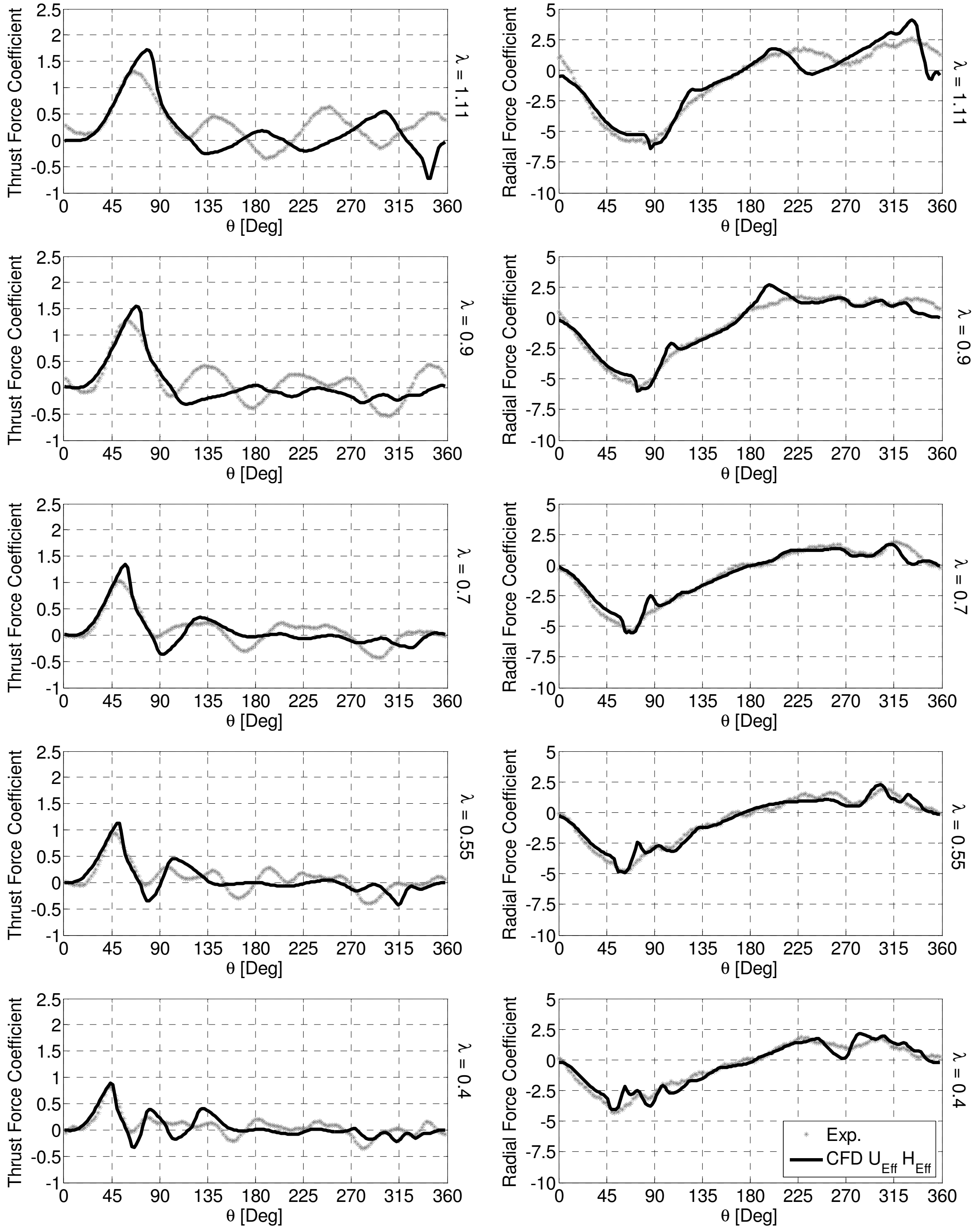

Figure A.19 Continued: Aerodynamic force coefficients (NACA 0015, *c* = 420 mm, *β* = 0°)

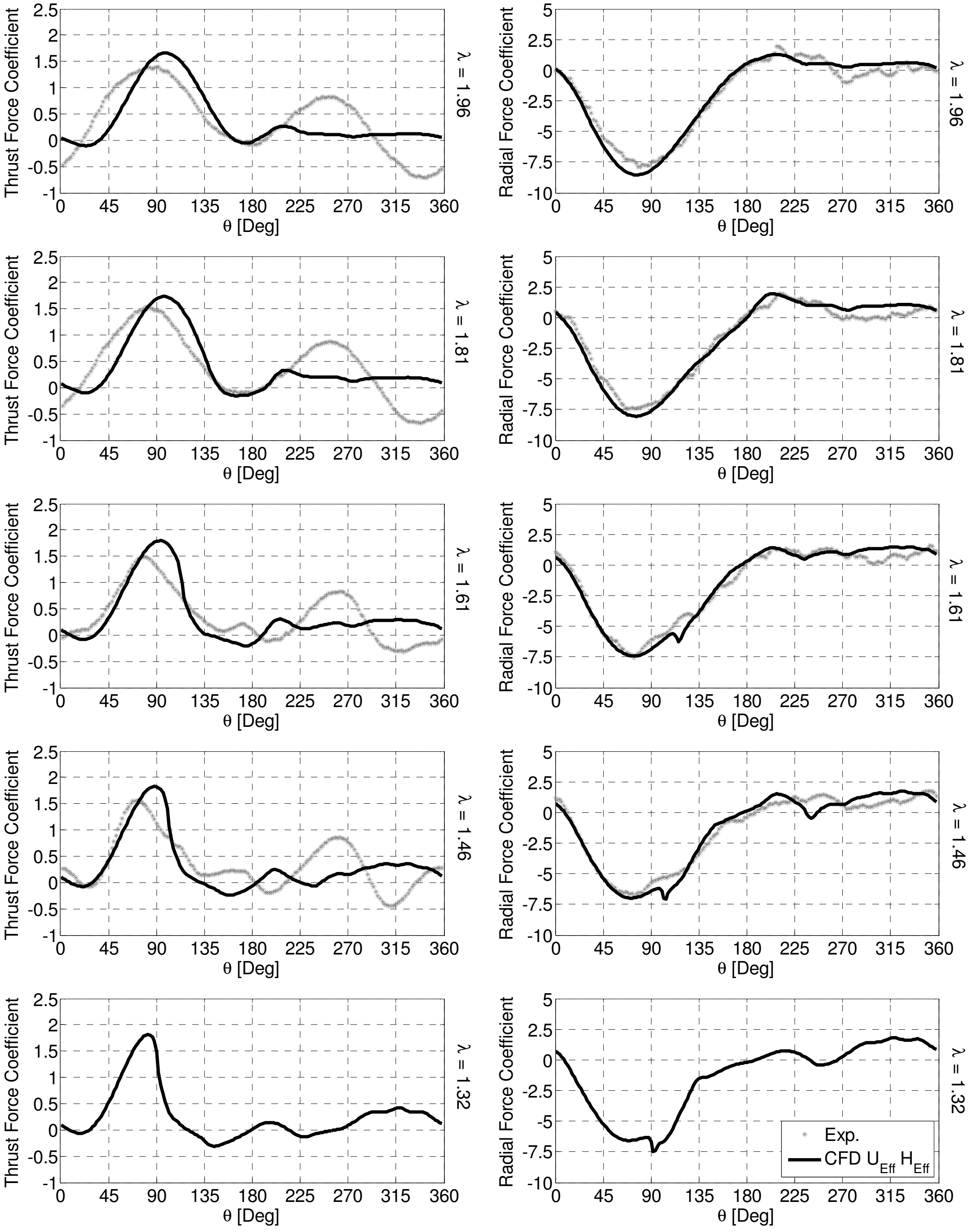

Figure A.20: Aerodynamic force coefficients (NACA 0015, *c* = 420 mm, *β* = 2.66°)

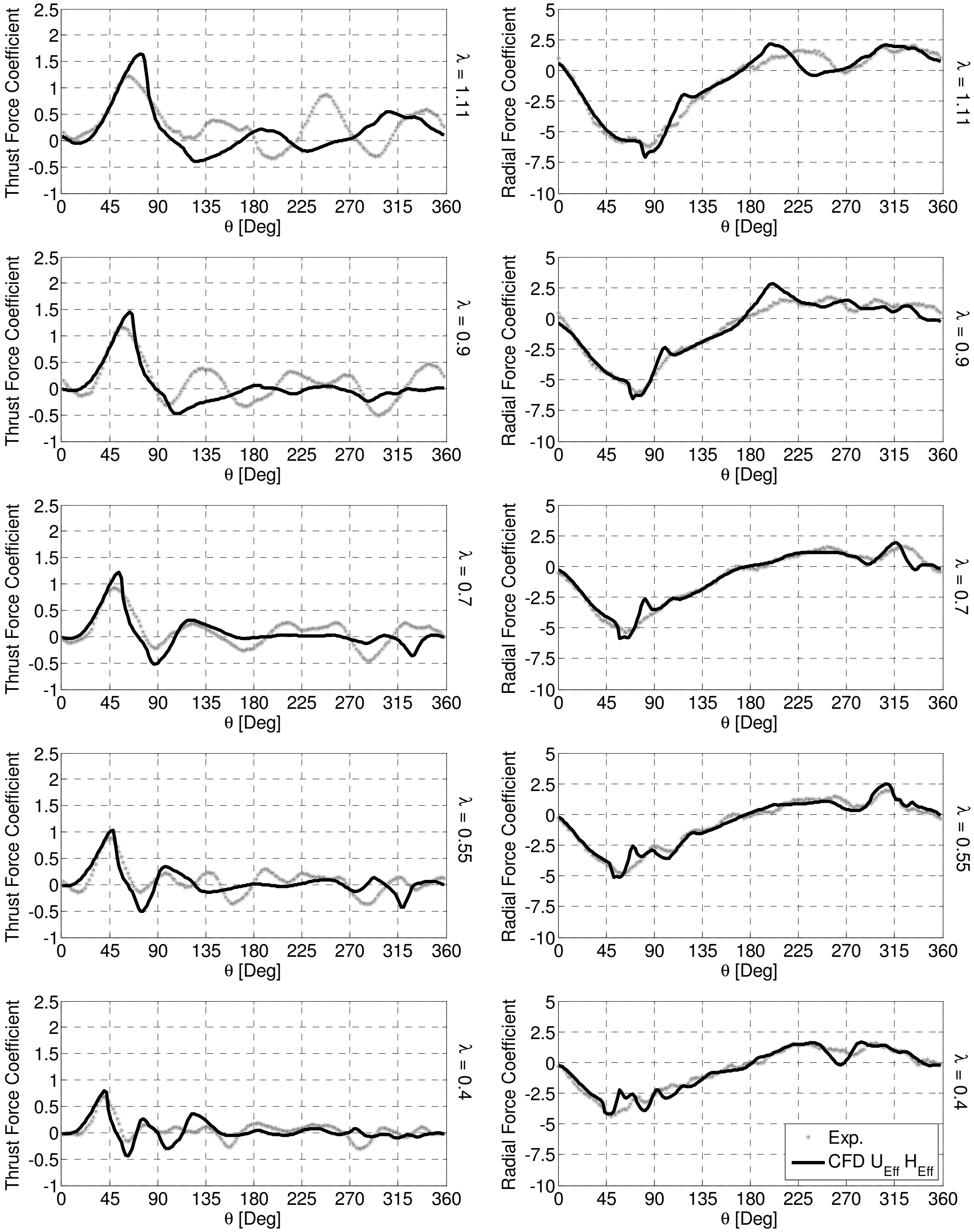

Figure A.20 Continued: Aerodynamic force coefficients (NACA 0015, *c* = 420 mm, *β* = 2.66°)

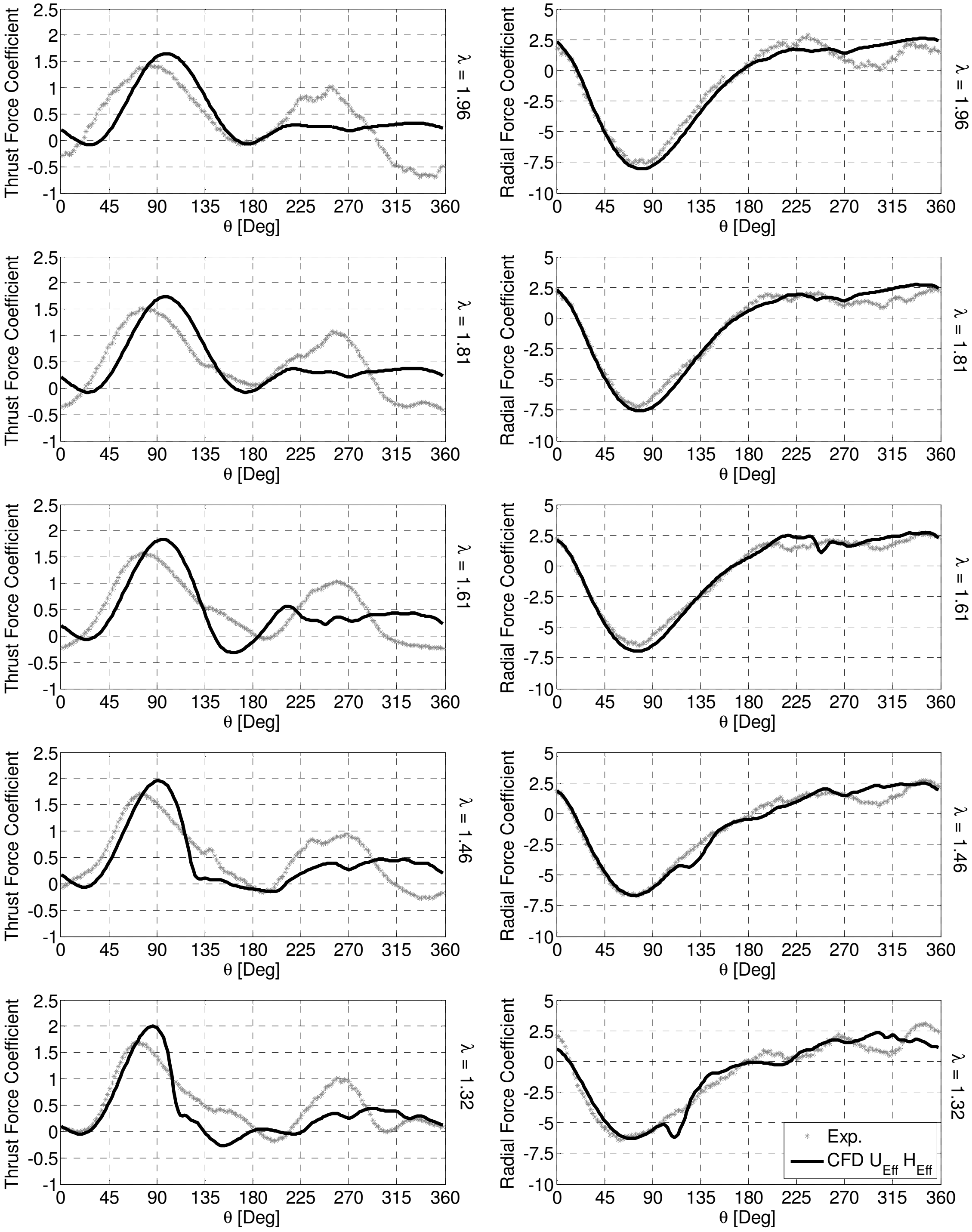

Figure A.21: Aerodynamic force coefficients (NACA 0021, *c* = 400 mm, *β* = 0°)

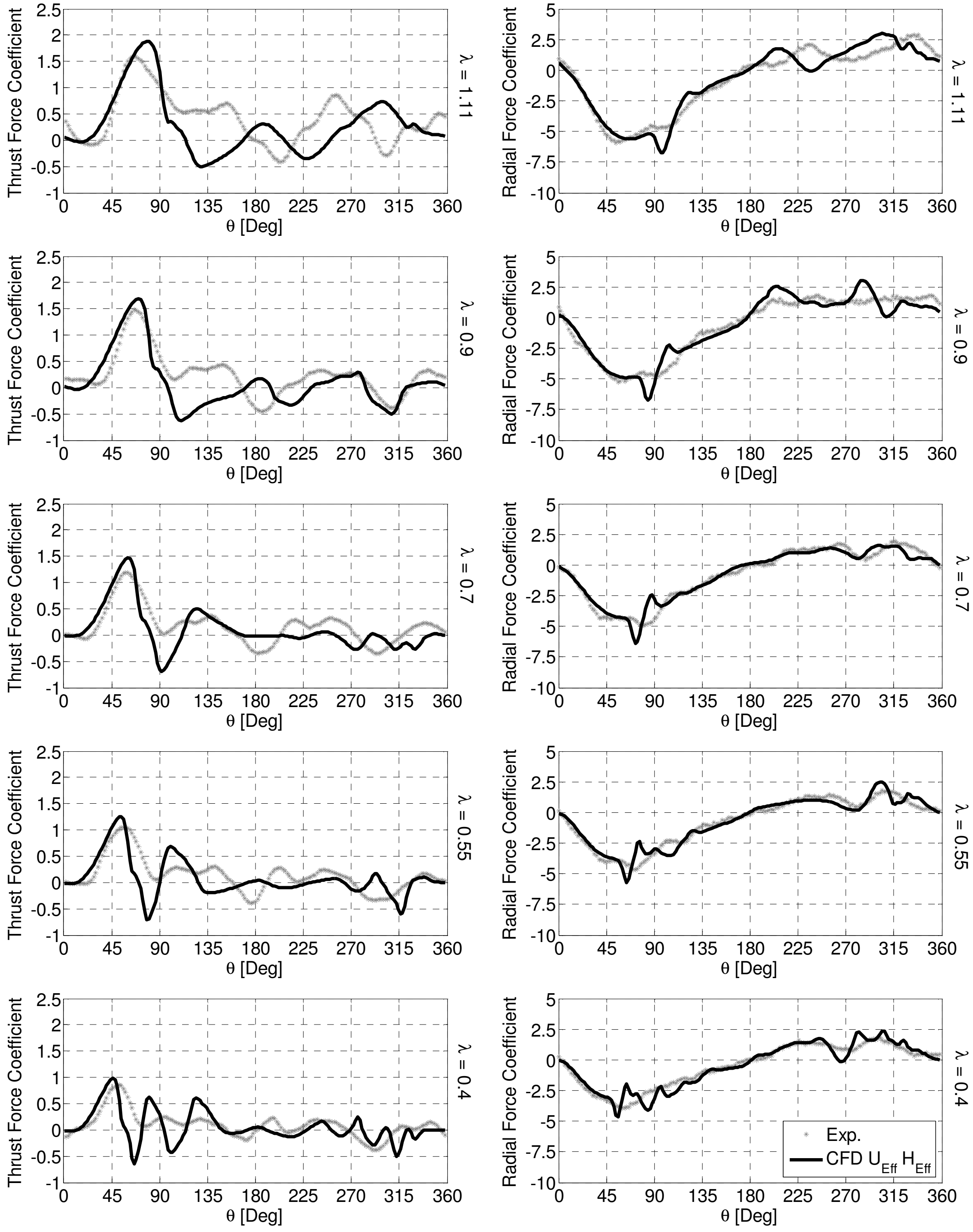

Figure A.21 Continued: Aerodynamic force coefficients (NACA 0021, *c* = 400 mm, *β* = 0°)

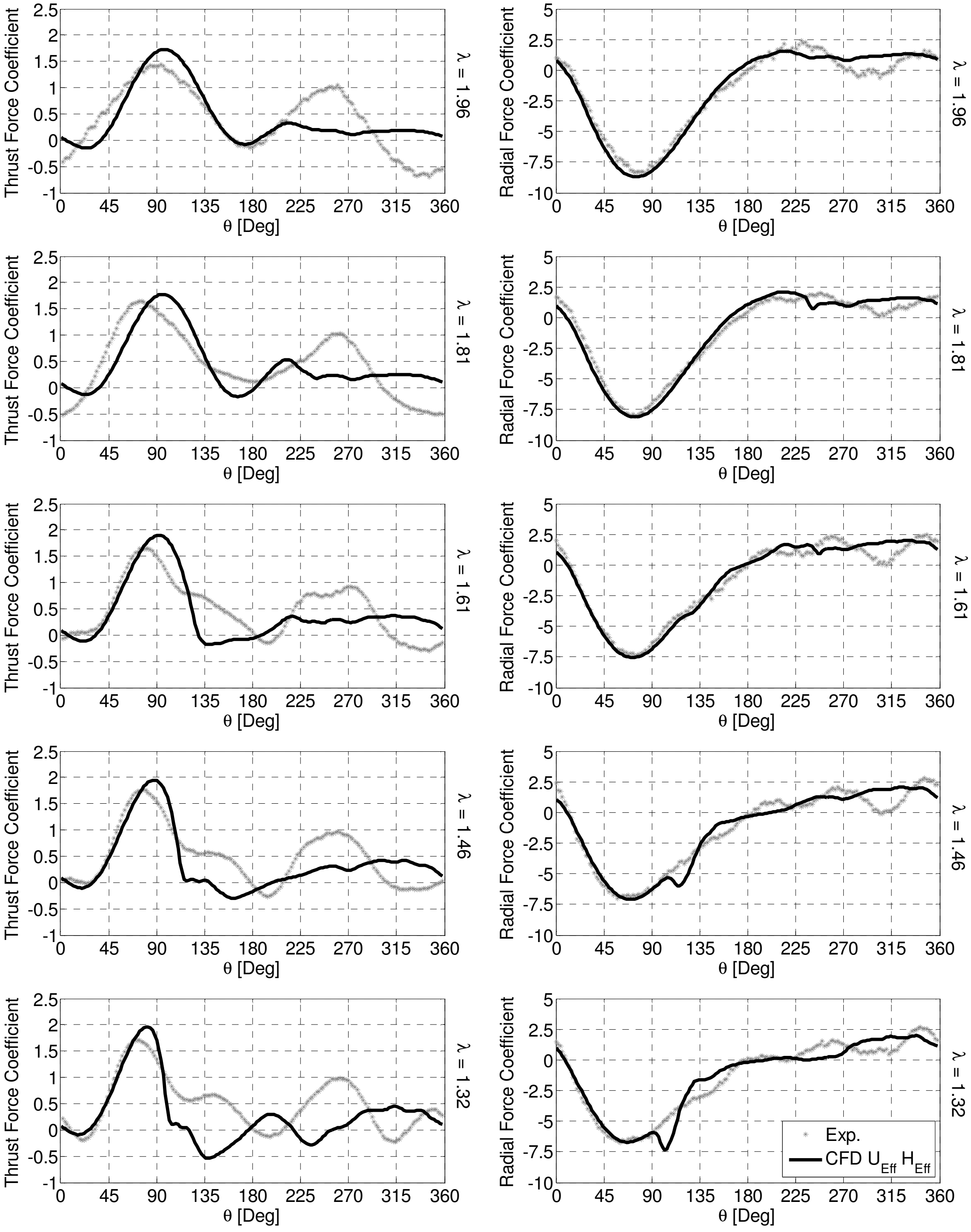

Figure A.22: Aerodynamic force coefficients (NACA 0021, *c* = 400 mm, *β* = 2.25°)

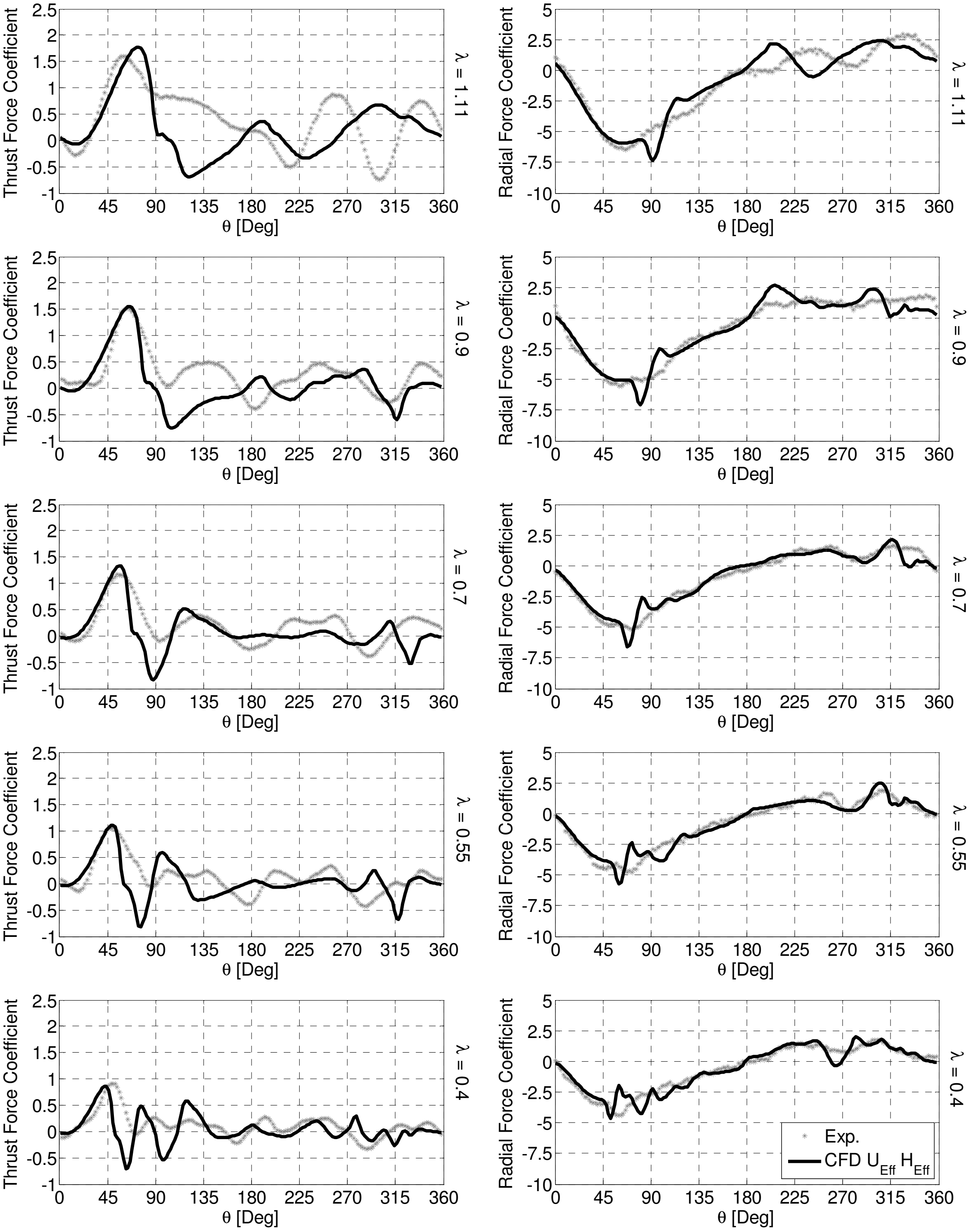

Figure A.22 Continued: Aerodynamic force coefficients (NACA 0021, *c* = 400 mm, *β* = 2.25°)

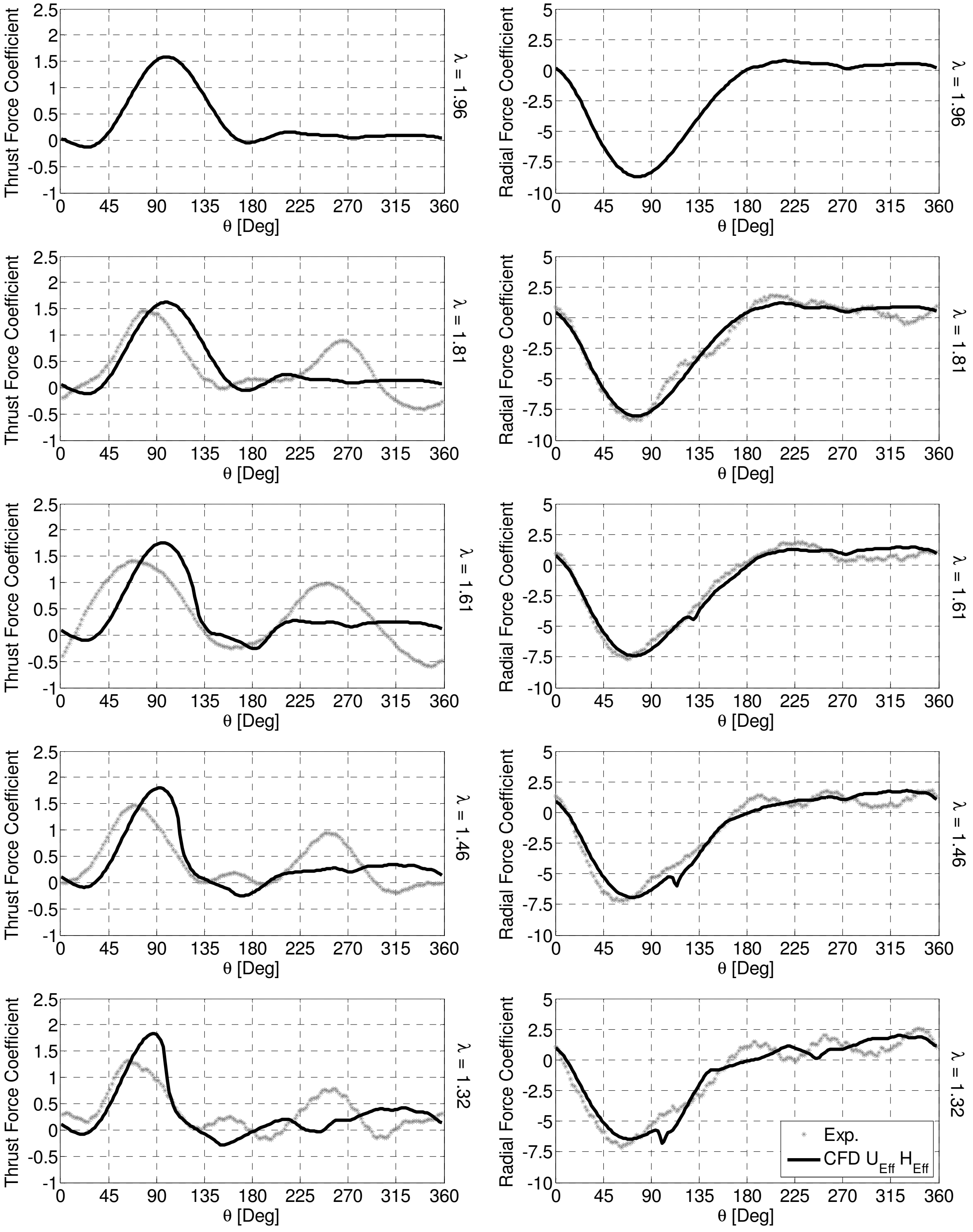

Figure A.23: Aerodynamic force coefficients (NACA 0015, *c* = 400 mm, *β* = 2.25°)

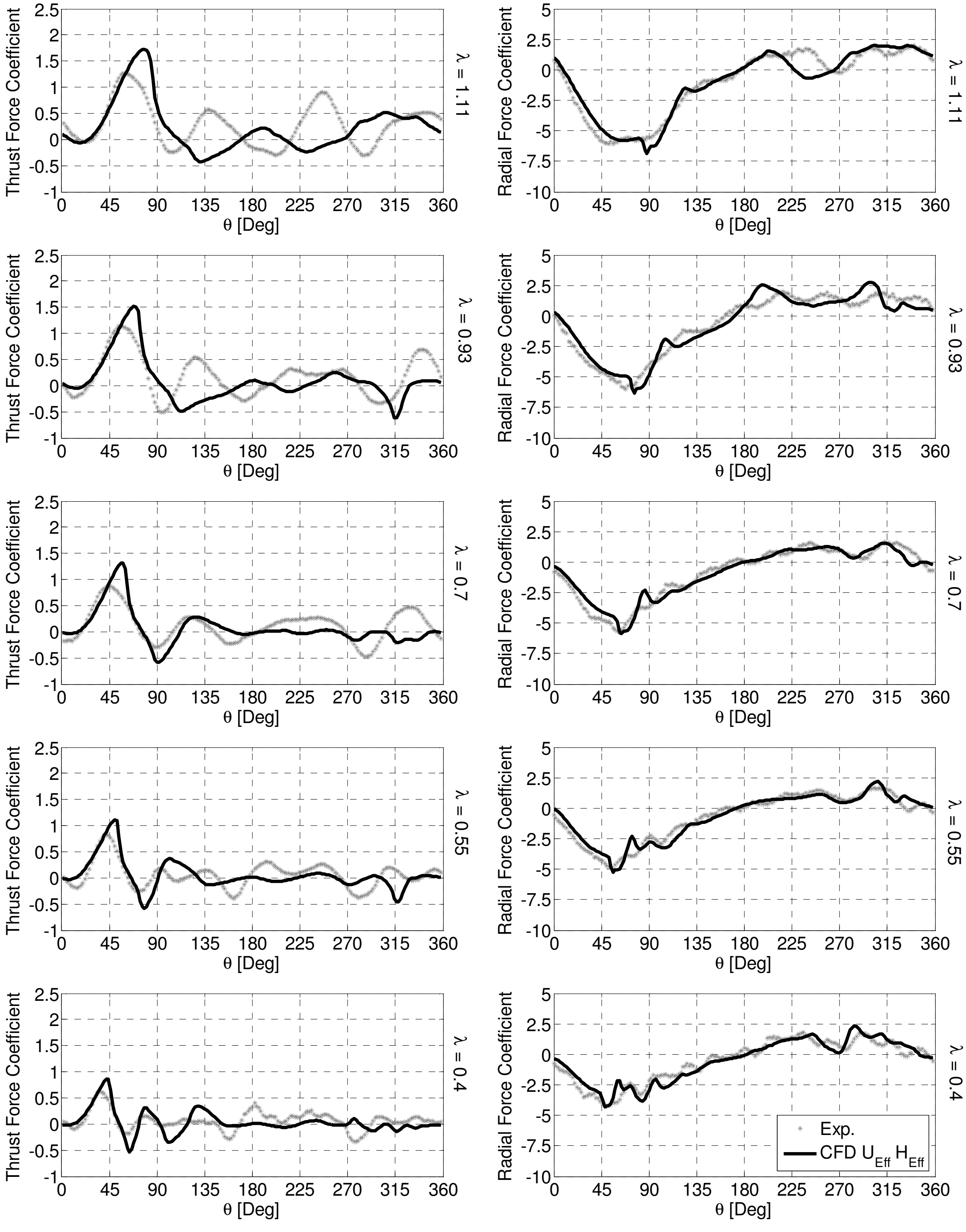

Figure A.23 Continued: Aerodynamic force coefficients (NACA 0015, *c* = 400 mm, *β* = 2.25°)

A.6. Wind Turbine Noise Production

The goal of this preliminary investigation was to obtain quantitative data on the noise production of the small scale VAWT. Qualitative measurements of the turbine noise (listening to the turbine in operation) indicated that the noise production of the turbine was insignificant. However, nearby environmental factors such as vehicular traffic may have strongly affected these assessments. Evaluation of the turbine noise was accomplished by taking pressure measurements with a G.R.A.S. microphone at several different locations on the rooftop where the turbine is located both with and without the turbine in operation. These measurements were analyzed to determine the sound pressure level (SPL), octave bands, overall SPL and A-weighted SPL of the turbine alone. This information was then used to conclusively determine whether the noise production of the VAWT under investigation is significant or not based upon accepted noise standards.

For this study, the turbine was mounted atop a tower on the rooftop of the McMaster Innovation Park building in Hamilton, Canada. In order to acquire turbine noise level data for the given turbine under normal operating conditions, on-site pressure measurements were obtained. To this end, a portable measurement system was developed. This system consisted of a ¼” G.R.A.S microphone covered with a 3” diameter microphone cover mounted on a rigid mast at a height of 4.5 m (mid height of the turbine), a signal amplifier, a USB powered portable data acquisition card and a laptop for data processing and storage. This entire set-up was mounted on a utility cart to allow for measurements to be taken at different locations on the roof, and can be seen in Figure A.24 (power was supplied to the set-up via a 50 ft extension cord). In addition to the data acquisition system outlined above, a system to quantify local wind speed was employed. Due to the random nature of the wind, measurements of the wind speed over time needed to be obtained for future correlation of data. A propeller type anemometer was mounted on an additional mast at a height of 9 m and was located at a distance of 1 diameter (2.5 m) from the leading edge of the turbine (Figure A.24).

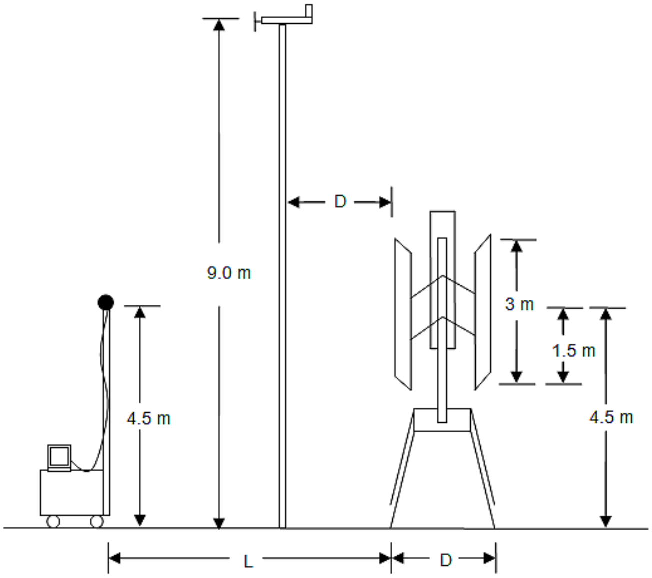

Figure A.24: Experimental noise measurement set-up

In order to obtain a large cross-section of data to work with, a wide range of measurements were taken. Pressure measurements were recorded at 1 second intervals and averaged over a period of 1, 2, and 5 minutes in an effort to moderate the effects of the random nature of the wind velocity. These measurements were obtained at distances of L/D = 1, 2, 4, 7, and 10 in order to capture the effect of proximity to the wind turbine. Measurements at each location were acquired with the turbine stationary in order to capture the background noise level as well as with the turbine in operation in order to capture the combined noise level of the turbine and background. Subtracting these two noise levels produces the noise level of the turbine in operation alone. In addition, multiple measurements were taken at each location at different times of the day in order to obtain data at a number of wind speeds. The ranges used to classify the wind speed will henceforth be classified as Low (< 11 m/s), Moderate (11 – 12 m/s) or High (> 13 m/s) where the available data permits. Unfortunately, data for small L/D at high wind speeds was not captured so these points were omitted from the results. Furthermore, inadequate data was obtained for low wind speed at L/D = 10 so this data is also omitted. Wind speed measurements were constantly recorded and logged at 1 second intervals through the use of a battery operated data logger mounted on the anemometer mast.

The initial signal obtained from the microphone was output as a voltage over time and a certain degree of data processing was required to convert this data into a useable form. First, taking the Fourier transform of this signal translated the data into the frequency domain at a sampling frequency of 1 Hz, but with uncalibrated signal amplitude. The pressure spectrum was calibrated using a microphone calibrator which produces a 1000 Hz signal at a sound pressure level of 114.02 dB. The octave and 1/3 octave bands could then be calculated from the power spectrum of the signal. Figure A.25 below is a comparison of the pressure spectrum to the octave and 1/3 octave levels in dB.

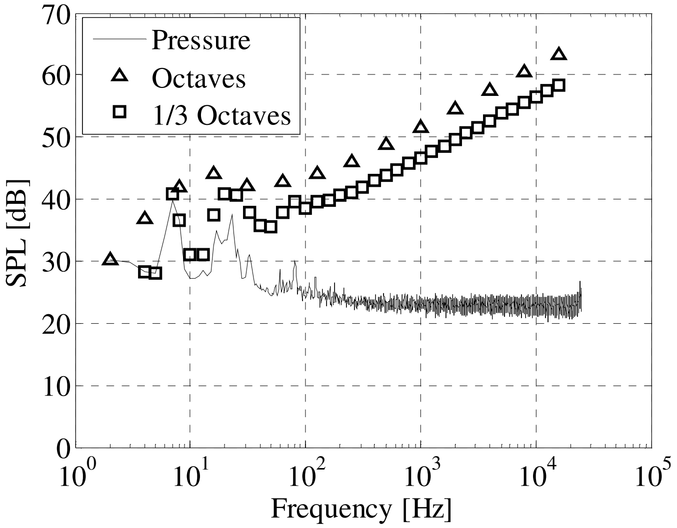

Figure A.25: Sample pressure spectrum including octave and 1/3 octave levels

From this example it is apparent that dominant peaks in pressure at 7, 17, 23 and 33 Hz clearly exist within the pressure signal. For the given sample results, the turbine was operating at a rotational velocity of approximately 140 RPM. This translates into a blade passing the upwind side of the turbine at $f \approx 7$ Hz and it can be speculated that this accounts for the large peak in pressure at this "blade pass" frequency. The peak occurring at 23 Hz appears to be a higher harmonic of this frequency as it occurs at approximately 3 times the dominant fundamental frequency. The less dominant peak at 17 Hz is most likely generated by background noise and interestingly enough has its first harmonic at a frequency of approximately 33 Hz. Further investigation into this behaviour is appropriate only after the background noise has been removed from the octave and 1/3 octave levels. Because the octave bands are too large to capture the finer details of the pressure spectrum, while the 1/3 octave bands are able to properly represent this behaviour, the 1/3 octave bands were used for all analysis henceforth. To obtain an overall sound pressure level for the turbine at a given distance for a particular wind speed it is first necessary to subtract the 1/3 octave levels obtained without the turbine in operation, from the 1/3 octave levels with the turbine in operation (Figure A.26).

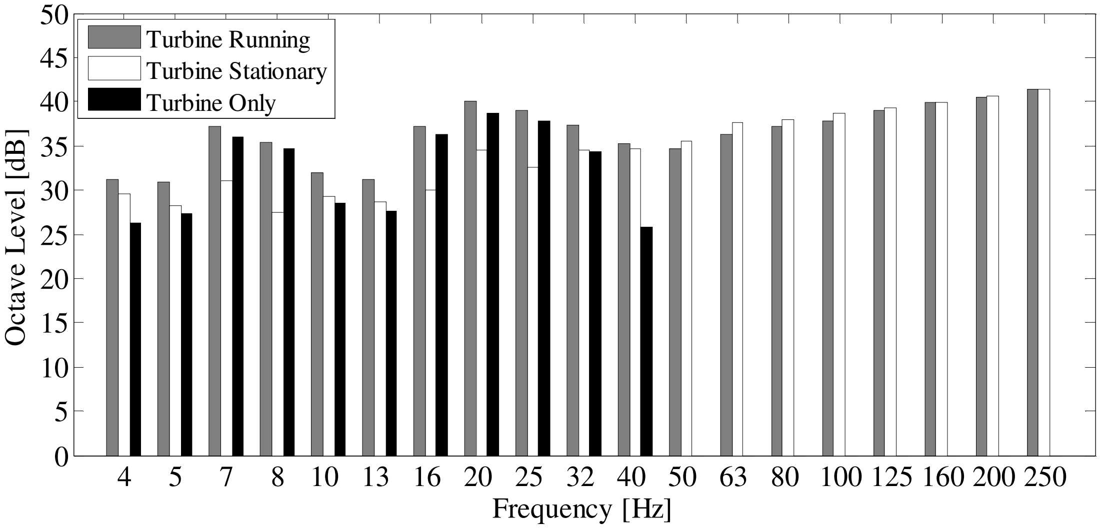

Figure A.26: Sample octave level subtraction

Observation of these results reveals that under these conditions the turbine produces negligible noise in the 1/3 octave bands beyond f_c = 40 Hz (Figure A.26). Additionally, the majority of the turbine noise is generated at or near the blade passing frequency of 7 Hz and its higher harmonic at 20 Hz, while the pressure spikes at 17 and 33 Hz have been all but eliminated. The overall sound pressure level can now be determined by summing the octave levels of the turbine alone. Figure A.27 below shows the dB level of the turbine alone as a function of wind speed and proximity to the turbine. As mentioned earlier, due to available wind conditions and adequate data, no measurements were obtained for high wind speeds at close proximity to the turbine or low wind speeds at large distances from the turbine.

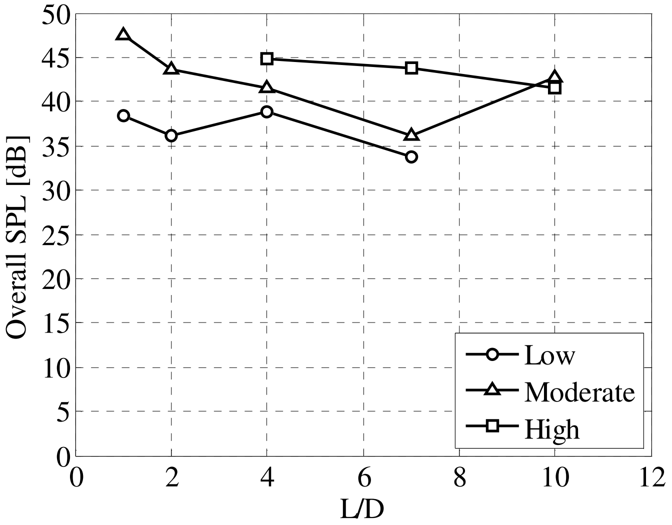

Figure A.27: Overall turbine noise in dB

From Figure A.27 it can be observed that the noise level of the turbine is both a function of the proximity to the wind turbine as well as the magnitude of the wind speed. In general, as one moves toward the turbine the overall noise level increases by a small amount up until a distance of 1 diameter, which is the minimum safe distance that a person may approach the turbine while in operation. Furthermore, as the wind speed increases, so does the noise level of the turbine. Again, this increase is minimal and the overall noise level of the turbine remains below 50 dB for all normal operating conditions (the turbine rarely operates at a wind speed beyond 15 m/s). In order to determine how the human ear perceives the turbine noise level, the dB level is given an A-weighting based upon the average human hearing capability. Transferring the dB level of the turbine into the dBA scale (Figure A.28) reveals that there is no strong correlation of the turbine noise with either proximity to the turbine or the wind speed level, as was previously observed in the prior qualitative tests. Because the majority of the turbine noise is produced in the infrasound range (frequencies below human perception) the dBA level is greatly reduced from the dB level. This is because the A-weighting procedure minimizes the effect of very low and very high frequency noise on the overall sound pressure level.

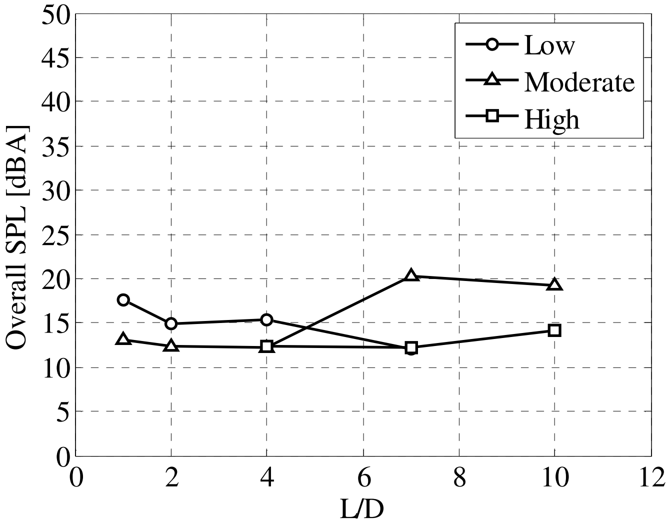

Figure A.28: Overall turbine noise in dBA

Ultimately, the turbine noise production at even just 1 diameter from the turbine is nearly imperceptible to the human ear. Furthermore, most regional standards place a maximum noise level production limit at 50 dBA, which is well above that of the given turbine. Based on the results of the preceding study it can be concluded that the noise level production of the small scale VAWT under investigation is insignificant, and poses no threat to the comfort of nearby persons or wildlife.